Precision measurements with atomic hydrogen masers

A thesis presented

by

Marc Andrew Humphrey

to

The Department of Physics

in partial fulfillment of the requirements

for the degree of

Doctor of Philosophy

in the subject of

Physics

Harvard University

Cambridge, Massachusetts

May 2003

Advisor: Dr. Ronald Walsworth Author: Marc Andrew Humphrey

Precision measurements with atomic hydrogen masers

We report two experimental results and a theoretical study involving atomic hydrogen masers oscillating on the $\Delta F = 1$, $\Delta m_F = 0$ hyperfine transition. In the first experiment, we placed a new limit on Lorentz and CPT violation of the proton in terms of a recent standard model extension. By placing a bound on sidereal variation of the $F = 1$, $\Delta m_F = \pm 1$ Zeeman frequency in atomic hydrogen, our search set a limit on violation of Lorentz and CPT symmetry of the proton at the 10^{-27} GeV level, independent of nuclear model uncertainty, and improved significantly on previous bounds. This test utilized a double resonance technique in which the oscillation frequency of a hydrogen maser is shifted by applied radiation near the $F = 1$, $\Delta m_F = \pm 1$ Zeeman resonance. We used the dressed atom formalism to calculate this frequency shift and found excellent agreement with a previous calculation made in the bare atom basis. Qualitatively, the dressed atom analysis gave a simpler physical interpretation of the double resonance process. In the second experiment, we investigated low temperature hydrogen-hydrogen spin-exchange collisions using a cryogenic hydrogen maser. Operational details of the apparatus are presented and a description of our measurement of the semi-classical spin-exchange shift cross section $\bar{\lambda}_0$ at 0.5 K is given. We report a value of $\bar{\lambda}_0 = 56.70$ Å^2 with a statistical error of 15.51 Å^2 and a systematic uncertainty between 80.6 and 318.8 Å^2. A discussion of this systematic is given and the possiblity of an improved measurement is discussed.

Contents

Acknowledgments

No page of this thesis could have been written without the positive leadership of Ron Walsworth. His countless ideas, broad physical insight, and experimental inventiveness underly every result, while his support, motivation, and management set the stage on which all of this work was performed. Much the same echos true for David Phillips. A scientist, teacher, and friend, David taught me how to survive in graduate school, and equally important, how to get out. With Ron at the helm and David in the trenches this thesis was brought to completion.

My understanding and appreciation of hydrogen masers would have been much less complete without the ubiquitous presence of Bob Vessot and Ed Mattison. They taught me what only world-class experts could, and did so wearing nothing but smiles. I am grateful that I could conduct my research under their distinguished guidance. Moreover, the SAO hydrogen maser lab would be wholly incomplete without the presence of Jim Maddox. Much extra effort was spared and unnecessary grief avoided because of his technical ingenuity.

The offices and labs of the SAO were filled with life by each of the past and current members of the Walsworth group. Many smiles were shown, some tears suppressed, and much camaraderie shared by the great people who made my days less lonely. David Bear showed me how to live life outside the lab; Glenn Wong showed me how to do so while in. Rick Stoner taught me the value of perseverance and attention to detail. Caspar van der Wal and Federico Canè kept my mind from growing flat. In their different ways, Ross Mair and Matt Rosen always brought the same broad smile to my face. I thank Ruopeng Wang, Yanhong Xiao, Leo Tsai, Mason Klein and John Ng for letting me show that one really can make it through the PhD. Of course, we would have all gone mad were it not for Kristi Armstrong.

Beyond the four walls of B-112, my life has been rounded out by a few very special people. I thank Bob Michniak for the many fruitful discussions about everything but

physics, and Mike Bassik for the numerous hours over numerous pints and the numerous trips to Fenway. I thank Brandon Johnson for saving me early on from being far too serious. Above all, I thank Kathrin Könitzer for her patience, for her cheer, and for showing me that one really can strike gold in the foothills of Nepal.

From the very beginning to the very last day, I have relied on and benefitted from the constant and unconditional support of Christie Hong. While working on our own, we made it through graduate school together. Time after time she offered me her ear and lent me her shoulder, and during the darkest days it was she who pulled me through when nobody else could. I would not have survived without her, nor will I ever find the words to show her my full gratitude.

It goes without saying that I would not have finished my PhD without the love and support of my family. More importantly, without them I would have never even begun. I thank my brother for showing me what it means to succeed, and my parents for sharing in our achievements. Their simple lesson that hard work and determination are all one needs to reach their dreams gave me the courage to begin, the strength to continue, and the will to finish this chapter of my life. I thank my family for being my biggest fans, my closest friends, and my greatest inspiration.

List of Figures

List of Tables

This thesis is dedicated to my mom,

the only genuine hero that I have ever known.

Chapter 1

Introduction

The atomic hydrogen maser [1–4] was developed in the early 1960s in the laboratory of Norman Ramsey at Harvard University. Its realization came as an extension of the attempt to increase the precision of atomic beam magnetic resonance experiments by narrowing the atomic linewidth. In a hydrogen maser, a beam of hydrogen atoms is magnetically state selected such that the higher energy, low-field-seeking hyperfine states flow into a storage bulb situated inside a microwave cavity resonant with the 1420 MHz hyperfine transition. The atoms reside inside the storage bulb for about 1 s, during which time they interact coherently with the microwave field. The microwave field stimulates a macroscopic magnetization within the atomic ensemble, and this magnetization in turn stimulates the microwave cavity field. This continuous coherent interaction is referred to as active maser oscillation.

The hydrogen maser utilizes two ideas that were under investigation at the time of its development. First, it applies the concept of narrowing the atomic linewidth by increasing the coherent interaction time between the atom and the field. This was essentially an extension of Ramsey's separated oscillatory fields technique [5] where atoms are prepared and then detected using two separated but coherent microwave fields. The atomic linewidth is reduced as the transit time between the separated fields is increased. Hydrogen masers dramatically increase this interaction time by storing the coherent atomic

ensemble in the presence of the microwave field. This was enabled by the discovery of suitable wall coatings which allow the atoms to be stored in a cell for times greatly exceeding the atom transit time across the cell. Indeed, the choice of hydrogen was made since its small atomic polarizability allows for considerably longer storage times before losing coherence due to collisions with the cell wall. In a room temperature maser, a wall coating of Teflon[1] was found to be optimal; in a cryogenic hydrogen maser [6–11], a superfluid ^{4}He film is employed.

Second, the concept of microwave amplification by stimulated emission is utilized, as first demonstrated with the ammonia beam maser [12, 13]. Since the choice of hydrogen as the atomic species precluded typical atomic detection schemes, such as the hot wire method, the use of maser oscillation allowed for the interrogation of the atoms by detecting their radiation field rather than by direct detection of the atoms themselves.

Soon after its original demonstration 40 years ago, it was realized that hydrogen masers could be employed as ultra-stable atomic frequency standards. Today, well engineered hydrogen masers have fractional frequency stabilities of about 10^{-15} over intervals of 10^3 - 10^5 s [4]. This stability is enabled by the long atom-field interaction time and the reduced atom-wall interaction, plus reduced Doppler effects (the atoms are confined to a region of uniform microwave field phase), reduced Zeeman effects (the hyperfine transition is magnetic-field-independent to first order), mechanically stable resonant cavity materials, and multiple layers of thermal and magnetic field control. Hydrogen masers are currently used for applications including radioastronomy and geophysics [14], deep-space tracking and navigation, and metrology [15]. The hydrogen maser has also served as a robust tool capable of making high-precision measurements by utilizing its excellent frequency stability. Hydrogen masers have been used to make precision atomic physics measurements [16–19] and for sensitive tests of general relativity [20, 21] and quantum mechanics [22, 23].

The contents of this thesis are as follows. We begin in Chapter 2 with a complete

[1]Teflon is a trademark of E.I. duPont de Nemours and Co., Inc.

theoretical description of the hydrogen maser. We first review standard hydrogen maser theory and develop analytic expressions for maser oscillation frequency and maser power. Then we review a treatment of double resonance in hydrogen masers in which the effects of radiation resonant with the $F = 1$, $\Delta m_F = \pm 1$ Zeeman transitions [24] are studied. Finally we present an analysis of these double resonance effects using the dressed atom formalism [25], an analysis we made in an attempt to gain physical insight into this double resonance process.

In Chapter 3 we discuss the practical realization of a room temperature hydrogen maser. A thorough description of the technical development of Smithsonian Astrophysical Observatory VLG-10 and VLG-12 series masers is presented. We begin with a detailed description of the maser apparatus, then discuss its characterization and typical operating parameters. We conclude with a discussion of frequency stability of room temperature hydrogen masers.

In Chapter 4 we present an application of hydrogen maser double resonance in a test of Lorentz and CPT symmetry. By searching for sidereal variations in the hydrogen $F = 1$, $\Delta m_F = \pm 1$ Zeeman frequency, we set a limit on violation of Lorentz and CPT symmetry of the proton at the 10^{-27} GeV level, the cleanest such bound placed to date [26]. First we review a theoretical framework recently developed which incorporates possible CPT and Lorentz symmetry violation into the standard model [27, 28]. Then we describe the experimental procedure we used to test it and present our results within the context of the standard model extension.

In Chapter 5 we describe the principles and development of a cryogenic hydrogen maser (CHM). Compared to a room temperature hydrogen maser, a cryogenic maser has the potential for a three-order-of-magnitude improvement in frequency stability [6], however the realization of this improvement is compromised by technical challenges and by low temperature hydrogen-hydrogen collisional effects. After reviewing the motivation for a cryogenic maser, we discuss in detail the technical development of such a device, including the employment of a superfluid ^{4}He film wall coating, the construction of the

maser apparatus, and the cryogenic requirements needed to maintain a hydrogen maser at 0.5 K. We conclude with a discussion of the performance of our CHM.

Finally, in Chapter 6 we discuss the effects of hydrogen-hydrogen spin-exchange collisions in hydrogen masers. There currently remain a number of discrepancies between experiment and the theory for these effects. We begin with a historical overview of hydrogen maser spin-exchange theory and then discuss several experimental studies. Finally, we present our measurement of the semi-classical spin-exchange shift parameter $\bar{\lambda}_0$ at 0.5 K. Within systematic error, our measurement is in agreement with previous experimental [29] and theoretical [30, 31] values, however it lacks the precision to resolve the discrepancy between them. We conclude with a discussion on the source of our systematic error and on possible routes with which to improve the measurement.

Chapter 2

Hydrogen maser theory

In this chapter we will develop a theoretical treatment for the hydrogen maser. We begin with a description of the atomic hydrogen hyperfine levels and an overview of standard hydrogen maser operation. In Section 2.1 we will assume a single coupling between the $F = 1$, $m_F = 0$ and $F = 0$, $m_F = 0$ hyperfine levels. In Section 2.2, we will examine the effect of a transverse field tuned near the $F = 1$, $\Delta m_F = \pm 1$ Zeeman transitions. For simplicity, we also assume throughout a simplified relaxation effect of spin-exchange collisions. The effect of these collisions will be considered in more detail in Chapter 6.

The electronic ground state of hydrogen is split into four levels by the hyperfine interaction, labeled $|1\rangle$ to $|4\rangle$ in order of decreasing energy (Figure 2.1). The energies of atoms in states $|1\rangle$ and $|2\rangle$ decrease as the magnetic field decreases; these are therefore low-field seeking states. Conversely, $|3\rangle$ and $|4\rangle$ are high-field seeking states. In low fields, the energies of states $|2\rangle$ and $|4\rangle$ have only a second-order dependence on magnetic field. A hydrogen maser typically oscillates on the $|2\rangle \leftrightarrow |4\rangle$ transition. This transition frequency (in hertz) as a function of static magnetic field (in gauss) is given by $\nu_{24} = \nu_{hfs} + 2750B^2$, where $\nu_{hfs} \approx 1{,}420{,}405{,}752$ Hz is the zero-field hyperfine frequency. Hydrogen masers typically operate with low static fields (less than 1 mG), such that the two $F = 1$, $\Delta m_F = \pm 1$ Zeeman frequencies are given by $\nu_{12} = 1.4\times10^6 B - 1375B^2$ and $\nu_{23} = 1.4\times10^6 B + 1375B^2$. At $B = 0.5$ mG these Zeeman splittings are nearly degenerate, with $\nu_{12} - \nu_{23} \approx 1$ mHz,

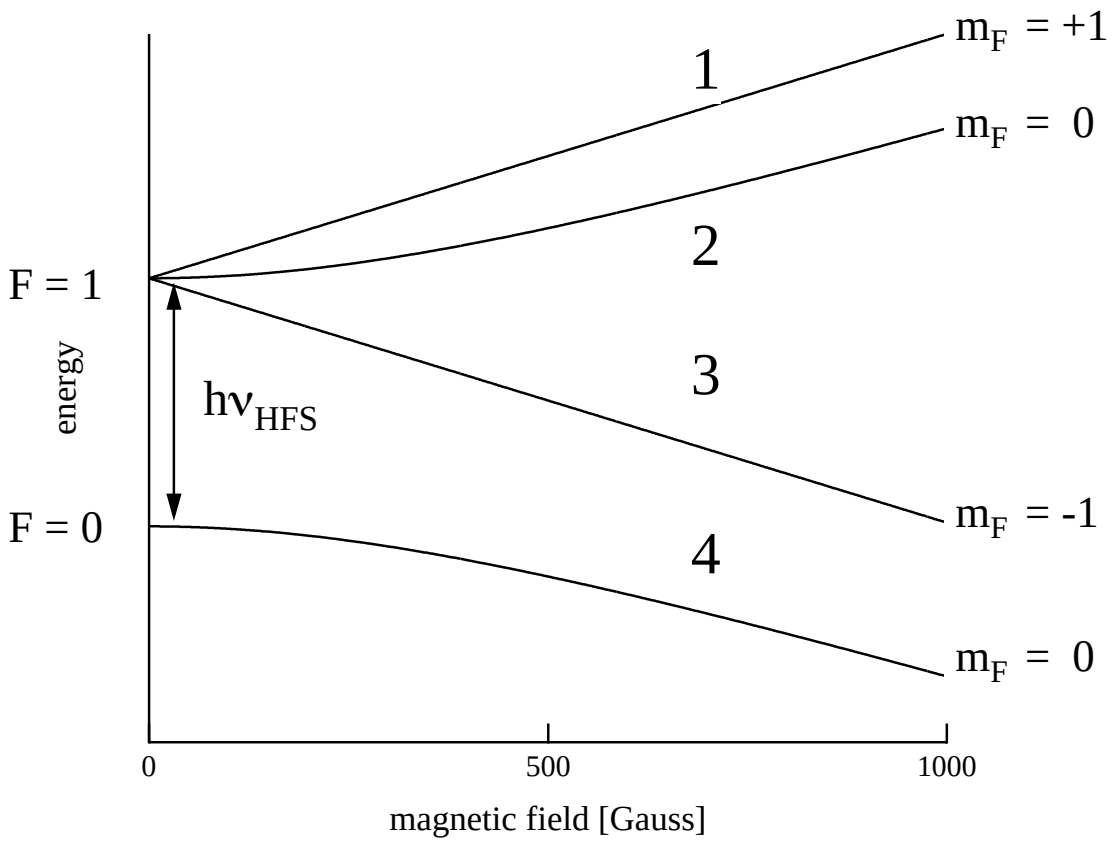

Figure 2.1: Hydrogen hyperfine structure. A hydrogen maser oscillates on the first-order magnetic-field-independent $|2\rangle \leftrightarrow |4\rangle$ hyperfine transition near 1420 MHz. The maser typically operates with a static field less than 1 mG. For these low field strengths, the two $F = 1$, $\Delta m_F = \pm 1$ Zeeman frequencies are nearly degenerate, and $\nu_{12} \approx \nu_{23} \approx 1$ kHz.

much less than the typical Zeeman linewidth of approximately 1 Hz.

In a conventional hydrogen maser [1–4], which operates near room temperature, molecular hydrogen is dissociated in an rf discharge and a beam of hydrogen atoms is formed, as shown schematically in Figure 2.2. A hexapole state selecting magnet focuses the low-field-seeking hyperfine states $|1\rangle$ and $|2\rangle$ into a quartz maser bulb at about 10^{12} atoms/sec. Inside the bulb (volume $\sim 10^3$ cm^3), the atoms travel ballistically for about 1 second before escaping, making $\sim 10^4$ collisions with the bulb wall. A Teflon coating reduces the atom-wall interaction and thus inhibits decoherence of the masing atomic ensemble due to wall collisions. The maser bulb is centered inside a cylindrical TE_{011} microwave cavity

resonant with the 1420 MHz hyperfine transition. The thermal microwave field stimulates a coherent magnetization $\mathbf{M}$ on the $|2\rangle$ to $|4\rangle$ transition in the atomic ensemble, and this magnetization acts as a source to stimulate the microwave cavity field $\mathbf{H}_C$. With sufficiently high atomic flux and low cavity losses, this feedback induces active maser oscillation.

The maser signal (typically about 10^{-13} W) is inductively coupled out of the microwave cavity, amplified, and detected with a low noise heterodyne external receiver. Surrounding the cavity, a main solenoid and two end coils produce a weak static magnetic field ($\mathbf{B}_0 \approx 1$ mG) which establishes the quantization axis inside the maser bulb and sets the Zeeman frequency (≈ 1 kHz). Another pair of coils can be used to produce the oscillating transverse magnetic field $\mathbf{H}_T$ that drives the $F = 1$, $\Delta m_F = \pm 1$ Zeeman transitions. The cavity, solenoid and Zeeman coils are all enclosed within several layers of high permeability magnetic shielding.

2.1 Standard hydrogen maser theory

In this section, we will derive analytic expressions for the hydrogen maser oscillation frequency and power. These relations are found by first considering the effect of the microwave cavity field on the atoms, which acts to establish a macroscopic magnetization in the atomic ensemble. This magnetization is then coupled back to the cavity, by treating it as a source term for the microwave cavity field, and the steady state maser frequency and amplitude are found.

2.1.1 Interaction of atoms with cavity field

The dynamics of the atomic ensemble inside of the storage bulb are governed by the Bloch equation

$$\dot{\rho} = \frac{i}{\hbar}[\rho, H_0] + \frac{i}{\hbar}[\rho, H_{int}] + \dot{\rho}_{flux} + \dot{\rho}_{relax}. \tag{2.1}$$

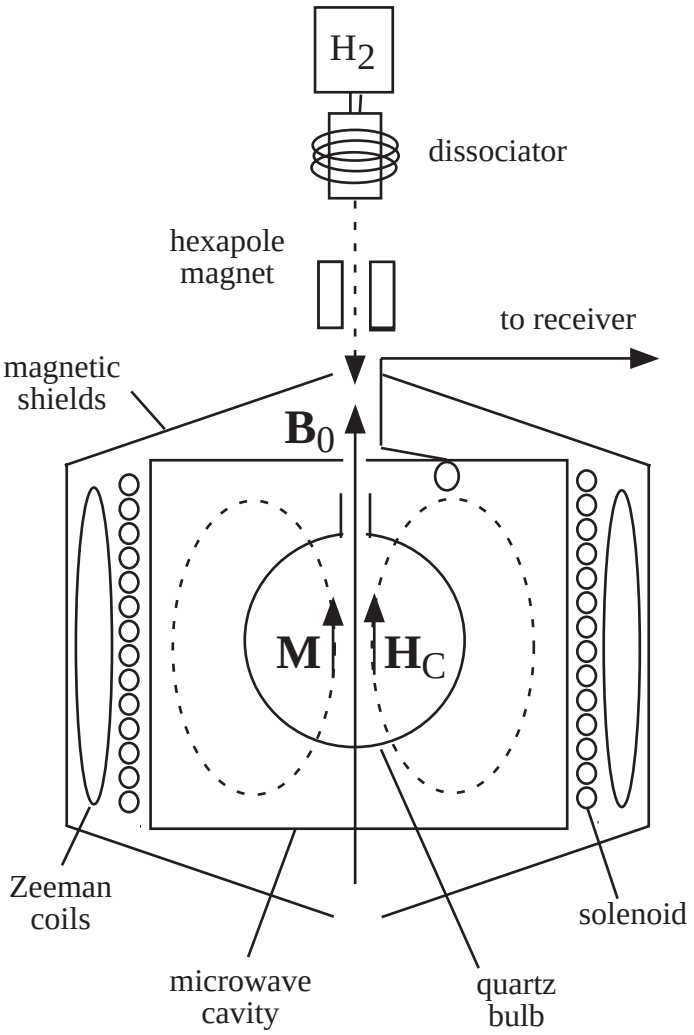

Figure 2.2: Hydrogen maser schematic. The solenoid generates a weak static magnetic field $\mathbf{B}_0$ which defines a quantization axis inside the maser bulb. The microwave cavity field $\mathbf{H}_C$ (dashed field lines) and the coherent magnetization $\mathbf{M}$ of the atomic ensemble form the coupled actively oscillating system.

The first term describes the interaction of the atoms with the static solenoid field. Taking the energy of state $|4\rangle$ as our energy zero, and assuming the hyperfine and Zeeman splittings are fixed, then H_0 is given by

$$H_0 = \hbar\omega_{14}|1\rangle\langle 1| + \hbar\omega_{24}|2\rangle\langle 2| + \hbar\omega_{34}|3\rangle\langle 3| \tag{2.2}$$

where the difference frequency between levels i and j is denoted by $\omega_{ij} = \omega_i - \omega_j$.

The second term of the Bloch equation (Eqn. 2.1) describes the interaction of the atoms with the microwave cavity field, with the interaction Hamiltonian given by $H_{int} = -\hat{\mu}\cdot\mathbf{H}_C$, where $\hat{\mu}$ is the net magnetic moment of the atomic ensemble. Since the cavity field $\mathbf{H}_C$ is parallel to the quantization axis (the static field $\mathbf{B}_0$) in the atomic storage region, it therefore couples states $|2\rangle$ and $|4\rangle$:

$$H_{int} = H_{24}|2\rangle\langle 4| + h.c. \tag{2.3}$$

where $h.c.$ denotes Hermitian conjugate. If we denote the cavity field by $\mathbf{H}_C = H_C\hat{\mathbf{z}}\cos(\omega t)$, then

$$H_{24} = -\frac{\hbar}{2}X_{24}\left(e^{i\omega t} + e^{-i\omega t}\right) \tag{2.4}$$

where X_{24} is the Rabi frequency, given by $\hbar X_{24} = \mu_{24}H_C$, with the dipole matrix element

$$\mu_{24} = \langle 2|\hat{\mu}_z|4\rangle = \frac{1}{2}\mu_B(g_J - g_I) \approx \mu_B, \tag{2.5}$$

where g_J and g_I are the electron on proton g-factors and μ_B is the Bohr magneton.

The third term of the Bloch equation (Eqn. 2.1) describes the atomic flux into the bulb. For perfect hexapole state selection, this term is written

$$\dot{\rho}_{flux} = \frac{r}{2}\left(|1\rangle\langle 1| + |2\rangle\langle 2|\right), \tag{2.6}$$

accounting for the injection of atoms in states $|1\rangle$ and $|2\rangle$ at rate r.

The final term of the Bloch equation (Eqn. 2.1) is a relaxation term that describes population decay and decoherence. Population decay is characterized by

$$\dot{\rho}_{relax,ii} = -\gamma_1(\rho_{ii} - \frac{1}{4}), \tag{2.7}$$

where we assume relaxation to an equipopulation of the four states, and decoherence is described by

$$\dot{\rho}_{relax,ij} = -\gamma_2\rho_{ij}. \tag{2.8}$$

The relaxation rates, written as

$$\gamma_i = \frac{1}{T_i} = r + \frac{1}{T_{i,m}} + \frac{1}{T_{i,w}} + \frac{1}{T_{i,se}}, \tag{2.9}$$

account for relaxation due to bulb escape, magnetic field inhomogeneities, wall collisions, and spin-exchange collisions. Here we assume a simplified spin-exchange model where the relaxation rate is given by the collision rate, so that $\gamma_{1,se} = n\bar{v}_r\sigma$, with n the atomic density, $\bar{v}_r$ the mean relative atomic velocity, and σ the hydrogen-hydrogen spin-exchange cross section. Note that $\gamma_{2,se} = \frac{1}{2}\gamma_{1,se}$ in a hydrogen maser.

In the absence of any other couplings, we are solely interested in the population difference and coherence between states $|2\rangle$ and $|4\rangle$. Therefore, we are only concerned with three terms of the full Bloch equations: ρ_{22}, ρ_{24}, and ρ_{44}. These terms are most easily handled by moving to the interaction picture, in which the rapid secular variation at frequency ω_{24} drops out. This transformation is given by $\hat{O} = e^{-i\hat{H}_0t/\hbar}\ \tilde{\hat{O}}\ e^{i\hat{H}_0t/\hbar}$, where $\tilde{\hat{O}}$ is an interaction picture operator. After making the rotating wave approximation, the Bloch equations in the interaction picture become

$$\begin{aligned}
\dot{\tilde{\rho}}_{22} &= i\left(\frac{X_{24}}{2}\tilde{\rho}_{42}e^{-i\Delta t} - \frac{X_{42}}{2}\tilde{\rho}_{24}e^{i\Delta t}\right) - \gamma_1\tilde{\rho}_{22} + \frac{r}{2} + \frac{\gamma_1}{4} \\
\dot{\tilde{\rho}}_{24}e^{-i\omega_{24}t} &= -i\left(\frac{X_{24}}{2}(\tilde{\rho}_{22} - \tilde{\rho}_{44})e^{-i\Delta t}e^{-i\omega_{24}t}\right) - \gamma_2\tilde{\rho}_{24}e^{-i\omega_{24}t} \\
\dot{\tilde{\rho}}_{44} &= i\left(\frac{X_{42}}{2}\tilde{\rho}_{24}e^{i\Delta t} - \frac{X_{24}}{2}\tilde{\rho}_{42}e^{-i\Delta t}\right) - \gamma_1\tilde{\rho}_{44} + \frac{\gamma_1}{4}
\end{aligned} \tag{2.10}$$

where $\Delta = \omega - \omega_{24}$ is the difference frequency between the microwave field and the hyperfine frequency.

In the steady state, the populations in the interaction picture are static, $\dot{\tilde{\rho}}_{22} = \dot{\tilde{\rho}}_{44} = 0$. The coherence exhibits sinusoidal precession, $\tilde{\rho}_{24} = R_{24}e^{-i\Delta t}$, where R_{24} is constant. Substituting these into Eqn. 2.10, we find the following set of algebraic, time-independent equations:

$$\begin{aligned} 0 &= i(\frac{X_{24}}{2}R_{42} - \frac{X_{42}}{2}R_{24}) - \gamma_1\tilde{\rho}_{22} + \frac{r}{2} + \frac{\gamma_1}{4} \\ -i(\omega - \omega_{24})R_{24} &= -i\frac{X_{24}}{2}(\tilde{\rho}_{22} - \tilde{\rho}_{44}) - \gamma_2 R_{24} \\ 0 &= i(\frac{X_{42}}{2}R_{24} - \frac{X_{24}}{2}R_{42}) - \gamma_1\tilde{\rho}_{44} + \frac{\gamma_1}{4}. \end{aligned} \tag{2.11}$$

Rearranging these, and moving out of the interaction picture, we arrive at simple relations for the steady state population inversion and the steady state atomic coherence. In terms of $T_1 = 1/\gamma_1$ and $T_2 = 1/\gamma_2$, these can be written as

$$\rho_{22} - \rho_{44} = \frac{rT_1}{2}\frac{1 + T_2^2(\omega - \omega_{24})^2}{1 + T_2^2(\omega - \omega_{24})^2 + T_1T_2|X_{24}|^2} \tag{2.12}$$

and

$$\rho_{24}(\omega) = \frac{rX_{24}T_1T_2}{4}\left(\frac{i + T_2(\omega - \omega_{24})}{1 + T_2^2(\omega - \omega_{24})^2 + T_1T_2|X_{24}|^2}\right)e^{i\omega t}. \tag{2.13}$$

We note that the coherence can be decomposed into a component in phase and a component in quadrature with the microwave field. As a function of oscillation frequency ω, the in-phase component (real part of Eqn. 2.13) has a dispersive lineshape, and this leads to phenomena such as frequency shifts. The quadrature component (the imaginary part of Eqn. 2.13) has a Lorentzian lineshape, with a maximum for $\omega = \omega_{24}$, and this leads to absorption or amplification. This will be explored later in Section 2.1.4 where we find an analytic expression for maser power. Equations 2.12 and 2.13 show that both the population difference and the coherence are decreasing functions of the saturation factor $T_1T_2|X_{24}|^2$. This quantity is proportional to the square of the amplitude of the

magnetic induction and therefore to the energy stored in the cavity. As the saturation factor increases, the populations of states $|2\rangle$ and $|4\rangle$ tend to equalize and the coherence is reduced.

Finally, the macroscopic magnetization produced by the oscillating atomic ensemble is given by (neglecting the term oscillating at -ω)

$$M(\omega) = n\langle\hat{\mu}\rangle = n\ Tr(\hat{\rho}\hat{\mu}) = n\mu_{24}\rho_{42}(\omega) \approx n\mu_B\rho_{42}(\omega). \tag{2.14}$$

Since the coherence is set by X_{24} and therefore the microwave cavity field, Eqn. 2.14 shows that the macroscopic magnetization is driven by the microwave cavity field. We will discuss the effect of this at the end of Sec 2.1.2.

2.1.2 Interaction of cavity and magnetization

We will now calculate the effect of the ensemble's magnetization on the microwave cavity field. In a charge-free, external-current-free, polarization-free, lossless medium, Maxwell's equations take the form

$$\nabla \cdot \mathbf{B} = 0 \tag{2.15}$$

$$\nabla \times \mathbf{H} = \frac{1}{c}\frac{\partial \mathbf{D}}{\partial t} \tag{2.16}$$

$$\nabla \cdot \mathbf{D} = 0 \tag{2.17}$$

$$\nabla \times \mathbf{E} = -\frac{1}{c}\frac{\partial \mathbf{B}}{\partial t}, \tag{2.18}$$

with $\mathbf{D} = \mathbf{E} + 4\pi\mathbf{P} = \mathbf{E}$ and $\mathbf{H} = \mathbf{B} - 4\pi\mathbf{M}$. If we take the curl of Eqn. 2.16 and combine it with the time derivative of Eqn. 2.18, we see

$$\nabla \times \nabla \times \mathbf{H} = -\frac{1}{c^2}\frac{\partial^2}{\partial t^2}\left(\mathbf{H} + 4\pi\mathbf{M}\right). \tag{2.19}$$

Within the cavity, we can expand the magnetic field into orthonormal cavity modes [32]

$$\mathbf{H}(\mathbf{r},t) = \sqrt{4\pi}\sum_{\lambda} p_\lambda(t)\mathbf{H}_\lambda(\mathbf{r}) \tag{2.20}$$

where $p_\lambda(t)$ is the time varying amplitude and $\mathbf{H}_\lambda(\mathbf{r})$ is the time-independent spatial variation of the mode λ. For a particular mode, $\mathbf{E}_\lambda$ and $\mathbf{H}_\lambda$ obey

$$\begin{aligned} \nabla \times \mathbf{E}_\lambda &= \left(\frac{\omega_\lambda}{c}\right)\mathbf{H}_\lambda \\ \nabla \times \mathbf{H}_\lambda &= \left(\frac{\omega_\lambda}{c}\right)\mathbf{E}_\lambda. \end{aligned} \tag{2.21}$$

The orthonormality condition implies

$$\int_{cav} |H_\lambda|^2 dV = 1 \tag{2.22}$$

and thus the average magnitude of $\mathbf{H}_\lambda$ in the cavity is

$$\langle H_\lambda^2 \rangle_{cav} = \frac{1}{V_C}\int_{cav} |H_\lambda|^2 dV = \frac{1}{V_C} \tag{2.23}$$

where V_C is the cavity volume.

If we combine Eqns. 2.19 and 2.20, and apply Eqn. 2.21, we see

$$\nabla \times \nabla \times \mathbf{H} = \frac{\sqrt{4\pi}}{c^2}\sum_{\lambda} p_\lambda(t)\mathbf{H}_\lambda(\mathbf{r})\omega_\lambda^2. \tag{2.24}$$

Next, if we apply Eqn. 2.19 to Eqn. 2.20, we have

$$\nabla \times \nabla \times \mathbf{H} = -\frac{\sqrt{4\pi}}{c^2}\sum_{\lambda} \ddot{p_\lambda}(t)\mathbf{H}_\lambda(\mathbf{r}) - \frac{4\pi}{c^2}\ddot{\mathbf{M}}. \tag{2.25}$$

Combining Eqns. 2.24 and 2.25, we see

$$\sum_{\lambda} \ddot{p_\lambda}(t)\mathbf{H}_\lambda(\mathbf{r}) + \sum_{\lambda} p_\lambda(t)\mathbf{H}_\lambda(\mathbf{r})\omega_\lambda^2 = -\sqrt{4\pi}\ddot{\mathbf{M}}. \tag{2.26}$$

If we multiply both sides by $\mathbf{H}_\lambda(\mathbf{r})$ and integrate over the cavity volume, we obtain (using the orthonormality condition)

$$\ddot{p_\lambda}(t) + \frac{\omega_C}{Q_C}\dot{p_\lambda}(t) + \omega_C^2 p_\lambda(t) = -\sqrt{4\pi}\int_{cav} \ddot{\mathbf{M}}(\mathbf{r},t)\cdot\mathbf{H}_\lambda(\mathbf{r})dV. \tag{2.27}$$

The second term on the left side has been added phenomenologically to account for the effect of losses in the cavity walls [33]. Here Q_C is the cavity quality factor (cavity-Q) and $\omega_C = \omega_\lambda$ is the cavity's resonant frequency for mode λ. The cavity-Q is defined as the ratio of energy stored in the cavity to energy dissipated (per radian) and it essentially is a measure of inverse cavity linewidth. For our room temperature and cryogenic hydrogen masers, the cavity quality factors are typically about 10^4.

Within the maser storage bulb, the atoms' fast thermal motion averages the magnetization over the bulb, making $\mathbf{M}(\mathbf{r},t)$ independent of position, so

$$\int_{cav} \ddot{\mathbf{M}}(\mathbf{r},t)\cdot\mathbf{H}_\lambda(\mathbf{r})dV = \ddot{M}_z(t)\langle H_\lambda\rangle_b V_b. \tag{2.28}$$

where $\langle H_\lambda\rangle_b$ is the average of the z-component of $\mathbf{H}_\lambda$ over the maser bulb (volume = V_b), a restriction made since the $|2\rangle$ - $|4\rangle$ maser transition is a $\Delta m_F = 0$ transition which is only driven by the component of the microwave field that is parallel to the the quantization axis. We combine Eqns. 2.27 and 2.28, and then rewrite the result in the frequency domain. We do so by replacing the time-dependent amplitudes $p_\lambda(t)$ and $M_z(t)$ by their complex representations $p_\lambda(\omega)$ and $M(\omega)$, found by taking their Fourier transforms [34]. We obtain

$$\left(-\omega^2 + i\frac{\omega_C\omega}{Q_C} + \omega_C^2\right) p_\lambda(\omega) = \sqrt{4\pi}\omega^2 M(\omega)\langle H_\lambda\rangle_b V_b. \tag{2.29}$$

This equation shows that the microwave cavity field is driven by the source magnetization, which is generated by the coherent atomic ensemble. At the end of Section 2.1.1, however, we saw that this magnetization is driven by the microwave cavity field. These two effects then provide the positive feedback which allows for active maser oscillation. Together,

Eqns. 2.14 and 2.29 provide the self-consistent description of maser oscillation.

2.1.3 Maser oscillation frequency

To determine the maser oscillation frequency, we treat the magnetization due to the coherent atomic ensemble, Eqns. 2.13 and 2.14 as the source for the microwave cavity field in Eqn. 2.29. From the real part of this equation,

$$\omega_C^2 - \omega^2 = \frac{\sqrt{4\pi}\omega^2 \langle H_\lambda \rangle_b V_b n \mu_B}{4 p_\lambda(\omega)} \cdot \frac{r X_{24} T_1 T_2^2 (\omega - \omega_{24})}{1 + T_2^2(\omega - \omega_{24})^2 + T_1 T_2 |X_{24}|^2} \tag{2.30}$$

and for the imaginary part,

$$\frac{\omega_C \omega}{Q_C} = \frac{\sqrt{4\pi}\omega^2 \langle H_\lambda \rangle_b V_b n \mu_B}{4 p_\lambda(\omega)} \cdot \frac{r X_{24} T_1 T_2}{1 + T_2^2(\omega - \omega_{24})^2 + T_1 T_2 |X_{24}|^2}. \tag{2.31}$$

Combining these, we find

$$\omega_C^2 - \omega^2 = \frac{T_2 \omega_C \omega}{Q_C} (\omega - \omega_{24}) . \tag{2.32}$$

If we assume that the maser frequency ω, cavity frequency ω_C, and atomic hyperfine frequency ω_{24} are all very close to one another, then $(\omega_C^2 - \omega^2) = (\omega_C - \omega)(\omega_C + \omega) \approx (\omega_C - \omega_{24})(2\omega_C)$, and $\omega_C \omega \approx \omega_C \omega_{24}$. Therefore, Eqn. 2.32 takes the form of the familiar cavity pulling equation

$$\omega - \omega_{24} = \frac{Q_C}{Q_l} (\omega_C - \omega_{24}) \tag{2.33}$$

where we have introduced the maser's line-Q parameter, $Q_l = \omega_{24} T_2/2$. This relation tells us that the maser oscillation frequency will be shifted from the atomic hyperfine frequency by an amount proportional to the detuning of the cavity frequency from the hyperfine frequency. However, the pulling is diminished by the ratio of cavity-Q to line-Q, a factor of about 10^{-5} in most hydrogen masers for which $Q_l \approx 10^9$ (since $T_2 \approx 1$ s) and $Q_C \approx 10^4$.

2.1.4 Maser power

Since the maser Rabi frequency is given in terms of the magnitude of the cavity field, $X_{42} = \mu_B H_C/\hbar$, Eqns. 2.13 and 2.14 allow us to write the macroscopic magnetization in terms of the cavity field. We may extract a magnetic susceptibility, defined as

$$\chi = \frac{M(\omega)}{H_C(\omega)} = \chi' + i\chi''. \tag{2.34}$$

The component of the magnetic susceptibility in phase with the cavity field is therefore

$$\chi' = \frac{nrT_1T_2\mu_B^2}{2\hbar}\frac{T_2(\omega-\omega_{24})}{1+T_2^2(\omega-\omega_{24})^2+T_1T_2|X_{24}|^2} \tag{2.35}$$

and the quadrature component is

$$\chi'' = \frac{nrT_1T_2\mu_B^2}{2\hbar}\frac{1}{1+T_2^2(\omega-\omega_{24})^2+T_1T_2|X_{24}|^2}. \tag{2.36}$$

In terms of the quadrature susceptibility component, the average power radiated by the atomic ensemble in the storage bulb is given by [35]

$$P = \frac{H_C^2 V_b}{2}\omega\chi'' = \frac{\hbar^2|X_{24}|^2 V_b}{2\mu_B^2}\omega\chi''. \tag{2.37}$$

Therefore, using Eqn. 2.36 we find that the average power radiated by the atoms is given by

$$P = \frac{I\hbar\omega}{2}\frac{T_1T_2|X_{24}|^2}{1+T_2^2(\omega-\omega_{24})^2+T_1T_2|X_{24}|^2} \tag{2.38}$$

where I is the input flux of atoms in state $|2\rangle$, which for perfect state selection is 1/2 the total atomic flux, $I = \frac{1}{2}I_{tot} = \frac{1}{2}nrV_b$.

2.2 Double resonance theory

Hydrogen masers can also be used as sensitive probes of the $F = 1$, $\Delta m_F = \pm 1$ Zeeman transitions through a double resonance technique [24], in which an oscillating transverse magnetic field tuned near the atomic Zeeman resonance shifts the $\Delta F = 1$, $\Delta m_F = 0$ maser frequency. At low static magnetic fields, this maser frequency shift is an antisymmetric function of the detuning of the applied transverse field from the Zeeman resonance. Thus, by observing the antisymmetric pulling of the otherwise stable maser frequency, the hydrogen Zeeman frequency can be determined with high precision.

2.2.1 Bare atom analysis

An early investigation of atomic double resonance was made by Ramsey [36], who calculated the frequency shift between two levels coupled by radiation to other levels. This calculation treated the problem perturbatively to first order in the coupling field strength, and it neglected damping.

The first rigorous calculation of double resonance in the hydrogen maser was performed by Andresen [24,37], who calculated the maser frequency shift to second order in the transverse field strength. His calculation used the same approach as in Section 2.1: the maser frequency and power were found by coupling the atomic magnetization to the microwave cavity using Eqn. 2.29, and the magnetization was found using Eqns. 2.1 and 2.14. The same flux and relaxation terms were used, including the same simplified spin-exchange relaxation terms.

In Andresen's bare atom calculation, the effect of the applied transverse field was included in the interaction Hamiltonian. The transverse field, written as $\mathbf{H}_T = H_T \hat{\mathbf{x}} \cos(\omega_T t)$, acts to couple states $|1\rangle$ to $|2\rangle$ and $|2\rangle$ to $|3\rangle$. The interaction Hamiltonian therefore takes the form

$$H_{int} = H_{24}|2\rangle\langle 4| + H_{12}|1\rangle\langle 2| + H_{23}|2\rangle\langle 3| + h.c. \tag{2.39}$$

where H_{24} is defined in Eqn. 2.4 and H_{12} is given similarly by

$$H_{12} = -\frac{\hbar}{2} X_{12} \left(e^{i\omega_T t} + e^{-i\omega_T t} \right). \tag{2.40}$$

The transverse field Rabi frequency, X_{12}, is defined as $\hbar X_{12} = \mu_{12} H_T$ and the dipole matrix element is given by

$$\mu_{12} = \langle 1|\hat{\mu}_x|2\rangle = \frac{\mu_B}{2\sqrt{2}}(g_J - g_I) \approx \frac{1}{\sqrt{2}}\mu_B. \tag{2.41}$$

The terms H_{23} and X_{23} are defined analogously, and $X_{12} = X_{23}$.

To second order in the transverse field Rabi frequency, $|X_{12}|$, and in terms of the unperturbed maser Rabi frequency $|X_{24}^0|$, atom flow rate r, population decay rate γ_1, hyperfine decoherence rate γ_2, and Zeeman decoherence rate γ_Z, Andresen found that the small static field limit of the maser shift is given by[1]

$$\Delta\omega = -|X_{12}|^2 \frac{\gamma_Z}{r}(\gamma_1\gamma_2 + |X_{24}^0|^2) \frac{\delta\ (\rho_{11}^0 - \rho_{33}^0)}{(\gamma_Z^2 - \delta^2 + \frac{1}{4}|X_{24}^0|^2)^2 + (2\delta\gamma_Z)^2} \tag{2.42}$$

where $\delta = \omega_T - \omega_Z$ is the detuning of the transverse field from the mean atomic Zeeman frequency $\omega_Z = \frac{1}{2}(\omega_{12} + \omega_{23})$, and $\rho_{11}^0 - \rho_{33}^0 = r/(2\gamma_1)$ is the steady state population difference between states $|1\rangle$ and $|3\rangle$ in the absence of the applied transverse field (following Eqn. 8 of reference [24]). Physically, the population difference between states $|1\rangle$ and $|3\rangle$ represents the electronic spin polarization of the hydrogen ensemble [37]:

$$P = \frac{\langle S_Z \rangle}{S} = 2\ Tr(\hat{\rho}\hat{S_Z}) = \rho_{11} - \rho_{33}. \tag{2.43}$$

Equation 2.42 implies that a steady state electronic polarization, and hence a population difference between states $|1\rangle$ and $|3\rangle$ injected into the maser bulb, is a necessary condition for the maser to exhibit a double resonance frequency shift. Walsworth et al. demon-

[1] We have introduced a factor of $\frac{1}{2}$ to the values for the Rabi frequencies $|X_{24}|$, $|X_{12}|$, and $|X_{23}|$ to account for the use of the rotating wave approximation.

strated this polarization dependence experimentally by operating a hydrogen maser in three configurations: (i) with the usual input flux of atoms in states $|1\rangle$ and $|2\rangle$; (ii) with a pure input flux of atoms in state $|2\rangle$, where the maser frequency shift vanishes; and (iii) with an input beam of atoms in states $|2\rangle$ and $|3\rangle$, where the maser shift is inverted [19].

For typical applied transverse Zeeman field strengths (about 1 μG near the Zeeman transitions at about 1 kHz), the 1420 MHz maser frequency is shifted tens of mHz by the double resonance effect (see Figure 2.3), a fractional shift of $\approx 10^{-11}$. This shift is easily resolved because of the excellent fractional maser frequency stability (parts in 10^{15} over the tens of minutes typically required to carefully probe the antisymmetric lineshape).

In addition to the maser frequency shift due to the applied transverse field, there is a reduction in the maser power as the transverse field is swept through the Zeeman resonance. This amplitude reduction has also been calculated by Andresen [37] to second order in the transverse field strength. Savard [38] revisited the double resonance problem with a more realistic spin-exchange relaxation description [39], and found a small correction to the earlier work.

2.2.2 Dressed atom analysis

Although the work of Andresen and Savard provides a thorough description for the double resonance maser frequency shift, intuitive understanding is obscured by the length of the calculations and their use of the bare atom basis. In particular, these works demonstrate that the amplitude of the antisymmetric maser frequency shift is directly proportional to the electronic polarization of the masing atomic ensemble. The maser frequency shift vanishes as this polarization goes to zero. The previous bare atom analyses provide no physical interpretation of this effect.

Since the dressed atom formalism [40] often adds physical insight to the understanding of the interaction of matter and radiation, we apply it here to the double resonance frequency shift in a hydrogen maser [25]. We retain the same approach as in Section 2.1, however we determine the steady state coherence $\rho_{42}(\omega)$ in a dressed atom basis. In a

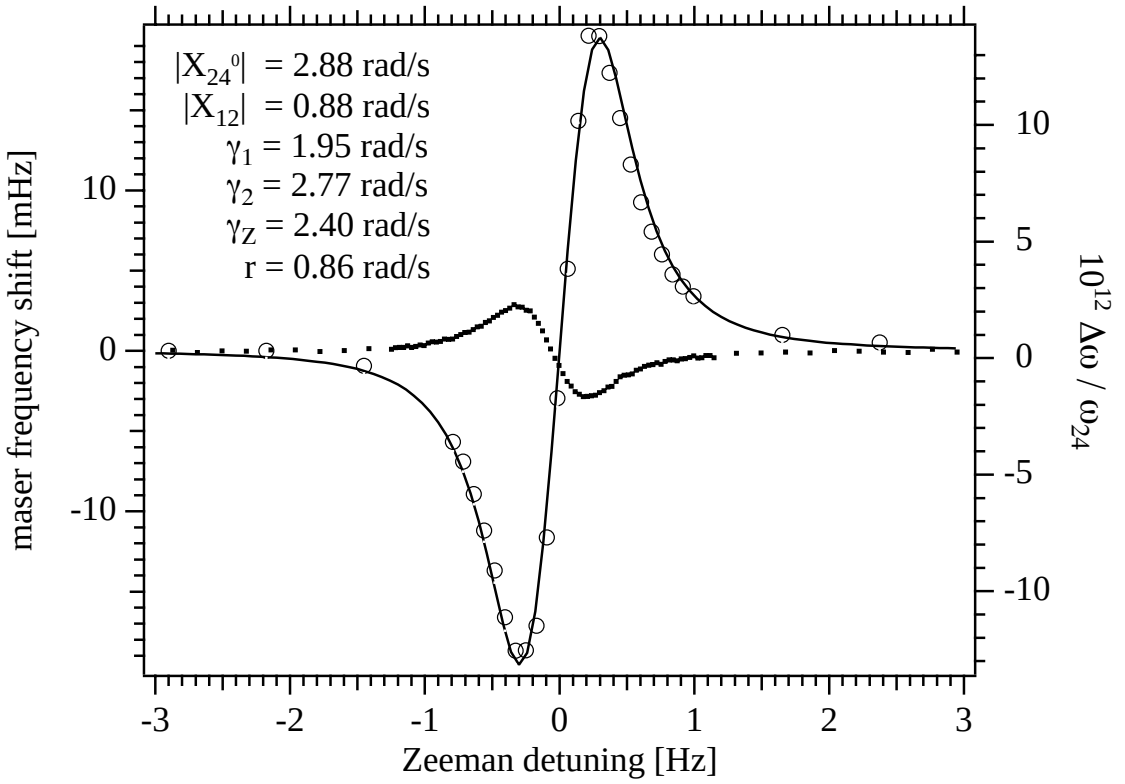

Figure 2.3: Examples of double resonance maser frequency shifts. The large open circles are data taken with an input beam of $|1\rangle$ and $|2\rangle$ hydrogen atoms. These are compared with Eqn. 2.42 (full curve) using the parameter values shown. The values of $|X_{12}|$ and γ_Z were chosen to fit the data, while the remaining parameters were independently measured. The experimental error of each measurement is smaller than the circle marking it. The electronic polarization dependence of the double resonance effect is illustrated with the dotted data points: with an input beam of $|2\rangle$ and $|3\rangle$ atoms, the shift is inverted. Note that the maser frequency shift amplitude for the dotted points was smaller since these data were acquired with a much weaker applied Zeeman field. The large variation of the maser frequency shift with Zeeman detuning near resonance, along with the excellent maser frequency stability, allows the Zeeman frequency ($\approx$ 800 Hz) to be determined to about 3 mHz in a single scan of the double resonance such as the dotted data shown here (requiring $\approx$ 20 minutes of data acquisition).

two-step process, we will first use the dressed atom picture to determine the effect of the applied transverse field on the atomic states. Then we will analyze the effect of the microwave cavity field on the dressed states, and determine the maser frequency shift. For simplicity, we assume the static magnetic field is sufficiently low that the two $F = 1$, $\Delta m_F = \pm 1$ Zeeman frequencies are nearly degenerate, $\omega_{12} - \omega_{23} \ll \gamma_Z$, as is the case for typical hydrogen maser operation. We use the simplified spin-exchange relaxation model [24] and neglect Savard's small spin-exchange correction to the double resonance maser frequency shift [38].

Dressed atom basis

By incorporating the applied transverse field into the unperturbed Hamiltonian, it takes the form $H_0 = H_a + H_f + V_{af}$. The atomic states (defining state $|2\rangle$ as energy zero) are described by $H_a = \hbar\omega_{12}|1\rangle\langle 1| - \hbar\omega_{23}|3\rangle\langle 3| - \hbar\omega_{24}|4\rangle\langle 4|$; the applied transverse field (at frequency ω_T) is described by $H_f = \hbar\omega_T a^\dagger a$; and the interaction between them is given by

$$V_{af} = \hbar g \left(a + a^\dagger\right) \left[|1\rangle\langle 2| + |2\rangle\langle 3| + h.c.\right]. \tag{2.44}$$

Here, the transverse field creation and annihilation operators are $a^\dagger$ and a, and g is the single-photon Rabi frequency for the Zeeman transitions. We will use eigenkets with two indices to account for the atomic state and the number of photons in the transverse field, denoted by n. We select four of these as our bare atom/transverse field basis, $\{|1, n-1\rangle, |2, n\rangle, |3, n+1\rangle, |4, n\rangle\}$, where the first entry indicates the atomic state and the second entry indicates the transverse field photon number. We note that for a resonant field, $\omega_T = \omega_{12} = \omega_{23}$, the first three basis states are degenerate. Also, $n \gg 1$ in practice for there to be a measurable double resonance maser frequency shift: e.g., $n \approx 10^{12}$ for a 1 μG transverse field which for a typical SAO hydrogen maser creates a double resonance frequency shift of about 10 mHz.

In this bare atom/transverse field basis, the unperturbed Hamiltonian operator takes

the following matrix form:

$$H_0 = \hbar \begin{pmatrix} -\delta & \frac{1}{2}X_{12} & 0 & 0 \\ \frac{1}{2}X_{12} & 0 & \frac{1}{2}X_{23} & 0 \\ 0 & \frac{1}{2}X_{23} & \delta & 0 \\ 0 & 0 & 0 & -\omega_{24} \end{pmatrix}, \tag{2.45}$$

where $\delta = \omega_T - \omega_{12}$ is the detuning of the applied transverse field, and

$$\frac{X_{12}}{2} = g\sqrt{n} \approx g\sqrt{n+1} = \frac{X_{23}}{2} \tag{2.46}$$

define the transverse field Rabi frequency (the factor of two has been inserted to be consistent with our rotating wave approximation convention).

By diagonalizing H_0, we find new basis states which physically represent the atomic states dressed by the applied transverse field. The dressed energy levels are the eigenvalues of H_0: $E_a = \hbar\Omega$, $E_b = 0$, $E_c = -\hbar\Omega$, and $E_4 = -\hbar\omega_{24}$, where $\Omega = \sqrt{\delta^2 + \frac{1}{2}X_{12}^2}$ represents the generalized Rabi frequency of the driven Zeeman transition. The dressed states are the eigenvectors of H_0:

$$\begin{aligned} |a\rangle &= \frac{1}{2}\left(1 - \frac{\delta}{\Omega}\right)|1, n-1\rangle + \frac{X_{12}}{2\Omega}|2, n\rangle + \frac{1}{2}\left(1 + \frac{\delta}{\Omega}\right)|3, n+1\rangle \\ |b\rangle &= \frac{X_{12}}{2\Omega}|1, n-1\rangle + \frac{\delta}{\Omega}|2, n\rangle - \frac{X_{12}}{2\Omega}|3, n+1\rangle \\ |c\rangle &= \frac{1}{2}\left(1 + \frac{\delta}{\Omega}\right)|1, n-1\rangle - \frac{X_{12}}{2\Omega}|2, n\rangle + \frac{1}{2}\left(1 - \frac{\delta}{\Omega}\right)|3, n+1\rangle \\ |4\rangle &= |4, n\rangle. \end{aligned} \tag{2.47}$$

Note that in the limit of large negative δ, $|a\rangle \to |1\rangle$ and $|c\rangle \to |3\rangle$, while in the limit of large positive δ, $|a\rangle \to |3\rangle$ and $|c\rangle \to |1\rangle$. This will become important in the physical interpretation of the maser frequency shift (see Section 2.2.2).

An operator $\hat{O}$ transforms between bare and dressed atom bases as $\hat{O^d} = T^{-1}\hat{O}^b T$, where T is the unitary matrix linking the dressed atom and bare atom basis states (com-

prised of the coefficients of Eqn. 2.47). The dressed and bare atom energies and eigenvectors are equivalent for the $F = 0$ hyperfine state $|4\rangle$ because this state is unaffected by the applied transverse field.

Dressed basis Bloch equations

We now couple the dressed states to the microwave cavity using the Bloch equation, which remains of the form

$$\dot{\rho^d} = \frac{i}{\hbar}[\rho^d, H_0^d] + \frac{i}{\hbar}[\rho^d, H_{int}^d] + \dot{\rho^d}_{relax} + \dot{\rho^d}_{flux}. \tag{2.48}$$

The unperturbed Hamiltonian, H_0, now accounts for the bare atom energies and the applied transverse field, while the microwave cavity field alone is included in the interaction Hamiltonian, H_{int}. Since the dressed states $|a\rangle, |b\rangle$, and $|c\rangle$ all have a component of the atomic state $|2\rangle$ (see Eqn. 2.47), the microwave field couples state $|4\rangle$ to each:

$$H_{int}^d = \frac{X_{12}}{2\Omega} H_{24}|a\rangle\langle 4| + \frac{\delta}{\Omega} H_{24}|b\rangle\langle 4| - \frac{X_{12}}{2\Omega} H_{24}|c\rangle\langle 4| + h.c. \tag{2.49}$$

Recall that $H_{24} = -\langle 2|\hat{\mu} \cdot \mathbf{H_C}|4\rangle$ is the only nonzero coupling between state $|4\rangle$ and the other bare atom states that is supported by the TE_{011} mode microwave cavity. To simplify the relaxation terms in the dressed basis, we make the approximation that all relaxation rates (population decay γ_1, hyperfine decoherence γ_2, and Zeeman decoherence γ_Z) have the same value, $\gamma + r$ (γ includes all relaxation exclusive of bulb loss). Typically, these rates are within a factor of two (see the values listed in Figure 2.3). Then,

$$\dot{\rho}_{relax}^d = -\gamma\rho^d + \frac{\gamma}{4}\mathbf{1}. \tag{2.50}$$

In the bare atom basis, the flux term has a very simple form (Eqn. 2.6) with no off-diagonal input entries since the injected beam has no coherence between the bare atomic states. In the dressed basis, however, there is an injected Zeeman coherence, so the flux term takes

a considerably more complicated form

$$\dot{\rho}^d_{flux} = \frac{r}{2} F^d - r\rho^d \tag{2.51}$$

where $F^d = T^{-1}\left(|1\rangle\langle 1| + |2\rangle\langle 2|\right) T$ is given by

$$F^d = \begin{pmatrix} \left(\frac{X_{12}}{2\Omega}\right)^2 + \frac{1}{4}(1-\frac{\delta}{\Omega})^2 & \frac{X_{12}}{4\Omega}(1+\frac{\delta}{\Omega}) & \frac{1}{4}(1-\frac{\delta^2}{\Omega^2}) - \left(\frac{X_{12}}{2\Omega}\right)^2 & 0 \\ \frac{X_{12}}{4\Omega}(1+\frac{\delta}{\Omega}) & \frac{\delta^2+(X_{12}/2)^2}{\Omega^2} & \frac{X_{12}}{4\Omega}(1-\frac{\delta}{\Omega}) & 0 \\ \frac{1}{4}(1-\frac{\delta^2}{\Omega^2}) - \left(\frac{X_{12}}{2\Omega}\right)^2 & \frac{X_{12}}{4\Omega}(1-\frac{\delta}{\Omega}) & \left(\frac{X_{12}}{2\Omega}\right)^2 + \frac{1}{4}(1+\frac{\delta}{\Omega})^2 & 0 \\ 0 & 0 & 0 & 0 \end{pmatrix}. \tag{2.52}$$

Steady state solution

The Bloch equations are most easily handled by moving to the interaction picture, given by $\hat{O} = e^{-i\hat{H}_0 t/\hbar}\ \tilde{\hat{O}}\ e^{i\hat{H}_0 t/\hbar}$, where $\tilde{\hat{O}}$ is an interaction picture operator.

The 4×4 matrix equation (Eqn. 2.48) yields sixteen independent equations that we give in Appendix A. We solve these in the steady state, where the populations in the interaction picture are static, $\dot{\tilde{\rho}}_{\nu\nu} = 0$, and the coherences exhibit sinusoidal precession. In particular, $\tilde{\rho}_{4a} = R_{4a}e^{-i(\Omega-\Delta)t}$, $\tilde{\rho}_{4b} = R_{4b}e^{i\Delta t}$, and $\tilde{\rho}_{4c} = R_{4c}e^{i(\Omega+\Delta)t}$, where the $R_{\mu\nu}$ are time independent, and $\Delta = \omega - \omega_{24}$. The other coherences precess at frequencies $\omega_{\mu\nu} = (E_\mu - E_\nu)/\hbar$. Making these steady state substitutions, the sixteen Bloch differential equations transform to a set of time-independent algebraic equations, also presented in Appendix A. We assume that $\omega_C = \omega_{24}$, so that the small cavity pulling shift vanishes. The total maser frequency shift due to the applied transverse field is then given by Δ.

In terms of dressed basis density matrix elements (rotated out of the interaction picture), the atomic coherence $\rho_{42}(\omega)$ is given by

$$\rho_{42}(\omega) = \left(\frac{X_{12}}{2\Omega}\rho_{4a} + \frac{\delta}{\Omega}\rho_{4b} - \frac{X_{12}}{2\Omega}\rho_{4c}\right) = \left(\frac{X_{12}}{2\Omega}R_{4a} + \frac{\delta}{\Omega}R_{4b} - \frac{X_{12}}{2\Omega}R_{4c}\right)e^{i\omega t} \tag{2.53}$$

and the magnetization is found from Eqn. 2.14. Inserting this into Eqn. 2.29 we find the

following two conditions which determine the maser amplitude and oscillation frequency

$$\omega_C^2 - \omega^2 = \frac{\sqrt{4\pi}\omega^2 \langle H_\lambda \rangle_b V_b n \mu_B}{p_\lambda(\omega)} Re\left(\frac{X_{12}}{2\Omega} R_{4a} + \frac{\delta}{\Omega} R_{4b} - \frac{X_{12}}{2\Omega} R_{4c}\right) \tag{2.54}$$
$$\frac{\omega_C \omega}{Q_C} = \frac{\sqrt{4\pi}\omega^2 \langle H_\lambda \rangle_b V_b n \mu_B}{p_\lambda(\omega)} Im\left(\frac{X_{12}}{2\Omega} R_{4a} + \frac{\delta}{\Omega} R_{4b} - \frac{X_{12}}{2\Omega} R_{4c}\right).$$

In terms of more experimentally accessible parameters, these relations can be expressed as

$$Re\left(\frac{X_{12}}{2} R_{4a} + \delta R_{4b} - \frac{X_{12}}{2} R_{4c}\right) = -|X_{24}| \left(\frac{2Q_C \Delta}{\omega_C}\right) \left[\frac{(\gamma + r)^2}{r\Omega} \left(\frac{I_{tot}}{I_{th}}\right)\right]^{-1} \tag{2.55}$$
$$Im\left(\frac{X_{12}}{2} R_{4a} + \delta R_{4b} - \frac{X_{12}}{2} R_{4c}\right) = -|X_{24}| \left[\frac{(\gamma + r)^2}{r\Omega} \left(\frac{I_{tot}}{I_{th}}\right)\right]^{-1}$$

where $|X_{24}| \approx \mu_B H_C/\hbar$ and we have used the fact that $H_C = \sqrt{4\pi} p_\lambda(\omega) \langle H_\lambda \rangle_b$ for our properly tuned cavity. Also, $I_{tot} = r V_b n$ is the total atomic flux into the maser bulb, and we assume that $\omega \approx \omega_C$ and I_{th} is the threshold flux for maser oscillation with the simplified spin-exchange model [3]:

$$I_{th} = \frac{\hbar V_C (\gamma + r)^2}{4\pi |\mu_B|^2 Q_C \eta}. \tag{2.56}$$

Here, V_C is the cavity volume and η is a dimensionless filling factor [2, 3], given by $\eta = \langle H_\lambda \rangle_b^2 / \langle H_\lambda^2 \rangle_C = \langle H_\lambda \rangle_b^2 V_C$, where we have used the cavity field's orthonormality (Eqn. 2.23).

We numerically solve the time-independent algebraic system of sixteen Bloch equations plus equations (2.55) to determine the maser frequency shift Δ as a function of transverse field detuning δ. We find excellent agreement with the previous theoretical bare atom analysis [24], as shown in Figure 2.4, within the approximation of equal population decay and decoherence rates.

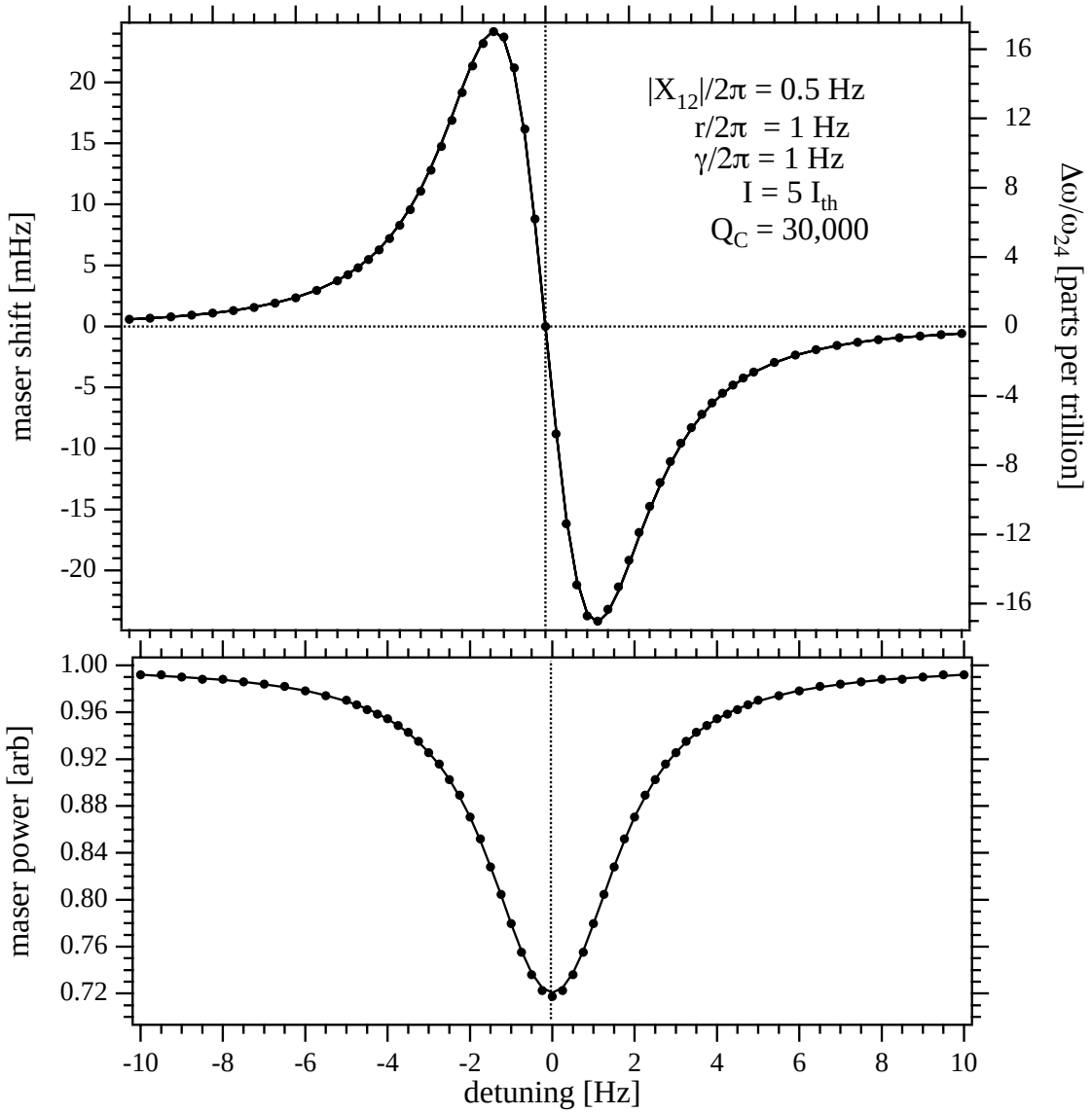

Figure 2.4: Comparison of the numerical solution to the Bloch equations using the dressed atom basis (open circles) and Andresen's bare atom basis for the parameters shown.

Physical interpretation

The dressed state analysis provides a straightforward physical interpretation of the double resonance maser frequency shift. In the absence of the applied Zeeman field, atoms injected in bare state $|2\rangle$ are the sole source of the magnetization that provides the positive feedback needed for active oscillation. However, when the near-resonant transverse field is applied, it also allows atoms injected in the $m_F = \pm 1$ states (bare states $|1\rangle$ and $|3\rangle$) to contribute via a two-photon process.

A dressed atom interpretation shows how these $m_F = \pm 1$ state atoms can become the dominant source of maser magnetization as the applied Zeeman field nears resonance. Viewed from this basis, three factors contribute to this interpretation. First, as shown in Figure 2.5(a), the applied Zeeman field shifts the energies of the two dressed levels $|a\rangle$ and $|c\rangle$ symmetrically relative to level $|b\rangle$, which remains unperturbed. Second, near the Zeeman resonance, the $\Delta F = 1$ dipole coupling $H_{4b}^2 = \langle 4|\hat{\mu} \cdot \mathbf{H_C}|b\rangle^2$ vanishes while H_{4a}^2 and H_{4c}^2 become equally dominant, as shown in Figure 2.5(b). Third, below resonance ($\delta < 0$) the steady state population of state $|a\rangle$ is greater than that of state $|c\rangle$ ($\rho_{aa} > \rho_{cc}$), while above resonance ($\delta > 0$) the opposite is true ($\rho_{cc} > \rho_{aa}$), as shown in Figure 2.5(c). These dressed state population differences arise from the fact that atoms in bare state $|1\rangle$ are injected into the maser while those in bare state $|3\rangle$ are not, under normal operation, so in the steady state $\rho_{11} > \rho_{33}$. For large negative Zeeman detunings, $|a\rangle \rightarrow |1\rangle$ and $|c\rangle \rightarrow |3\rangle$ (see discussion following Eqn. 2.47). The opposite holds for positive detuning, where $|a\rangle \rightarrow |3\rangle$ and $|c\rangle \rightarrow |1\rangle$.

These three ingredients combine to create the double resonance shift of the maser frequency, shown in Figure 2.5(d). For small negative Zeeman detunings ($|\delta| < 2\gamma_Z$), the excess of ρ_{aa} over ρ_{cc} and the relatively small size of H_{4b}^2 leads to maser oscillation primarily on the $|a\rangle \leftrightarrow |4\rangle$ transition. That is, atoms injected into the maser cavity in the bare state $|1\rangle$ contribute significantly to the maser oscillation via a two-photon process: one Zeeman transition photon and one microwave photon within the resonant cavity linewidth. This $|a\rangle \leftrightarrow |4\rangle$ transition is at a slightly higher frequency than in the unperturbed (no applied

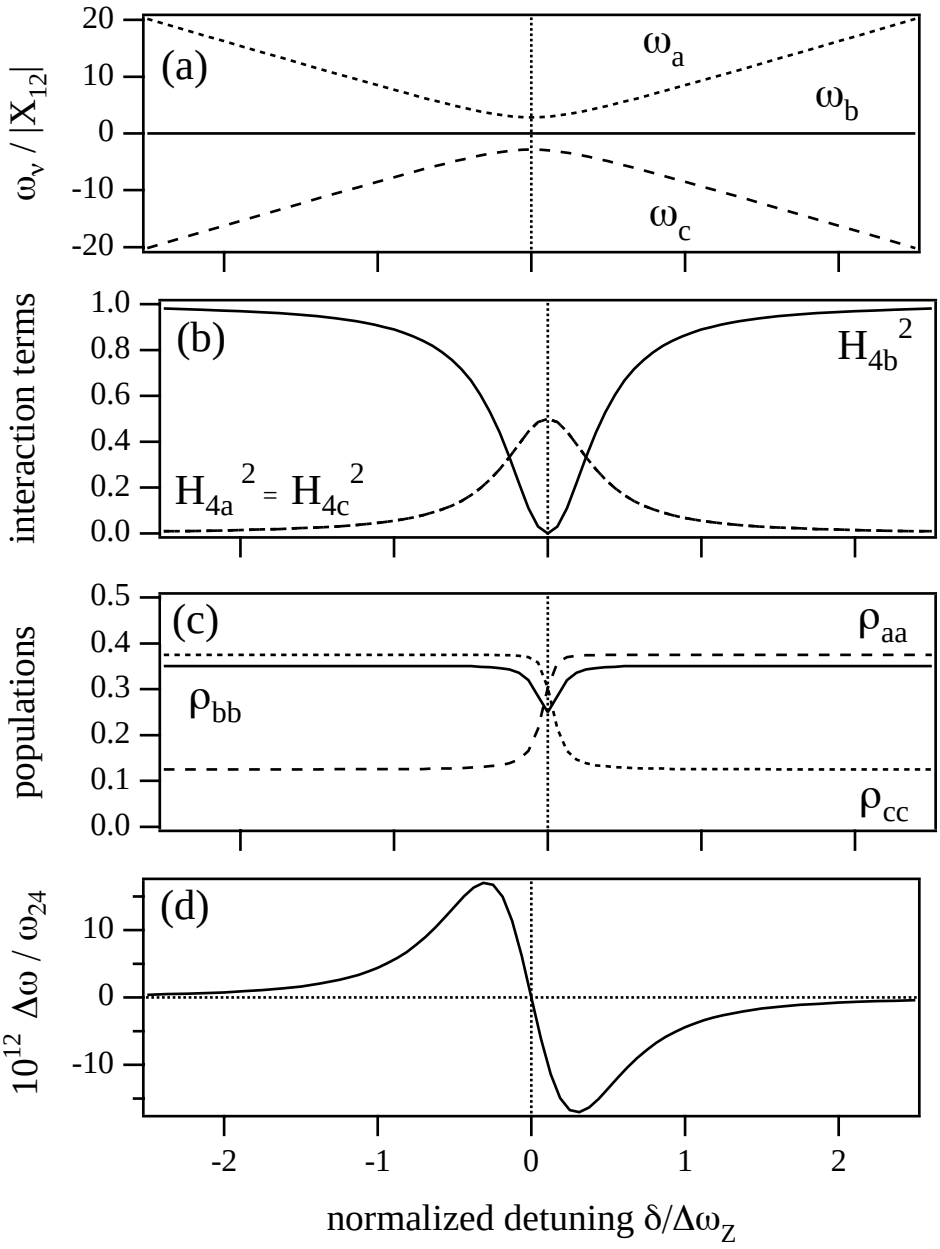

Figure 2.5: Calculated dressed atom quantities plotted against detuning of the applied Zeeman field (in units of Zeeman linewidth, $\Delta\omega_Z = 2\gamma_Z$). The dotted, full, and dashed curves correspond to dressed states $|a\rangle$, $|b\rangle$, and $|c\rangle$, respectively. (a) Dressed atom frequencies normalized to the Zeeman Rabi frequency. For $\delta = 0$, ω_a and ω_c differ from ω_b by $\pm|X_{12}|/\sqrt{2}$. (b) Interaction Hamiltonian matrix elements (squared) from Eqn. 2.49 in units of $\langle 2|\hat{\mu}\cdot\mathbf{H_C}|4\rangle^2$. (c) Steady state populations of dressed states. (d) Fractional double resonance maser frequency shift.

field) maser, so the maser frequency is increased. Conversely, for small positive Zeeman detunings ($\delta < 2\gamma_Z$), the maser oscillates preferentially on the $|c\rangle \leftrightarrow |4\rangle$ transition, and the maser frequency is decreased. For larger Zeeman detunings (positive or negative), the coupling of state $|4\rangle$ to unshifted dressed state $|b\rangle$ becomes dominant, and the magnitude of the frequency shift is reduced. For zero Zeeman detuning, dressed states $|a\rangle$ and $|c\rangle$ are equally populated in the steady state and the maser frequency shift exactly vanishes.

We see now why the injection of an electronic polarization into the maser bulb is needed for the applied Zeeman field to induce a maser frequency shift. Since ω_a and ω_c are spaced equally about the unperturbed maser frequency ω_b, and since $H_{4a}^2 = H_{4c}^2$, a necessary condition for a maser shift is a difference in the steady state values of ρ_{aa} and ρ_{cc}, which is a direct consequence of a difference in the injected populations of bare states $|1\rangle$ and $|3\rangle$, i.e., a net electronic polarization.

2.2.3 Application of double resonance

The double resonance hydrogen maser technique was originally studied for use in auto-tuning the maser cavity [24]. In addition to the double resonance frequency shift, there is a cavity pulling shift for a mistuned maser cavity, with magnitude dependent on the linewidth of the hyperfine transitions, through the line-Q (see Eqn. 2.33). The applied Zeeman radiation depletes the population of bare state $|2\rangle$, thereby increasing the linewidth of the hyperfine transition. Andresen [24] showed that the cavity can be tuned to the atomic frequency by modulating the hyperfine linewidth with applied Zeeman radiation and adjusting the cavity frequency such that there is no modulation of the maser frequency. However, this method requires accurate setting of the applied Zeeman field to the Zeeman resonance (i.e., $\delta = 0$).

The standard method in hydrogen masers for determining the average static magnetic field strength, and thus the Zeeman frequency, is to scan the Zeeman resonance with a large amplitude oscillating magnetic field and record the reduced maser power (such as that shown in Figure 2.4). From the applied field frequency which yields minimum maser

power, typically at the center of a "power resonance" with a width of about 1 Hz, the magnetic field can be found with a resolution of a fraction of 1 μG and the average Zeeman frequency can be determined only to ≈ 0.1 Hz.

The double resonance maser frequency shift can be used for precision Zeeman spectroscopy in a hydrogen maser. By utilizing the sharp, antisymmetric profile of this double resonance maser frequency shift, the hydrogen Zeeman frequency can be determined with a resolution of about 1 mHz. In Chapter 4 we will discuss the use of this double resonance technique in a search for Lorentz and CPT symmetry violation of the hydrogen atom's electron and proton spin [26], a search motivated by a general extension of the standard model of elementary particle physics [41].

Chapter 3

Practical realization of the hydrogen maser

The hydrogen maser was designed and first realized in the group of Norman Ramsey at Harvard University in 1960 [1–3]. Soon after, the development of hydrogen masers as frequency standards began at the Bomac laboratories of the Varian company in Beverly, MA. A continuation of this production was eventually moved to the Smithsonian Astrophysical Observatory (SAO) where all of the work described in this thesis was conducted. In Section 3.1, we present the construction of an SAO VLG-12 series atomic hydrogen maser, such as that used (maser P-28) for the experiment described in Chapter 4. In Section 3.2 we discuss a series of measurements used to characterized the operational parameters of a hydrogen maser. These measurements were made with maser P-8, an SAO VLG-10 series maser. Finally, in Section 3.3 we discuss frequency stability in room temperature hydrogen masers.

3.1 Hydrogen maser apparatus

In a hydrogen maser [1–4], molecular hydrogen is dissociated in an rf discharge and a beam of hydrogen atoms is formed, as shown schematically in Figure 3.1. A hexapole

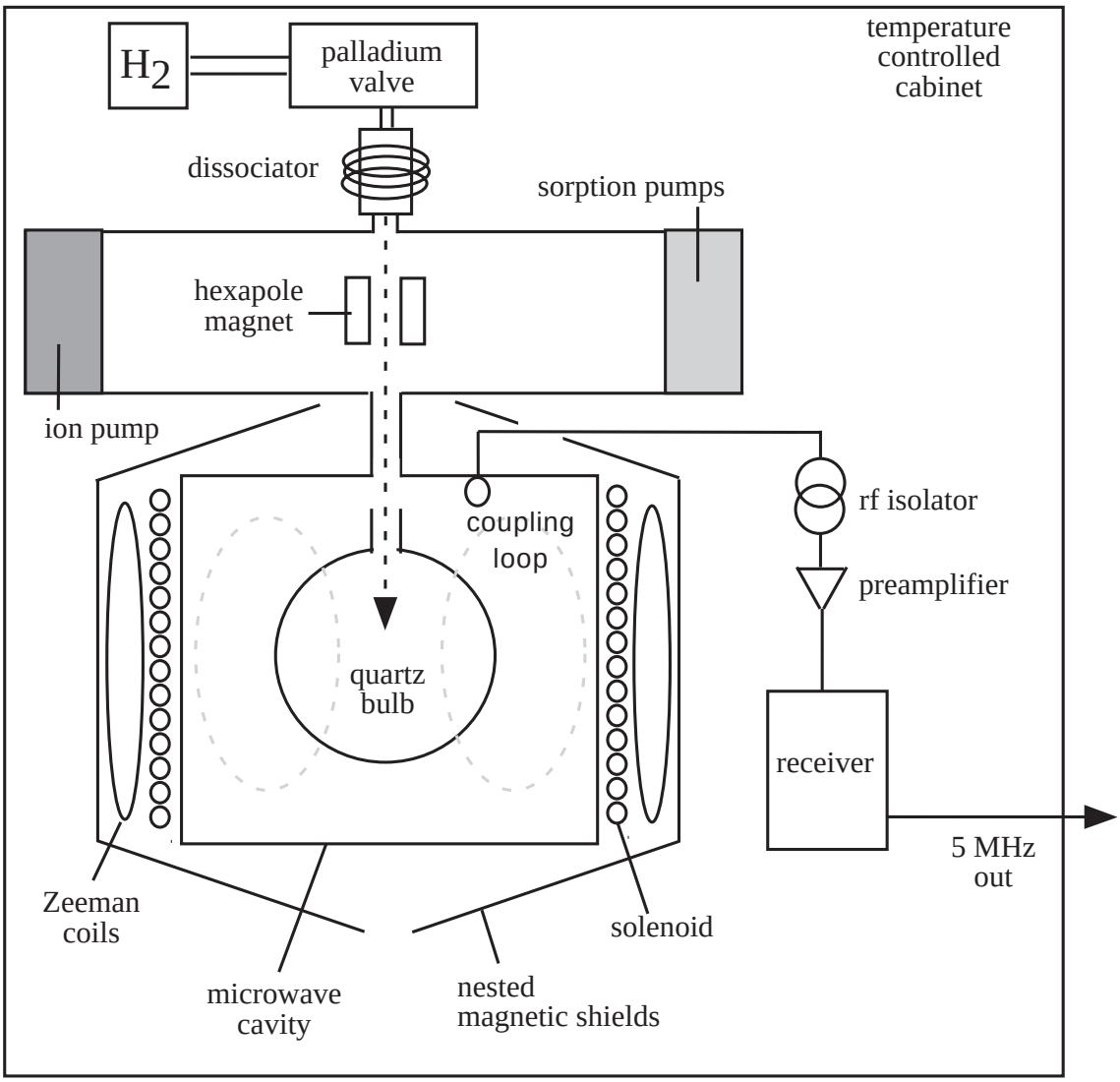

Figure 3.1: Schematic of a room temperature hydrogen maser assembly.

state selecting magnet focuses the low-field-seeking hyperfine states $|1\rangle$ and $|2\rangle$ into a quartz maser bulb at about 10^{12} atoms/sec. Inside the bulb (volume $\sim 10^3$ cm^3), the atoms travel ballistically for about 1 second before escaping, making $\sim 10^4$ collisions with the bulb wall. A Teflon coating reduces the atom-wall interaction and thus inhibits decoherence of the masing atomic ensemble due to wall collisions. The maser bulb is centered inside a cylindrical TE_{011} microwave cavity resonant with the 1420 MHz hyperfine transition. The thermal microwave field stimulates a coherent magnetization in the atomic ensemble, and this magnetization acts as a source to stimulate the microwave cavity field. With sufficiently high atomic flux and low cavity losses, this feedback induces active maser oscillation. Surrounding the cavity, a main solenoid and two end coils produce a weak static magnetic field ($\approx$ 1 mG) which establishes the quantization axis inside the maser bulb and sets the Zeeman frequency ($\approx$ 1 kHz). Another pair of coils produces the oscillating transverse magnetic field that drives the $F = 1$, $\Delta m_F = \pm 1$ Zeeman transitions. The cavity, solenoid and Zeeman coils are all enclosed within several layers of high permeability magnetic shielding, and the entire maser assembly and receiver are enclosed within a thermally controlled cabinet. The maser signal ($\approx$ 1420 MHz at about 10^{-13} W) is inductively coupled out of the microwave cavity, amplified, and detected with a low noise heterodyne receiver. Here, the signal is processed into a usable output of 5, 100 or 1200 MHz at about 10 mW.

3.1.1 Hydrogen source

A high pressure bottle of molecular hydrogen gas serves as the source of all hydrogen for the maser. A pressure regulator controls the pressure admitted into the dissociator, where molecular hydrogen is converted into atomic hydrogen, and a beam of atoms is formed and injected toward the state selecting magnet.

The pressure regulator consists of a Pirani gauge (a small thermistor bead suspended in front of the entrance to the dissociator) and a thermally controlled palladium valve. The Pirani thermistor is installed into a resistance bridge. The voltage across the bridge is

fed back to power the bridge and also compared to the setpoint with a voltage comparator. The output of the voltage comparator controls the thermal setting of the palladium valve. At low pressures, the small current in the bridge will warm the thermistor to match the set point. At higher pressure, the flux of the molecular hydrogen will act to cool the thermistor, so a larger current is needed to heat the thermistor to the set point. If the resistance bridge indicates that the pressure is higher than the setpoint, the output of the voltage comparator will be zero. If the pressure is below the setpoint, however, the (amplified) positive voltage comparator output will heat the palladium valve and increase the flow of molecular hydrogen. Generally, the setpoint is such that about 1 to 2 mTorr of molecular hydrogen will be input to the dissociator.

Since the pressure is sensed thermally, any variation in ambient temperature will be transformed into variations in molecular hydrogen flux. Therefore, a second Pirani gauge, well matched to the first, is installed at the high vacuum side ($\approx 10^{-8}$ Torr) of the dissociator. This reference Pirani is used to remove thermal fluctuations of the output from the pressure-sensing Pirani.

The pressure regulated beam of molecular hydrogen enters into the glass cell (V $\approx 10^2$ cm^3) of the rf dissociator. A tuned rf circuit with a (≈ 3 cm radius) rf coil surrounding the glass cell accelerates stray electrons and produces a hydrogen plasma discharge within the cell. The electrons accelerated by the rf electric field drive the hydrogen molecules into excited energy levels, causing the discharge to glow with a gray-pink color. Under proper conditions, the electron-molecular hydrogen collisions act to dissociate the molecules into hydrogen atoms. When the rate of dissociation exceeds the rate of recombination, the discharge glows with a bright reddish-pink color (the light coming chiefly from spontaneous emission from the atomic hydrogen Balmer series). At the exit end of the dissociator, a multitube collimator maintains the pressure difference between the discharge and the high vacuum region of the maser, and also directs the atomic hydrogen into a collimated beam.

3.1.2 State selection

The beam of atomic hydrogen atoms consists of nearly equal populations of all four hyperfine states. However, a hydrogen maser requires a population inversion in these hyperfine states. A beam of state $|2\rangle$ atoms would be ideal, since these are the only atoms that participate in the hyperfine transition. In practice, however, most hydrogen masers are designed to have an input flux of $|1\rangle$ and $|2\rangle$ atoms into the storage bulb. A hexapole state selecting magnet is used to focus these low-field-seeking states ($|1\rangle$ and $|2\rangle$) into the atomic storage bulb, while defocusing the high-field-seeking states ($|3\rangle$ and $|4\rangle$) away from the storage bulb. These unwanted hydrogen atoms, as well as hydrogen atoms which have exited the storage bulb, are then pumped away with a set of sorption pumps.

The collimated atomic hydrogen beam is directed along the axis of the the hexapole state selecting magnet. The magnet consists of six pole faces of alternating polarity mounted azimuthally around the atomic hydrogen beam. This cylindrical construction is about 10 cm in length with an outer radius of about 5 cm. The inner bore has a radius of approximately 1 cm.

On the axis, the magnetic fields from the six poles cancel and the net field is zero. The field grows quadratically in the radial direction, with a field amplitude approaching 1 Tesla at the pole tips. In the presence of this large field gradient, the atoms feel a force that depends on the hyperfine state i, given by $\mathbf{F}_i = \mu_i^{eff} \nabla B$, where $\mu_i^{eff} = -\partial U_i / \partial B$ is the effective magnetic moment of the ith hyperfine state. For fields greater than about 2000 G, atoms in low-field-seeking states $|1\rangle$ and $|2\rangle$ have $\mu^{eff} = -\mu_B$, while atoms in high field seeking states $|3\rangle$ and $|4\rangle$ have $\mu^{eff} = +\mu_B$ (μ_B is the Bohr magneton). Therefore, the low-field seeking atoms feel a force directed in the negative radial direction (i.e., are focused on axis) while the high-field seeking atoms feel a force in the positive radial direction (i.e., are defocused out of the beam).

The atoms travel through the hexapole with a thermal distribution of velocities. The atoms also have a distribution in the velocity component transverse to the beam, albeit reduced by the dissociator's collimator, therefore there will be a spread in the distance

required for the atoms to be properly focused. The geometry of the hexapole magnet and the relative placement of the storage bulb entrance are chosen to optimize the population inversion focused into the storage bulb. Typically, the total flux for a room temperature hydrogen maser is about 10^{13} atoms/s, with a state selection of about 80% equally in the $|1\rangle$ and $|2\rangle$ states (implying that about 40% of the total flux consists of atoms in the radiating $|2\rangle$ state).

The hydrogen atoms which do not enter the storage bulb, as well as those that have exited the storage bulb, are pumped out of the high vacuum space by one of four cylindrically mounted sorption pumps. In addition, other gases inside this space (including nitrogen, argon, and carbon dioxide) are removed by a small ion pump. The pressure in this high vacuum region is approximately 10^{-8} Torr.

3.1.3 Maser interaction region

The population inversion flux of atomic hydrogen is focused into a storage bulb centered inside a microwave cavity. The microwave cavity is tuned near the atomic hyperfine frequency, and this field drives stimulated emission transitions in the hydrogen atoms. Through this stimulated emission process, the atoms give energy back to the microwave cavity. If the atomic flux is high enough to counter the energy lost in the cavity, the system will actively oscillate.

The storage bulb is constructed from thin-walled quartz to minimize electromagnetic loss and loading of the resonant cavity. The spherical bulb has a diameter of approximately 21 cm (volume $\approx$ 3,000 cm^3). A thin collimator at the entrance aperture acts to lengthen the storage time inside the bulb to approximately 1 s. With an input flux of 10^{13} atoms/s, typical hydrogen densities in the storage bulb are about 10^9 atoms/cm^3. At room temperature, the atoms travel about 3×10^5 cm/s and therefore make about 10^4 collisions with the storage bulb wall.

In order to decrease the interaction of the atoms with the storage bulb wall, the inside of the bulb is coated with Teflon FEP. This helps to reduce the hydrogen recombination

rate at the bulb, and to reduce the decoherence of the coherently radiating ensemble. However, there is an appreciable hyperfine frequency shift due to wall collisions. When a hydrogen atom collides with the bulb wall, its electron cloud deforms, varying the hyperfine interaction between the electron cloud and the nucleus. A small phase shift is accumulated with each collision. The net wall frequency shift is given by the average phase shift per collision times the average collision rate. This shift is temperature dependent, is sensitive to the nature of a particular Teflon coating, and tends to change slightly as the wall coating ages. These factors limit the ability of a hydrogen maser to serve as an accurate frequency standard.

The quartz storage bulb is mounted in the center of a TE_{011} mode microwave cavity. The relative size and placement of the bulb are chosen so that the microwave cavity field is uniform and has a constant phase over the atomic storage region (as shown by the dashed field lines in Figure 3.1). The cylindrical cavity (volume $\approx$ 14,000 cm^3) is constructed out of Zerodur,[1] a ceramic material with a low thermal expansion coefficient, high mechanical stiffness and stability, and an absence of magnetism. The inner walls of the ceramic are coated with a thin layer of silver to form the electromagnetic resonant cavity, which has a resonant frequency of around 1,420,405,752 Hz and a resonant width of about 40 kHz for a cavity-Q of around 40,000.

In room temperature masers, the microwave cavity frequency is set using two methods. Course tuning is done with a mechanical tuning plunger. By inserting this plunger into the cavity, the effective length of the cavity is reduced and the frequency is therefore increased. Fine, resettable tuning of the cavity is made using a varactor diode which is inductively coupled to the cavity (via a coupling loop very similar to that used to couple the maser signal out, see below). The capacitance of this diode is changed when it is reverse biased, changing the reactance coupled into the microwave cavity and thereby shifting the cavity resonant frequency. With this system, the cavity frequency can be controllably varied over a range of about 10 kHz in 0.1 Hz steps.

[1] Zerodur is a trademark of Schott Optical Glass, Inc.

A solenoid coil assembly, consisting of one main solenoid and two trim coils wound around the microwave cavity, sets the static magnetic field of the hydrogen maser. In addition to establishing a quantization axis, this field sets the $F = 1$, $\Delta m_F = \pm 1$ Zeeman frequency. The current in each solenoid is generated by a voltage regulated supply and set with a adjustable voltage divider and a current-limiting precision 5 kΩ resistor. Typically, the solenoid field is set at about 1 mG, which sets the $\Delta m_F = \pm 1$ Zeeman frequency at about 1.4 kHz. In addition to this solenoid assembly, an orthogonal pair of coils mounted on the microwave cavity can generate an oscillating field transverse to the quantization axis to drive the $\Delta m_F = \pm 1$ Zeeman transitions. By doing so, the Zeeman frequency (and therefore the amplitude of the solenoid field) can be determined using the double resonance technique described in Chapter 2.

The entire maser assembly (bulb, cavity, and coils) is surrounded by four nested high-permeability magnetic shields. These are used to prevent ambient field variations from affecting the maser oscillation frequency. For the room temperature SAO masers, these magnetic shields have an axial shielding factor of about $\Delta H_{ext}/\Delta H_{int} = 30{,}000$. These act to attenuate the earth's field (about 0.5 G) to an insignificant level (about 20 μG) and to reduce the effect of ambient field fluctuations, about 3 mG in our laboratory, to a level of about 0.1 μG. Reducing ambient field fluctuations is especially important when using the hydrogen maser for precision Zeeman frequency spectroscopy, as discussed in Chapter 4.

3.1.4 Thermal shielding

Thermal variations in numerous components of the hydrogen maser will lead to instabilities in the maser oscillation frequency. For example, thermal variations in the cavity will alter the cavity frequency and effect the maser frequency via cavity pulling, thermal fluctuations in the solenoid setup will lead to a magnetic-field-dependent shift in the atomic hyperfine frequency, and thermally induced flux variation can lead to maser frequency variation due to spin-exchange effects. Therefore, steps have been taken to thermal control the various

components of room temperature hydrogen masers.

To isolate the hydrogen maser from ambient thermal variations, the maser and receiver electronics are housed inside an insulated, temperature controlled cabinet (22" wide × 33" deep × 60" high). This cabinet, whose temperature is controlled using blown air, provides a factor of ten isolation from ambient thermal variations. Within the cabinet, the maser assembly has several additional layers of thermal control, each with its own heater, thermal sensor and control loop. An oven located within the two outermost magnetic shields is controlled near 47 ˚C, while the vacuum belljar that surrounds the resonant cavity is maintained near 50 ˚C. The net fractional thermal isolation of the maser cavity from ambient fluctuations has been measured at about 10^{-5} [42].

Finally, the temperature of the coaxial cables leading to the microwave cavity is carefully controlled to reduce effects of changing coaxial line lengths, and the rf isolator and preamplifier are housed in an insulated temperature controlled box to reduce the effect of added white phase noise (discussed in more detail below in Section 3.3.2).

3.1.5 Microwave signal

The hydrogen maser's microwave signal is coupled out of the microwave cavity inductively using a small coupling loop. This signal, near 1,420,405,752 Hz has a typical magnitude of 10^{-13} W. It is passed through an rf isolator and a preamplifier and then input into a low noise heterodyne receiver.

The coupling loop, about 2 cm in diameter, is mounted to one end plate of the microwave cavity. It is oriented axially relative to the cavity such that the oscillating radial magnetic cavity field lines pass through the loop. The alternating magnetic flux sampled by the loop induces a voltage in the coil at a frequency near 1420 MHz. This microwave signal is coupled out from the loop with semi-rigid microcoaxial cable into an rf isolator which reduces the effects of external load changes on the microwave cavity frequency (the net isolation from this stage is more than 90 dB). After the isolator, the signal is input to a low noise preamplifier which provides 23 dB of gain.

3.1.6 Microwave receiver

In order to generate a useful reference signal, the low power maser signal is used to phase lock a quartz crystal oscillator in the maser's receiver system, as shown in the block diagram in Figure 3.2. The receiver produces three buffered outputs of about 10 mW at 5 MHz, 100 MHz and 1200 MHz. The hydrogen maser frequency at 1420... MHz is significantly more stable than the quartz crystal oscillator, so in what follows we will treat the maser frequency as constant.

The receiver consists of a voltage controlled crystal oscillator (VCXO), a frequency synthesizer, a phase detector (integrator), and numerous frequency mixers, multipliers, and dividers. The quartz crystal oscillator has a nominal frequency of about 100 MHz. This frequency is multiplied up to 1200 MHz and 200 MHz, and divided down to 20 MHz. Each of these frequencies is mixed in turn with the maser input signal, producing several intermediate frequencies at 220... MHz, 20... MHz, and 405... kHz (see Figure 3.2). This final intermediate frequency of 405...kHz is mixed with the output of a tunable frequency synthesizer. The synthesizer is locked to a 5 MHz signal divided down from the VCXO, and it is tunable from 405,750 Hz to 405,760 Hz in increments of 10^{-8} Hz. The synthesizer is set so that the output, after mixing with the maser signal, is nearly a DC voltage. The DC voltage from this final stage of frequency mixing is input into a phase detector (integrator), and the output of the integrator then controls the VCXO.

As the output frequency of the VCXO drifts, the synthesizer, which is locked to the VCXO, will drift correspondingly. Therefore the near-DC voltage at the final mixing stage will vary, and these variations will be integrated by the phase detector. The integrated, drift-induced signal is then fed back to the VCXO. As a result, the VCXO and all signals derived from it are phase locked to the hydrogen maser. Finally, an rf buffer system provides isolated outputs (at approximately 10 mW) derived from the VCXO at 5 MHz, 100 MHz, and 1200 MHz.

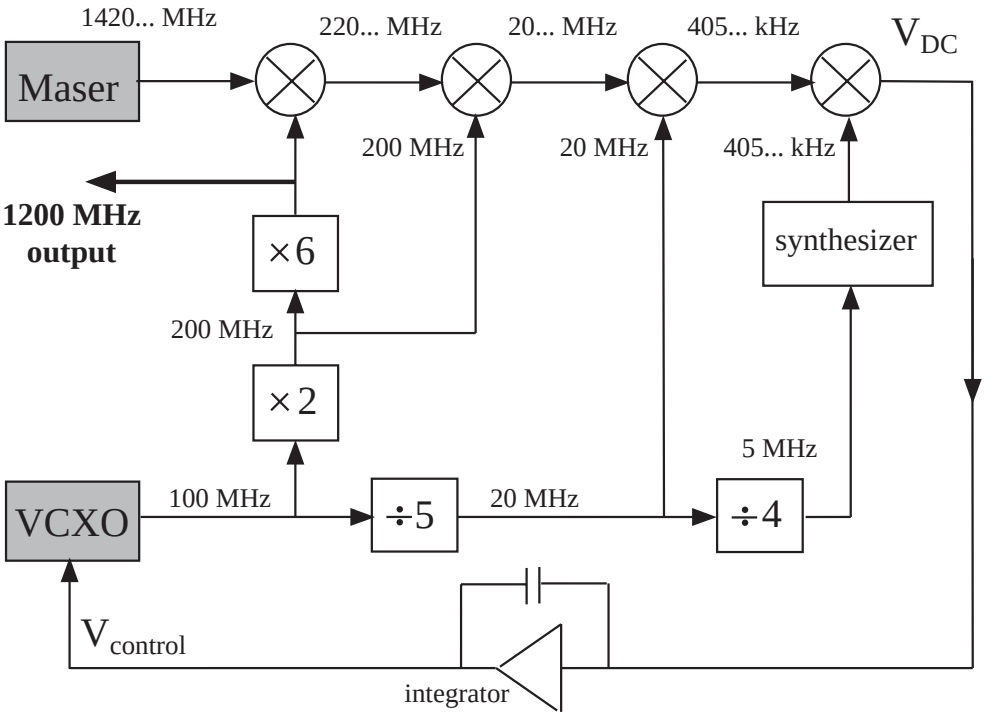

Figure 3.2: Schematic of the hydrogen maser receiver. Output voltages of 5 MHz, 100 MHz, and 1200 MHz are derived from a voltage controlled crystal oscillator which is phase locked to the maser signal. Only the 1200 MHz output is shown here.

3.2 Hydrogen maser characterization

In this section we discuss typical operating parameters for a room temperature hydrogen maser. Section 3.2.1 describes parameters set by the mechanical construction of the maser and it's electronic circuitry. Section 3.2.2 describes other maser parameters that depend on the operating conditions of the maser and must be extracted through measurement. In Section 3.2.3, we discuss the effect of spin-exchange collisions on hydrogen maser operation. All parameters reported in this section are for SAO maser P-8 and in Table 3.1.

3.2.1 Mechanical and electronic parameters

The geometry of the maser's microwave cavity and storage bulb determine the cavity and bulb volumes. For maser P-8, $V_C = 1.4 \times 10^{-2}$ m^3 and $V_b = 2.9 \times 10^{-3}$ m^3. The filling factor, defined as [2]

$$\eta = \frac{\langle H_z \rangle_b^2}{\langle H^2 \rangle_C}, \tag{3.1}$$

quantifies the ratio of the energy inside the maser bulb stored in the microwave magnetic field component which couples to the atoms, to the average total microwave magnetic field energy in the cavity. For maser P-8, $\eta = 2.14$.

In the steady state, the single atom flow rate into the bulb is equal to the geometric escape rate from the bulb, given by $r = \bar{v}A/4KV_b$, where $\bar{v} = \sqrt{8kT/\pi m} = 2.5 \times 10^5$ cm/s is the mean thermal velocity of atoms in the bulb at the operating temperature of 50 ℃, $A = 0.254$ cm^3 is the area of the bulb entrance aperture, and $K \approx 6$ is the Klausing factor [43] which accounts for the effects of a collimating tube at the bulb entrance. For maser P-8, $r = 0.86$ rad/s.

The maser cavity quality factor (cavity-Q) quantifies the amount of loss in the microwave cavity, and it is defined as [44]

$$Q_C = \frac{\text{energy stored in cavity}}{\text{energy dissipated per radian}}. \tag{3.2}$$

By injecting microwave power into the cavity through the coupling loop, sweeping the frequency of this power through the cavity resonance and looking at the reflected power, the cavity's resonant frequency ω_C and cavity width $\Delta\omega_C$ can be determined.[2] In terms of these, the cavity-Q can be shown to be $Q_C = \omega_C/\Delta\omega_C$. For maser P-8, we find $Q_C =$ 39,300. The cavity coupling coefficient β, defined as the ratio of power coupled into the external receiver to internal power lost in the cavity, can also be found from the swept microwave power cavity resonance [44]. For maser P-8, $\beta = 0.23$.

Signals coupled out of the microwave cavity are typically too small for direct detection. Therefore, this signal is sent through an rf isolator and preamplifier. For maser P-8, the preamplifier has a power gain of 20 dB. The noise figure F, defined as the signal-to-noise at the amplifier input relative to the signal-to-noise at the output, is about $F = 5$ dB (corresponding to a noise temperature $T_N = 920$ K). Also, for maser P-8, the microwave receiver has a bandwidth of about $B = 6$ Hz.

3.2.2 Operational parameters

As described in Chapter 2, there are two important relaxation rates for standard hydrogen maser operation. For a room temperature hydrogen maser, the decay of the population inversion is described by the longitudinal relaxation rate [3, 45]

$$\gamma_1 = r + \gamma_r + 2\gamma_{se} + \gamma_1', \tag{3.3}$$

and the decay of the atomic coherence is described by the transverse relaxation rate [3,45]

$$\gamma_2 = r + \gamma_r + \gamma_{se} + \gamma_2'. \tag{3.4}$$

Here, r is the atomic flow rate into the bulb, γ_r is the rate of recombination into molecular hydrogen at the bulb wall (typically very small for properly made wall coatings), γ_{se} is the hydrogen-hydrogen spin-exchange collision rate, and γ_i' includes all other sources of

[2] See Chapter 6 for a detailed description of this measurement.

Parameter	Symbol	Room temperature value
cavity volume	V_C	1.4×10^{-2} m^3
bulb volume	V_b	2.9×10^{-3} m^3
filling factor	η	2.14
bulb escape rate	r	0.86 rad/s
cavity-Q (quality factor)	Q_C	39,300
cavity coupling coefficient	β	0.23
preamplifier gain		20 dB
preamplifier noise figure	F	5 dB
preamplifier noise temperature	T_N	920 K
receiver bandwidth	B	6 Hz
line-Q (quality factor)	Q_l	1.6×10^9
output power	P_o	112 fW
radiated power	P	600 fW
maser quality parameter	q	0.05
spin-exchange-independent relaxation rate	γ_t	1.71 rad/s
oscillation threshold power	P_c	220 fW
oscillation threshold flux	I_{th}	0.47×10^{12} atoms/s
atomic population inversion flux	I	2.11×10^{12} atoms/s
total atomic flux	I_{tot}	5.1×10^{12} atoms/s
atomic density	n	1.0×10^{15} atoms/m^3
spin-exchange rate	γ_{se}	0.38 rad/s
maser Rabi frequency	$\lvert X_{24}\rvert$	2.88 rad/s
population decay rate	γ_1	1.95 rad/s
maser decoherence rate	γ_2	2.77 rad/s

Table 3.1: Operational parameters for SAO room temperature hydrogen maser P-8. All quantities have been converted into SI units.

decay, such as decoherence during wall collisions and effects of magnetic field gradients. The spin-exchange rate is given approximately by [3, 45]

$$\gamma_{se} = \frac{1}{2} n \bar{v}_r \sigma \tag{3.5}$$

where $\bar{v}_r = 4\sqrt{kT/\pi m} = 3.6 \times 10^5$ cm/s is the mean relative velocity of atoms in the bulb and $\sigma = 21 \times 10^{-16}$ cm^2 is the hydrogen-hydrogen spin-exchange cross section at room

temperature.[3] The hydrogen density is given by [3, 45]

$$n = \frac{I_{tot}}{(r + \gamma_r)V_b} \tag{3.6}$$

where I_{tot} is the total flux of hydrogen atoms into the storage bulb.

The atomic line-Q is related to the transverse relaxation rate and the maser oscillation angular frequency ω by [2, 45]

$$Q_l = \frac{\omega}{2\gamma_2}. \tag{3.7}$$

We measure Q_l using the cavity pulling of the maser frequency (neglecting spin-exchange shifts):

$$\omega = \omega_{24} + \frac{Q_C}{Q_l}\left(\omega_C - \omega_{24}\right). \tag{3.8}$$

By measuring the maser frequency as a function of cavity frequency setting, the line-Q can be determined. For maser P-8, $Q_l = 1.6 \times 10^9$ and, from Eqn. 3.7 we see that the total decoherence rate is $\gamma_2 = 2.77$ rad/s.

A convenient single measure of spin-exchange-independent relaxation in a hydrogen maser is given by [3, 45]

$$\gamma_t = \left[(r + \gamma_r + \gamma_1')(r + \gamma_r + \gamma_2')\right]^{\frac{1}{2}}. \tag{3.9}$$

A useful form for γ_1 in terms of γ_t, is found by combining Eqn. 3.9 with Eqns. 3.3 and 3.4:

$$\gamma_1 = \frac{\gamma_t^2}{\gamma_2 - \gamma_{se}} + 2\gamma_{se}. \tag{3.10}$$

We can relate the line-Q to I, the net input flux of atomic population inversion (atoms in state $|2\rangle$ - state $|4\rangle$) using Eqns. 3.4-3.7:

$$\frac{1}{Q_l} = \frac{2}{\omega}\left[r + \gamma_r + \gamma_2' + q\frac{I}{I_{th}}\gamma_t\right]. \tag{3.11}$$

[3]See Chapter 6 for a more complete description of hydrogen-hydrogen spin-exchange collisions.

The threshold flux required for maser oscillation (in the absence of spin-exchange) is given by

$$I_{th} = \frac{\hbar V_C \gamma_t^2}{4\pi\mu_B^2 Q_C \eta}, \tag{3.12}$$

whereas the maser quality parameter [3, 45]

$$q = \left[\frac{\sigma \bar{v}_r \hbar}{8\pi\mu_B^2}\right] \frac{\gamma_t}{r+\gamma_r} \left[\frac{V_C}{\eta V_b}\right] \left(\frac{1}{Q_C}\right) \frac{I_{tot}}{I} \tag{3.13}$$

quantifies the effect of spin-exchange on the maser.

The ratio I/I_{tot} is a measure of the effectiveness of the state selection of atoms entering the bulb. While I is not directly measurable, it can be related to the power P radiated by the atoms by [3, 45]

$$\frac{P}{P_c} = -2q^2 \left(\frac{I}{I_{th}}\right)^2 + (1-3q)\left(\frac{I}{I_{th}}\right) - 1 \tag{3.14}$$

where the threshold power (in the absence of spin-exchange) is $P_c = \hbar\omega I_{th}/2$. As shown in Chapter 2, the maser power is also related to the maser Rabi frequency $|X_{24}|$ by

$$P = \frac{I\hbar\omega}{2} \frac{|X_{24}|^2}{\gamma_1\gamma_2} \left(1 + \frac{|X_{24}|^2}{\gamma_1\gamma_2}\right)^{-1}, \tag{3.15}$$

where we've assumed the cavity is tuned to the hyperfine transition frequency. The power coupled out of the maser (P_o) can be measured directly, and for maser P-8 we've recently measured $P_o = 112$ fW. Using the cavity coupling coefficient β, we therefore find [45] $P = P_o(1+\beta)/\beta = 600$ fW.

In order to measure q and γ_t, we make the approximation that $\gamma_1' = \gamma_2'$ (reasonable since magnetic relaxation and magnetic field inhomogeneities are typically averaged out quite well by the effusive hydrogen atoms). Then, by combining Eqns. 3.11 and 3.14 we see [46]

$$P = a_2(\frac{1}{Q_l})^2 + a_1(\frac{1}{Q_l}) + a_0 \tag{3.16}$$

where

$$a_2 = -\frac{E\omega^2}{2}, \tag{3.17}$$

$$a_1 = \frac{E\omega\gamma_t}{2}(1 + \frac{1}{q}), \tag{3.18}$$

and

$$a_0 = -\frac{E\gamma_t^2}{q}, \tag{3.19}$$

with

$$E = \frac{\hbar^2\omega V_C}{8\pi\mu_B^2 Q_C \eta}. \tag{3.20}$$

Therefore, by measuring the maser power as a function of inverse line-Q and performing a quadratic fit, we can determine q and γ_t. For maser P-8, $q = 0.05$ and $\gamma_t = 1.71$ rad/s.

With these values for q and γ_t for maser P-8, we find $I_{th} = 0.47 \times 10^{12}$ atoms/s (using Eqn. 3.12) and $P_c = 220$ fW. Then, from Eqn. 3.14 we find that the flux of state $|2\rangle$ atoms is $I = 2.11 \times 10^{12}$ atoms/s. Under the assumption that $\gamma_t \approx r + \gamma_r$ we find that the total flux is $I_{tot} = 5.1 \times 10^{12}$ atoms/s (Eqn. 3.13) and the density is $n = 1.0 \times 10^{15}$ atoms/m^3 (Eqn. 3.6). The spin-exchange collision rate is therefore $\gamma_{se} = 0.38$ rad/s (Eqn. 3.5). Finally, the population decay rate is $\gamma_1 = 1.95$ rad/s (Eqn. 3.10) and the maser Rabi frequency is $|X_{24}| = 2.88$ rad/s (Eqn. 3.15).

3.2.3 Spin-exchange characterization

We now consider the effect that spin-exchange relaxation has on hydrogen maser operation [3, 4]. According to Eqn. 3.14, the maser power is a (concave down) quadratic function of the atomic flux. Therefore, for a given set of maser parameters, there will be a maximum achievable power. Clearly, as the atomic flux tends to zero, the maser power is reduced since there are fewer atoms supplying energy to the cavity. In addition, since the relaxation rates γ_1 and γ_2 depend on density through spin-exchange broadening, as the atomic flux (and therefore atomic density) increases, the total relaxation rates increase and the overall

maser power is reduced. This implies that in addition to a flux *minimum*, there will also be *maximum* flux with which active maser oscillation can be achieved. Figure 3.3 shows a plot of Eqn. 3.14 for several values of the spin-exchange parameter q. Here it can be seen that for $q = 0$ (equivalent to the spin-exchange collision cross section $\sigma = 0$), the output power increases linearly without bound as the flux is increased. However, as the value of q increases (equivalent to an increase in the spin-exchange collision rate) the maximum output power decreases and the range of flux values that can support oscillation narrows. Therefore, the spin-exchange parameter q is essentially a measure of the effect of spin-exchange broadening on the hydrogen maser.

If we impose on Eqn. 3.14 the condition the maser power remain positive, we find the following condition for the allowable flux range [3]:

$$I_{max/min} = I_{th}\frac{1 - 3q \pm (1 - 6q + q^2)^{1/2}}{4q^2}. \tag{3.21}$$

If we also demand also that the maser power maximum for a given q remain positive, we find the following condition on the spin-exchange parameter q:

$$q < 3 - 2\sqrt{2} = 0.172. \tag{3.22}$$

Therefore, we see that if the parameters in Eqn. 3.13 are such that $q > 0.172$, the allowable flux range will shrink to zero and active maser oscillation will no longer be possible.

In Chapter 5, we will investigate the improvements in hydrogen maser performance expected while operating at reduced temperature. At cryogenic temperatures, the relative atomic hydrogen velocity $\bar{v}_r$ will be reduced, and it will be shown that the spin-exchange collision cross section σ also decreases significantly. These two effects could lead to a substantial reduction in the spin-exchange parameter q, so that a cryogenic hydrogen maser could be operated at higher fluxes for higher output powers than a room temperature hydrogen maser.

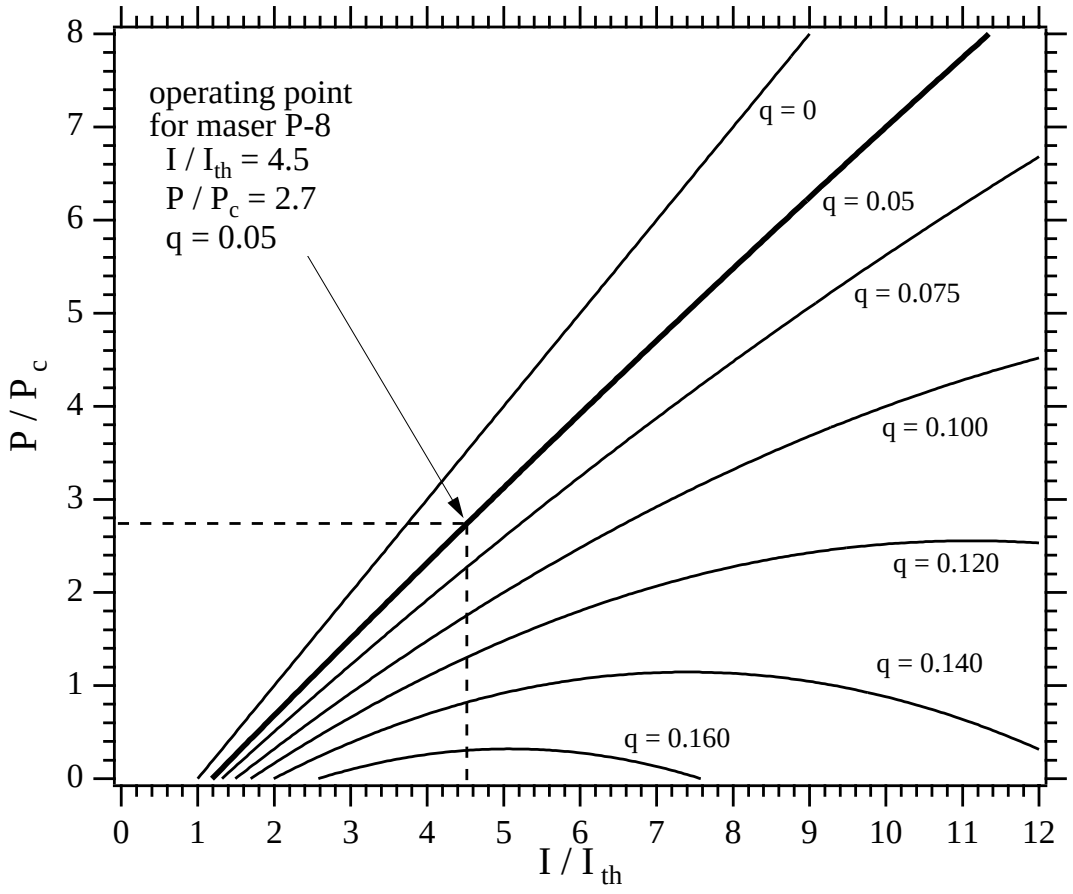

Figure 3.3: Maser power vs maser flux as a function of the spin-exchange parameter q. The maser power is normalized relative to the oscillation threshold power P_c and the flux is normalized to the oscillation threshold flux I_{th}.

3.3 Hydrogen maser frequency stability

Hydrogen masers are among the most stable oscillators available. Generally, the factors which determine the limit to hydrogen maser stability can be divided into two classes. Fundamental limits, which mostly stem from thermodynamic noise processes, determine hydrogen maser stability at short- to medium-term averaging times up to about 10,000 s. For averaging times $10 < \tau <$ 10,000 s, the fractional frequency stability is limited by thermal noise, from sources inside the maser cavity as well as in the receiver electronics. These effects are treated in Section 3.3.2. For averaging times longer than about 10,000 s, the frequency stability is limited by various systematic effects, predominantly related to slow changes in the frequency of the microwave resonant cavity. In Section 3.3.3 we treat these and other systematic effects which limit hydrogen maser stability.[4]

3.3.1 General definition of clock stability

Typically, hydrogen maser frequency stability is characterized in the time domain using a standard measure of stability, the two-sample Allan variance [47, 48]. This variance is defined using the following model. We assume the oscillator signal voltage can be written as

$$V(t) = [V_0 + \epsilon(t)] \sin [2\pi\nu_0 t + \phi(t)] \tag{3.23}$$

where V_0 and ν_0 are the nominal amplitude and frequency, while $\epsilon(t)$ and $\phi(t)$ represent time-varying amplitude and phase variations. We will assume that these variations are small, such that $|\epsilon(t)/V_0| \ll 1$ and $|\dot{\phi}(t)/\nu_0| \ll 1$. The time varying phase of the signal is then

$$\Phi(t) = 2\pi\nu_0 t + \phi(t) \tag{3.24}$$

[4]For averaging times $\tau <$ 1-10 s, (i.e., less than the interaction time of the hydrogen atoms with the microwave cavity field) the fractional frequency stability of the hydrogen maser is set by the quartz crystal oscillator in the maser receiver.

and the time varying instantaneous frequency, defined by $2\pi\nu(t) = \dot{\Phi}(t)$, is therefore

$$\nu(t) = \nu_0 + \frac{1}{2\pi}\dot{\phi}(t). \tag{3.25}$$

We now define the parameter

$$y(t) = \frac{\dot{\phi}(t)}{2\pi\nu_0} \tag{3.26}$$

as a measure of the instantaneous fractional frequency deviation on which the time-domain frequency stability definition will be based.

If we measure the fractional frequency deviation for a time τ beginning at time t_k, the average over this time is given by

$$\bar{y}_k = \frac{1}{\tau}\int_{t_k}^{t_k+\tau} y(t)dt = \frac{\phi(t_k+\tau) - \phi(t_k)}{2\pi\nu_0\tau}. \tag{3.27}$$

If we allow no dead time between measurements, then $t_{k+1} = t_k + \tau$. The two-sample Allan variance is then defined as the variance of the differences between adjacent fractional frequency deviations $(\bar{y}_{k+1} - \bar{y}_k)$ given by [48]

$$\sigma^2_{Allan}(\tau) = \left\langle \frac{(\bar{y}_{k+1} - \bar{y}_k)^2}{2} \right\rangle. \tag{3.28}$$

In practice, one first measures the oscillator frequency for a time T, and the data stream is broken up into m intervals of time $\tau = T/m$. Then, the average fractional frequency deviation $\bar{y}_k$ is computed for each interval. The differences between the fractional frequency deviations for adjacent intervals are then computed, forming a set of $(m-1)$ differences $(\bar{y}_{k+1} - \bar{y}_k)$. Finally, the Allan variance is found as the variance of these differences using

$$\sigma^2_{Allan}(\tau) = \frac{1}{m}\sum_{k=1}^{m} \frac{(\bar{y}_{k+1} - \bar{y}_k)^2}{2}. \tag{3.29}$$

With this definition, an Allan variance for multiple averaging times (up to $\tau = T/2$) can be computed from a single data set of length T, and the stability of an oscillator as a

function of averaging times can be found.

3.3.2 Fundamental limits to frequency stability

In addition to the coherent microwave cavity field stimulated by the oscillating atomic ensemble, there is also a thermal microwave field present in the maser cavity. The presence of this thermal field is the chief limitation to hydrogen maser stability at short- to medium-term averaging times up to about 10,000 s.

The thermal microwave field leads directly to white frequency noise in the coherent maser output signal. Along with the hyperfine transitions stimulated by the coherent microwave field, there are also hyperfine transitions stimulated by the incoherent thermal microwave cavity field. The addition of this incoherent radiation leads to a random walk through time in the phase of the microwave field and introduces a $\sqrt{\tau}$ dependence in this phase. Since the maser frequency over this interval is given by the net accumulated phase divided by $2\pi\tau$, the thermal cavity noise leads to a frequency instability that varies as $1/\sqrt{\tau}$. The magnitude of this instability will be determined by the ratio of noise power of the thermal cavity field (given by kT times the maser linewidth, with T the cavity temperature) to the power P delivered by the atoms to the cavity. The Allan deviation for this process is found to be [2, 7, 42]

$$\sigma_c(\tau) = \frac{1}{Q_l}\sqrt{\frac{kT}{2P\tau}} \tag{3.30}$$

where Q_l is the maser's line-Q.

To obtain an estimate of the thermal white frequency noise stability limit for one of the SAO room temperature hydrogen masers, we will use the parameters from Section 3.2 for maser P-8. Operating at $T = 290$ K, this maser has $Q_l = 1.6 \times 10^9$ and $P = 6 \times 10^{-13}$ W. Therefore, the thermal stability limit due to white frequency noise is approximately $\sigma_c(\tau) = 3.6{\times}10^{-14}/\sqrt{\tau}$.

A fraction of the energy from the coherent microwave field is coupled out of the cavity

and transmitted though a preamplifier into the receiver. However, a fraction of the thermal noise field is likewise coupled out, amplified and input to the receiver. This thermal noise field adds white phase noise to the coherent maser output signal. Since the noise figure of the receiver is primarily set by the initial preamplifier stage, the total added phase noise power input to the receiver is kTB (with T the maser temperature and B the receiver bandwidth) plus kT_NB (with T_N the noise temperature of the preamplifier). The added phase noise leads to an average variation in the coherent signal's phase given by [49] $\Delta\phi = \sqrt{Bk(T+T_N)/P_0}$, where P_0 is the power coupled out of the maser. The Allan deviation for this process is then found to be [7, 42]

$$\sigma_r(\tau) = \frac{1}{\tau}\sqrt{\frac{Bk(T+T_N)}{\omega^2 P}\left(\frac{1+\beta}{\beta}\right)} \tag{3.31}$$

where ω is the maser frequency and we have written the power coupled out P_0 in terms of the total power radiated by the atoms P and the output coupling β.

An estimate of the thermal white phase noise stability limit for SAO room temperature masers can be found using the parameters from Section 3.2 for maser P-8. Here, the maser temperature is $T = 290$ K, the cavity coupling is $\beta = 0.23$, and the maser frequency is $\omega = 2\pi\times$ 1,420,405,752 Hz. The maser receiver has a bandwidth of about 6 Hz, and the preamplifier has a noise figure of about 5 dB (noise temperature $T_N = 920$ K). Therefore the thermal stability limit due to white phase noise is approximately $\sigma_r(\tau) = 1.1\times10^{-13}/\tau$.

Since these two noise processes are uncorrelated, the net Allan deviation due to thermal noise can be written as [7]

$$\sigma(\tau) = \left[\sigma_c^2(\tau) + \sigma_r^2(\tau)\right]^{\frac{1}{2}}. \tag{3.32}$$

For maser P-8 and the parameters given above, the white frequency noise limit, white phase noise limit, and net thermal limit are shown in Figure 3.4. In this case, the thermal noise limit is set by white phase noise for averaging times less than 10 s, and by white frequency noise for averaging times greater than 10 s. In reality, the stability limit for times less than 1-10 s is set by the quartz crystal oscillator; for times greater than about

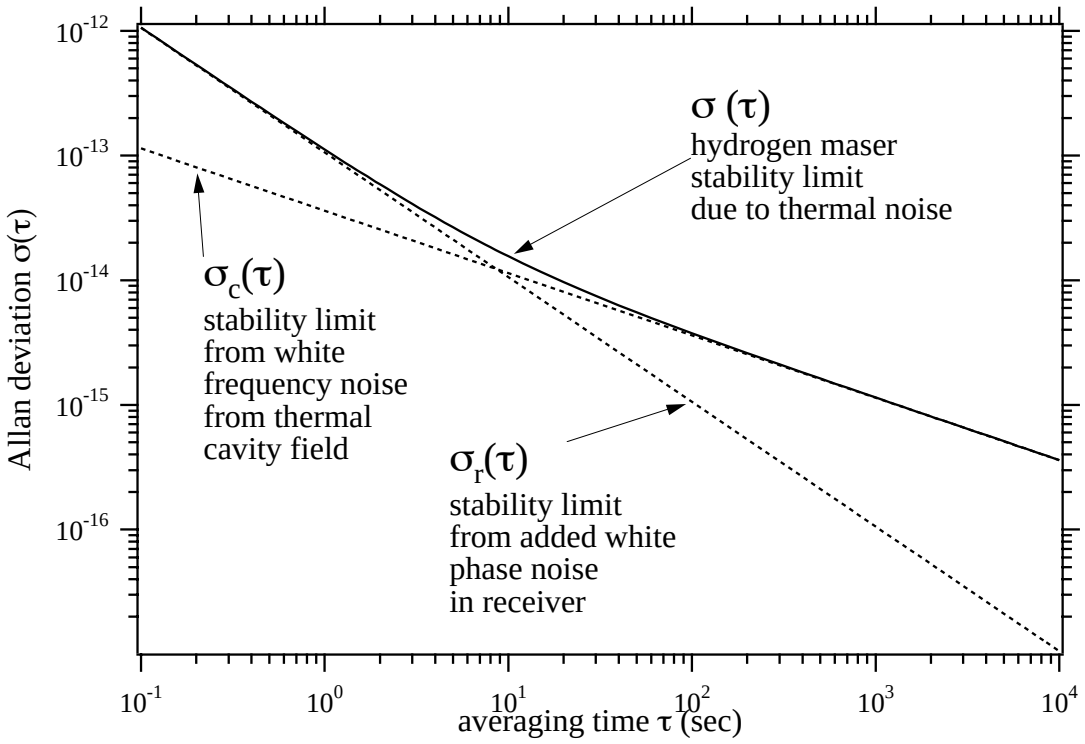

Figure 3.4: Hydrogen maser frequency stability due to thermal noise at room temperature. The dotted lines depict the limit due to added white phase noise (Eqn. 3.31), and white frequency noise (Eqn. 3.30), and the solid line shows the net limit due to thermal sources. We have used $T = 290$ K, $Q_l = 1.6{\times}10^9$, $P = 6{\times}10^{-13}$ W, $T_N = 920$ K, $B = 6$ Hz, and $\beta = 0.23$, the values for SAO maser P-8.

10,000 s the limit is determined by systematic effects, as will be described in Section 3.3.3.

3.3.3 Systematic effects on frequency stability

While state-of-the-art room temperature hydrogen masers have demonstrated frequency stabilities close to the thermal noise limit for short- to medium-term averaging times, the stability tends to degrade significantly for averaging times greater than about 10,000 s. At these times, the stability is diminished mainly by variation and drift in the resonant cavity frequency. These effects are covered in detail in references [4] and [42], and are summarized here along with other sources of systematic variation in maser frequency.

Effects on resonant cavity frequency

The maser oscillation frequency ω depends directly on the resonant cavity frequency ω_C, as shown in Eqn. 3.8, although this dependence is diminished by the ratio of cavity-Q to line-Q (typically a factor of 10^{-5}). Since the cavity frequency will be set by its mechanical dimensions, the maser frequency will be affected by thermal expansion and contraction of the cavity. Therefore, the microwave cavities are constructed from ceramic material with a low thermal expansion coefficient. For Zerodur, the ceramic from which SAO VLG-12 maser cavities are constructed, the cavity frequency temperature coefficient is about 140 Hz/K [42]. Therefore, typical short-term (tens of minutes) ambient temperature fluctuations of 1 ℃, which cause 10^{-5} ℃ changes in the cavity temperature, would induce a 1.4 mHz cavity frequency shift and a negligible 1×10^{-17} fractional maser frequency shift. Furthermore, the relatively longer maser cavity time constant (approximately 10 hours [42]) further attenuates the effect of short-term room temperature variations.

Over longer timescales, the cavity frequency can be affected by slow drift of the temperature control setpoint (due to imperfect tuning of the temperature control loop) or drift in the temperature sensor itself. However, the dominant sources of long-term cavity frequency shifts are mechanical relaxation and stress. For example, the joints between the cavity cylinder and endcaps are known to shrink with time. Also, following the heating process with which the cavity's silver coating is applied, the endcaps are known to flatten with time. Both of these effects act to raise the microwave's cavity frequency, and the estimated rate of fractional maser frequency shifts due to these effects is on the order of 7×10^{-16}/day. [42]

Additional thermal effects

Along with thermally-induced microwave cavity shifts, other thermal effects can limit maser frequency stability. These include changes in the storage bulb's dielectric constant, variation in the storage bulb's Teflon coating, variation in the length of the transmission line from the coupling loop to the receiver (both length and dielectric constant), and the

second-order Doppler effect. These are treated in detail in references [4] and [42].

Magnetic field effects

The maser oscillation frequency also depends directly on the atomic hyperfine frequency ω_{24}. The hyperfine frequency is a second-order function of the static solenoid magnetic field, given by $\omega_{24} = 2\pi\nu_{hfs} + 17300B_0^2$ with ω_{24} in radians per second for B_0 in gauss, and $\nu_{hfs} \approx$ 1,420,405,752 Hz is the zero-field hyperfine frequency. To decrease the sensitivity to fractional variations in the static field, hydrogen masers are operated at very low fields typically less than 1 mG. At this field, the fractional frequency dependence is given by $d\omega_{24}/\omega_{24} = (3.9 \times 10^{-9}/G)dB_0$. We have measured long-term (10,000 s) solenoid field fluctuations on the order of 6 nG, which would lead to negligible fractional frequency variations of $2{\times}10^{-17}$ (see Chapter 4).

In addition to running at a low, carefully stabilized field, the maser is shielded from ambient magnetic fields and field gradients with high permeability magnetic shielding. As described in Section 3.1.3, an SAO VLG-12 maser has an axial shielding factor of about $\Delta H_{ext}/\Delta H_{int} =$ 30,000. Typical short-term (10-100 s) ambient field fluctuations in our laboratory at about 3 mG. These are then shielded to a level of about 0.1 μG which would lead to a short-term fractional frequency stability limit of about $4{\times}10^{-16}$.

Spin-exchange effects

Throughout our discussion of hydrogen maser theory (Chapter 2) and hydrogen maser characterization (Section 3.2) we have used a simple treatment of spin-exchange relaxation, where the population decay rate ($\gamma_{1,se} = n\bar{v}_r\sigma$) and the decoherence rate ($\gamma_{2,se} = \gamma_{1,se}/2$) can be combined additively to the other forms of decay. In Chapter 6 we will remove this simplification, and it will be shown that a more complete treatment of spin-exchange collisions predicts an additional, hydrogen-density-dependent maser frequency shift. For

a room temperature hydrogen maser,[5] the frequency is found to be approximately

$$\omega = \omega_{24} + \frac{Q_C}{Q_l}\left(\omega_C - \omega_{24}\right) + \alpha\bar{\lambda}_0\gamma_2 = \omega_{24} + \left(\Delta + \alpha\bar{\lambda}_0\right)\gamma_2 \tag{3.33}$$

where γ_2 is the total broadening (including spin-exchange and all other sources) and we have introduced the cavity detuning parameter $\Delta = 2Q_C(\omega_C - \omega_{24})/\omega_{24}$, the spin-exchange shift cross-section $\bar{\lambda}_0$, and a system constant

$$\alpha = \frac{\hbar V_C \bar{v}_r}{\mu_0 \mu_B^2 \eta Q_C V_b} \tag{3.34}$$

where V_C and V_b are the cavity and bulb volumes, $\bar{v}_r$ is the average relative atomic velocity, and η is the filling factor.

If the maser cavity is tuned exactly to the hyperfine frequency (eliminating the frequency pulling term), then the maser frequency will be shifted from the atomic frequency by an amount proportional to the total broadening γ_2. Since this broadening will depend on the hydrogen density in the bulb, the overall maser stability will be degraded by density or flux variations, which are difficult to eliminate in practice. However, as pointed out in 1967 by Crampton [17], if the maser is instead tuned so that $\Delta = -\alpha\bar{\lambda}_0$, then the maser frequency will become independent of γ_2 and therefore insensitive to density fluctuations. This procedure, known as "spin-exchange tuning" is typically employed in room temperature hydrogen masers.

[5] We will discuss spin-exchange tuning for a cryogenic hydrogen maser in Chapter 6.

Chapter 4

Testing CPT and Lorentz symmetry with hydrogen masers

A theoretical framework has recently been developed which incorporates possible spontaneous CPT and Lorentz symmetry violation into a realistic extension of the standard model of elementary particle physics [27,28,50–60]. One branch of this framework emphasizes low energy, experimental searches for symmetry violating effects in atomic energy levels [27,28]. In particular, it has been shown that Lorentz and CPT violation results in variations in the atomic hydrogen $F = 1$, $\Delta m_F = \pm 1$ Zeeman frequency as a function of the orientation of the quantization axis (set by the maser's static magnetic field) relative to a preferred frame (e.g., the cosmic microwave background) [41]. Motivated by this theoretical framework, we conducted a search for sidereal variations in the hydrogen Zeeman frequency and placed a new, clean bound of approximately 10^{-27} GeV on Lorentz and CPT violation of the proton [26].

In this chapter we will discuss the theoretical framework, experiment, and analysis that underly our hydrogen maser test of CPT and Lorentz symmetry. In Section 4.1 we discuss the standard model extension. In Section 4.2 we discuss the procedure used to collect data and extract a sidereal bound on the Zeeman frequency. In Section 4.3 we describe efforts to reduce and characterize systematic effects. Finally, in Section 4.4 we

compare our result to other clock-comparison tests of CPT and Lorentz symmetry, and discuss potential means of improving our measurement.

4.1 Lorentz and CPT violation in the standard model

Experimental investigations of Lorentz symmetry provide important tests of the standard model of particle physics as well as general relativity. While the standard model successfully describes particle phenomenology, it is believed to be the low energy limit of a fundamental theory that incorporates gravity. This underlying theory may be Lorentz invariant, yet contain spontaneous symmetry-breaking that could result in small violations of Lorentz invariance and CPT at the level of the standard model [50–52].

A theoretical framework has been developed by Kostelecký and coworkers to describe Lorentz and CPT violation at the level of the standard model [27,28,50–60]. This standard-model extension is quite general: it emerges as the low-energy limit of any underlying theory that generates the standard model and contains spontaneous Lorentz symmetry violation, and hence can include CPT violation [50–52]. For example, such characteristics might emerge from string theory [53–56]. A key feature of the standard model extension is that it is formulated at the level of the known elementary particles, and thus enables quantitative comparison of a wide array of searches for Lorentz and CPT violation [57–60].

"Clock comparison experiments" are high precision searches for temporal variations in atomic energy levels. According to the standard model extension considered here, Lorentz and CPT violation may produce shifts in certain atomic levels, with magnitudes of the shifts that depend on the orientation of the atom's spin quantization axis relative to some unknown, fixed inertial frame [27,28]. (Boosts relative to the preferred inertial frame may also cause atomic energy level shifts.) Certain atomic transition frequencies, therefore, may exhibit sinusoidal variation as the earth rotates on its axis. New limits can be placed on Lorentz and CPT violation by bounding sidereal variation of these atomic transition frequencies.

Specifically, the description of Lorentz and CPT violation is included in the relativistic Lagrange density of the constituent particles of the atom. For example, the modified electron Lagrangian becomes [27]

$$\mathcal{L} = \frac{1}{2} i\bar{\psi}\Gamma_\nu \partial^\nu \psi - \bar{\psi} M \psi + \mathcal{L}_{int}^{QED} \tag{4.1}$$

where

$$\Gamma_\nu = \gamma_\nu + \left(c_{\mu\nu}\gamma^\mu + d_{\mu\nu}\gamma_5\gamma^\mu + e_\nu + i f_\nu \gamma_5 + \frac{1}{2} g_{\lambda\mu\nu}\sigma^{\lambda\mu} \right) \tag{4.2}$$

and

$$M = m + \left(a_\mu \gamma^\mu + b_\mu \gamma_5 \gamma^\mu + \frac{1}{2} H_{\mu\nu}\sigma^{\mu\nu} \right). \tag{4.3}$$

The parameters a_μ, b_μ, $c_{\mu\nu}$, $d_{\mu\nu}$, e_ν, f_ν, $g_{\lambda\mu\nu}$ and $H_{\mu\nu}$ represent possible vacuum expectation values of Lorentz tensors generated through spontaneous Lorentz symmetry breaking in an underlying theory. These parameters and associated terms are absent in the standard model. The parameters a_μ, b_μ, e_ν, f_ν and $g_{\lambda\mu\nu}$ represent coupling strengths for terms that violate both CPT and Lorentz symmetry, while $c_{\mu\nu}$, $d_{\mu\nu}$, and $H_{\mu\nu}$ violate Lorentz symmetry only. An analogous expression exists for the modified proton and neutron Lagrangians (a superscript will be appended to differentiate between the sets of parameters for different particle types). The standard model extension treats only the free particle properties of constituent systems (nuclei, atoms, etc.), estimating that all interaction effects will be of higher order [27]. As a result, the interaction term $\mathcal{L}_{int}^{QED}$ of Eqn. 4.1 is unchanged from the conventional, Lorentz invariant, QED interaction term.

Within this framework, the values of the parameters that characterize Lorentz violation are not presently calculable; instead, values or constraints must be determined experimentally. The general nature of this theory ensures that different experimental searches may place bounds on different combinations of Lorentz and CPT violating terms, and direct comparisons between these experiments are possible (see Table 4.1 and reference [27]).

The leading-order Lorentz and CPT violating energy level shifts for a given atom are

Experiment	$\tilde{b}^e_{X,Y}$ [GeV]	$\tilde{b}^p_{X,Y}$ [GeV]	$\tilde{b}^n_{X,Y}$ [GeV]
anomaly frequency of e^- in Penning trap [61]	10^{-25}	-	-
^{199}Hg and ^{133}Cs precession frequencies [62]	10^{-27}	10^{-27}	10^{-30}
hydrogen maser double resonance [26]	10^{-27}	10^{-27}	-
spin polarized torsion pendulum [63]	10^{-29}	-	-
dual species ^{129}Xe/^{3}He maser [64]	-	-	10^{-31}

Table 4.1: Experimental bounds on Lorentz and CPT violation for the electron, proton, and neutron. Bounds are listed by order of magnitude and in terms of a sum of Lorentz violating parameters in the standard model extension (see Eqns. 4.2, 4.3, and 4.13).

obtained by summing over the free particle shifts of the atomic constituents. From the symmetry violating correction to the relativistic Lagrangian, a non-relativistic correction Hamiltonian δh is found using standard field theory techniques [27]. Assuming Lorentz and CPT violating effects to be small, the energy level shifts are calculated perturbatively by taking the expectation value of the correction Hamiltonian with respect to the unperturbed atomic states, leading to a shift in an atomic (F, m_F) sublevel given by [27]

$$\Delta E_{F,m_F} = \langle F, m_F | n_e \delta h^e + n_p \delta h^p + n_n \delta h^n | F, m_F \rangle. \tag{4.4}$$

Here n_w is the number of each type of particle that contributes to the atomic spin and δh^w is the corresponding correction Hamiltonian. Note that for most atoms, the interpretation of energy level shifts in terms of the standard model extension is reliant on the particular model used to describe the atomic nucleus (e.g., the Schmidt model). One key advantage of an experimental study in hydrogen is the simplicity of the nuclear structure (a single proton), with results that are not compromised by any nuclear model uncertainty.

Among the most recent clock comparison experiments are Penning trap tests by Dehmelt and co-workers with the electron and positron [61, 65] which place a limit on electron Lorentz and CPT violation at a level of approximately 10^{-25} GeV. A recent re-analysis by Adelberger, Gundlach, Heckel, and co-workers of existing data from the "Eöt-Wash II" spin-polarized torsion pendulum [66, 67] has improved this limit to a level

of approximately 10^{-29} GeV [63], the most stringent bound to date on Lorentz and CPT violation of the electron. Also, a limit on neutron Lorentz and CPT violation of about 10^{-31} GeV has been set by Bear et al. [64] using a dual species noble gas maser to compare the nuclear Zeeman frequencies of ^{129}Xe and ^{3}He. Stringent limits on Lorentz and CPT violation of the electron, proton, and neutron have also been derived from the results of an experiment by Berglund et al. [62] which compared the Zeeman frequencies of ^{199}Hg and ^{133}Cs [27].

Figure 4.1 illustrates the Lorentz violating corrections to the hyperfine/Zeeman energy levels of the ground electronic state of atomic hydrogen [41]. In particular, the shift in the $F = 1$, $\Delta m_F = \pm 1$ Zeeman frequency is:[1]

$$|\Delta\nu_Z| = \frac{1}{h}|(b_z^e - d_{zt}^e m_e - H_{xy}^e) + (b_z^p - d_{zt}^p m_p - H_{xy}^p)|. \tag{4.5}$$

The spatial subscripts (x, y, z) denote the projection of the tensor couplings onto the laboratory frame, and t is the time subscript. Therefore, as the Earth rotates relative to a fixed inertial frame, the Zeeman frequency ν_Z will exhibit a sidereal variation. Our recent search for a variation of the hydrogen $F = 1$, $\Delta m_F = \pm 1$ Zeeman frequency using hydrogen masers [26] has placed a new, clean bound on Lorentz and CPT violation of the proton at a level of about 10^{-27} GeV [26].

4.2 Experimental procedure

4.2.1 Double resonance technique

In our test of CPT and Lorentz symmetry, we used the double resonance technique described in Chapter 2 to make high precision measurements of the $F = 1$, $\Delta m_F = \pm 1$ Zeeman frequency [24, 25, 38]. We applied an oscillating magnetic field ω_T transverse to the maser's quantization axis, swept the field's frequency through the atomic Zeeman tran-

[1] Gauge invariance and renormalizability exclude the parameters e_ν, f_ν, and $g_{\lambda\mu\nu}$ in the standard model extension. We therefore neglected them relative to the other terms.

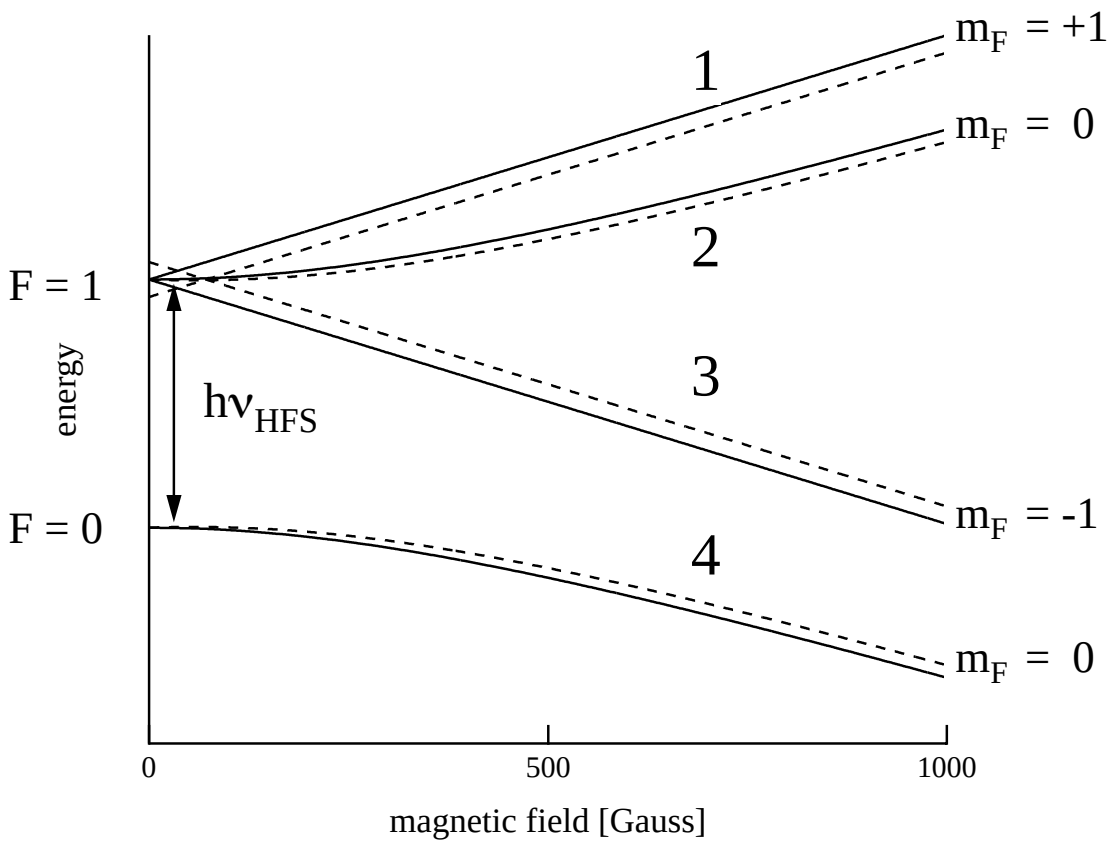

Figure 4.1: Hydrogen hyperfine structure. The full curves are the unperturbed hyperfine levels, while the dashed curves illustrate the shifts due to Lorentz and CPT violating effects with the exaggerated values of $|b^e_z - d^e_{zt} m_e - H^e_{xy}| = 90$ MHz and $|b^p_z - d^p_{zt} m_p - H^p_{xy}| = 10$ MHz. We have set a bound of less than 1 mHz for these terms [26]. A hydrogen maser oscillates on the first-order magnetic-field-independent $|2\rangle \leftrightarrow |4\rangle$ hyperfine transition near 1420 MHz. The maser typically operates with a static field less than 1 mG. For these low field strengths, the two $F = 1$, $\Delta m_F = \pm 1$ Zeeman frequencies are nearly degenerate, and $\nu_{12} \approx \nu_{23} \approx 1$ kHz.

sition, and measured a dispersion-like shift in the maser frequency (Figure 4.2). When the transverse field is near the Zeeman frequency, two-photon transitions (one audio photon plus one microwave photon) link states $|1\rangle$ and $|3\rangle$ to state $|4\rangle$, in addition to the single microwave photon transition between states $|2\rangle$ and $|4\rangle$. The two photon coupling shifts the maser frequency antisymmetrically with respect to the detuning of the applied audio field from the Zeeman resonance [25]. The large variation of the maser frequency with the applied audio field frequency allows the Zeeman frequency to be determined to ≈ 1 mHz.

To second order in the Rabi frequency of the applied Zeeman field, $|X_{12}|$, the small static-field limit of the maser frequency shift from the unperturbed frequency is given by [24]

$$\begin{aligned} \Delta\omega &= -|X_{12}|^2(\rho_{11}^0 - \rho_{33}^0)\frac{\delta(\gamma_1\gamma_2 + |X_{24}^0|^2)(\gamma_Z/r)}{(\gamma_Z^2 - \delta^2 + \frac{1}{4}|X_{24}^0|^2)^2 + (2\delta\gamma_Z)^2} \\ &\quad +|X_{12}|^2\left(\frac{\omega_C - \omega_{24}}{\omega_{24}}\right)\frac{Q_C\gamma_Z(1+K)}{\gamma_Z^2(1+K)^2 + \delta^2(1-K)^2} \end{aligned} \tag{4.6}$$

where γ_Z is the Zeeman decoherence rate, $\delta = \omega_T - \omega_{23}$ is the detuning of the applied field from the atomic Zeeman frequency, $K = \frac{1}{4}|X_{24}^0|^2/(\gamma_Z^2 + \delta^2)$, and $(\rho_{11}^0 - \rho_{33}^0)$ is the steady state population difference between states $|1\rangle$ and $|3\rangle$ in the absence of the applied Zeeman field. For perfect state selection, this population difference is $(\rho_{11}^0 - \rho_{33}^0) = r/(2\gamma_1)$. The first term in Eqn. 4.6 results from the coherent two-photon mixing of the $F = 1$ levels as described above [25], while the second term (not included in the analysis of Chapter 2) is a modified cavity pulling term that results from the reduced line-Q in the presence of the applied Zeeman field. We compared Eqn. 4.6 to experimental data from maser P-8, inserting the independently measured values of $|X_{24}^0|$, r, γ_1, and γ_2. By matching the fit to the data we extracted the Zeeman field parameters $|X_{12}|$ and γ_Z listed in Figure 4.2, as well as the target parameter δ.

In addition to the shift given by Eqn. 4.6, there is a small symmetric maser frequency shift due to the slight non-degeneracy of the two $F = 1$, $\Delta m_F = \pm 1$ Zeeman frequencies. This symmetric shift causes a small offset of the zero crossing of the double resonance

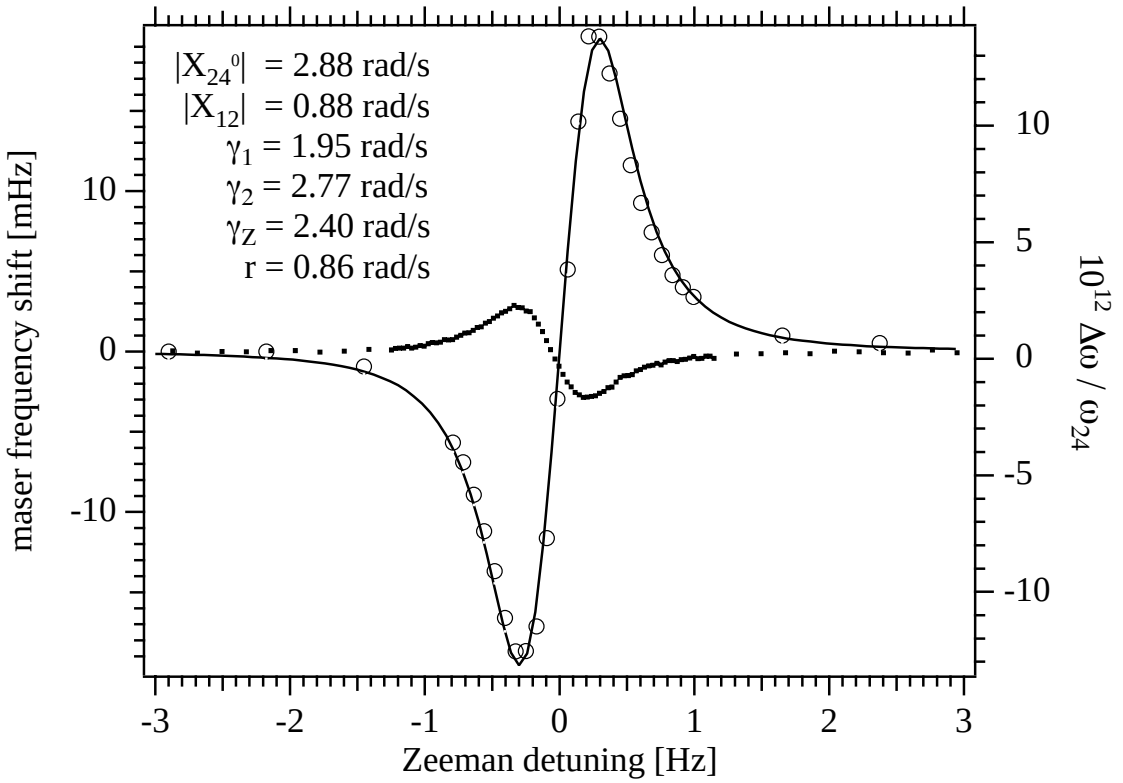

Figure 4.2: Examples of double resonance maser frequency shifts. The large open circles (maser P-8) are compared with Eqn. 4.6 (full curve) using the parameter values shown. The values of $|X_{12}|$, γ_Z, and δ (which yields the average Zeeman frequency) were chosen to fit the data, while the remaining parameters were independently measured as outlined in Chapter 3. The experimental error of each maser frequency measurement (about 40 μHz) is smaller than the circle marking it. The solid square data points are data from the CPT/Lorentz symmetry test (maser P-28). Note that the maser frequency shift amplitude for these points was smaller since these data were acquired with a much weaker applied Zeeman field. The large variation of maser frequency with Zeeman detuning near resonance, along with the excellent maser frequency stability, allows the Zeeman frequency ($\approx$ 800 Hz) to be determined to 3 mHz from a single sweep of the resonance (requiring 18 minutes of data acquisition). The inversion of the shift between the two data sets is due to the fact that maser P-8 operated with an input flux of $|2\rangle$ and $|3\rangle$ atoms, while maser P-28 operated with an input flux of $|1\rangle$ and $|2\rangle$ atoms. In both masers (and others built in our laboratory), inverting the direction of the static solenoid field relative to the fixed quantization axis provided by the state selecting hexapole magnet causes atoms in state $|3\rangle$ to be admitted to the bulb instead of atoms in state $|1\rangle$ because of sudden transitions while the atoms move rapidly through the beam tube (see Section 4.2.5).

curve away from the average Zeeman frequency, $\frac{1}{2}(\nu_{12}+\nu_{23})$. (Under typical conditions for maser P-8, the offset was approximately +1.5 mHz.) The symmetric shift was included with the antisymmetric shift (Eqn. 4.6) in our fits to the double resonance data to determine the Zeeman frequency.

Also, a previous reanalysis of the double resonance maser shift [38], which included the effects of spin-exchange collisions [68], showed that there is an additional hydrogen-density-dependent offset of the zero crossing of the maser shift resonance from the average Zeeman frequency. Using the full spin-exchange corrected formula for the maser frequency shift [38], we calculated this offset and found that for typical hydrogen maser densities ($n \approx 3 \times 10^{15}$ m^{-3}), the offset varied with average maser power as approximately -50 μHz/fW (assuming a linear relation between maser power and atomic density of $\frac{\Delta P}{\Delta n} \approx \frac{100\ fW}{3\times 10^{15}\ m^{-3}}$). For typical maser powers of $\approx$ 100 fW, there is thus a spin-exchange shift of about -5 mHz in the average Zeeman frequency. As described below, our masers typically have sidereal power fluctuations of less than 1 fW, making variations in the spin-exchange Zeeman frequency shift negligible for the test of CPT and Lorentz symmetry.

The applied Zeeman field also acts to diminish the maser power, as shown in Figure 4.3, and to decrease the maser's line-Q. By driving the $F = 1$, $\Delta m_F = \pm 1$ Zeeman transitions, the applied field depletes the population of the upper masing state $|2\rangle$, thereby diminishing the number of atoms undergoing the maser transition and reducing the maser power. Also, by decreasing the lifetime of atoms in state $|2\rangle$, the line-Q is reduced. We found that a very weak Zeeman field of about 50 nG (as used in our CPT/Lorentz symmetry test) decreases the maser power by less than 2% on resonance and reduces the line-Q by 2% (as calculated using Eqn. 6 of [24]).

4.2.2 Zeeman frequency measurement

In our test of CPT and Lorentz symmetry, we measured the atomic hydrogen $F = 1$, $\Delta m_F = \pm 1$ Zeeman frequency by applying to the masing ensemble a transverse oscillating

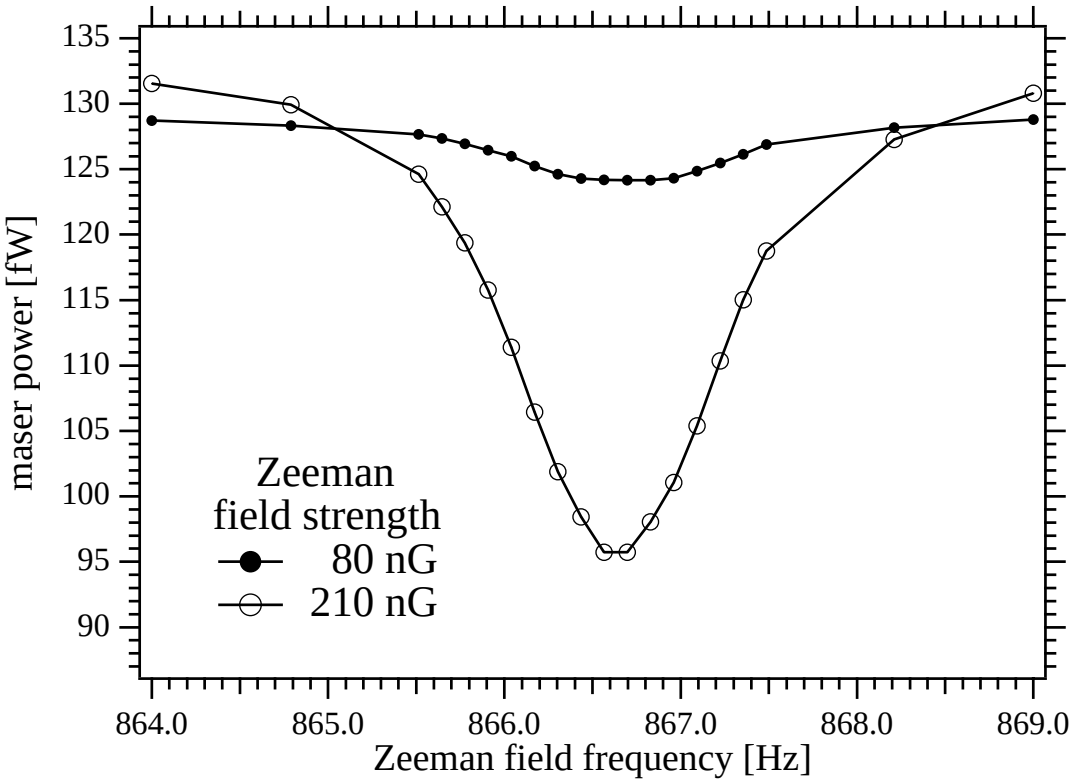

Figure 4.3: Examples of maser power reduction due to an applied Zeeman field in maser P-28. The open circles, taken with an applied Zeeman field strength of about 210 nG, represent typical data for the standard "power resonance" method used to determine the static magnetic field in the maser bulb. The filled circles are maser power curves for an applied Zeeman field strength of about 80 nG. These field strengths were determined by fitting the data to Andresen's analytical power dip lineshape [37], extracting the transverse field Rabi frequency X_{12}, then determining the field strength from the relation $\hbar X_{12} = \mu_{12} H_T = \frac{1}{\sqrt{2}} \mu_B H_T$. Our CPT/Lorentz symmetry test data were taken using the double resonance technique with a field strength of about 50 nG, inducing a power reduction of less than 2%.

magnetic field of about 50 nG peak amplitude,[2] and then sweeping the frequency of this transverse field through the Zeeman resonance. As described above, the applied transverse field shifted the maser frequency in a dispersive-like manner by a few mHz (at the extrema), a fractional shift of about 2 parts in 10^{12}. Because of the excellent fractional frequency stability of the maser (2 parts in 10^{14} over averaging times of 10 s), the shift was easily resolved (see the solid square data points in Figure 4.2). As the frequency of the applied field was stepped through the Zeeman resonance, the perturbed maser frequency (maser P-28) was compared to a second, unperturbed hydrogen maser frequency (maser P-13).[3] Independent voltage controlled crystal oscillators were phase locked to the signals from the two masers. The output frequencies of the two oscillators were set by tunable synthesizers as part of heterodyne receivers for each maser, such that there was about a 1.2 Hz offset between the oscillators. The two output signals were combined in a double-balanced mixer and the resulting beat note (period ≈ 0.8 s) was averaged for 10 s (about 12 periods) with a counter.[4] From this measured beat period we straightforwardly determined the frequency of maser P-28 relative to that of maser P-13. Typically we made 100 such relative maser frequency measurements to map out a full double resonance spectrum. For each spectrum, 80% of the points were taken over the middle 40% of the scan range, where the frequency shift varied the most.

Each double resonance spectrum of beat period vs applied transverse field frequency was fit to the function

$$\begin{aligned} T_b \quad = A_0 \quad &+ \frac{A_3\delta(1-\kappa)}{A_1(1+\kappa)^2+\delta^2(1-\kappa)^2} - \frac{A_3(\delta+\tau)(1-\kappa)}{A_1(1+\kappa)^2+(\delta+\tau)^2(1-\kappa)^2} \\ &+ \frac{A_5\delta}{(A_1-\delta^2+A_4)^2+4\delta^2A_1} + \frac{A_6(1+\kappa)}{A_1(1+\kappa)^2+\delta^2(1-\kappa)^2} \end{aligned} \tag{4.7}$$

to determine the hydrogen Zeeman frequency. Here $\delta = \nu_T - \nu_Z$ is the detuning of

[2]This field strength was determined from the transverse field Rabi frequency X_{12} (extracted from the maser frequency shift fits) using the relation $\hbar X_{12} = \mu_{12} H_T = \frac{1}{\sqrt{2}}\mu_B H_T$.

[3]Maser P-28 was chosen for Zeeman interrogation since it had the best magnetic shielding of the masers in our laboratory. Maser P-13 was chosen as the unperturbed reference since its stability was the best out of the remaining masers.

[4]Hewlett-Packard model HP 5334B.

the transverse field ν_T away from the Zeeman frequency ν_Z, $\kappa = A_4/(A_1 + \delta^2)$ is the analog of the parameter K from Eqn. 4.6 (and hence $A_4 = \frac{1}{4}|X^0_{24}|^2$ and $A_1 = \gamma^2_Z$), and $\tau = (1.403 \times 10^{-9}/Hz) \times \nu^2_Z$ is the small difference between the two Zeeman frequencies ν_{12} and ν_{23}. The first term A_0 is the constant offset representing the unperturbed beat period between the two masers. The second and third terms comprise the first-order symmetric maser shift (not included in Eqn. 4.6 but described in the text above); these two terms nearly cancel at low static magnetic field where τ is very small. The final two terms account for the two shifts given in Eqn. 4.6.

For the double resonance spectra obtained with maser P-28 for small amplitude applied transverse fields (e.g., the solid square data points of Figure 4.2), typical fit parameters were: $A_0 = 0.84550$ s $\pm$ 0.00001 s, $A_1 = 0.141$ Hz^2 $\pm$ 0.005 Hz^2, $\nu_Z = 857.063$ Hz $\pm$ 0.003 Hz (and hence $\tau = 0.001$ Hz), $A_3 = 0.006 \pm 0.010$, $A_4 = 0.029$ Hz^2 $\pm$ 0.003 Hz^2, $A_5 = (3.2 \pm 0.1) \times 10^{-4}$ Hz^2, and $A_6 = (-1 \pm 5) \times 10^{-6}$ Hz. Note that the typical uncertainty in the Zeeman frequency determination was 3 mHz and that A_3 and A_6, the amplitude coefficients of the residual first-order shift and the cavity pulling term, were consistent with zero.

With our measured values of $r = 0.86$ rad/s and $\gamma_2 = 2.33$ rad/s, the above set of fit parameters imply that $X^0_{24} = 2.14$ rad/s, $\gamma_Z = 2.36$ rad/s, $\gamma_1 = 1.13$ rad/s, with $X_{12} = 0.32$ rad/s. Since A_3 had such a large error bar (because of the small value of the first-order symmetric frequency shift at low static magnetic fields), the value of X_{12} for maser P-28 was chosen such that the ratio of the square of X_{12} for P-28 to that for P-8 was equal to the ratio of the measured maser shift amplitudes for P-28 and P-8, shown in Figure 4.2. These values, for maser P-28, are compared in Table 4.2 to the values reported in Chapter 3 for maser P-8. We note that the parameter values inferred from the double resonance fit coefficients may include errors due to the perfect state selection approximation of Eqn. 4.6. We speculate that this is the reason for the discrepancy between measured and inferred values for maser P-8 (shown in columns 2 and 3 of Table 4.2).

To optimize the Zeeman frequency resolution of our experimental procedure, we recorded

Parameter	P-8 (measured)	P-8 (inferred)	P-28 (inferred)
V_C	1.4×10^{-2} m^3	1.4×10^{-2} m^3	1.4×10^{-2} m^3
V_b	2.9×10^{-3} m^3	2.9×10^{-3} m^3	2.9×10^{-3} m^3
η	2.14	2.14	2.14
r	0.86 rad/s	0.86 rad/s	0.86 rad/s
Q_C	39,300	39,300	39,400
β	0.23	0.23	0.23
Q_l	1.6×10^9	1.6×10^9	1.9×10^9
P_o	112 fW	112 fW	75 fW
P	600 fW	600 fW	400 fW
q	0.05		
γ_t	1.71 rad/s		
P_c	220 fW		
I_{th}	0.47×10^{12} atoms/s		
I	2.11×10^{12} atoms/s		
I_{tot}	5.1×10^{12} atoms/s		
n	1.0×10^{15} atoms/m^3		
γ_{se}	0.38 rad/s		
$\lvert X_{12}\rvert$	0.88 rad/s	0.88 rad/s	0.32 rad/s
γ_Z	2.42 rad/s	2.42 rad/s	2.36 rad/s
$\lvert X_{24}\rvert$	2.88 rad/s	2.21 rad/s	2.14 rad/s
γ_1	1.95 rad/s	1.28 rad/s	1.13 rad/s
γ_2	2.77 rad/s	2.77 rad/s	2.33 rad/s

Table 4.2: Operational parameters for masers P-8 and P-28. All values have been converted into SI units. All parameters were defined previously in Chapter 3, with the exception of the Zeeman field Rabi frequency $|X_{12}|$ and the Zeeman decoherence rate γ_Z. The second column depicts parameters measured directly as in Chapter 3 for maser P-8. The last two columns depict parameters inferred from the double resonance fit parameters for both masers P-8 and P-28, as described in Section 4.2.2. Note that in the third column, the audio field Rabi frequency $|X_{12}|$ and Zeeman decoherence rate γ_Z for P-8 were inferred by comparing the Andresen fit function (Eqn. 4.6) to data and inserting the measured values for γ_1, γ_2, r, and $|X_{24}|$. When inferring maser parameters from the P-28 double resonance fit (last columns), the value of $|X_{12}|$ for P-28 was set such that the ratio of the square of $|X_{12}|$ for P-28 to that for P-8 was equal to the ratio of the measured maser frequency shift amplitudes. We speculate that the discrepancy between measured and inferred maser parameters for maser P-8 (between columns 2 and 3) is due to the perfect state selection approximation in Eqn. 4.6.

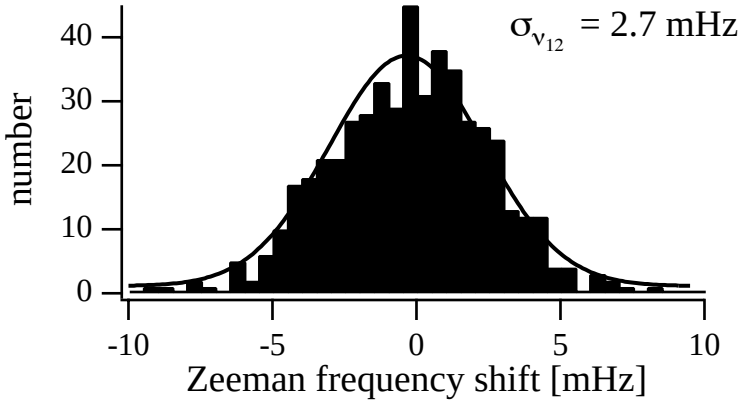

Figure 4.4: Example results from a Monte Carlo analysis of the resolution of the double resonance method for determining the hydrogen Zeeman frequency. The horizontal axis represents the shift of the Zeeman frequency as determined by our fits of over 100 synthetic data sets constructed as described in the body of the paper text; the vertical axis is the number of data sets within each frequency shift bin. The width of the Gaussian fit to the data is 2.7 mHz, representing the estimated resolution of a Zeeman frequency determination from a single, complete double resonance spectrum.

several spectra with 50, 100, and 150 points at 5 s and 10 s averaging. We also varied the distribution of points along the drive frequency axis, including spectra where the middle 40% of the scan contained 80% of the points and those where the middle 30% contained 80% of the points (thus increasing the number of points in the region where the maser frequency varies the most). With each of these spectra, we ran the following Monte Carlo analysis [69]: after fitting each scan to Eqn. 4.7, we constructed 100 synthetic data sets by adding Gaussian noise to the fit, with the noise amplitude determined by the unperturbed maser frequency resolution of about 40 μHz. Each of these synthetic data sets was fit and a histogram of the fitted Zeeman frequencies was constructed. The resolution of the fit was taken as the Gaussian width of the fitted Zeeman histogram (see Figure 4.4). As the total length of the scans increased, the resolution improved and converged to a limit of around 2.5 mHz. While the resolution improved slowly with increased acquisition time, it eventually began to degrade due to long-term drifting of the Zeeman frequency. (As will be described below, we found that the Zeeman frequency exhibited slow drifts

of about 10-100 mHz/day.) We therefore chose a scan of 100 points at 10 s averaging, for a total length of about 18 minutes for each double resonance spectrum used in the Lorentz symmetry test. As mentioned above, we also chose to operate with 80% of the points acquired over the middle 40% of the scan range. As an example, Figure 4.4 shows the results from the Monte Carlo analysis for one of the test spectra, indicating a Zeeman frequency resolution of 2.7 mHz.

4.2.3 Data analysis

Our net bound on a sidereal variation of the atomic hydrogen $F = 1$, $\Delta m_F = \pm 1$ Zeeman frequency combines data from three multi-day runs. During each data run, the 18 minute Zeeman frequency scans were automated and run consecutively. After every 10 scans, 20 minutes of "unperturbed" maser frequency stability data was taken to track the maser's unperturbed frequency. Each run contained about 10 continuous days of data and more than 500 Zeeman frequency measurements.

For each day in a run, the Zeeman frequency data, corrected for measured variations in the solenoid current (see Section 4.3.1), was fit to a function of the form

$$fit \;=\; (\textit{piecewise continuous linear function}) + \delta\nu_{Z,\alpha}\cos(\omega_{sid}t) + \delta\nu_{Z,\beta}\sin(\omega_{sid}t) \quad (4.8)$$

where $\delta\nu_{Z,\alpha}$ and $\delta\nu_{Z,\beta}$ represent the cosine and sine components of a sidereal-day-period sinusoid. For all times in the nth sidereal day, the piecewise continuous linear function was given by

$$f_n(t) = \sum_{i=0}^{n} A_i + A_{n+1}(t - n). \quad (4.9)$$

The time origin of the sinusoids for all three runs was taken as midnight (00:00) of November 19, 1999. The subscripts α and β refer to two non-rotating orthogonal axes perpendicular to the rotation axis of the earth. The total amplitude of a sidereal-period modulation of ν_Z was determined by adding $\delta\nu_{Z,\alpha}$ and $\delta\nu_{Z,\beta}$ in quadrature. During each run, the Zeeman frequency drifted hundreds of mHz over tens of days (see discussion in Section 4.3.2).

The piecewise continuous linear function, consisting of segments of one sidereal day in length, was included to account for these long-term Zeeman frequency drifts. This function was continuous at each break, while the derivative was discontinuous.

The result of the above analysis procedure was in good agreement with a second analysis method in which each day of Zeeman frequency data was fit to a line plus the sidereal-period sinusoid, and the cosine and sine amplitudes for all days were averaged separately and then combined in quadrature to find the total sidereal-period amplitude.

In addition to our automated acquisition of Zeeman frequency data, we continuously monitored the maser's environment. At every ten second step, in addition to the applied Zeeman frequency and maser beat period, we recorded room temperature, maser cabinet temperature, solenoid current, maser power, and ambient magnetic field. Estimates of systematic effects are discussed in Section 4.3.

4.2.4 Run 1

The cumulative data from the first run (November, 1999) are shown in Figure 4.5(a) and the residuals from the fit to Eqn. 4.8 are shown in Figure 4.5(b). The data set consisted of 11 full days of data and had an overall drift of about 250 mHz.

To avoid a biased choice of fitting, we varied the times of the slope discontinuities in the piecewise continuous linear function throughout a sidereal day. We made eight separate fits, each with the times of the slope discontinuities shifted by three sidereal hours. The total sidereal amplitude and reduced chi square (χ^2_ν [70]) for each is shown in Figure 4.6. We chose our result from the fit with minimum χ^2_ν.

As noted above, the uncertainty in a single Zeeman frequency determination was about 3 mHz. However, when analyzing a typical day of Zeeman frequency data we found a residual estimated error in the mean of about 5 mHz. We believe this discrepancy in short- and long-term Zeeman frequency determination is due mainly to residual thermal fluctuations, as discussed in Section 4.3.2.

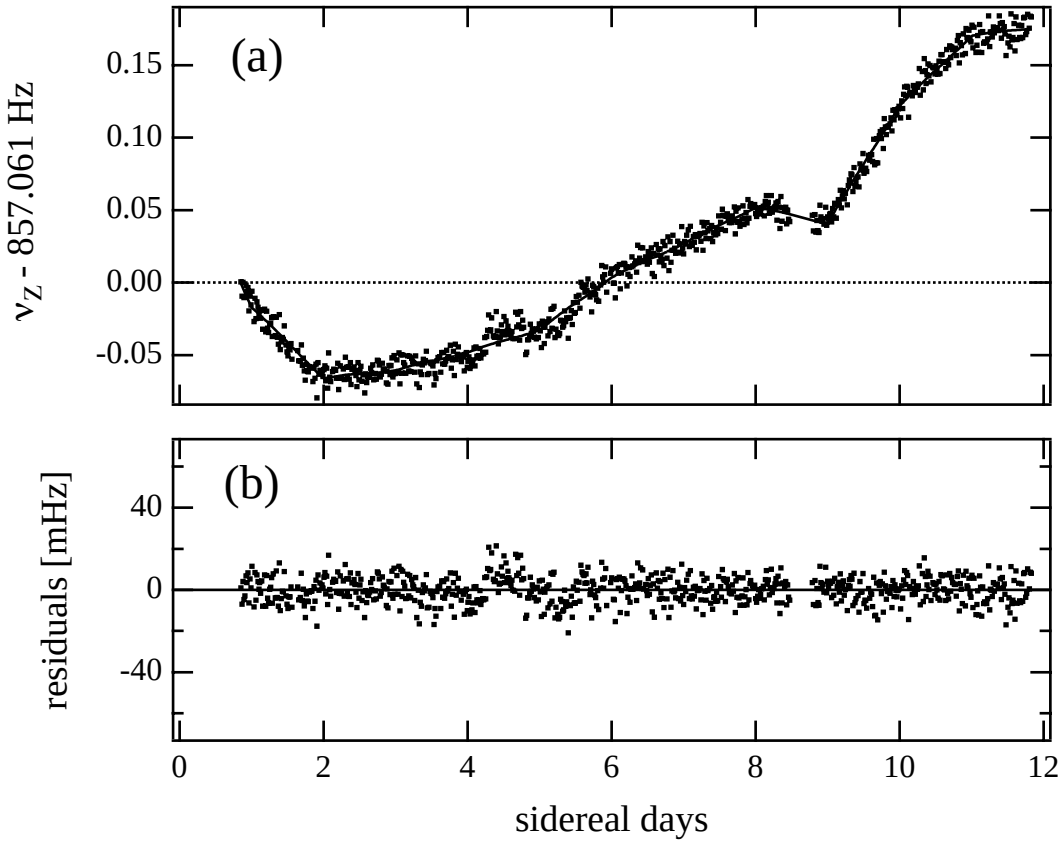

Figure 4.5: (a) Run 1 Zeeman frequency data (November, 1999) and the corresponding fit function (solid line). From the measured Zeeman frequencies, we subtracted the initial value, 857.061 Hz, and the effect of measured solenoid current variations. (b) Residuals after fitting the data to Eqn. 4.8; i.e., difference between Zeeman frequency data and fit function.

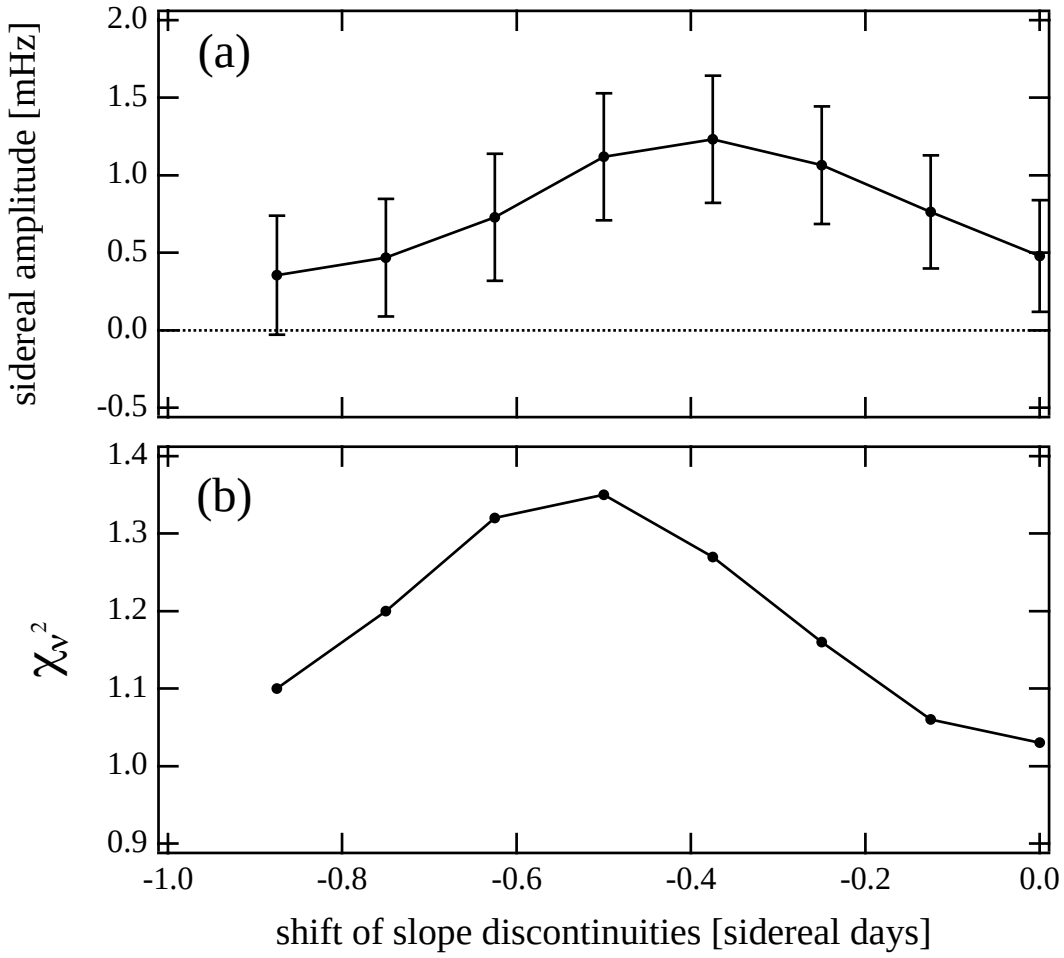

Figure 4.6: (a) Total sidereal amplitudes for Run 1 data as a function of the time of slope discontinuity locations in the piecewise continuous fit function. (b) Corresponding reduced chi square (χ^2_ν) parameters. The minimum value occurs with a slope break origin of midnight (00:00) at the beginning of November 19, 1999.

For the choice of slope discontinuity with minimum χ^2_ν,[5] the cosine amplitude was 0.43 mHz $\pm$ 0.36 mHz, and the sine amplitude was -0.21 mHz $\pm$ 0.36 mHz. The total sidereal-period amplitude was therefore 0.48 mHz $\pm$ 0.36 mHz. Note that this total amplitude is, by definition, positive with the most probable value (for a normal distribution consistent with no Lorentz-violating effect) equal to one standard deviation. Thus the mean value (0.48 mHz) for run 1 is less than one standard deviation away from the most probable value (0.36 mHz) (see Section 4.2.6).

4.2.5 Field-inverted runs 2 and 3

In runs 2 and 3, the static solenoid magnetic field orientation was opposite that of the initial run, which enabled us to investigate potential systematics associated with the solenoid field. With the static field inverted, and therefore directed opposite to the quantization axis at the exit of the state selecting hexapole magnet, the input flux consisted of atoms in states $|2\rangle$ and $|3\rangle$ (rather than the states $|1\rangle$ and $|2\rangle$). Thus, reversing the field inverted the steady state population difference $(\rho^0_{11} - \rho^0_{33})$ of Eqn. 4.6 and acted to invert the antisymmetric double resonance maser frequency shift [25].

Operating the maser in the field reversed mode also degraded the maser frequency stability and hence the Zeeman frequency measurement sensitivity (see Figures 4.7(a) and 4.8(a)). With opposed quantization fields inside the maser bulb and at the exit of the state selecting hexapole magnet, a narrow region of field inversion was created. Where the field passed through zero, Majorana transitions between the different m_F sublevels of the $F = 1$ manifold could occur. This reduced the number of atoms in the upper maser state ($F = 1$, $m_F = 0$, state $|2\rangle$), diminishing the overall maser amplitude (by $\approx 30\%$ in maser P-28) and degrading the frequency stability. In addition, the overall Zeeman frequency drift was larger in runs 2 and 3 than in run 1 (nearly 800 mHz over about 10 days); also, the scatter in the data was increased, as can be seen from the residual plots Figures 4.7(b) and 4.8(b) which have been plotted on the same scale as the residuals from

[5]Had we chosen the slope discontinuity with maximum χ^2_ν, the total sidereal amplitude for this run would have been 1.1 mHz $\pm$ 0.4 mHz.

the first run (Figure 4.5(b)).[6]

The latter two runs also had more frequent changes of the slope of long-term Zeeman frequency drift (often on timescales < 1 day) than did the first run. Therefore, only certain selected portions of runs 2 and 3 could be fit to the piecewise continuous linear drift model (Eqn. 4.8) with $\chi^2_\nu \approx 1$, significantly truncating the data sets. In all, the sidereal-period amplitudes and associated uncertainties' error bars were up to an order of magnitude larger for the field-inverted runs than the first run. The results from all three runs are shown together in Table 4.3.

Run	$\delta\nu_{Z,\alpha}$ [mHz]	$\delta\nu_{Z,\beta}$ [mHz]
1	0.43 ± 0.36	-0.21 ± 0.36
2	-2.02 ± 1.27	-2.75 ± 1.41
3	4.30 ± 1.86	1.70 ± 1.94

Table 4.3: Sidereal-period amplitudes from all runs.

4.2.6 Combined result

We calculated a final bound on the amplitude A of a sidereal variation of the $F = 1$, $\Delta m_F = \pm 1$ hydrogen Zeeman frequency by adding the weighted mean cosine and sine amplitudes from all three runs in quadrature: $A = \sqrt{\bar{\delta\nu}^2_{Z,\alpha} + \bar{\delta\nu}^2_{Z,\beta}} = 0.49 \pm 0.34$ mHz. In calculating the weighted mean sidereal amplitudes, $\bar{\delta\nu}_{Z,\alpha}$ and $\bar{\delta\nu}_{Z,\beta}$, we accounted for the sign reversal due to the magnetic field inversion in the raw data. We note that since the sidereal variation amplitude A is a strictly positive quantity, the present result is consistent with no sidereal variation at the 1-sigma level: in the case where $\bar{\delta\nu}_{Z,\alpha}$ and $\bar{\delta\nu}_{Z,\beta}$ have zero mean value and the same variance σ, the probability distribution for A takes the form $P(A) = A\sigma^{-2}\exp(-A^2/2\sigma^2)$, which has the most probable value occurring

[6] Maser P-28 was only temporarily available for our use during the time it was in our lab for refurbishing. As a result, the amount of data we could acquire with maser P-28 was limited. Maser P-8 is housed permanently in our laboratory, so we could perform more extensive characterization of this maser. Note that maser P-8 was not suitable for a CPT/Lorentz symmetry test because it suffered from large, long-term Zeeman frequency drifts, attributed to less effective magnetic shielding and greater extraneous magnetic fields (e.g., from heating elements), than maser P-28.

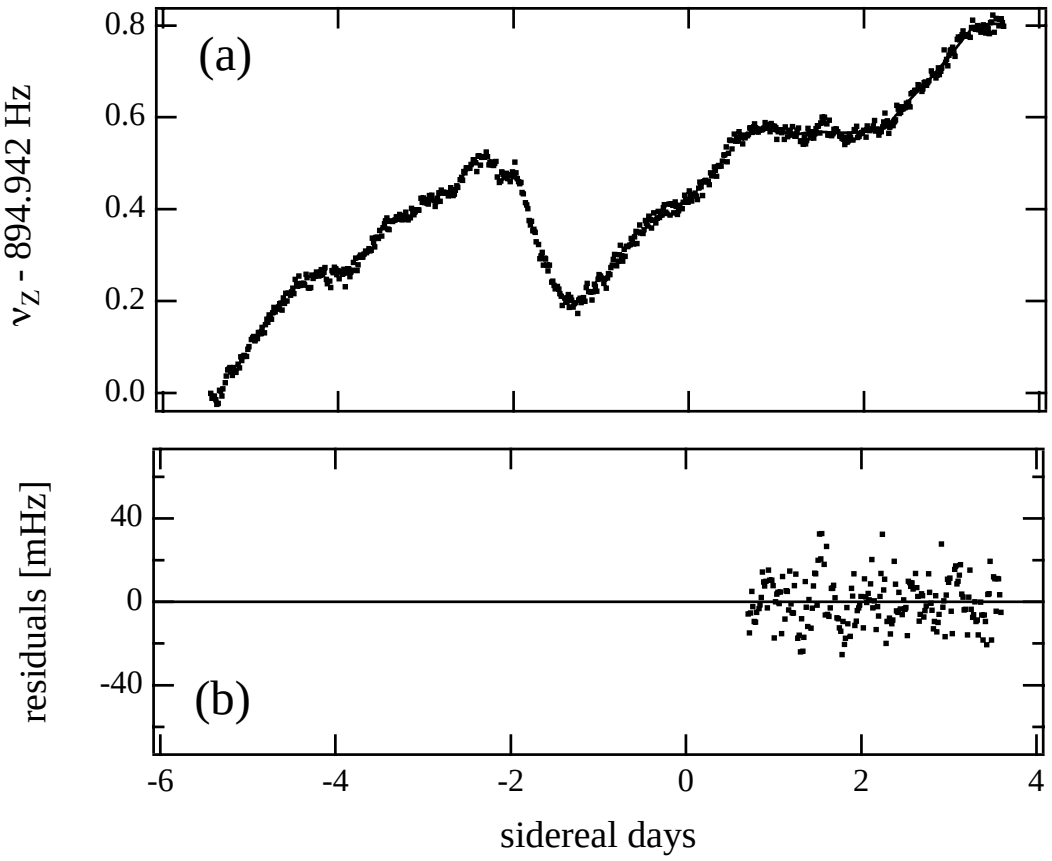

Figure 4.7: (a) Run 2 Zeeman frequency data (December, 1999) and the corresponding fit function (solid line). From the measured Zeeman frequencies, we subtracted the initial value, 894.942 Hz, and the effect of measured solenoid current variations. (b) Residuals after fitting the data to Eqn. 4.8; i.e., difference between Zeeman frequency data and fit function. Note that only three sidereal days of data could be well fit by the piecewise continuous linear drift model.

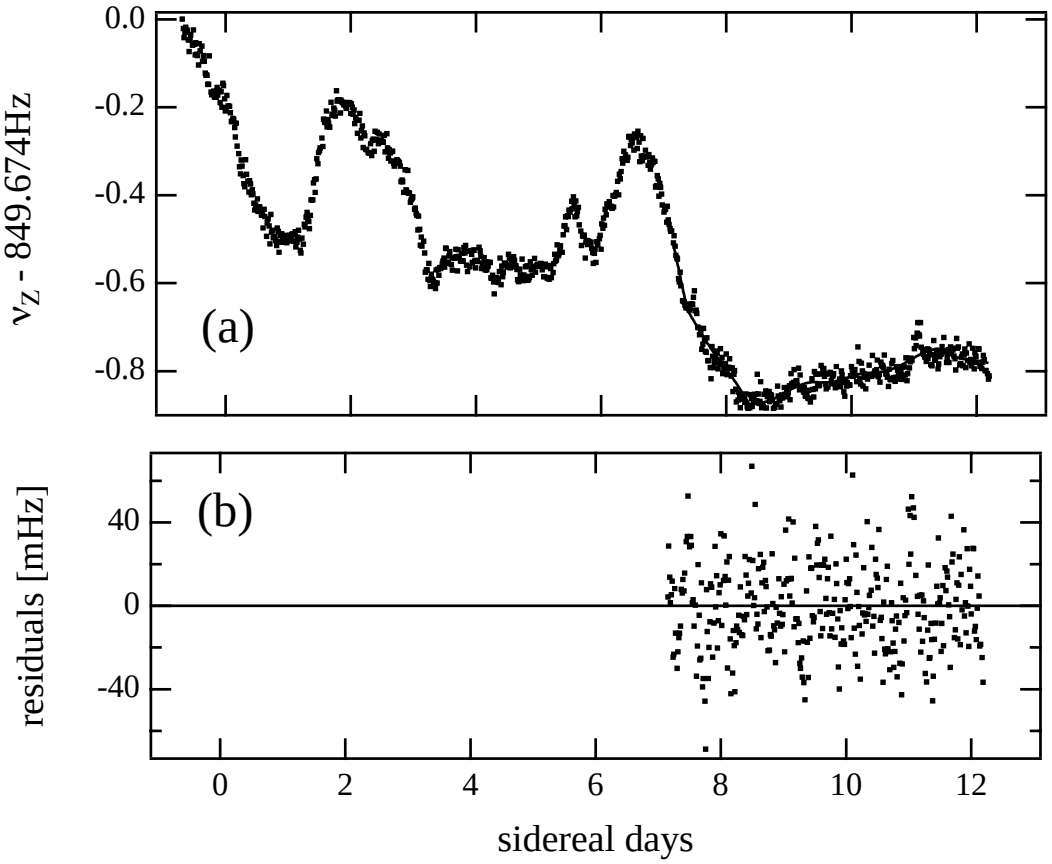

Figure 4.8: (a) Run 3 Zeeman frequency data (March, 2000) and the corresponding fit function (solid line). From the measured Zeeman frequencies, we subtracted the initial value, 849.674 Hz, and the effect of measured solenoid current variations. (b) Residuals after fitting the data to Eqn. 4.8; i.e., difference between Zeeman frequency data and fit function. Note that only five sidereal days of data could be well fit by the piecewise continuous linear drift model.

at $A = \sigma$.

4.3 Systematics and error analysis

4.3.1 Magnetic field systematics

The $F = 1$, $m_F = \pm 1$ Zeeman frequency depends to first order on the z-component of the magnetic field in the storage bulb. Thus, all external field fluctuations had to be sufficiently screened to enable high sensitivity to frequency shifts from CPT and Lorentz symmetry violation. The maser cavity and bulb were therefore surrounded by a set of four nested magnetic shields that reduce the ambient z-component field by a factor of about 32,000. We measured unshielded fluctuations in the ambient field of about 3 mG (peak-peak) throughout any given day, and even when shielded these fluctuations added significant noise to each Zeeman frequency determination using the double resonance technique ("Zeeman scan"), as illustrated in Figure 4.9(a). Furthermore, the amplitude of the field fluctuations was significantly reduced late at night, due to the cessation of the local subway and electric bus lines, which could have generated a diurnal systematic effect in our data.

To reduce the effect of fluctuations in the ambient magnetic field, we installed an active feedback system (see Figure 4.10) consisting of two large Helmholtz coil pairs (2.4 m diameter) and a fluxgate magnetometer. The magnetometer probe[7] was placed inside the maser's outermost magnetic shield near the maser cavity and had a magnetic field sensitivity of $s = 1.7$ mG/V. Due to its location inside one magnetic shield, the probe was shielded by a factor of about six from external fields, reducing the effective sensitivity to $s' = 0.3$ mG/V, and producing a differential shielding of 5300 between the magnetometer probe and the hydrogen atoms in the maser bulb. The first pair of Helmholtz coils (50 turns) produced a uniform, static field that canceled most of the z-component of the ambient field, leaving a residual field of around 5 mG (as measured by the shielded probe).

[7] RFL Industries model 101.

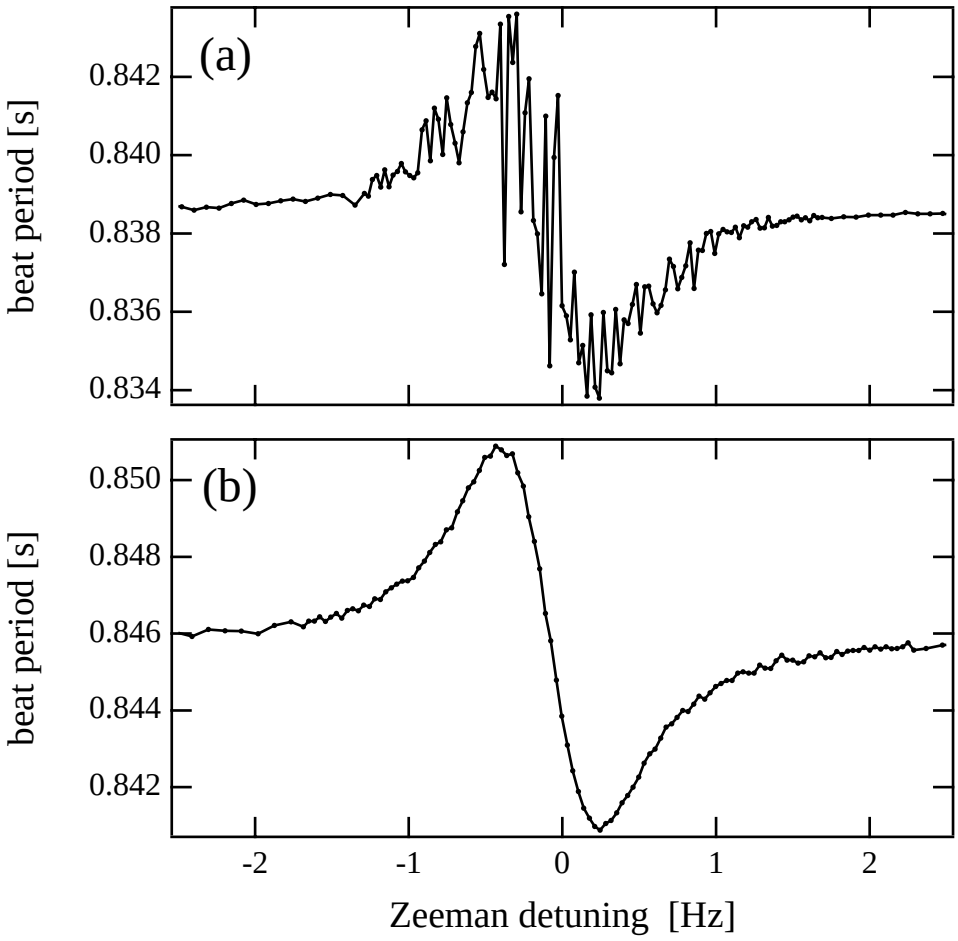

Figure 4.9: (a) Double resonance "Zeeman scan" without active compensation for ambient magnetic field fluctuations. The noise on the data is due to left and right shifting of the antisymmetric resonance as the Zeeman frequency is changed by ambient field fluctuations (unshielded magnitude about 3 mG). (b) Zeeman scan with active compensation for ambient magnetic field fluctuations using a Helmholtz coil feedback loop. Ambient field fluctuations outside the maser's passive magnetic shields were effectively reduced to less than 5 μG.

The magnetometer output was passed into a PID servoloop,[8] which contained proportional (gain $G = 33$), integral (time constant $T_i = 0.1$ s) and derivative (time constant $T_d = 0.01$ s) stages. The correction voltage was applied to the second pair of Helmholtz coils (3 turns) which produced a uniform field ($p = 14$ mG/V) along the z-axis to nullify the residual field and actively counter any fluctuations. The overall time constant of this system was approximately $\tau = T_i(1+s'/pG) \approx 0.1$ s (neglecting the derivative stage), about 100 times shorter than the averaging time of our typical maser frequency measurements (10 s).

With this system we were able to reduce ambient field fluctuations at the magnetometer by a factor of 1,000 in addition to the passive shielding provided by the magnetic shields. The resulting measured field fluctuations, at the magnetometer position within the outermost magnetic shield, were less than 1 μG peak-peak (see Figure 4.11). The noise on a single Zeeman scan was thus reduced below our Zeeman frequency measurement resolution, as shown in Figure 4.9(b). During the CPT and Lorentz symmetry test, the sidereal component of the magnetic field variation measured at the probe was ≤ 1 nG, corresponding to a shift of less than 0.2 μHz on the hydrogen Zeeman frequency, three orders of magnitude smaller than the sidereal Zeeman frequency bound set by our experiment. This small systematic uncertainty in the Zeeman frequency was included in the net error analysis, as described in Sec. 4.3.3.

The magnetometer used in the feedback loop was a fluxgate magnetometer probe which consisted of two parallel high-permeability magnetic cores each surrounded by an excitation coil (the excitation coils were wound in the opposite sense of each other). A separate pickup coil was wound around the pair of cores. An AC current (about 2.5 kHz) in the excitation coils drove the cores into saturation, and, in the presence of any slowly varying external magnetic field oriented along the magnetic cores' axes, an EMF was generated in the pickup coil at the second and higher harmonics of the excitation frequency. The magnitude of the time-averaged EMF was proportional to the external field. The probe had a sensitivity of approximately 1 nG.

[8] Linear Research model LR-130.

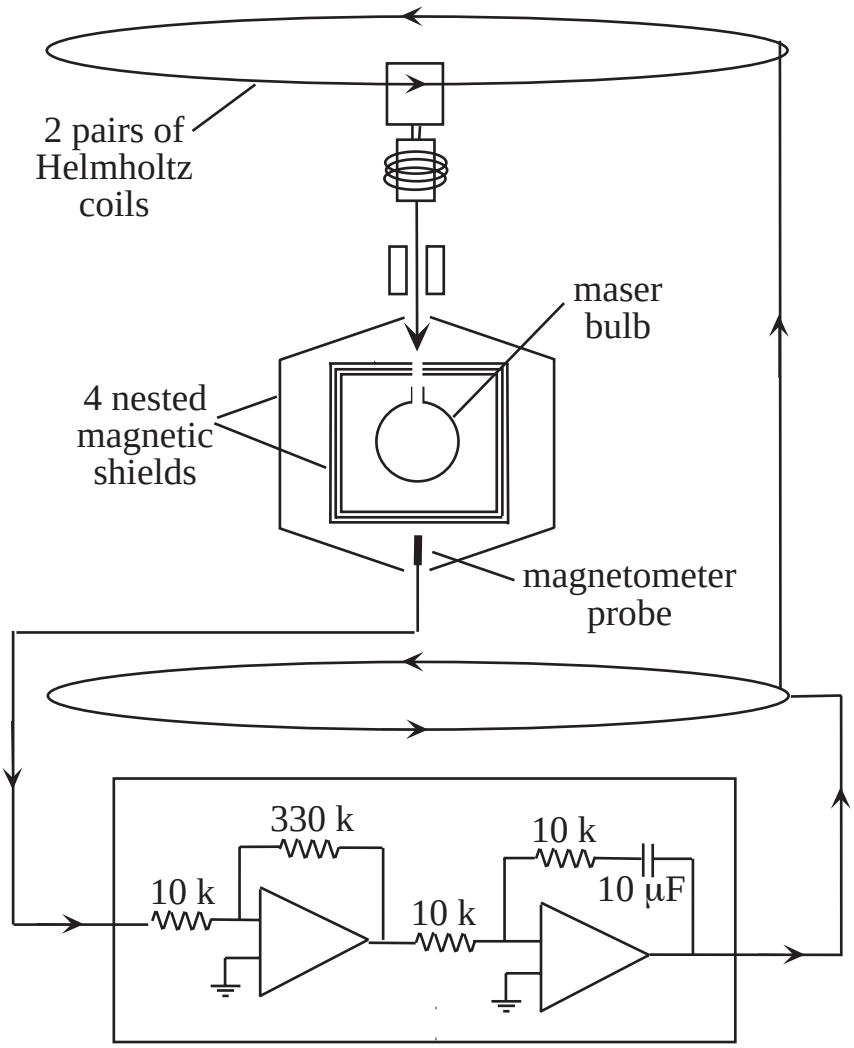

Figure 4.10: Schematic of the active system used to compensate for ambient magnetic field fluctuations. A large set of Helmholtz coils (50 turns) canceled all but a residual ~ 5 mG of the z-component of the ambient field. This residual field, detected with a fluxgate magnetometer probe, was actively canceled by a servoloop and a second pair of Helmholtz coils (3 turns). The servoloop consisted of a proportional stage (gain = 33), an integral stage (time constant = 0.1 s) and a derivative stage (time constant = 0.01, not shown). The overall time constant of the loop was about $\tau = 0.1$ s.

Any Lorentz violating spin-orientation dependence of the energy of the electrons in the magnetic cores of the fluxgate magnetometer would have induced a sidereal variation in the cores' magnetization and could have generated, or masked, a sidereal variation in the hydrogen Zeeman frequency through the ambient field control system. However, based on the latest bound on electron Lorentz violation (10^{-29} GeV [66]), any Lorentz violating effect on the magnetometer corresponds to an effective magnetic field change of less than $\delta B = \frac{1}{\mu_B}\delta E = 10^{-12}$ G, far below the level of residual ambient field fluctuations. Also, the additional shielding factor of 5300 between the magnetometer probe and the hydrogen atoms further reduced the effect of any Lorentz violating shift in the probe electrons' energies.

With the ambient field well controlled near zero, the Zeeman frequency was set by the magnetic field generated by the three coil maser solenoid, and hence by the solenoid current. Each low-resistance coil (main and two end coils) of the maser solenoid was driven by a voltage-regulated supply in series with an adjustable voltage divider and a current-limiting precision 5 kΩ resistor. We monitored solenoid current fluctuations by measuring the voltage across the main coil's current-limiting resistor with a 5 1/2 digit multimeter.[9] By measuring the Zeeman frequency shift caused by large current changes, we found a dependence of 8 mHz/nA. Long-term drifts in the current were typically about 5 nA (see Figure 4.12), significant enough to produce detectable shifts in the Zeeman frequency. In particular, the measured sidereal component of the solenoid current variation was 25 $\pm$ 10 pA, corresponding to a sidereal Zeeman frequency variation of 0.16 $\pm$ 0.08 mHz. We corrected for these drifts directly in the Zeeman data during data analysis using the above current/Zeeman frequency calibration. The resultant sidereals systematic uncertainty in the Zeeman frequency was included in the net error analysis for the Lorentz/CPT symmetry test (Sec. 4.3.3).

[9]Fluke model 8840A/AF.

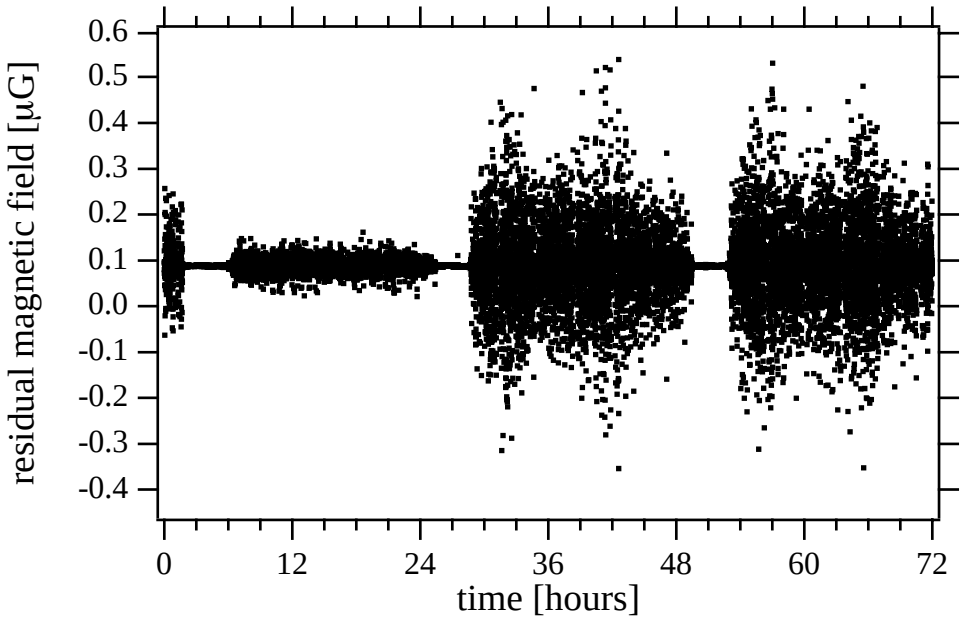

Figure 4.11: Residual ambient magnetic field, after cancellation by the active Helmholtz control loop, sensed by the magnetometer probe located within the outermost magnetic shield. Each point is a 10 s average. These three days of typical data depict a Sunday, Monday and Tuesday, with the time origin corresponding to 00:00 Sunday. From these data it can be seen that for three hours every night the magnetic noise dies out dramatically due to subway and electric bus cessation, and that the noise level is significantly lower on weekends than weekdays. Nevertheless, with the active feedback system even the largest fluctuations (1 μG peak-peak) cause changes in the Zeeman frequency below our sensitivity ($\Delta B = 1\mu G \Rightarrow \Delta\nu_Z = 0.3$ mHz).

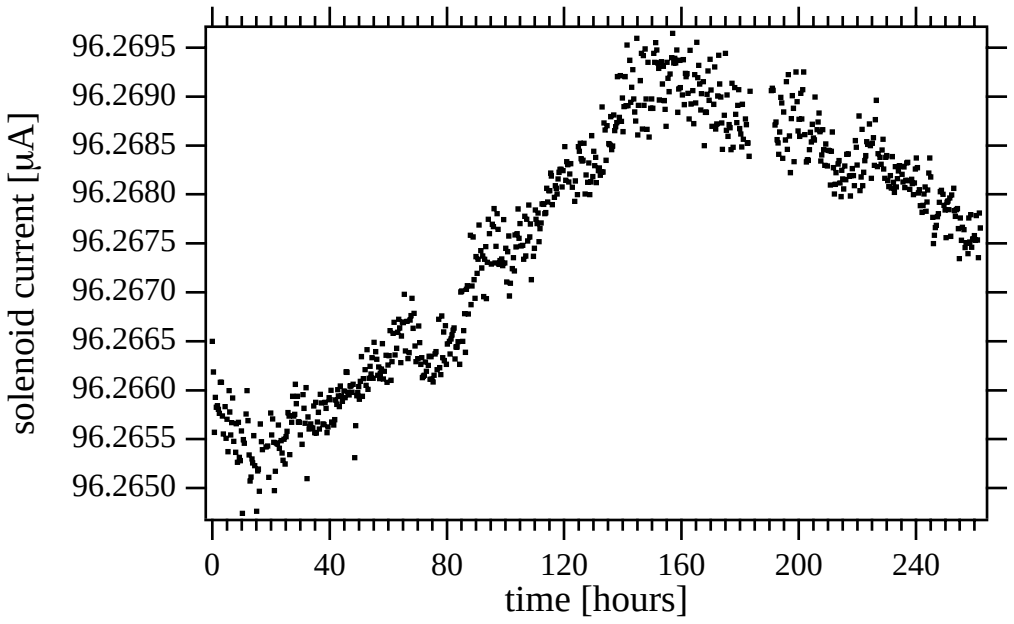

Figure 4.12: Solenoid current during the first data run. Each point is an average over one full Zeeman frequency measurement (18 mins). Since the Zeeman frequency is directly proportional to the solenoid current, we subtracted these solenoid current drifts directly from the raw Zeeman data, using a measured calibration. We found a sidereal component of 25 ± 10 pA to the solenoid current variation, corresponding to a sidereal variation of 0.16 ± 0.08 mHz in the Zeeman frequency.

4.3.2 Other systematics

During the Lorentz symmetry test, maser P-28 resided in a closed, temperature stabilized room where the temperature oscillated with a peak-peak amplitude of slightly less than 0.5 ˚C with a period of around 15 minutes (driven by the room air-conditioning system). The outermost shell of the maser was an insulated and thermally controlled cabinet, which provided a factor of ten isolation from temperature fluctuations of the room, as shown in Figure 4.13. By making changes to the temperature within the maser cabinet and measuring the effect on the Zeeman frequency, we found a relation of about 200 mHz/ ˚C. This frequency shift was due mainly to the solenoid current-limiting 5 kΩ resistors, which have 100 ppm/ ˚C temperature coefficients. We accounted for temperature-induced (and other) changes in the solenoid current by monitoring the voltage across the main coil's

current-limiting resistor, as described above.

However, remnant temperature-induced changes in the magnetic field and hence the Zeeman frequency could arise from adjusting currents in the 4-layer system of maser temperature control. On an intermediate timescale of a few hours, we estimate that such temperature-induced effects produced additional variations of about 1 mHz in the measured Zeeman frequency, increasing the estimated error in the mean of the fitted residual Zeeman frequency in a given day from about 3 mHz to 5 mHz. On a longer timescale, our measurements placed a bound of 0.5 mK on the sidereal component of the cabinet temperature fluctuations, which would produce a systematic sidereal variation of 100 μHz on the Zeeman frequency, about a factor of 3 smaller than the measured limit on sidereal variation in Zeeman frequency.

The Zeeman frequency data from all runs (Figures 4.5, 4.7, and 4.8) show that the Zeeman frequency drift over longer time scales (i.e., days) was up to hundreds of mHz. While this long-term drift was accounted for by a fit to a linear drift function, its presence certainly degraded our overall sensitivity to Zeeman frequency variation. Indeed, the rapid changes in this drift in runs 2 and 3 precluded our use of a sizable fraction of the Zeeman frequency data. We speculate that possible sources of these long-term drifts were changing magnetic fields near the maser bulb caused by stray currents in heaters or power supplies or drift of the thermal control loops of the temperature control system.

As mentioned in Section 4.2.1, spin-exchange effects induce a small offset of the Zeeman frequency determined by the double resonance technique from the actual Zeeman frequency [38]. Thus, variations in the input atomic flux (and therefore the atomic density and the maser power) could cause variations in the Zeeman frequency measurement. We measured a limit on the shift of the Zeeman frequency due to large changes in average maser power of less than 0.8 mHz/fW. (Expected shifts from spin-exchange are ten times smaller than this level, see Section 4.2.1. We believe the measured limit is related to heating of the maser as the flux is increased). During long-term operation, the average maser power drifted approximately 1 fW/day (see Figure 4.14). The sidereal component of the variations

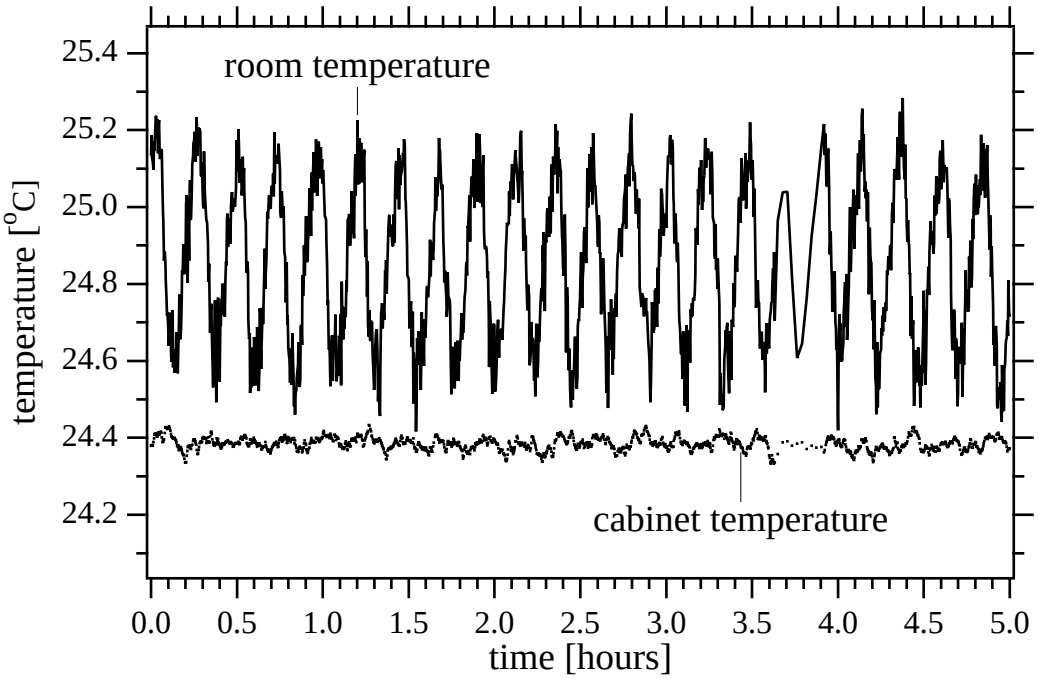

Figure 4.13: Temperature data during the first run. Each point is a 10 second average. The top trace shows the characteristic 0.5 ˚C peak-peak, 15 minute period oscillation of the room temperature. The bottom trace shows the screened oscillations inside the maser cabinet. The cabinet is insulated and temperature controlled with a blown air system. In addition, the innermost regions of the maser, including the microwave cavity, are further insulated from the maser cabinet air temperature, and independently temperature controlled. The residual temperature variation of the maser cabinet air had a sidereal variation of 0.5 mK, resulting in an additional systematic uncertainty of 0.1 mHz on the Zeeman frequency. This value is included in the net error analysis.

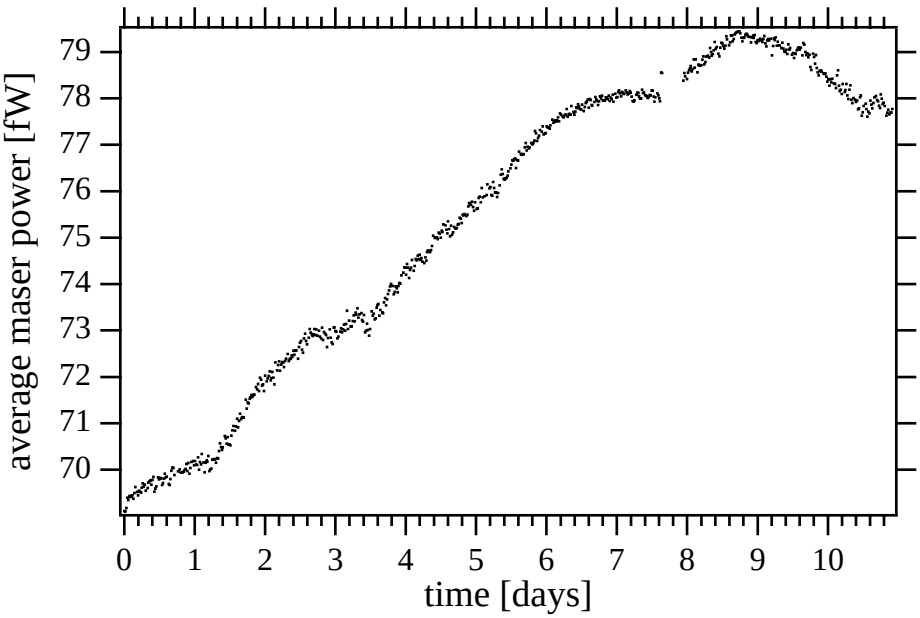

Figure 4.14: Average maser power during the first data run. Each point is an average over one full Zeeman frequency measurement (18 mins). We measured a sidereal variation in this power to be less than 0.05 fW, leading to an additional systematic uncertainty in the Zeeman frequency of 0.04 mHz, which is included in the net error analysis.

of the maser power were less than 0.05 fW, implying a sidereal variation in the Zeeman frequency of less than 40 μHz, an order of magnitude smaller than our experimental bound for sidereal Zeeman frequency variation.

4.3.3 Final result

We measured systematic errors in sidereal Zeeman frequency variation (as described in Secs. 4.3.1 and 4.3.2) due to ambient magnetic field (0.2 μHz), solenoid field (80 μHz), maser cabinet temperature (100 μHz), and hydrogen density induced spin-exchange shifts (40 μHz). Combining these errors in quadrature with the 0.34 mHz statistical uncertainty in Zeeman frequency variation, we find the absolute magnitude of a sidereal variation of the $F = 1$, $\Delta m_F = \pm 1$ Zeeman frequency in atomic hydrogen to be 0.44 ± 0.37 mHz at the 1-sigma level. This 0.37 mHz bound corresponds to 1.5×10^{-27} GeV in energy units.

4.4 Discussion

4.4.1 Transformation to fixed frame

Our experimental bound of 0.37 mHz on a sidereal variation of the hydrogen Zeeman frequency may be interpreted in terms of Eqn. 4.5 as a bound on spin couplings to background vector and tensor fields, as interpreted in the standard model extension. To make meaningful comparisons to other experiments, we transform our result into a fixed reference frame. Following the construction in reference [27], we label the fixed frame with coordinates (X,Y,Z) and the laboratory frame with coordinates (x,y,z), as shown in Figure 4.15. We select the earth's rotation axis as the fixed Z axis, (declination = 90 degrees). We then define fixed X as declination = right ascension = 0 degrees, and fixed Y as declination = 0 degrees, right ascension = 90 degrees. With this convention, the X and Y axes lie in the plane of the earth's equator. Note that the α, β axes of Section 4.2.6, also in the earth's equatorial plane, are rotated about the earth's rotation axis from the X,Y axes by an angle equivalent to the right ascension of 71° 7' longitude at 00:00 of November 19, 1999.

For our experiment, the quantization axis (which we denote z) was vertical in the lab frame, making an angle $\chi \approx 48$ degrees relative to Z, accounted for by rotating the entire (x,y,z) system by χ about Y. The lab frame (x,y,z) rotates about Z by an angle Ωt, where Ω is the frequency of the earth's (sidereal) rotation.

These two coordinate systems are related through the transformation

$$\begin{pmatrix} t \\ x \\ y \\ z \end{pmatrix} = \begin{pmatrix} 1 & 0 & 0 & 0 \\ 0 & \cos\chi\cos\Omega t & \cos\chi\sin\Omega t & -\sin\chi \\ 0 & -\sin\Omega t & \cos\Omega t & 0 \\ 0 & \sin\chi\cos\Omega t & \sin\chi\sin\Omega t & \cos\chi \end{pmatrix} \begin{pmatrix} 0 \\ X \\ Y \\ Z \end{pmatrix} = \mathbf{T} \begin{pmatrix} 0 \\ X \\ Y \\ Z \end{pmatrix}. \qquad (4.10)$$

Then, vectors transform as $\vec{b}_{lab} = \mathbf{T}\,\vec{b}_{fixed}$, while tensors transform as $\mathbf{d}_{lab} = \mathbf{T}\,\mathbf{d}_{fixed}\mathbf{T}^{-1}$.

As shown in Eqn. 4.5, our signal depends on the following combination of terms (for

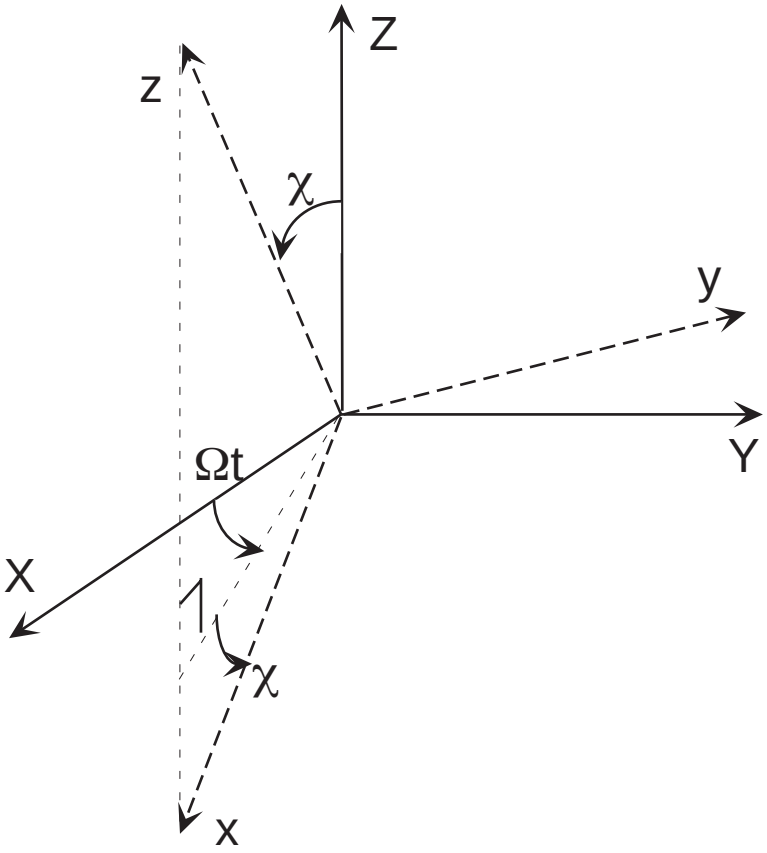

Figure 4.15: Coordinate systems used. The (X,Y,Z) set refers to a fixed reference frame, and the (x,y,z) set refers to the laboratory frame. The lab frame is tilted from the fixed Z-axis by our co-latitude, and it rotates about Z as the earth rotates. The α and β axes, described in Section 4.2, span a plane parallel to the X-Y plane.

both electron and proton):

$$\tilde{b}_z = b_z - m d_{zt} - H_{xy}. \tag{4.11}$$

Transforming these to the fixed frame, we see

$$\begin{aligned} b_z &= b_Z \cos\chi + b_X \sin\chi \cos\Omega t + b_Y \sin\chi \sin\Omega t, \\ d_{zt} &= d_{Z0} \cos\chi + d_{X0} \sin\chi \cos\Omega t + d_{Y0} \sin\chi \sin\Omega t, \\ H_{xy} &= H_{XY} \cos\chi + H_{YZ} \sin\chi \cos\Omega t + H_{ZX} \sin\chi \sin\Omega t, \end{aligned} \tag{4.12}$$

so our observable is given by

$$\begin{aligned} \tilde{b}_z &= (b_Z - m d_{Z0} - H_{XY}) \cos\chi \\ &+ (b_Y - m d_{Y0} - H_{ZX}) \sin\chi \sin\Omega t \\ &+ (b_X - m d_{X0} - H_{YZ}) \sin\chi \cos\Omega t. \end{aligned} \tag{4.13}$$

The first term on the right of Eqn. 4.13 is a constant offset, not bounded by our experiment. The second and third terms each vary at the sidereal frequency. Combining Eqn. 4.13 (for both electron and proton) with Eqn. 4.5, we see

$$\begin{aligned} |\Delta\nu_Z|^2 &= [(b_Y^e - m_e d_{Y0}^e - H_{ZX}^e) + (b_Y^p - m_p d_{Y0}^p - H_{ZX}^p)]^2 \frac{\sin^2\chi}{h^2} \\ &+ [(b_X^e - m_e d_{X0}^e - H_{YZ}^e) + (b_X^p - m_p d_{X0}^p - H_{YZ}^p)]^2 \frac{\sin^2\chi}{h^2}. \end{aligned} \tag{4.14}$$

Inserting $\chi = 48$ degrees, we obtain the final result

$$\sqrt{\left(\tilde{b}_X^e + \tilde{b}_X^p\right)^2 + \left(\tilde{b}_Y^e + \tilde{b}_Y^p\right)^2} = (3 \pm 2) \times 10^{-27}\ GeV. \tag{4.15}$$

Our 1-sigma bound on Lorentz and CPT violation of the proton and electron is therefore 2×10^{-27} GeV.

4.4.2 Comparison to previous experiments

We compare our result with other recent tests of Lorentz and CPT symmetry in Table 4.1. Although our bounds are numerically similar to the those from the ^{199}Hg/^{133}Cs experiment, the simplicity of the hydrogen atom allows us to place bounds directly on the electron and proton; uncertainties in nuclear structure models do not complicate the interpretation of our result. The recent limit of $\approx 10^{-29}$ GeV on electron Lorentz and CPT violation set by the torsion pendulum experiment of Adelberger et al. [63] casts our result as a clean bound on Lorentz and CPT violation of the proton.

4.4.3 Future work

To make a more sensitive measure of the sidereal variation of the Zeeman frequency in a hydrogen maser, it will be important to clearly identify and reduce the magnitude of the long-term drifts of the Zeeman frequency. Possible sources of these drifts are magnetic fields near the maser bulb caused by stray currents in heaters or power supplies in the inner regions of the maser. Also, the scatter of the Zeeman data points, believed to be due mainly to residual thermal fluctuations, should be reduced. Both of these objectives could be accomplished by carefully rebuilding a hydrogen maser, with better engineered power and temperature control systems.

Chapter 5

The cryogenic hydrogen maser

In 1978 Crampton, Phillips and Kleppner [6] first pointed out that the frequency stability of a hydrogen maser could be improved by operating at low temperature due to a decrease in thermal noise and a decrease in the rate of hydrogen-hydrogen spin-exchange collisions. The first detailed analyses of a cryogenic hydrogen maser (CHM) [7,8] predicted an improvement of two to three orders of magnitude in frequency stability over a room temperature hydrogen maser. A discussion of this predicted CHM stability will be presented in Section 5.1 and our technical strides to achieve it will be presented in Sections 5.2, 5.3, and 5.4.

In the years following its original proposal, theoretical studies of low temperature hydrogen-hydrogen spin-exchange collisions have demonstrated that these effects could in fact limit this expected frequency stability improvement. In this sense, the CHM has been recast as a useful tool with which to study low temperature hydrogen-hydrogen collisions. This topic will be treated in more detail in Chapter 6.

Eight years after its initial proposal, groups at MIT [9], the University of British Columbia (UBC) [10], and Harvard/SAO [11] independently achieved oscillation of a cryogenic hydrogen maser. The MIT cryogenic hydrogen maser resulted as an offshoot of their efforts to magnetically trap spin-polarized hydrogen. After their initial CHM demonstration, research in this area was discontinued. The UBC maser program continued for several

years, producing a number of important results, before its termination in the mid 1990s. The Harvard/SAO cryogenic hydrogen maser was developed following the conventional design of their numerous room temperature hydrogen masers. The Harvard/SAO group is the only group currently engaged in CHM research.

We report in this chapter the first oscillation of the SAO CHM in nearly five years and the first oscillation since the addition of a quartz atomic storage bulb. Originally intended to improve maser frequency stability, we will discuss below how overall maser stability has been degraded. A thorough survey of current SAO CHM performance will be presented in Section 5.5.

5.1 Cryogenic hydrogen maser frequency stability

For short-term averaging times (up to 10,000 s), the frequency stability of a room temperature hydrogen maser is limited by thermal noise. Therefore, the short-term performance of a hydrogen maser is expected to improve as the apparatus is cooled to lower temperature. White frequency noise due to thermal noise power in the microwave cavity will be reduced as the maser is cooled. Likewise, if the cryogenic environment is employed to cool the preamplifier, the white phase noise will also be reduced.

There are also a number of indirect factors which could lead to improved stability at lower temperatures. First, the hydrogen atoms will travel more slowly, thus reducing the wall collision rate and increasing the atomic storage time; this will act to increase the maser's line-Q. Second, because the hydrogen atoms' relative velocity and the spin-exchange collision cross sections both decrease at lower temperature, it is possible to operate a maser at an increased density and therefore increased output power. Finally, because the physical properties of materials (e.g., thermal contraction) tend to become more stable at lower temperatures, it is possible that some of the mechanically-induced systematic effects can be reduced with a cryogenic maser.

5.1.1 Decreased thermal noise

As shown in Chapter 3, for averaging times of $\tau < 100$ s, the stability limit of a room temperature maser is set by added white phase noise in the preamplifier and receiver. In this region, the Allan variance [47] as a function of averaging time τ is given by [7]

$$\sigma_r(\tau) = \frac{1}{\tau}\sqrt{\frac{Bk(T+T_N)}{\omega^2 P}\left(\frac{1+\beta}{\beta}\right)} \tag{5.1}$$

where B is the receiver bandwidth, T is the maser temperature, T_N is the preamplifier noise temperature, P is the power delivered by the atoms to the cavity, β is the cavity coupling constant, and $\omega = 2\pi\nu$ is the maser frequency. Note that for a room temperature amplifier, the amplifier's noise temperature T_N and noise figure F are related by $T + T_N = FT$. The room temperature preamplifier we use for our cryogenic maser has $T_N = 75$ K.[1] Assuming a bandwidth B = 6 Hz and a maser power $P = 6\times10^{-13}$ W, the Allan variance for a room temperature maser over this interval is typically about $\sigma_r(\tau) = 6\times10^{-14}/\tau$.

For longer averaging times, the room temperature maser stability is limited by white frequency noise from the incoherent thermal microwave cavity field. Over this interval, the Allan variance [47] as a function of averaging time τ is given by [7]

$$\sigma_c(\tau) = \frac{1}{Q_l}\sqrt{\frac{kT}{2P\tau}} \tag{5.2}$$

where Q_l is the maser's line-Q, T is the maser temperature, and P is the power delivered from the atoms to the cavity. For a room temperature maser with $Q_l = 1.6\times10^9$, the Allan variance over this interval is given by $\sigma_c(\tau) = 4 \times 10^{-14}/\sqrt{\tau}$.

Because these two processes are uncorrelated, we can compute the combined short-term ($\tau < 1000$ s) Allan variance as [7]

$$\sigma(\tau) = \left[\sigma_c^2(\tau) + \sigma_r^2(\tau)\right]^{\frac{1}{2}}. \tag{5.3}$$

[1] This room temperature preamplifier is considerably better than that of VLG-10 series maser P-8. Therefore these room temperature results are better than those presented in Chapter 3.

For times longer than about 10,000 s, the stability of the maser is limited by systemic effects, such as mechanical stability of the maser cavity.

We now attempt to quantify the expected improvements in the performance of a cryogenic hydrogen maser. We will assume the microwave cavity is cooled down to a temperature of 0.5 K (the reason for choosing this particular temperature will be described in Section 5.2.2). We will also assume the use of a cryogenic preamplifier (for example a GaAs FET amplifier) with a reduced noise temperature of $T_N = 10$ K, however the receiver bandwidth will remain unchanged ($B = 6$ Hz). As the microwave cavity is cooled we will assume an increase in the cavity coupling to $\beta = 0.5$. We will assume that the maser power is unchanged by a reduction in temperature (although this assumption will be modified in Section 5.1.2). Inserting these values into Eqn. 5.1, we find a reduced Allan variance due to white phase noise of $\sigma_r(\tau) = 7.4 \times 10^{-15}/\tau$.

As a direct consequence of operating a low temperature, the reduced thermal velocity of the atoms will increase the atomic storage time and thereby increase the atomic line-Q. We will assume $Q_l = 2 \times 10^{10}$, a factor of 10 increase over a typical room temperature value. Inserting this into Eqn. 5.2, we see a reduced Allan variance due to white frequency noise of $\sigma_c(\tau) = 1.2 \times 10^{-16}/\sqrt{\tau}$.

These cryogenic estimates, for the thermal limit to maser stability, are plotted as a function of averaging time τ and compared with room temperature values in Figure 5.1. It can be seen that for averaging times 10 s $< \tau <$ 10,000 s, the thermal limit to room temperature maser stability is set primarily by white frequency noise. As the maser is cooled, there is an improvement by a factor of 300 in the white frequency noise limit (for the cryogenic maser parameters assumed here), whereas the improvement in the white phase noise limit is only a factor of about eight. Therefore, for a cryogenic maser, the thermal limit to maser stability for averaging times less than about 10,000 s is set by added white phase noise from the receiver. In reality, for averaging times longer than about 10,000 s, the maser stability will most likely be dominated by non-thermal systematic effects.

The optimal averaging time for a room temperature maser is approximately 10,000

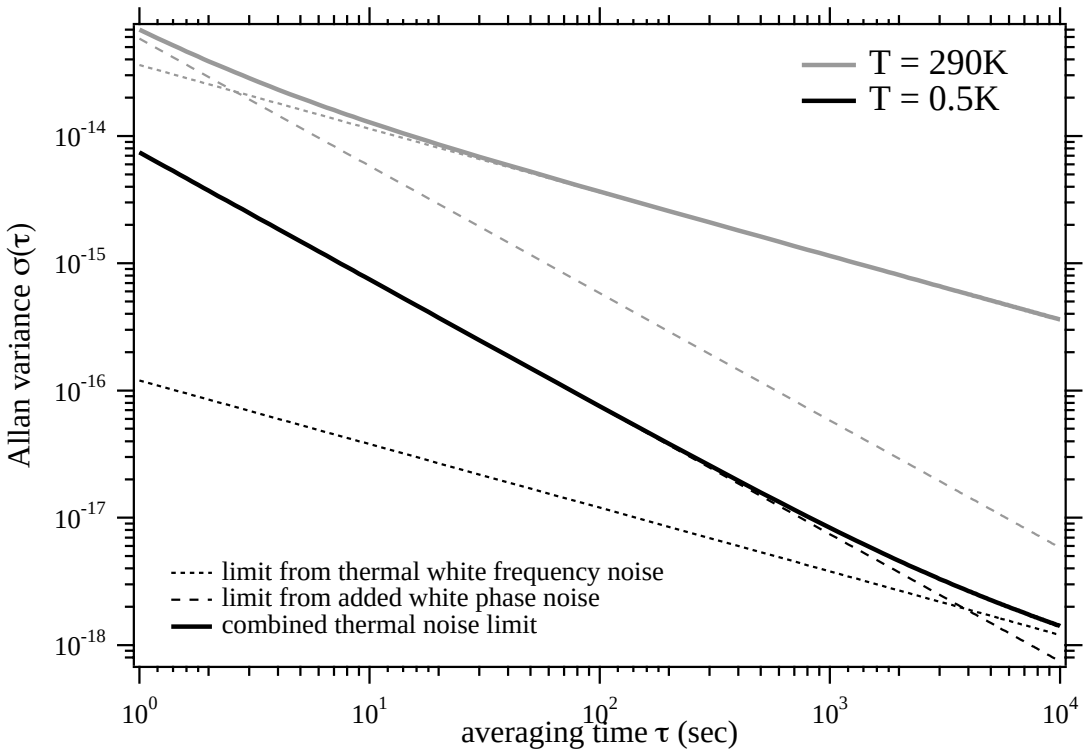

Figure 5.1: Hydrogen maser frequency stability limits due to thermal noise. The gray set of traces depict typical room temperature maser performance, while the black set of traces show the projected performance for a cryogenic maser. For each set, the dashed line depicts the limit due to added white phase noise (Eqn. 5.1), the dotted line depicts the limit due to white frequency noise (Eqn. 5.2), and the solid line shows the net limit due to thermal sources. For the room temperature curves, we have used $T = 290$ K, $Q_l = 1.6 \times 10^9$, $P = 6 \times 10^{-13}$ W, $T_N = 75$ K, $B = 6$ Hz, and $\beta = 0.23$. For the cryogenic estimate, we have assumed $T = 0.5$ K, $Q_l = 2 \times 10^{10}$, $P = 6 \times 10^{-13}$ W, $T_N = 10$ K, $B = 6$ Hz, and $\beta = 0.50$. Note that we have not assumed an increased maser power for the cryogenic maser, although such an increase is expected due to the reduced spin-exchange relaxation rates.

s. For times longer than this, systematic effects tend to reduce the maser's performance. From Figure 5.1, we see that at $\tau = 10{,}000$ s, the thermal noise limited stability of a room temperature maser is about $\sigma(\tau) = 3 \times 10^{-16}$, while the expected cryogenic maser stability is approximately $\sigma(\tau) = 2 \times 10^{-18}$. Therefore we see that by accounting for thermal effects alone, an improvement of over two orders of magnitude in hydrogen maser stability is predicted for a maser operating at cryogenic temperatures.

5.1.2 Increased maser power

In Chapter 3 we discussed the effect of spin-exchange broadening on the operation of a hydrogen maser. In particular, we introduced the spin-exchange parameter q, defined by

$$q = \left[\frac{\sigma \bar{v}_r \hbar}{8\pi\mu_B^2}\right] \frac{\gamma_t}{r + \gamma_r} \left[\frac{V_C}{\eta V_b}\right] \left(\frac{1}{Q_C}\right) \frac{I_{tot}}{I} \tag{5.4}$$

which essentially quantified the amount of spin-exchange broadening in the maser. Here, σ is the spin-exchange broadening cross section and $\bar{v}_r$ is the relative atomic velocity. For $q = 0$ (equivalent to no spin-exchange broadening) we saw that the maser power increased monotonically without bound with hydrogen flux. However, as the value of q increased, the maximum obtainable power decreased and the range of flux that would support active oscillation narrowed. For $q > 0.176$, active oscillation was no longer achievable.

Here we consider the effect of temperature on the spin-exchange collision rate, in particular the effect of reduced temperature on the broadening cross section σ and the relative atomic velocity $\bar{v}_r$. Prior to the work of Verhaar et al. [30, 31], all of the theoretical work on hydrogen-hydrogen spin-exchange collisions had been done using an approximation known as the degenerate internal states (DIS) approximation [17, 68, 71–77]. This approximation essentially neglects the small hyperfine splitting (about 0.07 K) in the atomic ground state relative to the thermal energies of the collisions and the electron exchange potential (about 50,000 K). The inclusion of the hyperfine interaction energies in a fully quantum mechanical treatment of hydrogen-hydrogen spin-exchange collisions led to new

hyperfine-induced (h-i) effects. In Chapter 6 we will discuss these h-i effects, however we consider here only the results of DIS theory.

The relative atomic velocity is given by $\bar{v}_r = 4\sqrt{kT/\pi m}$ and it therefore is a decreasing function with a reduction in T, as shown in Figure 5.2(a). For example, from room temperature to 0.5 K, $\bar{v}_r$ decreases by a factor of $\sqrt{290/0.5} = 24$. Since the hydrogen atoms are traveling at a reduced rate, the frequency of hydrogen-hydrogen collisions will be reduced, therefore reducing spin-exchange broadening. In addition, there is also a significant reduction in the spin-exchange broadening cross-section σ. A theoretical prediction of this is given in Figure 5.2(b). Here it can be seen that from room temperature to 0.5 K, there is a reduction by a factor of about 30 in σ [75, 77].

Therefore, because the spin-exchange collision rate is proportional to $\sigma\bar{v}_r$, there is a reduction by nearly three orders of magnitude in the collision rate from room temperature to 0.5 K, as shown in Figure 5.2. This reduction is directly incorporated in the spin-exchange parameter q, and as a result, we expect to be able to run at higher fluxes before spin-exchange broadening effects begin to play a limiting role. Since both forms of short- to medium-term frequency stability (Eqns. 5.1 and 5.2) are inversely proportional to $\sqrt{P}$, within the DIS theory the stability of a cryogenic hydrogen maser can be significantly improved over the estimate obtained in Section 5.1.1 above, where we considered thermal noise effects alone.

Of course, the primary assumption of DIS theory, that the hyperfine interaction energy ($\approx$ 70 mK) can be neglected relative to the collision energy, begins to break down as the temperature of the colliding atoms is reduced. Therefore, an accurate estimate of the improvement in cryogenic maser stability will need to include h-i effects. In Chapter 6 we will analyze these effects and how they limit the ultimate stability of a cryogenic hydrogen maser.

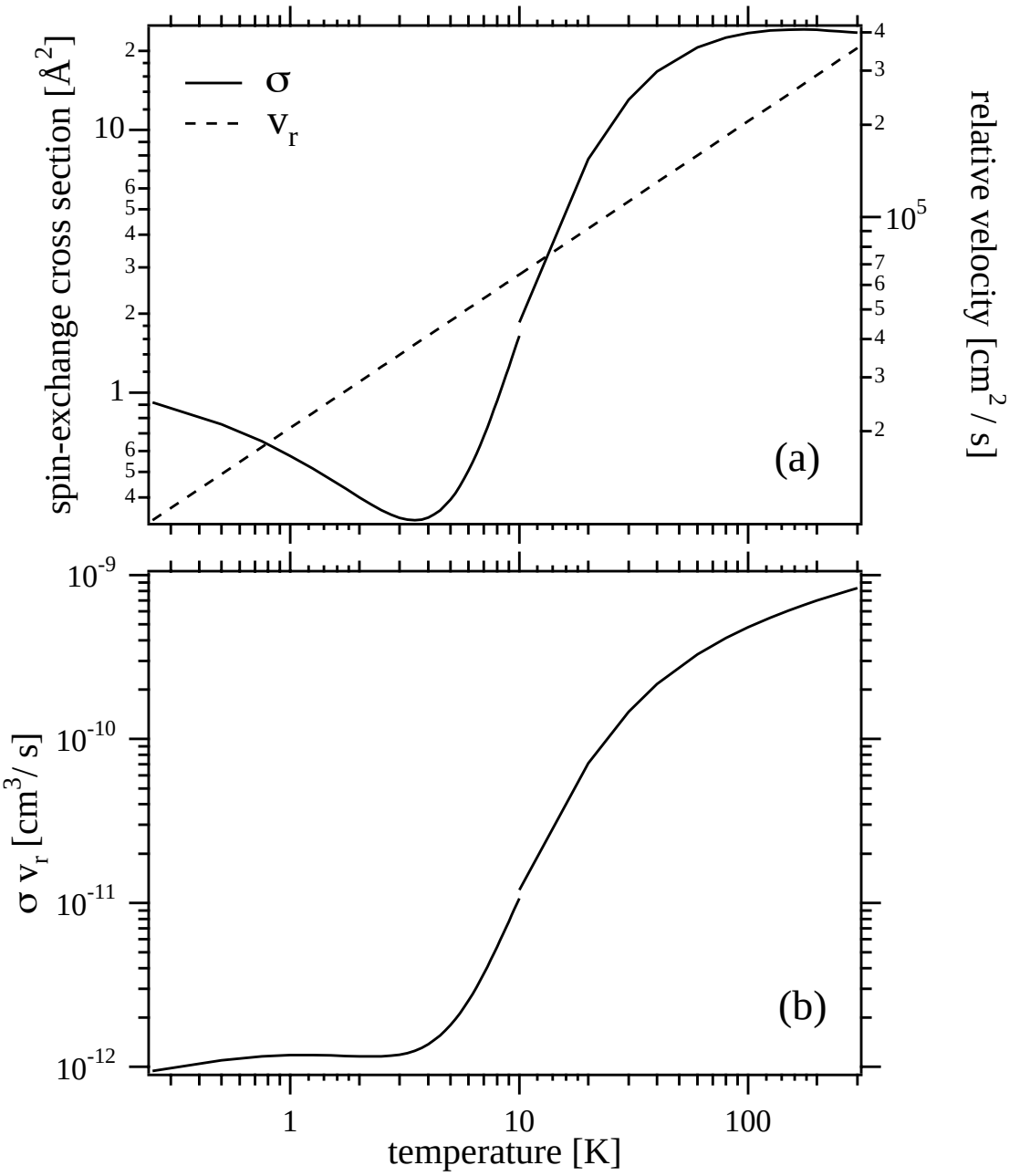

Figure 5.2: Theoretical spin-exchange broadening effects using the DIS approximation. In figure (a), we show the spin-exchange broadening cross section σ along with the relative atomic velocity $\bar{v}_r$. In figure (b), we show their product. Values for 10 K and above are from Allison [75] while data below 10 K are from Berlinksky and Shizgal [77].

5.1.3 Cryogenic systematics

Important systematic limits to hydrogen maser stability, magnetic and thermo-mechanical effects, can both be reduced by operating at low temperature [7, 8]. Operation at 0.5 K allows for the use of superconducting magnetic shields which can reduce maser frequency shifts due to variations in the magnetic-field-dependent atomic hyperfine frequency. In addition, since the thermal expansion coefficients of materials decrease significantly at low temperature, and since a hydrogen maser can be operated with a higher line-Q and lower cavity-Q, maser frequency shifts due to variations in the microwave cavity frequency will also be reduced.

5.2 Superfluid ^{4}He wall coating

5.2.1 Historic overview

The most serious technical complication for operating a hydrogen maser at cryogenic temperatures is finding an appropriate wall coating. The binding energy of hydrogen on Teflon is on the order of 200 K; therefore this no longer functions as an effective wall coating at cryogenic temperatures. Initial investigations into low temperature coatings included a study of Teflon from 372 K to 77 K [78], Teflon from 77 K to 48 K [79], solid neon at 10 K [80], and frozen molecular hydrogen at 4 K [81]. The best of these candidates, solid H_2, was found to have a binding energy of around 40 K, and was thus not effective at liquid helium temperatures or below.

However, in 1980, while working in an early attempt to realize a hydrogen BEC, Silvera and Walraven [82] successfully stabilized an atomic hydrogen gas within a storage vessel coated by a superfluid ^{4}He film. In their initial study, they reported that at 0.3 K, approximately 10^{15} atoms were confined for a period of about 500 s.

5.2.2 Effects of superfluid ^{4}He wall coating

In this section we will analyze the effects of confining cold atomic hydrogen within a storage cell lined with a saturated superfluid ^{4}He film. In particular, we quantify the hyperfine frequency shifts due the hydrogen-helium interactions, and determine the most stable operating point for our cryogenic hydrogen maser. It will be shown that the frequency stability of the cryogenic maser will be limited by the net hyperfine shift due to hydrogen-helium interactions, and this shift's variation as a function of temperature.

We consider a storage bulb of radius R, volume V and surface area A. Hydrogen atoms (of mass m) confined to this region at a temperature T will have a thermal de Broglie wavelength of $\Lambda = h/\sqrt{2\pi mkT}$ and an average velocity of $\bar{v} = \sqrt{8kT/\pi m}$. The average length of time between wall collisions is given by $\bar{\tau}_c = 4R/3\bar{v}$ [8]. Occasionally, a hydrogen atom will stick to the ^{4}He coated surface during a wall collision. If we define the average length of time between collisions where the hydrogen atoms stick to the wall as $\bar{\tau}_b$, and the average length of stay on the surface as $\bar{\tau}_s$, then the sticking probability is given by $\alpha = \bar{\tau}_c/\bar{\tau}_b$ [8]. For H on ^{4}He, this probability has been measured to be $\alpha = 0.04$ [83]. Finally, the fraction of time an atom spends on the wall is given by [84]

$$x = \frac{\bar{\tau}_s}{\bar{\tau}_b} = \frac{\Lambda A}{V} e^{E_B/kT} \tag{5.5}$$

where $E_B/k = 1.15$ K is the binding energy of hydrogen on a ^{4}He surface at 0.5 K [84,85].

Due to the interaction with the ^{4}He film during a sticking collision, the hyperfine frequency of the H atom is shifted by an amount Δ_s. This introduces an average hyperfine frequency shift due to surface interactions of [83]

$$\Delta\nu_s = \frac{1}{2\pi\bar{\tau}_b}\frac{\phi}{1+\phi^2} \approx \frac{\phi}{2\pi\bar{\tau}_b} = \frac{\bar{\tau}_s}{\bar{\tau}_b}\Delta_s \tag{5.6}$$

where the average phase accumulated during a sticking event is given by $\phi = 2\pi\bar{\tau}_s\Delta_s$, and we have used the fact that $\phi^2 \ll 1$. For hydrogen on a ^{4}He surface at 0.5 K, the hyperfine

shift has been measured to be Δ_s = -49 kHz [84,85].

Because a superfluid ^{4}He coated surface will also have a non-negligible ^{4}He vapor pressure above the surface, we also need to consider effects of H-^{4}He interactions in the vapor phase. Collisions of hydrogen with vapor phase ^{4}He introduces a pressure shift in the hyperfine frequency given by [8]

$$\Delta\nu_v = \beta_{He} n_{He}, \tag{5.7}$$

where β_{He} = -11.8 $\times$ 10^{-18} Hz/cm^3. From 0.06 to 1 K, the ^{4}He vapor density above a saturated ^{4}He film can be expressed as $n_{He} = (1.5\times10^{21})T^{3/2}\exp(-7.1688/T)$, where n_{He} is in cm^3 for T in K [8]. At normal cryogenic hydrogen maser operating temperatures, the ^{4}He vapor pressure is sufficiently high that the mean free path of the hydrogen atoms is no longer large relative to the bulb dimensions (as in a room temperature maser). For example, at 0.55 K, the mean free path of hydrogen is about 1 cm, hence the atoms move diffusively inside the storage bulb. This mean free path is also a strong function of temperature. From 0.45 to 0.6 K, the mean free path is reduced from about 10 cm down to about 0.1 cm, as shown in Figure 5.3.

The net hyperfine frequency shift due to H-He interactions at the wall and in the vapor is found by combining Eqns. 5.5 - 5.7,

$$\Delta\nu = \Delta_s \frac{\Lambda A}{V} e^{E_B/kT} + \beta_{He} n_{He}. \tag{5.8}$$

Figure 5.3 shows a plot of Eqn. 5.8 for our quartz atomic storage bulb (with V = 172 cm^3 and A = 176 cm^2). Here, the magnitude of the frequency shift is plotted; the sign of both the wall shift and the vapor shift is negative. Because the two shifts have the same sign but opposite trends, the net shift passes through an magnitude minimum of 110 mHz at 0.55 K. Here, the first-order temperature dependence is eliminated, so this is therefore the target operating temperature for our cryogenic hydrogen maser. At lower temperatures, the hydrogen atoms tend to stick longer at the wall and therefore accumulate more negative

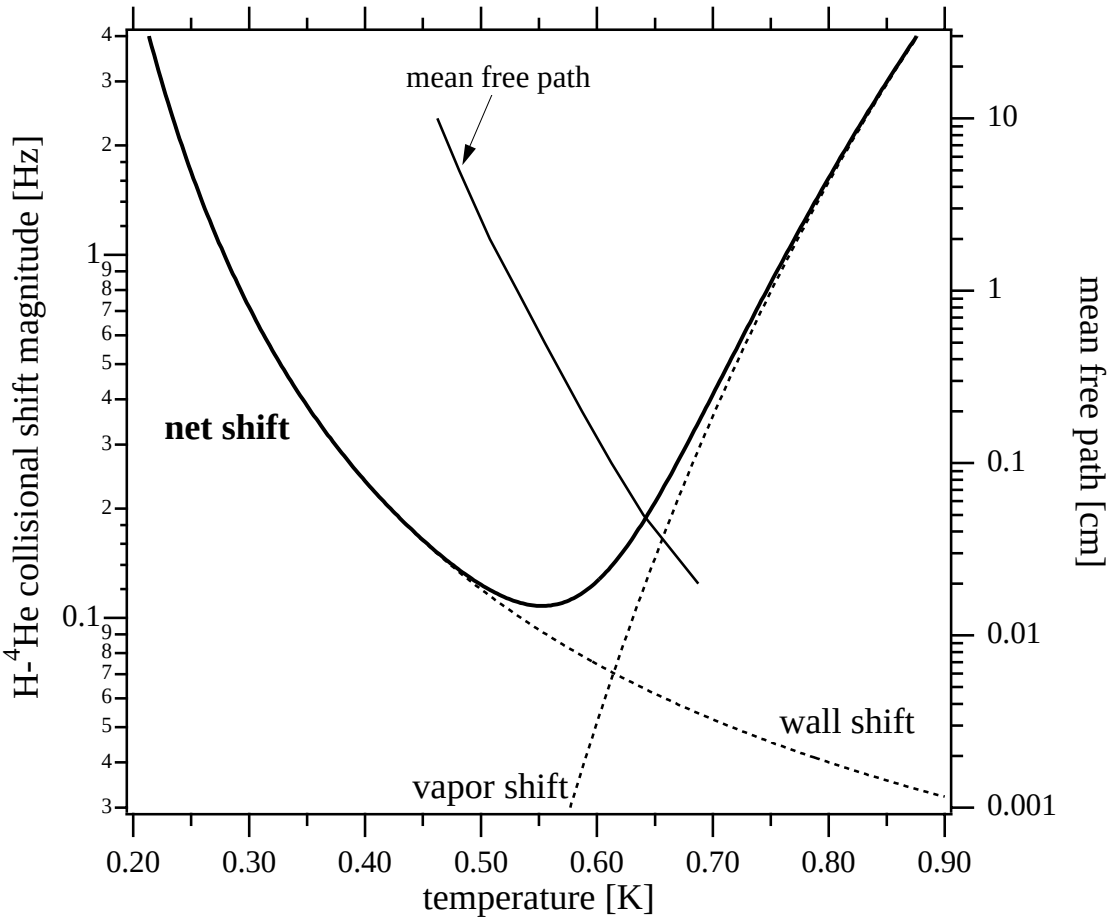

Figure 5.3: Magnitude of the (negative) hyperfine frequency shift for H atoms stored in a cell lined with a saturated superfluid ^{4}He film. The magnitude of the shifts due to H-^{4}He interactions at the wall and in the vapor are displayed. The most stable operating point due to our storage bulb geometry is 0.55 K, where the H-^{4}He collisional shift is -110 mHz. Also shown is the mean free path of hydrogen atoms in a ^{4}He vapor for a saturated film [86].

phase. At higher temperatures, the negative pressure shift in the bulk vapor dominates. Near the target operating temperature of 0.55 K, we estimate that for a good temperature control of 10 μK a fractional maser frequency stability of 10^{-18} could be achieved.

5.3 Maser setup

The SAO cryogenic hydrogen maser (Figure 5.4) was designed to be functionally similar to the SAO room temperature hydrogen masers with appropriate modifications made for operation at cryogenic temperatures. A beam of molecular hydrogen is dissociated at room temperature. The beam of atomic hydrogen is then cooled, magnetically state selected, and focused into a quartz storage bulb centered inside of a microwave cavity. The quartz storage bulb is coated with a superfluid ^{4}He film, and both the bulb and cavity are maintained near 0.5 K. The maser signal is coupled out inductively and carried to room temperature via semi-rigid coaxial cable. After passing through a room temperature isolator and preamp, the maser signal is detected with a low-noise heterodyne receiver as used in the room temperature SAO hydrogen masers.

The maser temperature is lowered to 0.5 K using a recirculating ^{3}He refrigerator. This refrigerator consists of several cooling stages: a liquid nitrogen stage at 77 K, a liquid ^{4}He bath at 4.2 K, a pumped ^{4}He pot at approximately 1.7 K, and the pumped, recirculating ^{3}He stage at 0.5 K. The atomic hydrogen beam, state selector, storage bulb and cavity are all connected inside a single, maser vacuum chamber (MVC). This space is pumped out from below by a turbo pump. Above the MVC, an inlet to the space allows for the input of flowing superfluid ^{4}He film. External to the MVC is a second, outer vacuum chamber (OVC), maintained for operation of the cryostat and also pumped by a turbo pump. Inside the OVC, there is radiation shielding at 77 K and 1.7 K.

The SAO cryogenic hydrogen maser lab is shown in Figure 5.5. The setup consists of the cryostat with its main vacuum chamber and pumps, the ^{3}He gas handling system and its recirculation pumps, the ^{4}He pot pumping line and pumps, the superfluid ^{4}He

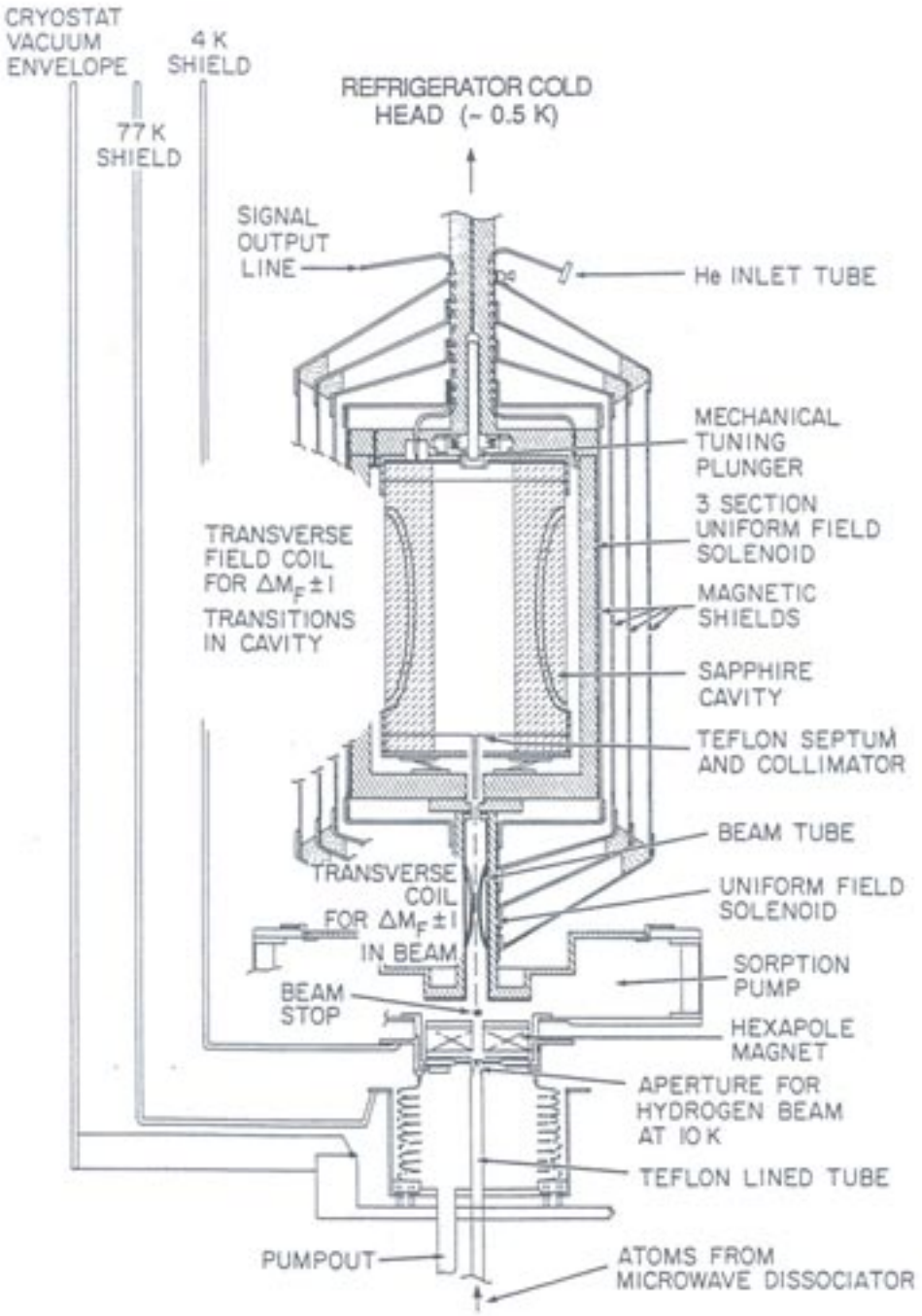

Figure 5.4: Schematic of the SAO cryogenic hydrogen maser. Not shown is the quartz atomic storage bulb which lines the inner bore of the cavity and replaces the Teflon septa and collimator. Also, in its present configuration, the "4 K shield" is actually maintained at 1.7 K.

Figure 5.5: SAO cryogenic hydrogen maser lab.

gas handling manifold, the hydrogen gas handling system and discharge apparatus, and several racks with temperature monitor and control electronics.

5.3.1 Hydrogen source and state selection

The atomic hydrogen for the maser is formed by dissociating molecular hydrogen in a microwave discharge [87]. The discharge cavity is mounted below the cryostat and maintained at room temperature, while the beam of atomic hydrogen is cooled down by thermalization with the walls of a Teflon transfer tube leading into the cryostat. The outer end of the tube is near room temperature, it is heat sunk midway near 77 K and at the far end near 2 K. The microwave discharge cavity is tuned near 2.4 GHz and driven by a microwave

generator[2] at about 40 W. A microwave isolator[3] between the generator and the discharge prevents frequency pulling of the generator. The molecular hydrogen pressure is regulated with a pressure controller[4] and maintained at approximately 1 Torr. The resulting beam of atomic hydrogen flows upward into the cryostat and is ultimately thermalized to 10 K by the 0.210" diameter Teflon tube and a 3 mm diameter copper nozzle, shown in Figure 5.4.

The 10 K beam of atomic hydrogen entering the cryostat consists of a near uniform population distribution between the four atomic hyperfine states. The population inversion necessary for maser action is created using magnetic state selection with a hexapole magnet. After passing through the magnet, atoms in states $|1\rangle$ and $|2\rangle$ are focused into the maser storage bulb while those in states $|3\rangle$ and $|4\rangle$ are defocused from the beam. Since the focusing of the hexapole is dependent on the velocity of the atoms, the thermalizing copper nozzle's temperature is monitored and adjusted (via a resistive heater) to optimize the population inversion flux. In practice, the nozzle temperature is set to maximize the maser power.

Since the 10 K atoms travel much slower than room temperature atoms, the low temperature hexapole magnet is significantly shorter that the room temperature hexapole. The cryogenic hexapole is about 1.3 cm in length, with a 3 mm bore diameter. The radial field is zero on axis and grows to about 0.88 T at the pole tips. A small beam stop mounted on axis at the exit of the magnet blocks undeflected atomic hydrogen and residual molecular hydrogen from entering the storage bulb.

Nominally, atoms in low-field-seeking states $|1\rangle$ and $|2\rangle$ are focused into the maser interaction region. After a few seconds, these atoms escape from the storage bulb and return toward the focusing region where they, along with the high-field-seeking atoms that were deflected out of the atomic beam, are pumped away with an activated charcoal filled sorption pump (see Figure 5.4). (The sorption pump also acts to pump away the

[2]Raytheon Microtherm, 2.45 GHz, 0 - 100 W.
[3]Alcatel model 20A111-11 coaxial isolator, 2.3 - 2.7 GHz.
[4]Edwards model 1501B pressure controller.

superfluid ^{4}He which has flowed from the atomic storage bulb). The sorption pump is constructed from two (largely copper) circular plates, about 24 cm in diameter and spaced about 4 cm apart. The plates are connected using six tubes of low thermal conductance Vespel.[5] The top copper plate of the sorption pump is in thermal contact with the maser (0.5 K) while the bottom copper plate is in thermal contact with the ^{4}He pot (1.7 K). The vacuum seal on the outer rim of the sorption pump (separating the MVC from the OVC) is made with a 0.010" thick Kapton[6] film epoxied around the perimeter of the plates with Stycast[7] 1266 epoxy.

The atoms focused into a beam by the state selecting hexapole travel through a 15 cm long (1.5 cm inner diameter) copper beam tube before entering the storage bulb. To maintain a static quantization field in this region, a small solenoid "neck coil" was installed inside the beam tube. This coil is about 4.5 cm long and contains about 160 turns of 30 AWG copper wire. Applying a field with this coil was seen to have only a small effect on overall maser power. Typically, a field of about 100 mG was found to optimize the power. About 2 mA of current was needed to produce this field, resulting in an insignificant 30 μW of heating.

In addition to the neck coil, a small coil capable of producing a transverse rf field was installed into the beam tube. This coil could be used to drive $F = 1$, $\Delta m_F = \pm 1$ Zeeman transitions in the incident atomic beam and therefore to alter the population distribution among the atoms in the beam. For a field with a Rabi frequency large compared to the inverse transit time of the atoms in the beam tube, the populations of the $F = 1$ states would be essentially equalized. These rectangular rf coils were 5 cm long and 1.5 cm wide and mounted so that the current in each coil had the same direction. Each coil had 15 turns of 32 AWG copper wire. A field of about 13 mG, which would have twice the Rabi frequency needed to mix the states during the atoms' transit time, is produced by 0.9 mA which would add about 7 μW of heating to the maser. The neck coil and the rf coil were

[5]Vespel is a trademark of E.I. duPont de Nemours and Co., Inc.
[6]Kapton is a trademark of E.I. duPont de Nemours and Co., Inc.
[7]Stycast is a trademark of Emerson and Cuming.

both wound around a Kapton form 5 cm in length and 1.3 cm in diameter and inserted into the copper beam tube.

5.3.2 Maser interaction region

The state selected atoms travel through the beam tube into the maser interaction region where they enter the quartz storage bulb centered inside the maser's microwave cavity. In contrast to a room temperature maser cavity, which is entirely evacuated, the cryogenic maser cavity is dielectric loaded to reduce the physical size of the 1420 MHz resonant cavity, and hence make the cavity more suitable for housing in a cryostat. The microwave cavity, shown in Figure 5.6, is constructed from single crystal sapphire cut into a cylinder 17 cm long and 10 cm in diameter. An inner bore, 4.5 cm in diameter has been cut and a quartz storage bulb is placed in this region. A pair of copper endcaps, at each end of the sapphire cylinder, and a thin layer of silver deposited around the outer surface of the cylinder serve as the electrically conducting surfaces which establish the TE_{011} microwave cavity mode. The two copper endcaps are thermally connected with a copper braid, and the entire cavity (sapphire cylinder plus endcaps) is sealed within a copper enclosure (the "copper pot") which separates the MVC and OVC and keeps the entire cavity in thermal equilibrium. The copper enclosure is vacuum sealed using 1 mm diameter indium wire. We note that since indium is a superconductor below 3.4 K [88], its presence leads to difficulties in removing unwanted (and applying desired) magnetic field gradients with the solenoid assembly.

A 1.5" diameter copper disk has been installed at the upper end of the microwave cavity which can be inserted and withdrawn into the cavity in order to tune the cavity's resonance frequency. This depth of this spring-loaded tuning plunger into the cavity can be set with a tuning knob easily accessible at the top of the cryostat, and the full tuning range is approximately 1 MHz.

Microwave signals are coupled into and out of the cavity inductively using a near-critically coupled inductive pickup loop, with a total area of about 1 cm^2. The loop is

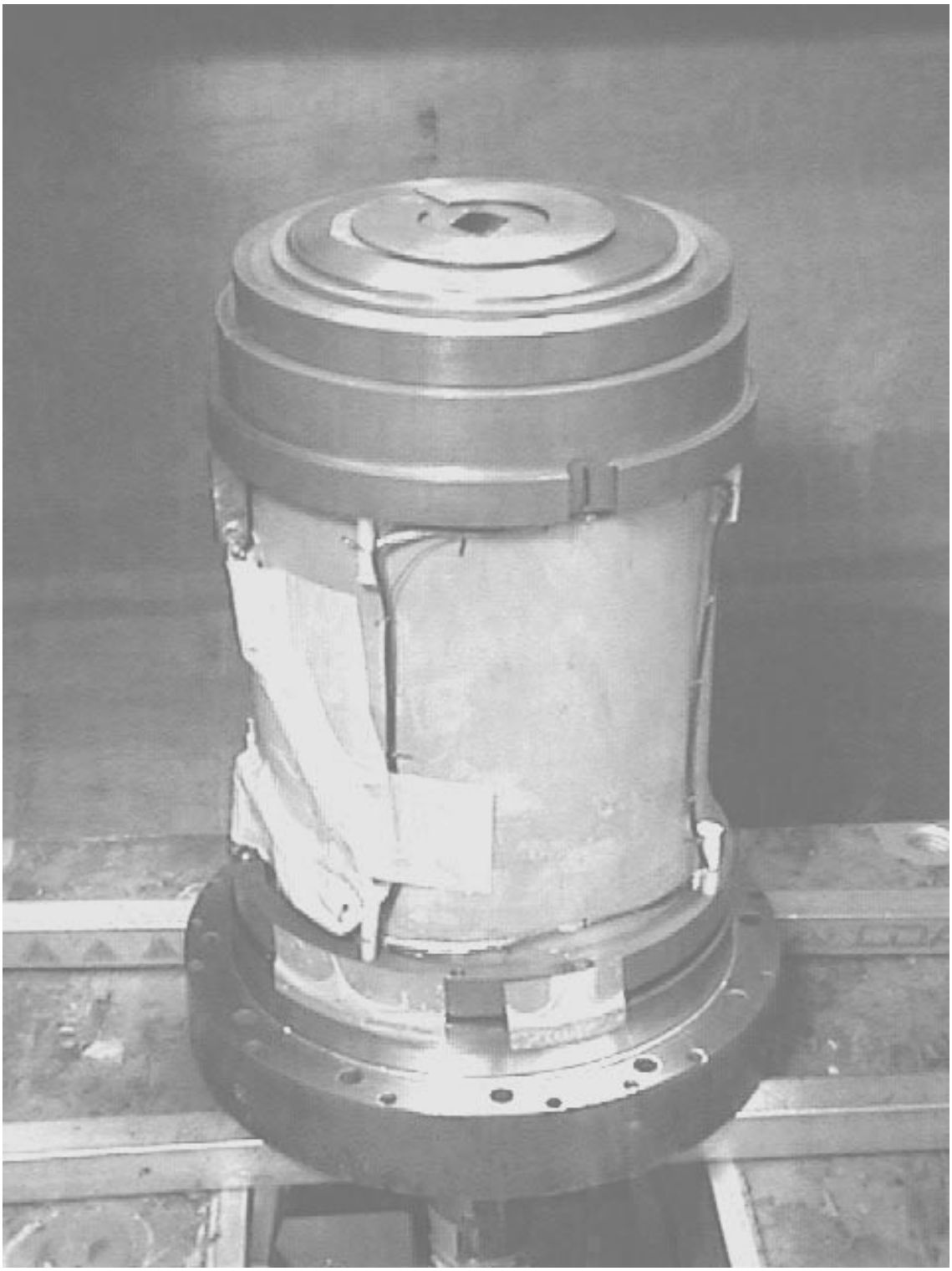

Figure 5.6: Cryomaser microwave cavity formed by a silver plated sapphire cylinder and a pair of copper endcaps. The sapphire acts to dielectrically load the cavity, allowing a reduction in its physical size. One coil from a Helmholtz pair used to drive the F=1, Δm_F=$\pm$1 Zeeman transitions is shown.

mounted at the top of the microwave cavity and oriented to maximize the flux of the microwave cavity's radial magnetic field through the loop. The loop is coupled to a 50 Ω semi-rigid coaxial line through a superfluid-leak-tight SMA feedthrough. At room temperature, the cavity resonant frequency is about 1410.5 MHz with a loaded cavity-Q (i.e., including losses due to coupling of power out through the pickup loop) of about 13,000 (full width ≈ 110 kHz) and a cavity coupling coefficient of $\beta = 0.15$. As the microwave cavity is cooled to 0.5 K, it's dimensions contract and the resistive losses are reduced. At 0.5 K, the cavity frequency can be tuned to the atomic hyperfine frequency of 1,420,405,752 Hz, it's loaded cavity-Q increases to about 27,000 (full width ≈ 53 kHz), and the cavity coupling coefficient increases nearly to $\beta = 0.33$.

As discussed in Chapter 3, each SAO room temperature hydrogen maser is equipped with a varactor diode, inductively coupled via a second coupling loop to the cavity, which serves for resettable fine tuning of the cavity frequency. To date, the cryogenic hydrogen maser has not been equipped with a second coupling port so this tuning scheme was not utilized. An attempt was made, however, to put a tuning diode in series with the single coupling loop. This diode was reverse biased with a positive voltage applied to the inner conductor of the semi-rigid coaxial cable used to couple out the maser signal (the negative terminal of the diode was kept at ground). When back biased, this diode shifted the microwave cavity frequency and it allowed for a resettable tuning range of approximately 10 kHz with only a mild modification of the cavity-Q and cavity coupling. Unfortunately, the diode that was installed had a small residual magnetism (tens of μG up to an inch away) so it generated a non-uniform DC magnetic field in close proximity to the atomic ensemble. This field inhomogeneity acted to decohere the atomic ensemble enough so that active maser oscillation could not be achieved.

Once the small field inhomogeneity was discovered, the diode was immediately removed. A number of attempts were then made to connect a varactor diode in parallel with the coupling loop, outside the cryostat, using various directional couplers. While this allowed for the placement of the diode outside of the maser's magnetic shields (eliminating

any ill-consequence of diode magnetic fields), it was found that due to reflections in the transmission line, no significant, resettable tuning of the resonant cavity could be achieved. Therefore, the cryogenic hydrogen maser is currently limited to mechanical tuning using the tuning plunger.

As described in Section 5.2, a superfluid ^{4}He film is used to coat the surface of the atomic storage region to reduce the interaction between the atoms and the storage region wall. As originally designed, the Teflon-coated inner bore of the sapphire cylinder served as the atomic storage region (with Teflon septa making the two ends) and the superfluid film simply flowed into the cavity from an inlet port and coated these walls. However, when operated in this configuration, the stability of the cryogenic maser was degraded and the maser frequency was found to be excessively sensitive to ^{4}He flow and temperature; indeed, the cryogenic maser was less stable than a room temperature maser for averaging times over 100 s. It was postulated that the source of this poor performance was a large frequency shift caused by the interaction between the masing atoms and paramagnetic impurities in the underlying sapphire crystal. Since this frequency shift will depend on the distance between the atoms and the impurities in the wall, and therefore the thickness of the superfluid helium film, fluctuations in this film thickness will lead to instability in the maser oscillation frequency. Therefore, it was decided to install a quartz maser bulb into the inner bore of the sapphire cylinder to create an inert "buffer" between the masing atoms and the sapphire wall.

A quartz bulb was designed (Figure 5.7) and constructed[8] to fit snugly into the inner bore of the sapphire. This bulb provides an approximately 0.025" thickness of inert quartz between the atoms and the sapphire wall. A transfer tube was constructed out of fine copper capillary (0.020" OD) to transport the superfluid from the cavity inlet port into the inner space of the bulb through an inlet spout. The copper capillary was epoxied with Stycast 2850 at the film entrance aperture into the cavity and at the inlet spout of the bulb. The transfer tube was coiled around one full turn between the copper tuning

[8]Mikoski Inc. Fused Quartz and Glass Specialists, Stow, MA.

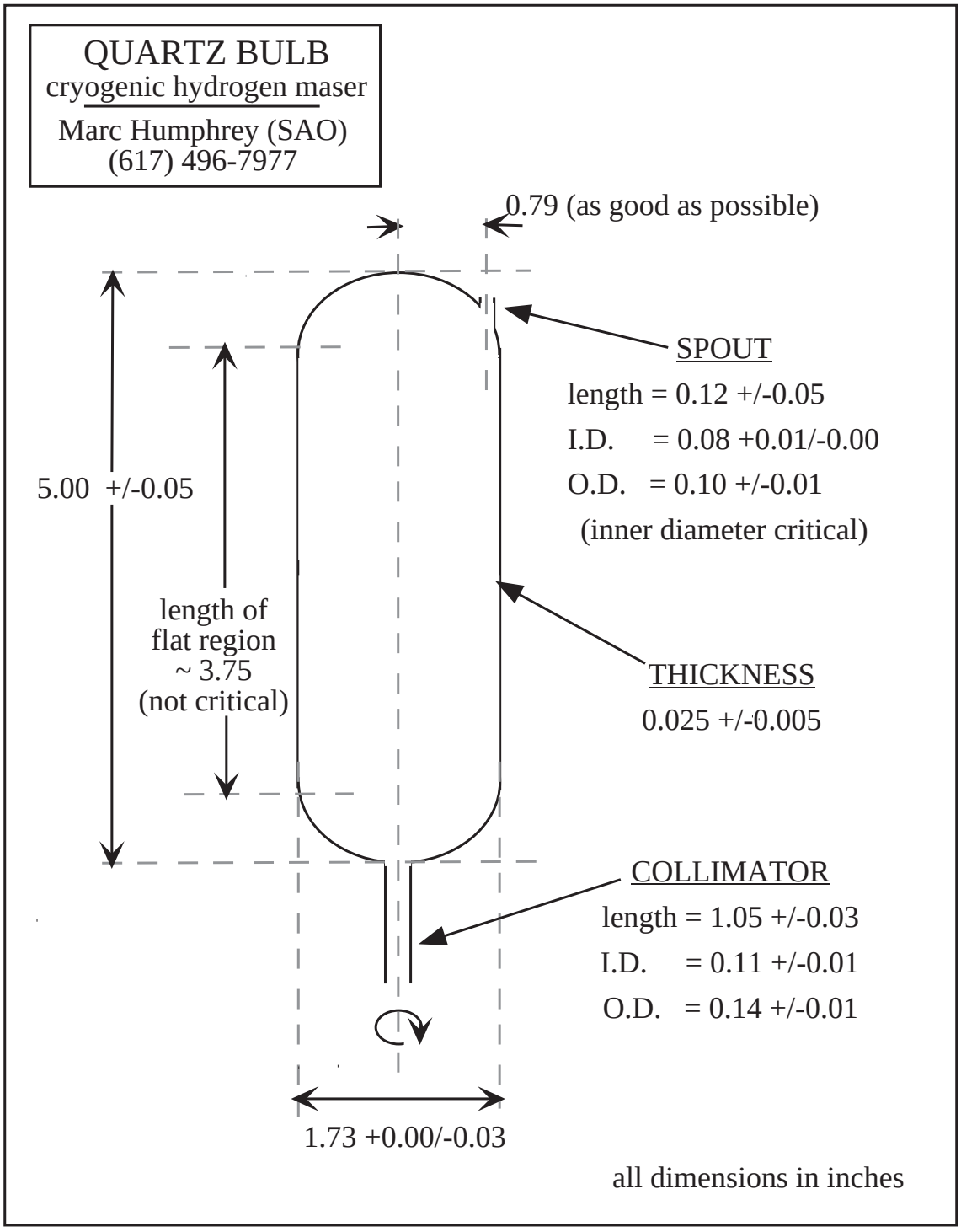

Figure 5.7: Quartz bulb for the cryogenic hydrogen maser.

plunger disk and the end of the cavity to provide elasticity and to maintain the radial symmetry inside of the microwave cavity. The tube caused a slight (5%) decrease in the cavity-Q.

The flow of superfluid helium is regulated at room temperature with a mass flow controller,[9] typically set near 0.2 standard cubic centimeters per minute. The regulated ^{4}He gas flows into the cryostat, is thermalized at 77 K and 4 K, and then passes through a flow impedance at about 1.7 K. The flow impedance liquifies the helium, which is then thermalized at a 0.5 K heat sink before entering the maser bulb. The superfluid film enters the bulb, evenly coats the quartz surface, and then drains out the entrance collimator into the beam tube. The helium film is eventually vaporized at higher temperatures in the focusing region and adsorbed by the activated charcoal sorption pump. As will be described in Section 5.5.2, the CHM could only be operated with thin, unsaturated ^{4}He films.

The helium film in the beam tube will produce a helium vapor above it which will attenuate the flow of hydrogen into the storage bulb (see Figure 5.3). Since the vapor pressure increases with temperature, every effort is made to reduce the base temperature of the maser and the temperature of the surfaces between the focusing region and the maser interaction region. Because of the hydrogen beam attenuation, the maser would not oscillate at maser temperatures above about 540 mK.

A pair of transverse rf-field-producing coils is mounted to the external surface of the microwave cavity sapphire. These coils are used to drive $F = 1$, $\Delta m_F = \pm 1$ Zeeman transitions in the atomic ensemble for double resonance maser studies. These rectangular coils are 3 $\frac{1}{8}$" $\times$ 3 $\frac{3}{4}$" and constructed from 20 turns of 32 AWG copper wire. The rf field generated by these coils is slightly screened by the thin layer of silver deposited on the external surface of the sapphire cylinder, however a current of 0.8 mA (dissipating 0.009 μW) is sufficient to produce a field strong enough to uniformly mix the $F = 1$ state populations on the order of 1 ms. These transverse field "Zeeman" coils (shown in

[9] Brooks Instrument Division model 5850E mass flow controller.

Figure 5.6) are mounted in Helmholtz configuration.

Immediately outside the sealed copper pot that holds the maser cavity, a solenoid coil is mounted (shown in Figure 5.8). The solenoid produces the static quantization field (typically about 2.4 mG) along the longitudinal axis of the maser. The solenoid consists of one main coil and an upper and lower trim coil, each separately controlled with its own power supply. The power to the three coils is supplied by the same method as with room temperature SAO masers, as described in Chapter 3. The copper pot is sealed using indium wire which becomes superconducting below 3.4 K. Therefore, to avoid flux expulsion of the solenoid field in these indium rings, the solenoid is powered up before cooling the maser below 3.4 K. While this will act to freeze in the original field setting, it does become problematic when fine tuning the field settings once the maser is oscillating. Typically, an iterative approach is used to determine the optimal field setting, with the optimum setting from the previous cooling used as the initial setting for the subsequent cooling.

The maser cavity and solenoid are surrounded by a set of four, nested high-permeability magnetic shields made from Cryoperm,[10] also shown in Figure 5.8. These shields are heat sunk to the ^{3}He pot (0.5 K) by four isolated copper straps. Each of the shields is electrically insulated from the others, and from ground, to prevent stray magnetic fields from thermoelectric currents. The shields have a longitudinal shielding factor of about 150,000 which will screen the ambient static magnetic field to below 5 μG.

The microwave signal inductively coupled out of the maser cavity with the coupling loop and SMA vacuum feedthrough is transmitted along a semi-rigid microcoaxial cable through a port in the magnetic shields. Immediately outside the shields, the signal passes through an inside/outside DC block[11] to prevent thermoelectric currents from passing down the line into the magnetic shields. The signal then travels along semi-rigid coaxial cable (with SMA connectors and heat sunk at 1.7 K, 4 K, and 77 K) up to a room temperature vacuum feedthrough where it is coupled out of the cryostat.

[10] Cryoperm is a trademark of Vacuumschmeltz, Inc., Hanau, Germany.
[11] Microlab/FXR HR series, 1.0 - 9.5 GHz.

Figure 5.8: Copper pot containing cryomaser cavity (top), magnetic shields (left), and solenoid (right).

5.3.3 Steady state operation

During normal, steady state maser oscillation, the raw maser signal coupled out of the cryostat (10^{-14} W at 1420 MHz) is passed through an rf isolator and then into a room temperature preamplifier[12] which provides a gain of 41 dB with a maximum noise figure of 1.0 dB. The amplified signal at 1420... MHz is then passed directly into the low-noise heterodyne receiver, described in detail in Chapter 3 and shown schematically in Figure 5.9. By phase locking a high quality, voltage controlled crystal oscillator (VCXO), the receiver converts the amplified maser signal (10^{-10} W at 1420... MHz) into a more useful reference signal (10 mW at 5, 100 and 1200 MHz).

The SAO laboratory is equipped with a pair of room temperature masers which serve as "house" frequency references, masers P-8 and P-13. By comparing the cryogenic maser directly against one of these sources, its stability relative to a room temperature maser can be determined. Each of the masers (cryogenic and room temperature) has its own independent receiver with its own phase locked voltage controlled crystal oscillator. To compare two masers, the relative output frequency of their oscillators is adjusted by tuning the receivers' synthesizers so that there is approximately a 1.2 Hz offset between them. These two signals are then combined with a double-balanced mixer, and the resulting 0.8 s beat note is averaged over 10 or 100 s intervals with a frequency counter.[13] By combining these 10 and 100 s averages, the relative Allan variance of the two masers being compared can be determined for various averaging times, and the Allan variance can be calculated independently using DOS and LabVIEW programs.

In order to measure the absolute frequency stability of the cryogenic maser, it would have to be compared to a device with equal or better frequency stability. However, there exists a method in which the cryogenic maser can be compared with the two different room temperature masers in a "three cornered hat" configuration [89] to determine the absolute frequency stability of each maser.

[12] MITEQ model AFS3-01300150-10-10P-4, 1.3 - 1.5 GHz.

[13] Hewlett-Packard model HP 5334B (for DOS program) and Hewlett-Packard model HP 53131A (for LabVIEW program).

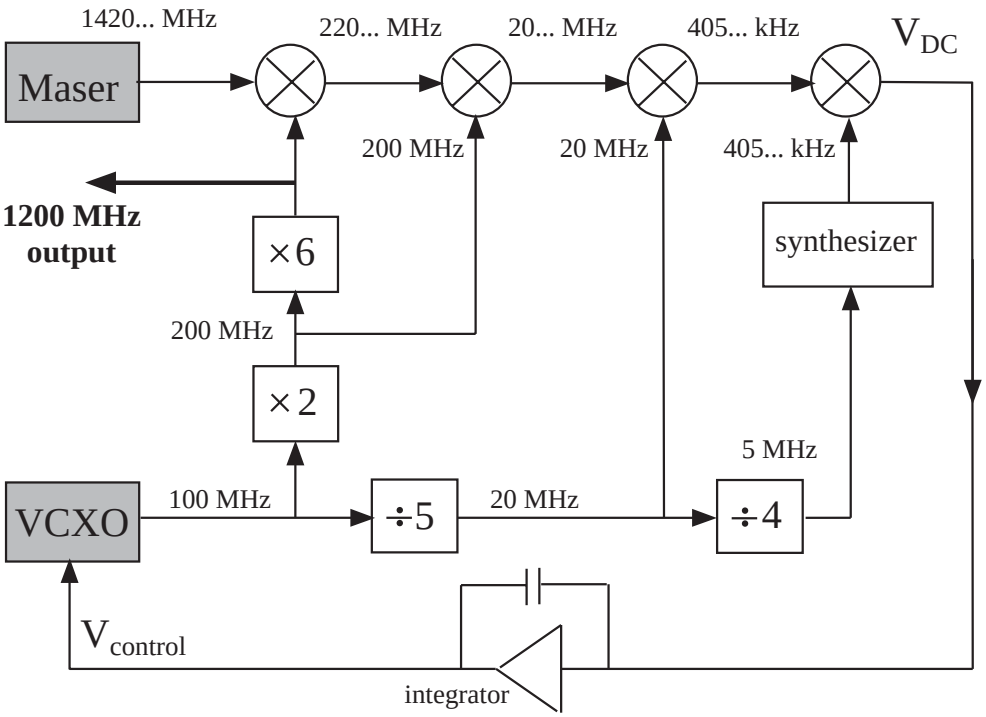

Figure 5.9: Cryogenic hydrogen maser receiver. The maser is used to phase lock a voltage controlled crystal oscillator (VCXO), from which output frequencies of 5, 100 and 1200 MHz are derived.

The SAO laboratory is also equipped with a common-view GPS connection to the National Institute of Standards and Technologies (NIST), allowing for absolute determination of the cryogenic hydrogen maser frequency relative to the primary time scale NIST(AT1) and the international time scales UTC(NIST) and UTC. These absolute frequency comparisons allow for the monitor of long-term maser frequency drift.

We have investigated the possibility of installing a low temperature preamplifier. A cryogenic preamp could be mounted to either the liquid nitrogen shield (cooling power about 40 W) or to the liquid helium bath (cooling power about 1 W). At 77 K, a MITEQ GaAs FET cryogenic preamplifier[14] would be suitable. The noise figure for this preamplifier is about 0.15 dB and the gain would remain nearly the same at 35 dB, while the power dissipation is about 600 mW. Based on the above analysis of thermal noise limited short-term maser stability (Section 5.1.1), we expect the stability limit would improve from $2.0\times10^{-14}/\tau$ to $7.4\times10^{-15}/\tau$ (over the limit with the current, room temperature preamplifier). At 4 K, a Berkshire Technologies HEMT cryogenic preamplifier[15] seems appropriate because it has significantly less power dissipation (about 50 mW). The noise figure of this preamplifier is reduced to 0.05 dB while the gain can be maintained at 40 dB. We estimate a thermal noise limit to maser stability of $4.8\times10^{-15}/\tau$ with this preamplifier.

5.3.4 Pulsed operation

If the conditions of the maser are such that active maser oscillation cannot be achieved, information about the system can be learned by operating in pulsed mode. In this configuration, a pulse of microwave energy at the atomic hyperfine frequency is injected into the maser cavity through the coupling loop and the response of the atomic ensemble is detected out through the coupling loop. If the amplitude and length of the pulse are set so that the product of the injected field's Rabi frequency and the pulse length are equal to $\pi/2$ radians (i.e., a "$\pi/2$ pulse"), atoms in the polarized state $|2\rangle$ will be put into the radiating superposition state $\frac{1}{\sqrt{2}}(|2\rangle + |4\rangle)$. The frequency of the radiation will include

[14]MITEQ model JS2-01350145-025-CR.
[15]Berkshire Technologies model L-1.4-30H or L-1.4-28H.

the hyperfine frequency plus any shifts such as cavity pulling or collisional shifts. If the atomic magnetization is sufficiently weak that radiation damping can be neglected, the amplitude of the radiation from the superposition state will decay exponentially with a time constant given by the decoherence time T_2. Such an exponentially damped sinusoidal signal is termed a "ringdown" or a free induction decay (FID).

The electronics used for pulsed operation include those for the generation of the pulse and those for the signal detection (see Figure 5.10). A directional coupler, installed at the maser output just outside the cryostat, allows the injected pulse into the cavity while coupling the atomic response out. A frequency synthesizer, set near the atomic hyperfine frequency is gated by pulse shaping electronics which set the length of the pulse as well as the interval between pulses. The output of the pulse shaping electronics is injected into the maser cavity. The atomic signal is input into an open-loop heterodyne receiver which mixes the 1420.405... MHz signal down to 405... kHz, then mixes it further with a tunable synthesizer. The resulting damped beat note can be displayed on an oscilloscope or sampled with data acquisition software triggered by the pulse shaping electronics. Both synthesizers and the open loop receiver are all locked to a 5 MHz reference signal from an SAO room temperature hydrogen maser.

Four types of information about the below-oscillation-threshold maser can be gained from the free induction decay signals. By calibrating the receiver with a synthesizer of known amplitude, the amplitude of the maser signal can be determined. By tuning the reference synthesizer for the open loop receiver so that the output signal has a zero beat, the maser frequency can be determined. By fitting an exponential decay envelope to the free induction decay, an estimate of the atomic hyperfine decoherence time T_2 can measured. Finally, by applying more sophisticated pulse sequences to the atomic ensemble, an estimate of the population decay time T_1 can also be made.

While monitoring the free induction decays, various maser parameters (such as hydrogen discharge pressure and power, hydrogen nozzle temperature, superfluid film flow, and main solenoid and trim field settings) can be tuned to maximize the signal amplitude,

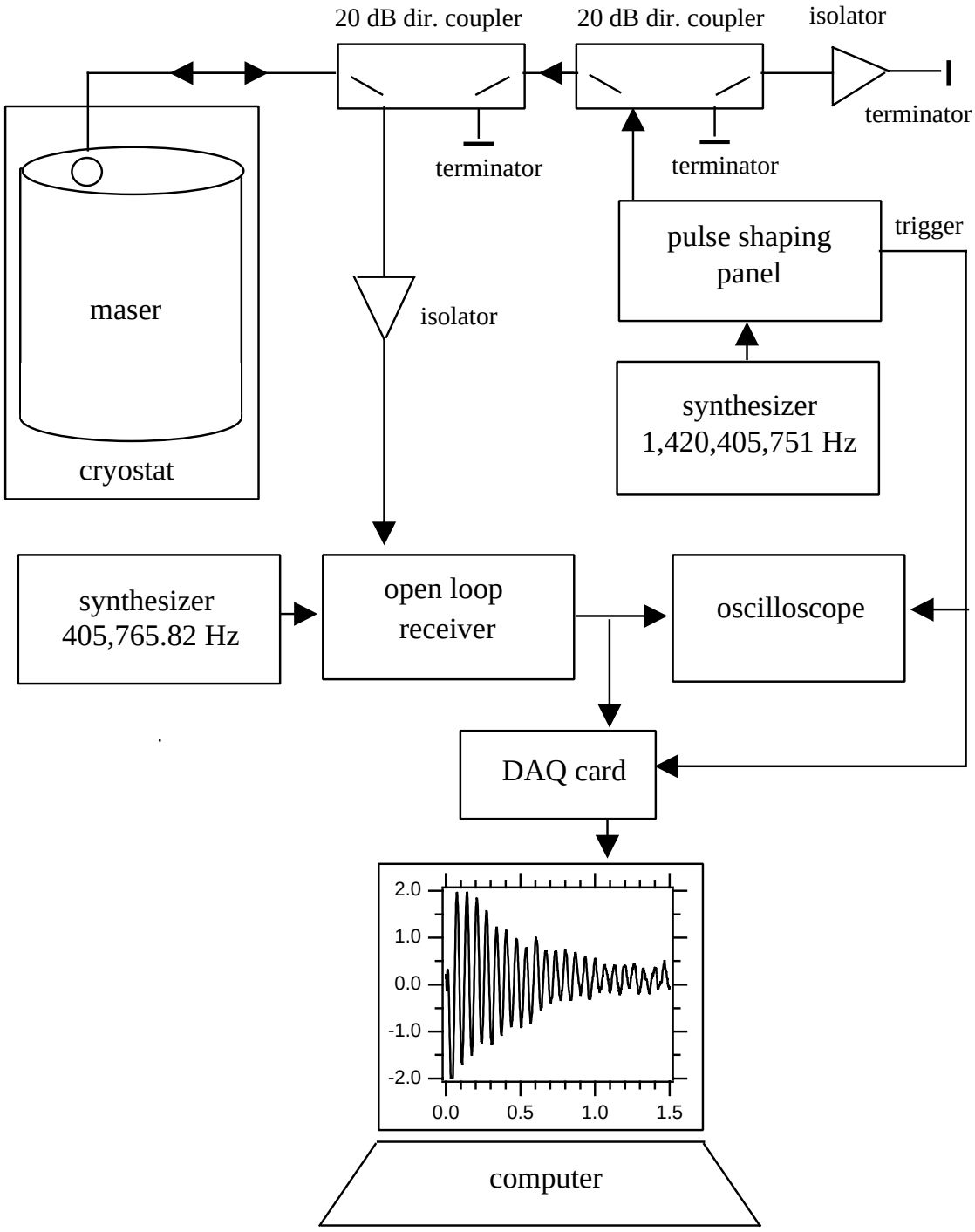

Figure 5.10: Electronics configuration for pulsed maser operation. See Section 5.3.4 for details.

reduce maser frequency shifts, or lengthen the decoherence or population decay times.

5.4 ^{3}He refrigerator

The refrigeration requirements for the SAO cryogenic hydrogen maser are a base temperature near 0.5 K and, equally important, a relatively large amount of cooling power. The latter requirement comes from the relatively large thermal mass of the system and as a result of the steady flow of hydrogen gas and superfluid ^{4}He into the maser during operation. A pumped, recirculating ^{3}He refrigerator best meets these criteria. The SAO ^{3}He cryostat was constructed from a modified 4 K liquid ^{4}He cryostat used by the SAO group for early investigations into cold hydrogen maser wall coatings [79]. It's transformation into a recirculating ^{3}He cryostat was undertaken by Alabama Cryogenic Engineering in collaboration with SAO and Harvard scientists.

Various constraints during the initial development of the SAO CHM led to a very cramped cryostat design. These limited the cryostat to only two vacuum spaces and reduced the vertical length of the device which leads to reduced isolation from the environment (hence higher heat loads) and requires increased cooling power.

The cryostat, shown schematically in Figure 5.11 contains two vacuum spaces and four thermal zones. The vacuum spaces, described above, include the outer vacuum chamber (OVC) used to evacuate gases from the cold regions of the cryostat and the maser vacuum chamber (MVC) used for the operation of the hydrogen maser. The thermal zones include an outer liquid-nitrogen-cooled shield at 77 K, a liquid ^{4}He bath at 4.2 K, a pumped ^{4}He pot at 1.7 K, and the pumped ^{3}He pot and recirculation system at about 0.5 K.

5.4.1 Vacuum system

The entire maser is sealed within a large, room temperature vacuum tank. A 450 liter/s turbomolecular pump[16] evacuates, in parallel, the OVC through a 2.75" Conflat flange and the MVC through a 1/4" tube with an o-ring seal. The pressure of both of these

[16]Leybold TURBOVAC model 450.

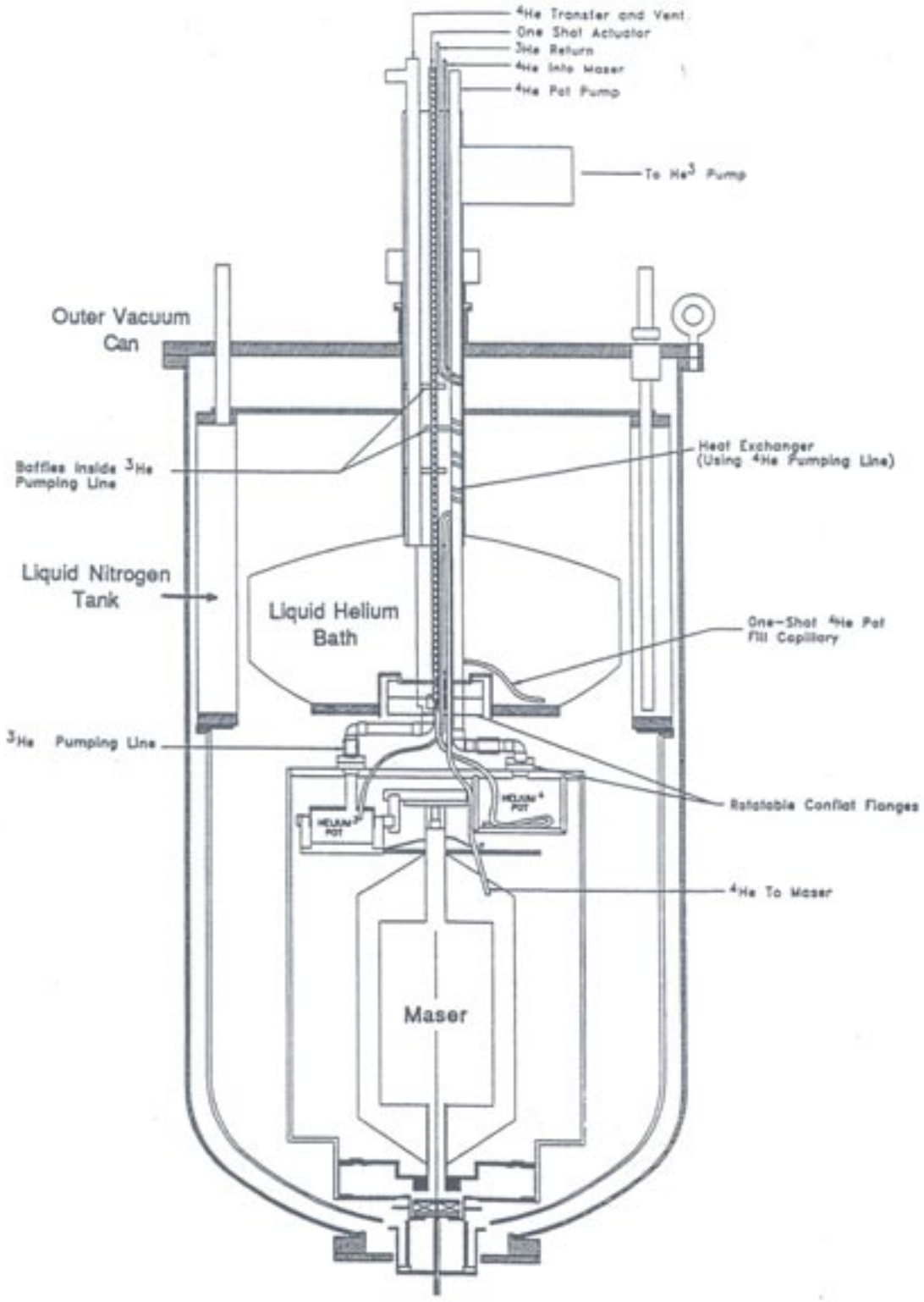

Figure 5.11: Pumped ^{3}He cryostat. See Section 5.4 for details.

regions is monitored with an ion gauge[17] and, while operating, is typically less than 10^{-8} Torr. A second, 145 liter/s turbomolecular pump[18] is used to evacuate the hydrogen gas manifold, the ^{3}He gas handling manifold, and the ^{4}He manifold for the superfluid ^{4}He film prior to operation.

5.4.2 Liquid nitrogen shield

As shown in Figure 5.11, immediately inside the vacuum chamber is a liquid nitrogen cooled radiation shield that surrounds the rest of the cryostat. The top half of this shield is an annular, liquid nitrogen filled jacket; the bottom half is a large copper hemisphere which is bolted into good thermal contact with the jacket. Both inner and outer surfaces of the liquid nitrogen shield are covered with highly reflective superinsulation to prevent the absorption of radiation. The shield, which holds nearly 30 l, requires filling about once every 36 hours, implying that there is a 40 W heat load on this thermal zone (liquid nitrogen latent heat = 160 kJ/l at 77 K).

5.4.3 Liquid ^{4}He bath

Inside the liquid nitrogen shield, a large liquid ^{4}He bath is suspended by thin walled stainless steel tubing. The bath is accessed from above by a 0.5" ID stainless steel tube which serves as an inlet and exhaust port. This bath, also having a capacity of about 30 l, requires filling about once every 25 hours during steady state operation. This implies that there is a heat load of 900 mW on the bath (liquid helium latent heat = 2.6 kJ/l at 4.2 K), due to thermal conduction through the support structures above and below and due to thermal radiation.

The temperature of the bath is monitored with a silicon diode temperature sensor[19] which has an operating range down to 1.4 K. In addition, a set of three 75 W power resistors are bolted in series to the base of the bath in order to quickly boil off its contents

[17] Varian Smart Gauge model 973-5028.
[18] Leybold TURBOVAC model 151.
[19] Lake Shore Cryotronics DT-470 Si diode with Lake Shore model 201 temperature monitor.

when necessary.

5.4.4 Pumped liquid ^{4}He pot

Below the liquid ^{4}He bath, the pumped liquid ^{4}He pot is situated. The ^{4}He pot is filled by a small transfer tube from the ^{4}He bath, and connected through an exhaust port to a large mechanical pump. By pumping on the pot, the vapor pressure of the ^{4}He is lowered, therefore lowering the temperature. Typically, the ^{4}He pot is pumped down to below 10 Torr, resulting in a temperature below 2 K.

The ^{4}He pot is constructed of copper and has a volume of about 500 cm^3. It is in good thermal contact with a copper platform (the "2K plate"), about 12 inches in diameter. To this platform are mounted numerous thermal sinks for electric leads, the superfluid ^{4}He film input line, and the ^{3}He recirculation input line.

The ^{4}He pot is suspended by low thermal conductivity stainless steel tubing. In addition, a graphite "heat switch" has been installed between the liquid ^{4}He bath and ^{4}He pot, which utilizes the property that graphite has moderately high thermal conductivity at higher temperatures (10^2 W/mK at 100 K) and a significantly lower thermal conductivity at lower temperatures (10^{-3} W/mK at 1 K). Therefore, the ^{4}He pot is in relatively good thermal contact with the bath during the cooldown, while it is thermally isolated from the bath at normal operating conditions.

Liquid ^{4}He flows from the bath into the ^{4}He pot through a stainless steel tube, which is spiral soldered to the bottom of the ^{4}He pot to improve the thermal link between the liquid and the copper pot, and the flow is regulated with an externally controlled needle valve.

The pumping line of the ^{4}He pot, made of 1/2" diameter stainless steel tubing from the pot to the top of the cryostat, is heat sunk at 4 K and 77 K before reaching room temperature. Room temperature pumping lines of 1.25" diameter extend to the inlet of several mechanical pumps connected in parallel[20] for a total pumping speed of about 2500

[20] Welch DuoSeal models 1397 and 1398.

liter/min. The pressure of the ^{4}He pot is monitored at room temperature at the top of the cryostat. Under normal operation, the ^{4}He pot is cooled to about 1.75 K, corresponding to a vapor pressure of about 11 Torr [88]. The cooling power of the ^{4}He pot has been measured and calculated [90] to be about 600 mW (latent heat of ^{4}He = 87 J/mol at 1.7 K [91]).

During the cooldown process, the ^{4}He pot temperature is measured using a silicon diode temperature sensor.[21] Below 2 K, however, a more accurate temperature reading is made using a RuO_2 resistive temperature sensor monitored with a bridge circuit (see Section 5.4.6). A 1000 Ω metal film resistor is mounted to the 2K plate which allows for temperature stabilization of this region if desired.

As depicted in Figure 5.11, a large, cylindrical radiation shield (the "2K shield") is suspended from the perimeter of the 2K plate. This copper shield, 12 inches in diameter and about 20 inches in length, is in good thermal contact with the 2K plate and acts to shield the 0.5 K maser region from thermal radiation from the 77 K radiation shield. The outer surface of the 2K shield is covered with highly reflective superinsulation (to minimize absorption of 77 K thermal radiation) while the inner surface is blackened (to absorb radiation from the 0.5 K region). At the bottom of the 2K shield, the lower plate of the sorption pump is pressed into good thermal contact at 1.7 K.

5.4.5 Pumped liquid ^{3}He pot

The final stage of cooling is achieved using a recirculating liquid ^{3}He system. Room temperature ^{3}He gas enters the cryostat, is liquified, and passes down to a ^{3}He pot. The ^{3}He pot is pumped to lower its vapor pressure, thereby cooling the ^{3}He liquid and lowering the ^{3}He pot temperature. The ^{3}He gas is pumped using hermetically sealed pumps behind which the ^{3}He is recollected. The gas is then input back into the cryostat, completing the circuit.

The ^{3}He pot is also constructed of copper and has a volume of about 200 cm^3. Silver

[21] Lake Shore Cryotronics DT-470 Si diode with Conductus LTC-20 temperature controller.

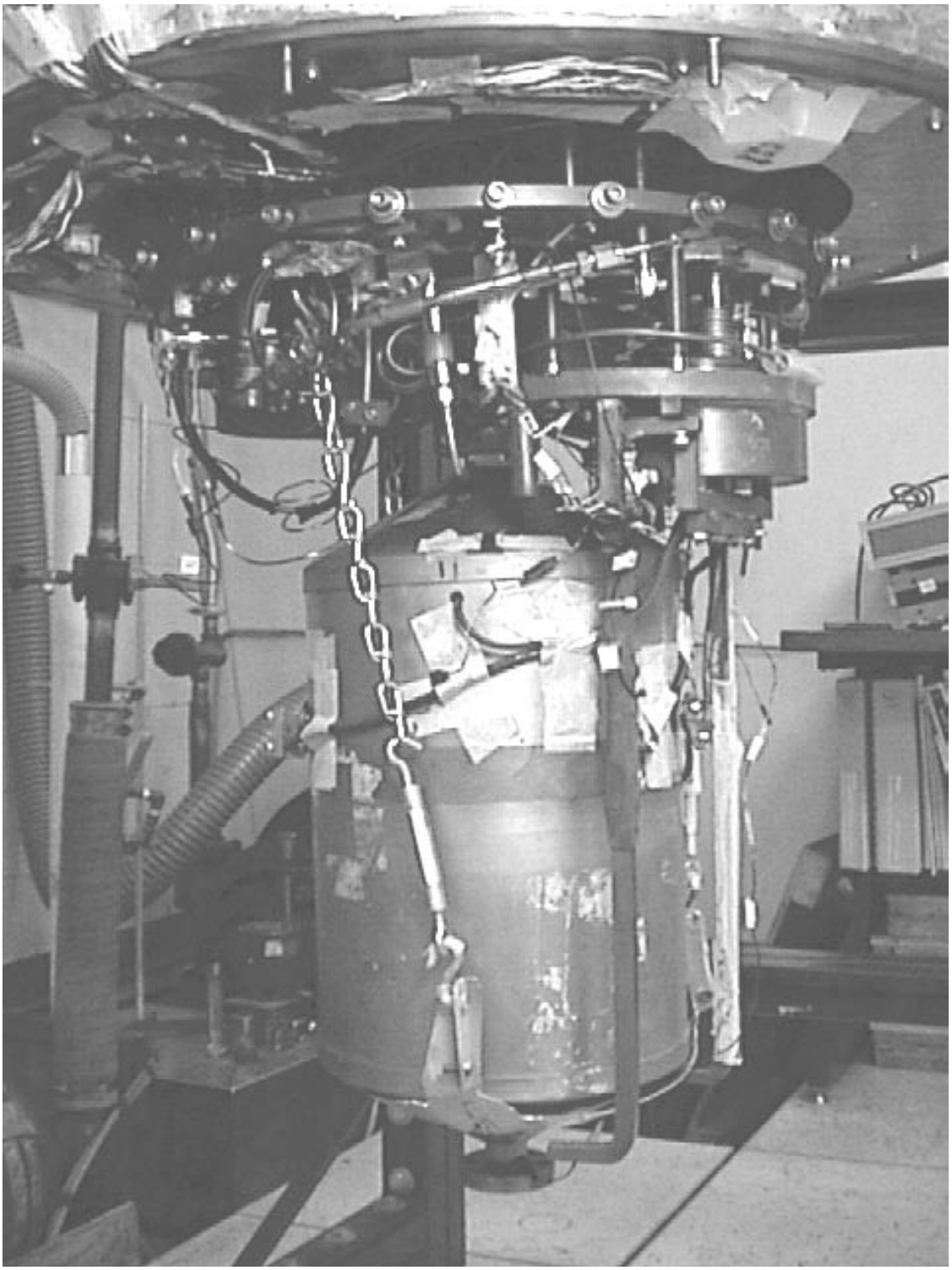

Figure 5.12: Cryostat and maser. At the top is the 77 K jacket (77 K shield not mounted). Below this is the perimeter of the 2K plate (without the 2K shield). The ^{4}He pot is at the left, the ^{3}He pot is to the right, and the maser's outermost magnetic shield is at center.

grains have been sintered to the bottom of the pot to reduce the Kapitza thermal boundary resistance [91] between the liquid ^{3}He and the copper walls of the pot. The ^{3}He pot is in good thermal contact with a small copper platform from which the copper pot enclosing the maser is suspended, as shown in Fig 5.12.

The ^{3}He pot is suspended from the 2K plate by its low thermal conductivity stainless steel pump line. Graphite heat switches have also been used here so that the ^{3}He pot is in relatively good thermal contact with the 2K plate during the cooldown, while thermally insulated from it at normal operating conditions.

A schematic of the ^{3}He recirculation system is shown in Figure 5.13. When the system is not in use, the ^{3}He gas is stored in a pair of storage dumps. Prior to use, the dumps are opened and the gas enters the system at valve j. Before entering the cryostat, the gas passes through a liquid nitrogen cold trap (to trap out any nitrogen, oxygen and water impurities) and a liquid helium cold trap (to trap out hydrogen impurities from cracked pump oil). The purified gas then enters the cryostat through valve q.

Once inside the cryostat, the ^{3}He return line is spiral soldered to the ^{4}He pump line to allow thermalization of the gas. Further downstream, the return line is spiral soldered to heat sinks at 4.2 K and 1.7 K. Immediately downstream from the 1.7 K heat sink, the gas enters a fine, stainless steel capillary that acts as a high flow impedance ($Z \approx 1\times10^{18}$ m^{-3} at 2 K) which allows the necessary pressure increase to liquify the ^{3}He at this low temperature (and to dump most of the heat of liquification into the ^{4}He pot). After liquification, ^{3}He flows into and collects in the ^{3}He pot. From the ^{3}He pot, evaporated ^{3}He gas is pumped out through a pump line. The first 10 inches of this line (from the pot to the top of the liquid ^{4}He bath) is 1/2" OD stainless steel; above the bath to the inlet of the pump (about 30 inches in length) the pump line is 3" OD and 4" OD stainless steel.

The ^{3}He pot is pumped with a 18 liter/s molecular drag pump[22] with a hermetically sealed 5 liter/s backing pump.[23] Under normal operation, the ^{3}He pot is cooled to about 500 mK, corresponding to a vapor pressure of about 0.16 Torr [88]. Pumping ^{3}He at this

[22] Alcatel model 5030, 18 l/s pump speed for He gas.
[23] Alcatel model 2012 AH.

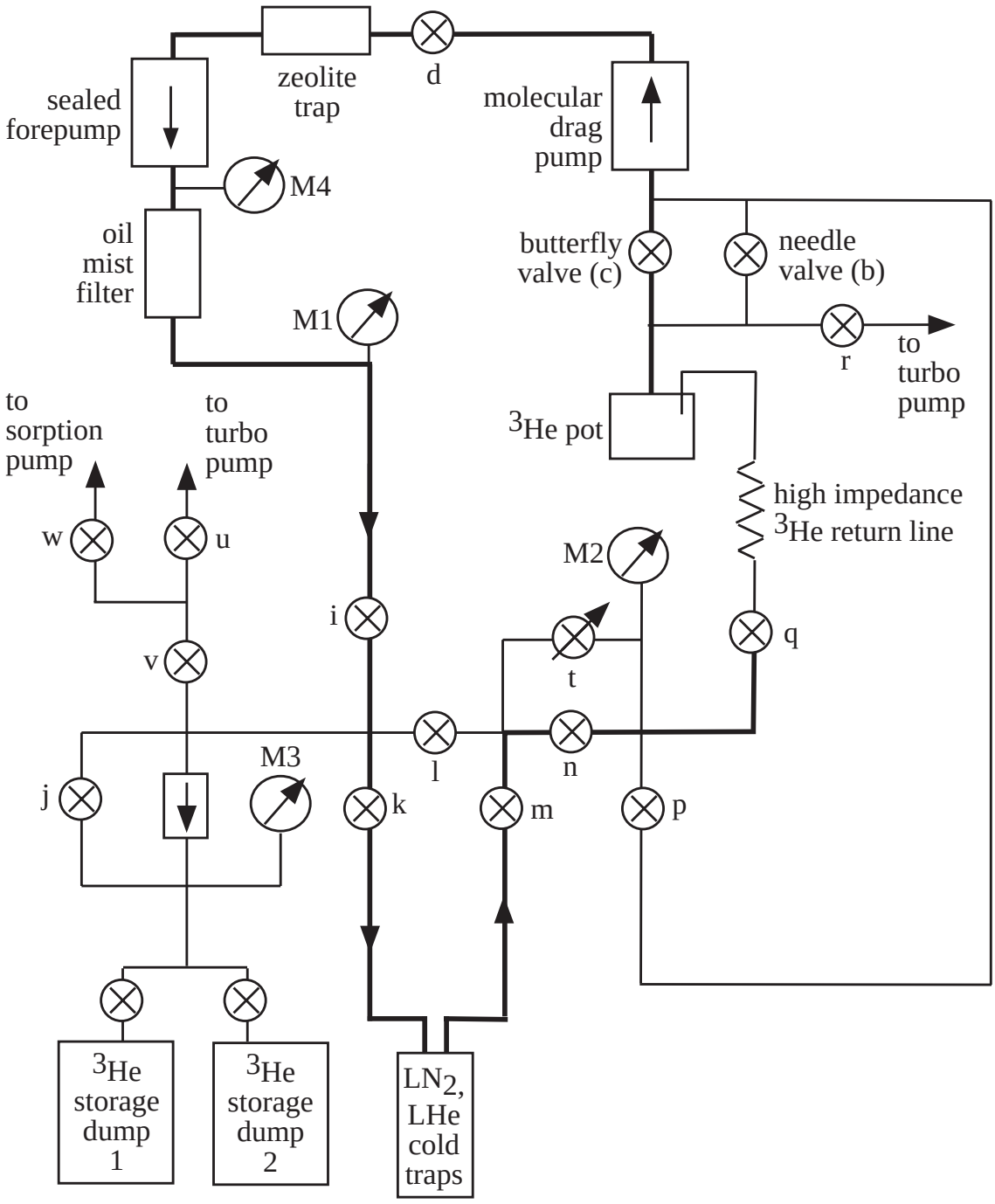

Figure 5.13: ^{3}He recirculation system. Prior to use, the ^{3}He is stored in the dumps at the lower left. Under normal operation, ^{3}He gas enters the cryostat at valve q, liquifies at the flow impedance, and collects in the ^{3}He pot. Evaporated gas is pumped away with a molecular drag pump and sealed forepump. A zeolite trap, oil mist filter, liquid nitrogen cold trap and liquid helium cold trap purify the ^{3}He gas before it reenters the cryostat.

speed and temperature (latent heat = 30 J/mol at 0.5 K [91]) gives a cooling power of the ^{3}He pot to be about 5 mW. In the absence of flowing hydrogen and flowing superfluid ^{4}He film, the heat load on the ^{3}He pot comes from conduction down the stainless steel pump line, conduction up the Vespel rods through the sorption pump, conduction along the maser signal coaxial cable, conduction along the numerous electrical leads, and thermal radiation. Measurements of this heat load on the ^{3}He pot give an estimate of 1.4 mW.

Oil vapor and its byproducts (such as H_2) can be a serious problem for the ^{3}He recirculation as these will be cryopumped at the cold regions of the return line and can block the return of ^{3}He. Therefore, a zeolite foreline trap is installed at the mechanical pump inlet and an oil mist filter is installed at the mechanical pump exhaust. The liquid nitrogen and liquid helium cold traps complete the removal of oil products from the ^{3}He gas supply. Both of the pumps are leak tight so that no ^{3}He is lost from the system and no contaminants leak in. The ^{3}He pumped from the pot is then recollected in a room temperature gas handling panel, where it passes through the cold traps and back into the cryostat, thus completing the cycle.

During the cooldown process, the ^{3}He pot and maser temperature are measured using a silicon diode temperature sensor.[24] Below 2 K, however, a more accurate temperature reading is made using a RuO_2 resistive temperature sensor monitored with a bridge circuit. For absolute temperature determination, we use a high quality germanium resistor which was previously calibrated up to 600 mK by comparison with ^{3}He vapor pressure measurements. A 10 kΩ resistor, mounted to the ^{3}He pot, serves as a heater. Using the RuO_2 sensor as a control thermometer and the resistive heater, we maintain thermal control of the maser using a PID servoloop.[25] Our system of thermometry and thermal control will be described in detail in Section 5.4.6.

[24] Lake Shore Cryotronics DT-470 Si diode with Conductus LTC-20 temperature controller.
[25] Linear Research model LR-130 temperature controller.

5.4.6 Temperature measurement and control

In general, there are two different types of temperature sensors used with the cryogenic hydrogen maser. The first are diode temperature sensors, where a fixed, forward current is supplied to the diode, the voltage drop across it is measured, and the temperature is deduced directly from a calibration table. The second are resistive devices which are incorporated into bridge circuits and monitored with lock-in detection. By balancing the bridge with a variable resistor, the resistance of the sensor is measured and the temperature is deduced using a calibration table.

During the cooldown from room temperature, the temperature of the liquid ^{4}He bath, pumped ^{4}He pot, and pumped ^{3}He pot are monitored with Si diode temperature sensors. These sensors are wired in series such that a single current passes through each of them. A 10 μA current is supplied either by the bath diode monitor or by the pot diodes controller, and the voltage drop across each diode is individual monitored. These voltages are compared with a voltage-temperature calibration supplied by the manufacturer and the temperature of each diode is displayed in units of Kelvin. The voltage drop across each diode can also be read with a suitable voltmeter, such as a strip chart recorder. These diodes dissipate about 20 μW of power when operated at 10 μA and therefore cause negligible heating to system. The diode calibrations are good from room temperature down to about 1.4 K, therefore the determination of the pot temperatures with these sensors is unreliable at standard operating conditions. For our purposes, these diodes are used only as rough indicators of temperature for diagnostic purposes.

The CHM is equipped with the following types of resistive temperature sensors. Ruthenium oxide (RuO_2) resistors are located at the ^{4}He pot, at the ^{3}He pot/maser junction, at the 4 K heat sink of the ^{3}He return line, at the state selection hexapole magnet, and at the Cu nozzle of the hydrogen inlet. A high quality germanium sensor is located at the ^{3}He pot/maser junction to determine absolute maser temperature.

Each of these resistive sensors can be individually monitored with one of three bridge circuits (see Figure 5.14). A pair of matched, 1 kΩ precision resistors make up one arm of

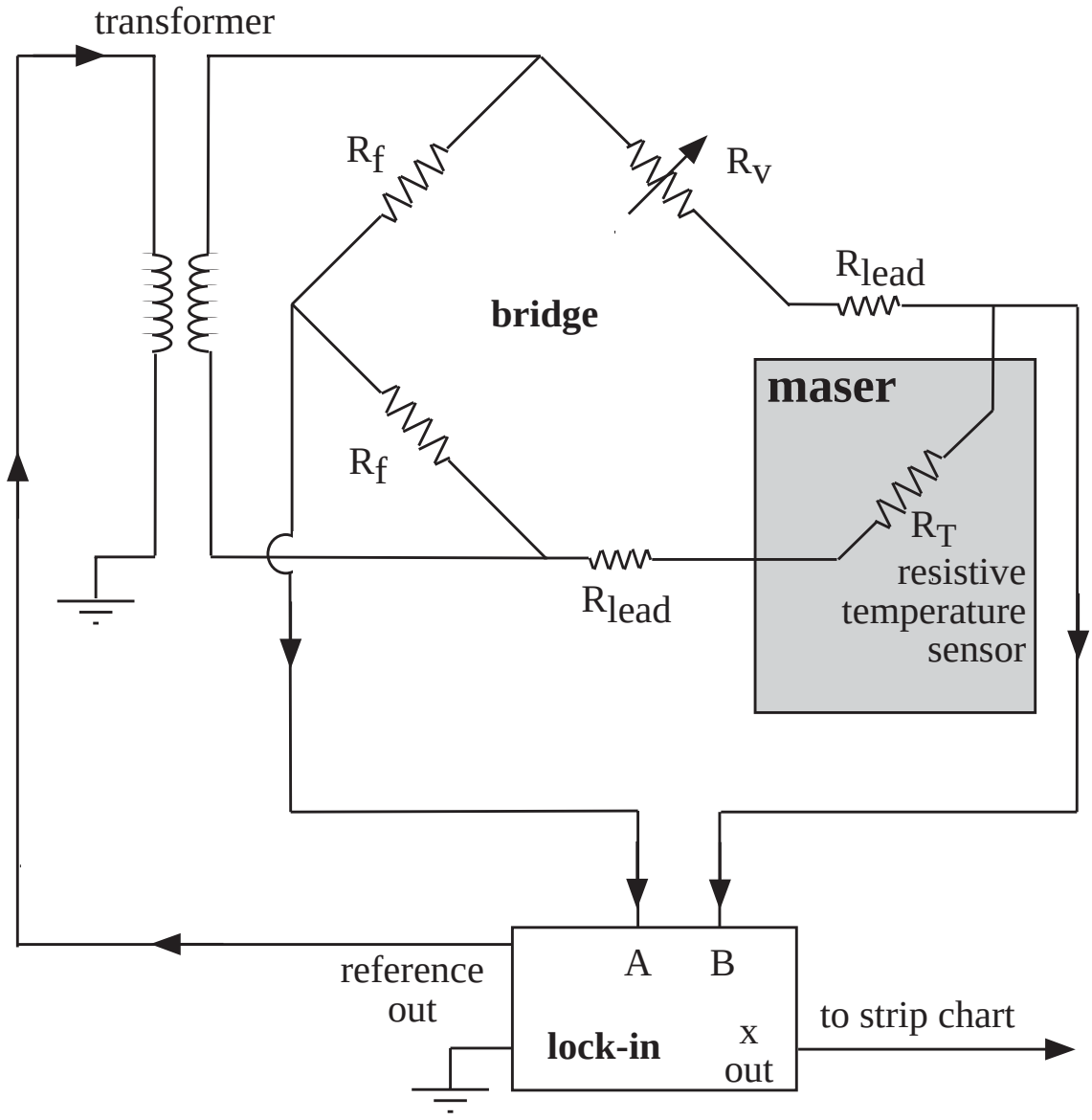

Figure 5.14: Bridge circuit to monitor resistive temperature sensors. The temperature is deduced by balancing the bridge with the variable resistor R_V and then comparing its value with the temperature sensor calibration table. See Section 5.4.6 for details.

a Wheatstone bridge while a variable decade resistor and temperature sensor make up the second arm. The output reference signal from a lock-in amplifier[26] is used to drive a low level, audio frequency current across the bridge. The voltage of this device is attenuated sufficiently to eliminate Joule heating of the sensor (typically about 4 mV plus 10 to 50 dB attenuation depending on the sensor). Then, the voltage across the bridge (from between the matched reference resistors and from between the sensor and decade resistor) is measured with the lock-in amplifier. By varying the setting of the decade resistor, the output voltage can be adjusted. For a decade resistor value equal to the sensor value, the output voltage is zero and the bridge is balanced. By comparing the decade resistor setting to the sensor calibration, the temperature of the sensor is determined. All of these resistive sensors is wired in "three lead" configuration to eliminate error due to lead resistances. As can be seen from Figure 5.14, in the balanced configuration, the resistances from the sensor leads cancel out.

In addition the the temperature sensors, a number of resistive heaters are installed throughout the cryostat. Some of these heaters are used for warming various parts of the maser during different stages of the cooling. A series of three 75 W power resistors mounted below the liquid ^{4}He bath (15 Ω total) are used when the liquid in the bath needs to be evaporated to allow the maser to warm. A resistive heater mounted to the 4 K heat sink of the ^{3}He return line (120 Ω) is used to warm this heat sink when hydrogen impurities in the ^{3}He have cryopumped to the walls of the tube and impeded the flow. A similar heater (10 kΩ) is mounted to the flow impedance used to liquify the incoming ^{4}He for the superfluid film wall coating.

There are also a number of resistive heaters used for temperature regulation. Resistors at the state selection hexapole magnet (1100 Ω) and the Cu nozzle of the hydrogen inlet (1100 Ω) allow for adjustment of the atomic hydrogen state selected flux. Resistors mounted onto the 2K plate (1000 Ω) and at the ^{3}He pot/maser junction (10 kΩ) enable temperature regulation of the 2K plate and the maser.

[26]Stanford Research Systems SR830 DSP.

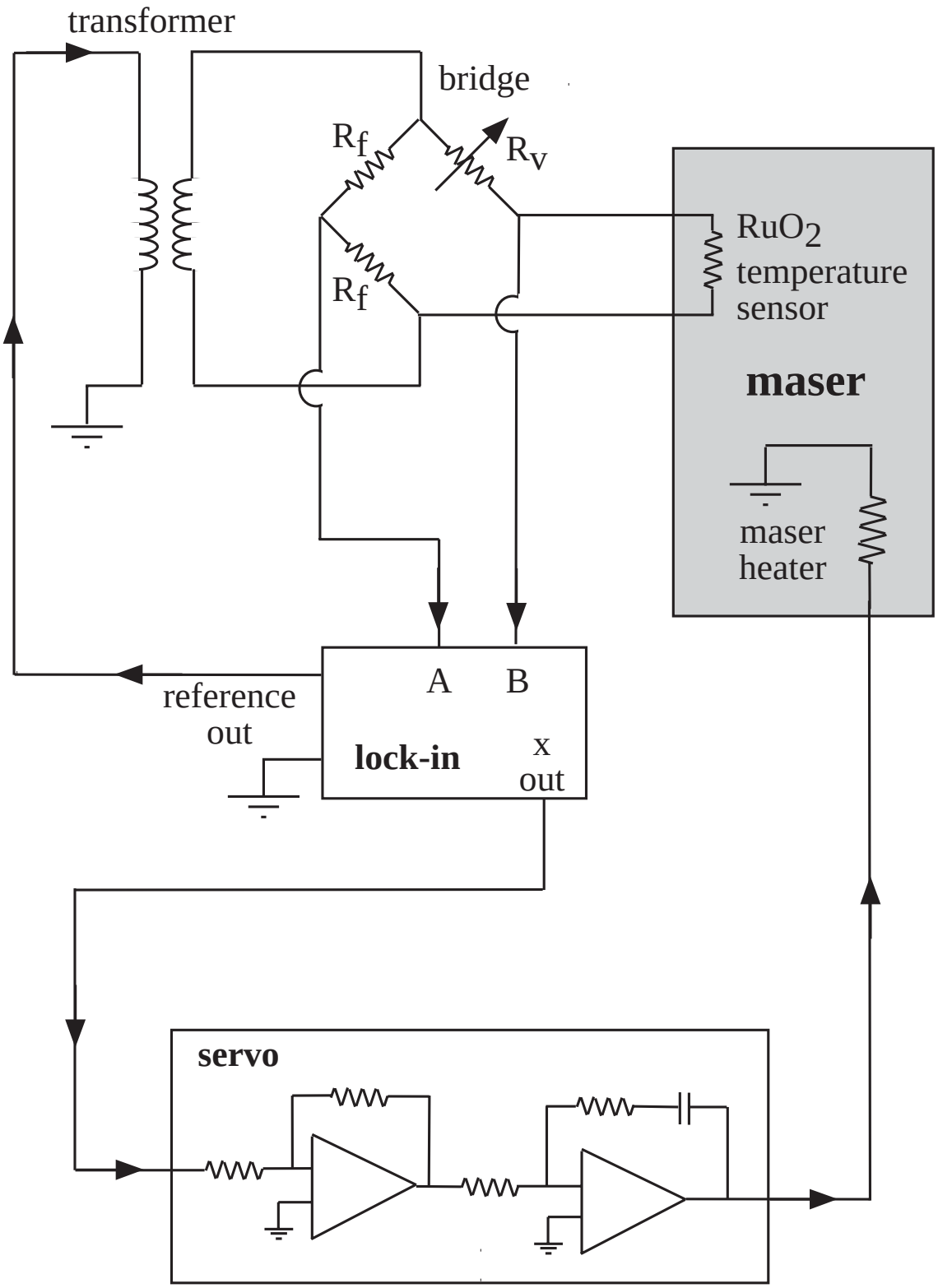

Figure 5.15: Control circuit for maser temperature regulation. An analogous circuit is used to control the 2K plate. See Section 5.4.6 for details.

Thermal control of various regions of the maser can be achieved using a thermal sensor, a heater, and a PID servo circuit (see Figure 5.15). To control the 2K plate temperature, the 2K plate RuO_2 sensor and 1000 Ω heater are used; to control the maser temperature the maser RuO_2 sensor and 10 kΩ heater are used. The output of the lock-in used for the temperature monitor bridge is used as the input to a PID servo[27]. The proportional gain, integration time constant, and differentiation time constant of the servo are all set to match the natural thermal time constants of the thermal region to be controlled, and the output of the servo is used to drive the heater.

The desired temperature is set by tuning the variable decade resistor to the corresponding resistance value. Because the feedback (the heater) can only raise the temperature, the setpoint is chosen to be at a slightly elevated temperature over the initial temperature, within the range of the heater. With the initial temperature below the setpoint, the output of the lock-in will be negative. This negative input into the servo loop will lead to an output at the heater. The temperature will then be raised until it crosses the setpoint, at which point a positive lock-in output will lead to a turning off of the heater. For proper PID settings, the system will converge to the setpoint temperature. Then, the heater power will be raised or lowered to compensate for thermal fluctuations. With these circuits, we achieve 150 μK (rms) control of the 2K plate and 30 μK (rms) control of the maser.

5.4.7 Cooldown procedure

Because of the large thermal mass of the maser, the cooldown of the CHM from room temperature to its operating point takes about one week. The cooldown is complicated by the existence of only a single cryogenic vacuum space (the OVC) which precludes any use of exchange gas to cool the innermost parts of the maser since any gas in the OVC will be in contact with the room temperature walls of the vacuum tank. Therefore, all cooling of the maser is limited to conductive cooling along the supports of the device or

[27]Linear Research model LR-130 temperature controller.

to controlled flow of evaporated liquids and gases through the ^{4}He and ^{3}He pots.

Typically, liquid nitrogen is employed as a precooling agent because of its large latent heat (60 times greater) and low cost (about 10 times less) relative to liquid ^{4}He [91]. Therefore, during precooling we initially fill the liquid ^{4}He bath with liquid nitrogen to cool the maser down to 77 K (the liquid nitrogen boiling point). The initial fill is done slowly to utilize the enthalpy of the evaporated nitrogen gas leaving the exhaust as well as the latent heat of the evaporating liquid [91, 92].

Once the bath is filled with liquid nitrogen, the needle valve controlling flow from the bath into the ^{4}He pot is opened, and the ^{4}He pot pump is used to draw some of the cold, evaporated gas out through the ^{4}He pot. This allows an acceleration of the cooling of the ^{4}He pot over the cooling strictly due to conduction along its support connections to the bath. The precooling of the ^{3}He pot, however, is limited solely to the conduction of heat along its support connections to the ^{4}He pot. Note that from room temperature to the 77 K, the heat switches in the support structures (described in Sections 5.4.4 and 5.4.5) are essentially "on," so there is a relative high thermal conductivity between the bath and the ^{4}He pot, and between the ^{4}He pot and the ^{3}He pot.

After about two days of precooling, the temperature of the ^{3}He pot/maser is lowered to about 77 K. At this point all of the liquid nitrogen in the bath is boiled away (using the 75 W bath heaters), and liquid ^{4}He is used to cool the maser. The bath is slowly filled with liquid ^{4}He, again allowing the enthalpy of the cold escaping gas to do much of the cooling. During this time, some of the cold evaporating gas is also pumped through the ^{4}He pot. Once the bath is filled with liquid ^{4}He, pumping of cold ^{4}He gas through the ^{4}He pot is continued for about one day. During the second day, enough heat has been removed from the ^{4}He pot that it can be filled with liquid ^{4}He. After about two days of liquid ^{4}He cooling, and four days of net cooling, the temperature of the ^{3}He pot/maser is reduced to below 10 K.

On about the fifth day of cooling, ^{3}He is able to condense in the ^{3}He pot. During this initial condensation, the ^{3}He is flowed into the pot through the pump port, rather than

through the high impedance return line, so that any residual impurities not filtered by the liquid nitrogen and liquid ^{4}He cold traps are harmlessly cryopumped to the walls of the large diameter pumping lines. This significantly reduces the probability of clogging any portion of the return line with cryopumped impurities. The ^{3}He gas is incrementally introduced to the ^{3}He pot over a period of about three hours, and during this time, the temperature of the ^{3}He pot is reduced from around 10 K to below 3 K, the normal boiling point of liquid ^{3}He.

On about the sixth day of cooling, after the ^{3}He pot/maser has had one day for thermal equilibration in this state, pumping of the ^{3}He pot and recirculation is begun. Initially, the ^{3}He is pumped on very slowly by opening a needle valve at the inlet of the molecular drag pump (see Figure 5.13). The vapor pressure above the ^{3}He is reduced and the temperature of the ^{3}He pot is lowered. The ^{3}He gas that was pumped away collects in the gas handling panel and a pressure head is established above the cryostat. Eventually a sufficient pressure gradient is established across the return line impedance so that the recirculated ^{3}He returns to the ^{3}He pot in the form of cold liquid. Incrementally, the pumping speed is increased (by opening the valves at the molecular drag pump inlet), and after about two hours the valves are fully open and the ^{3}He pot is pumped on with full pumping speed. During this time, the ^{3}He pot temperature is reduced from around 3 K down to about 0.5 K.

Typically, one full day is needed to remove all the heat from the innermost regions of the maser (for example, a lot of heat is trapped in the high heat capacity sapphire used to load the cavity). Therefore, about seven days after the initial cooling has begun, the maser is sufficiently cold that maser oscillation can be achieved.

5.5 CHM performance

Following the removal of the internal tuning diode installed in series with the transmission line inside the maser cavity (and the removal of its residual magnetization) the CHM first

oscillated with the quartz atomic storage bulb in the summer of 2001, its first oscillation in nearly 5 years. Once this was achieved, it was quickly discovered that a number of technical limitations significantly degraded the CHM performance. It was found that the CHM would only oscillate with relatively weak maser powers and that its running was restricted to thin, unsaturated films at relatively low temperatures (below 540 mK). In addition, with the removal of the internal tuning diode, all cavity tuning was restricted to the mechanical tuning plunger. These three difficulties significantly reduced the ability of the CHM to be used as an ultra stable frequency source or for ultra precise measurements of atomic physics processes.

During our spin-exchange studies with the CHM, the double resonance effect was employed. A discussion of this effect in the CHM will be presented in Chapter 6.

5.5.1 Maser power

Historically, a number of modifications have been made to the atomic state selection and beam tube region of the SAO CHM in order to increase the net population inversion flux into the atomic storage region. It was believed that the chief cause of population inversion flux loss between the hexapole magnet and atomic storage region was scattering of the H beam by ^{4}He vapor above the flowing superfluid ^{4}He film. A number of efforts were made to reduce the temperature of the beam tube, thereby decreasing the vapor pressure of the superfluid ^{4}He film in this region. Attempts were also made to lower the temperature at the top and bottom of the sorption pump. Finally an effort was made to increase the surface area inside the beam tube (by installing a multi-foil Cu tube, constructed by rolling a thin copper foil into a tube with many layers). As a result of these efforts, maser powers exceeding 100 fW were achieved in the mid 1990s.

However, with the installation of the quartz storage bulb and the present thermal environment of the beam tube, maser powers during this thesis work were seen to be significantly lower, with maximum powers of around 30 fW observed. Efforts made to cool the beam tube region by lowering the temperature of the ^{4}He pot, and therefore

the lower plate of the sorption pump, had no significant effect on maser power. An attempt made to vary the surface area of the beam tube over which the ^{4}He film flowed, by removing and reinstalling the multi-foil copper tube, likewise showed little effect on maser power. Finally, out of concern that population inversion flux was being lost due to Majorana transitions in the beam in the region between the hexapole magnet and atomic storage region, a quantization-axis-preserving neck coil was installed inside the beam tube. However, this led to only a slight increase in overall maser power.

This inability to improve overall maser power by decreasing population inversion flux loss between the hexapole magnet and the atomic storage bulb has led to speculation that a majority of the flux loss may occur at the collimator of the quartz storage bulb. While the collimator was designed to have an aperture equivalent to the Teflon collimator used previously, the actual bulb we received had wall thicknesses exceeding specifications which inevitably led to a small decrease in aperture size. Furthermore, the bulb was installed with a copper capillary which directed the superfluid ^{4}He flow straight into the bulb. With this design, the superfluid ^{4}He film flowed first through the bulb, out the collimator, then along the outer surface of the bulb to the cavity (i.e. the bulb and cavity were connected in series). This could increase the thickness of the superfluid film inside the bulb collimator, thereby increasing the ^{4}He vapor pressure inside the collimator and possibly reducing the population inversion flux into the bulb through H-^{4}He scattering. In the next section we will discuss the balance between scattering of the input flux and wall losses.

5.5.2 Superfluid film and operating temperature

As described in Section 5.2, for a saturated superfluid ^{4}He film, the CHM should exhibit a minimum in the magnitude of the negative H-^{4}He collisional shift at around 550 mK. At this temperature, the frequency shift due to collisions with ^{4}He at the wall (where shift magnitude decreases with increasing temperature) offsets the shift due to collisions with ^{4}He in the vapor (where shift magnitude increases with temperature) as shown in Figure 5.3. At 550 mK, for a saturated superfluid film, a negative shift of about 110 mHz

away from the atomic hyperfine frequency would be expected.

For an unsaturated superfluid ^{4}He film, it is observed that the magnitude of the H-^{4}He wall shift is increased, as shown in the plot of maser frequency vs temperature, for various unsaturated superfluid ^{4}He film flow settings (Figure 5.16(a)). The film flows are quantified by the flow control setting of room temperature ^{4}He gas in the outer manifold just above the cryostat. No atomic signals were observed for film flow settings below 0.2 standard cubic centimeters per minute (sccm), implying that below this temperature there is insufficient film thickness on the quartz bulb to prevent H-H recombination at the bulb wall. It can be seen that the magnitude of the negative shift decreases as the flow of superfluid film is increased, and the net shift approaches that of a saturated film for a superfluid film flow of 4.0 sccm. For each film flow, the shift magnitude decreased as temperature is increased (implying the wall shift dominates), and the slope $|df/dT|$ decreased as the film flow is increased.

Because of the reduction in maser power due to scattering of hydrogen atoms off of ^{4}He vapor in the beam tube and collimator, it is also observed that maser power is reduced for increased superfluid ^{4}He film flows. This can be seen in Figure 5.16(b), where the overall maser power is reduced for a given temperature as the film flow is increased. The highest maser powers are seen for the lowest film flow settings, while the maser is nearly quenched for film flows approaching those needed for a saturated ^{4}He film. For a saturated film at 0.5 K, the hydrogen mean free path is about 2 cm (see Figure 5.3) so that a hydrogen atom would make on the order of ten collisions with helium atoms while traveling from the hexapole magnet to the atomic storage bulb.

In addition to the strong dependence of maser frequency on temperature due to H-^{4}He collisions, there is also a dependence of maser power on temperature. As the temperature of the maser is raised, the vapor pressure above the ^{4}He film increases and the maser power is reduced. However, for low thin film settings (just above the minimum) it can also be seen that maser power decreases when the temperature is lowered. Here, the thin superfluid film is insufficient to act as a wall coating and H atoms in the bulb are lost due

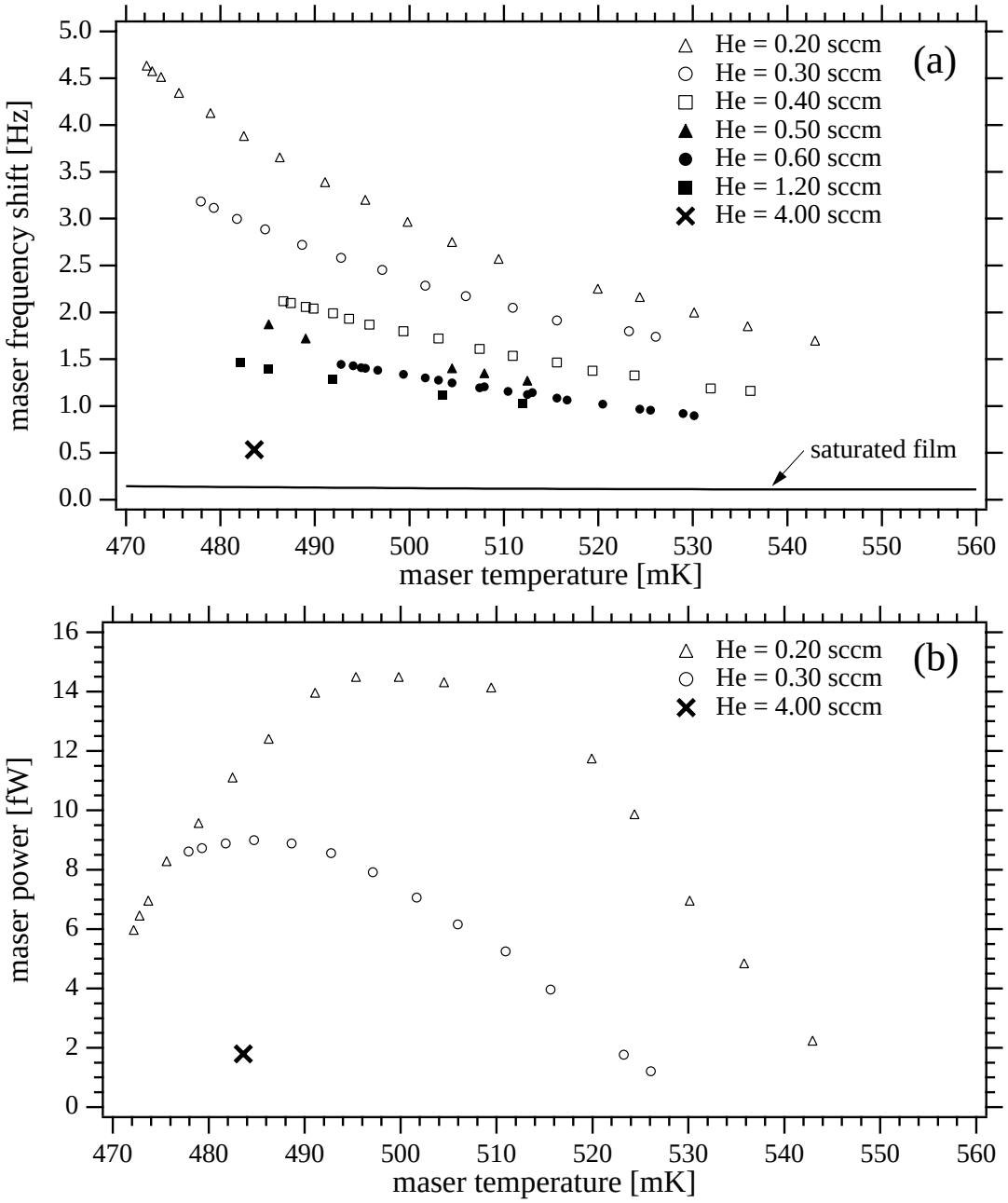

Figure 5.16: (a) Measured maser frequency (markers) vs temperature for different unsaturated superfluid ^{4}He film flows. The solid line is the expected net collisional shift for a saturated film (taken directly from Figure 5.3). (b) Measured maser power vs temperature for different unsaturated superfluid ^{4}He film flows.

to H-H recombination at the bulb wall.

Unfortunately it can be seen from Figure 5.16(b) that maser oscillation is quenched for the large superfluid film flows necessary for a saturated ^{4}He. It can also be seen that even for the thinnest possible He film flows, maser oscillation cannot be sustained up to 550 mK, the target operating point for a saturated film. Therefore, in its present state the CHM can only be operated with unsaturated superfluid ^{4}He films at temperatures below the target operating point in a regime where the H-^{4}He wall shift dominates.

From both panels of Figure 5.16 it can be seen that a compromise must be made when choosing which superfluid film flow setting to operate at. Thinner films lead to reduced H beam scattering and therefore higher maser powers, however the maser frequency's temperature sensitivity (characterized by the slope $|df/dT|$) is increased. This heightened temperature sensitivity leads to a reduction in CHM frequency stability for a given level of maser temperature control. Higher film flows have a lower temperature sensitivity but lead to reduced maser power. For this reason, all initial work with the CHM was conducted at an intermediate superfluid film flow of 0.50 sccm.

It was discovered that there exists a second drawback to operating the CHM with higher superfluid ^{4}He films due to the finite storage capacity of the CHM's sorption pump. Since all of the ^{4}He that flows through the storage bulb is ultimately adsorbed to the activated charcoal inside of the sorption pump, after a certain length of running time this charcoal was saturated and its ability to pump ^{4}He away was significantly reduced.

In Figure 5.17 we plot measured maser power as a function of net running time for a superfluid ^{4}He film flow of 0.5 sccm. Here is can be seen that there is an initial rapid increase in maser power which we attribute to the formation of a solid molecular hydrogen coating at key places in the hydrogen beam input region. Then, the maser power decreases steadily with a time constant of several hours. It has been observed that the decay rate increases as the superfluid ^{4}He flow is increased, and also as the flow rate of atomic hydrogen is increased. In this example, after about 400 minutes of running the H-^{4}He scattering rate is sufficient to bring the CHM below oscillation threshold. Once this has

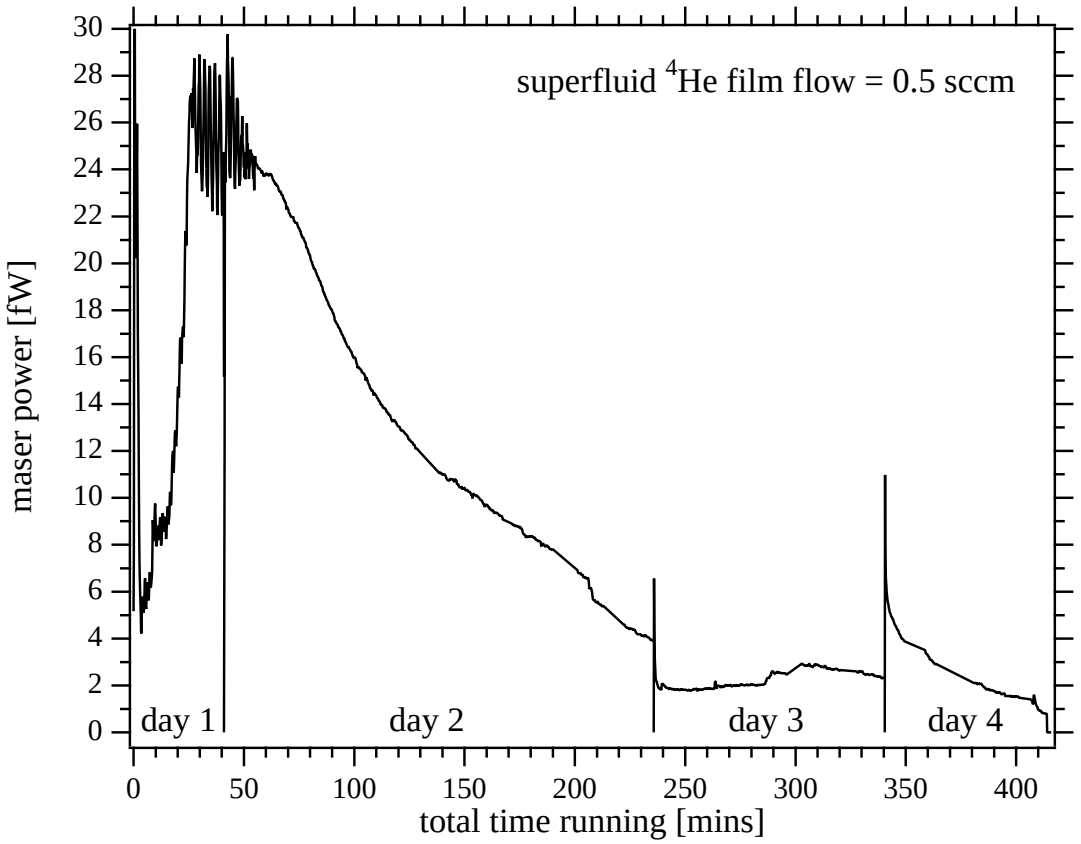

Figure 5.17: Typical maser power decay due to H_2 and ^{4}He accumulation in the sorption pump. These data were taken for a superfluid ^{4}He film flow of 0.50 sccm. It was later found that the net running time could be increased by running with a superfluid ^{4}He film of 0.20 sccm.

occurred, it is necessary to warm the sorption pump (and therefore the maser) above the hydrogen freezing point to about 20 K. This warming takes about 2 hours, and during this time there are significant MVC pressure spikes at 4 K (as the ^{4}He is pumped from the sorption pump) and at about 15 K (as the H_2 is pumped away). Once the maser is warmed to 20 K it is immediately recooled. Unfortunately, nearly one full day of recooling is needed to bring the base temperature down to a level where stable maser oscillation can again be achieved.

Since the power decay rate is decreased while running at lower films, it was decided to lower the superfluid film flow for typical operation from 0.5 sccm to 0.2 sccm. Doing so increased by roughly a factor of two the amount of time the maser could be run between 20 K warming cycles. For a typical hydrogen flux and a superfluid film setting of 0.2, the CHM could generally be run for four days before a warming cycle (with the maser running 3 to 4 hours per day).

5.5.3 Maser frequency stability

Since maser operating temperatures were limited to below the (saturated film) target operating point of 550 mK, the maser would only run in a regime where frequency stability would be compromised by the H-^{4}He collisional wall shift. Furthermore, this wall shift was accentuated due to the necessity of running with unsaturated superfluid films.

From Figure 5.16(b), it can be seen that with the superfluid film flow of 0.2 sccm, the maser power has a maximum near 500 mK. Therefore, this was chosen as the typical operating temperature for normal operation at 0.2 sccm. A plot of measured CHM Allan variance at 511 mK is given in Figure 5.18. This plot shows that for averaging times less than one minute the Allan variance is around 3×10^{-12}. These data were taken with a superfluid film flow of 0.2 sccm and maser temperature control of about 150 μK (rms).[28] Under these conditions, the frequency sensitivity on temperature was about $|df/dT| =$

[28] We note that this temperature control was not up to our optimal level of 30 μK. We attribute this to the fact that, during the run where these data were taken, the thermal contact between the ^{3}He pot, the maser, and the maser temperature sensors and heaters was not optimal.

35 mHz/mK, and this maser temperature control implies a short-term maser frequency stability of about 5 mHz (fractional stability of 4×10^{-12}). This indicates that in practice, the H-^{4}He collisional wall shift and maser thermal control are the primary limits to short-term maser frequency stability.

From Figure 5.3, it can be seen that for a saturated film at 500 mK, the maser frequency has a (wall shift dominated) temperature sensitivity of about $|df/dT| = 0.6$ mHz/mK. For maser temperature control of 150 μK, this would therefore imply a frequency stability on the order of 90 μHz, corresponding to an Allan variance near 6 $\times10^{-14}$. From Figure 5.18 it can be seen that this approaches the thermal limit to maser stability. The thermal limit was calculated here for a CHM line-Q of 3 $\times10^9$ and power of 2×10^{-14} W.

For averaging times longer than 10 s, the maser frequency stability is degraded further. We speculate that most of the instability is due to a slow variation in superfluid ^{4}He film thickness or possibly slow variations in temperature of or thermal gradients across the storage bulb. When making spin-exchange maser frequency shift measurements over periods of tens of minutes, it was necessary to correct the maser frequency data for long-term drifts. This will be described in more detail in Chapter 6.

5.5.4 Maser cavity tuning

For stable maser oscillation, it is necessary only to tune the maser cavity to atomic resonance and leave it unchanged. However, to characterize the maser (e.g., by measuring line-Q) or to use the maser to investigate spin-exchange effects, it is necessary to have tunabilty of the maser cavity. As described in Chapter 3, for these reasons each SAO room temperature hydrogen maser is equipped with an internal tuning diode mounted via a second coupling port to the maser cavity. The internal diode allows resettable, electronic tuning of the maser cavity.

As described in Section 5.3.2 the CHM is not equipped with a second coupling port with which to install such a tuning diode. An attempt was made, however, to install a tuning diode in series with the coupling loop used to couple out the maser signal. While this diode

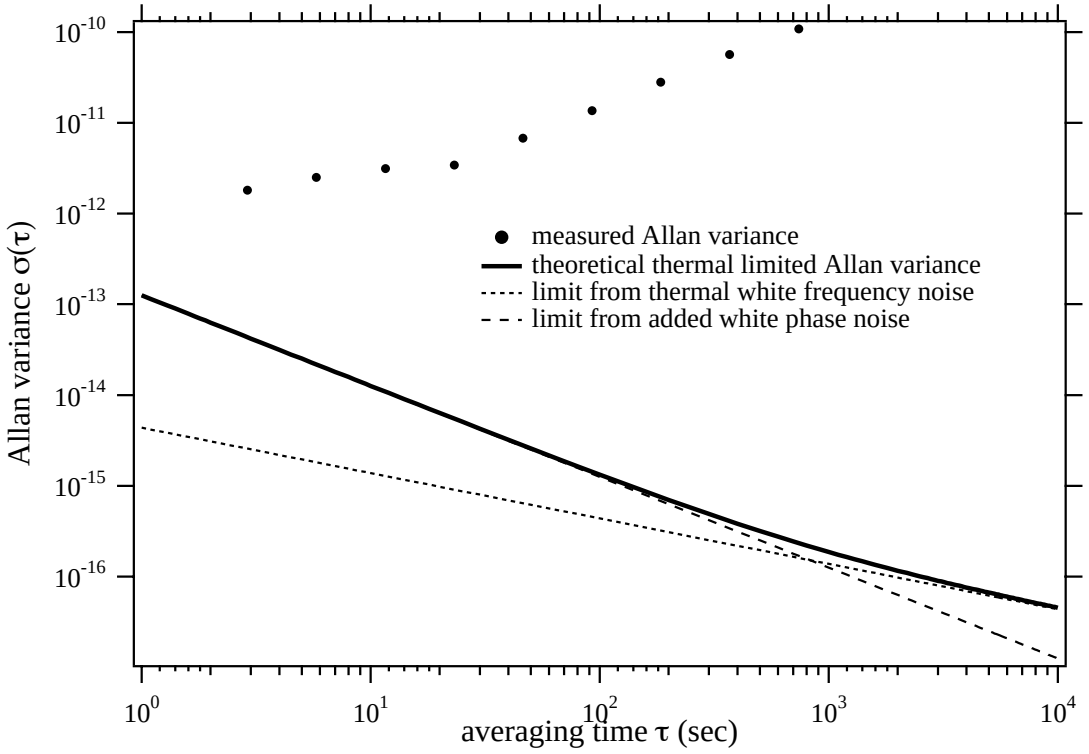

Figure 5.18: Measured CHM Allan variance (markers) and theoretical Allan variance limited only by thermal noise (lines). The thermal limit was calculated for the actual CHM line-Q (3×10^9) and maser power (2×10^{-14} W). The data were taken with the maser temperature controlled at 511 mK and the unsaturated superfluid ^{4}He film setting of 0.2 sccm. The maser frequency dependence on temperature was measured to be about 35 mHz/mK. The short-term (less than 10 s) Allan variance is therefore set by the residual 150 μK maser temperature fluctuations. For longer times, the maser stability is degraded due mainly to superfluid ^{4}He film thickness variation and slow drift of maser temperature and thermal gradients across the storage bulb.

was able to shift the maser cavity frequency, it also introduced a residual magnetization near the atomic storage region which decohered the atomic ensemble enough to quench maser oscillation. Therefore, this diode was removed.

Following this, attempts were made to couple an external diode in parallel with the transmission line outside of the cryostat. While biasing this diode had a small effect on the cavity resonance, the cavity shifting was small and reflections in the transmission line led to discrepancies between the apparent cavity frequency measured and the cavity frequency sensed by the atoms. For this reason, external diode tuning was not pursued further.

As a result, microwave cavity tuning of the CHM was restricted to the mechanical tuning plunger. The plunger could be thread into and out of the cavity by a wingnut connected to a small gear mounted on axis with the cavity. Movement of this gear was achieved with a Delrin[29] chain connected to a second gear mounted below the liquid nitrogen jacket. Movement of this gear was accomplished by turning a knob mounted on the top of the cryostat. The cavity could be tuned about 15 kHz per turn of this external knob over a total range of about 1 MHz.

Tuning by this mechanism had several drawbacks. First, the mechanical tuner was designed for coarse tuning of the microwave cavity. Therefore, resettable cavity tuning with any precision was not possible. Second, slack in the Delrin chain between the outer and inner gear led to hysteresis in the tuning. After moving the plunger in one direction, about two turns of the outer knob were needed to engage movement of the plunger in the opposite direction.

The third and most serious drawback arose from the fact that the Delrin chain was in thermal contact with the 77 K shield at one side and in thermal contact with the 0.5 K maser at the other. Therefore, a significant thermal gradient was established across the chain and any movement of the chain brought Delrin at an elevated temperature into thermal contact with the maser, thus warming the maser. This warming was significant, with one turn of the external knob (15 kHz shift in the cavity) warming the maser by tens

[29]Delrin is a trademark of E.I. duPont de Nemours and Co., Inc.

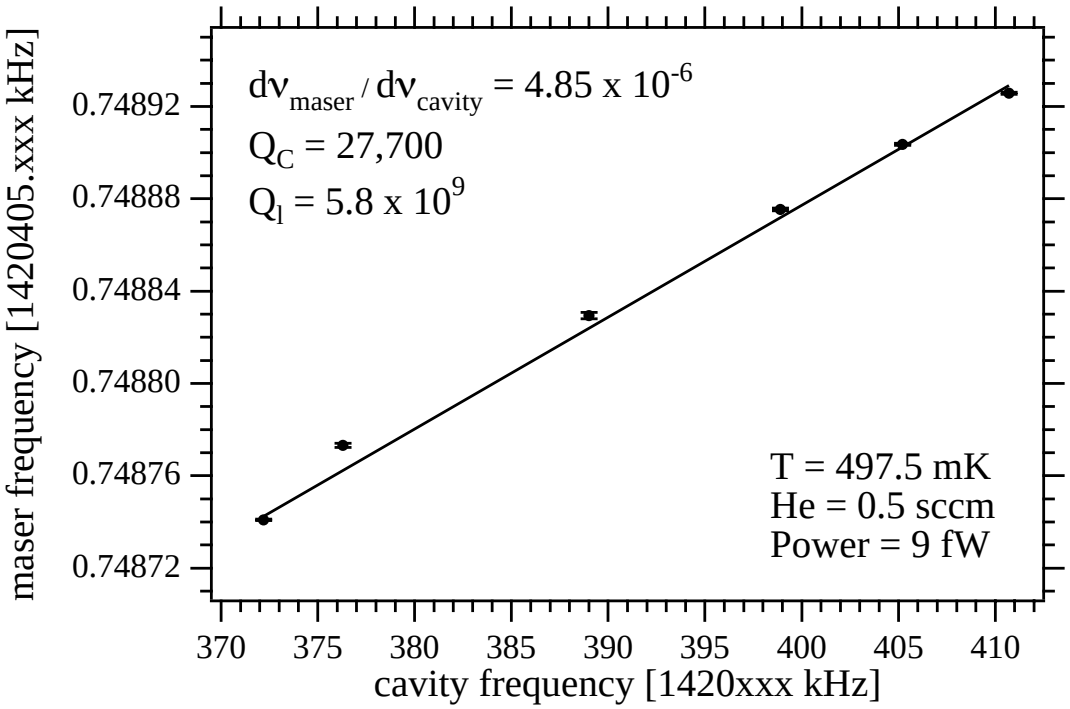

Figure 5.19: Typical line-Q measurement using the mechanical tuning plunger for maser cavity tuning.

of mK. Once warm, the maser required tens of minutes to recool. For a small amount of tuning, this heating could be compensated for by a reduction in the electronic heat supplied for maser temperature control (for a high enough setpoint), However, tuning over a range sufficient to measure the line-Q required tens of minutes of waiting for the maser to recool between cavity settings, during which time the frequency could drift and thereby compromise the measurement.

A typical line-Q measurement using the mechanical tuner is shown in Figure 5.19. Here, the cavity was tuned to one end of the tuning range and the maser frequency was measured. The maser cavity was then tuned to the second point, the temperature allowed to recool (up to fifteen minutes equilibration time), and the maser frequency was measured. This process was repeated for all six data points. As described in Chapter 2, a plot of maser frequency vs cavity frequency should be linear with a slope given by the

ratio of cavity-Q to atomic line-Q: $d\nu_{maser}/d\nu_{cavity} = Q_C/Q_l$. The error bars in this plot characterize the statistical uncertainty in the maser frequency at each cavity point. The fact that the linear fit to the data misses the error bars for these points is indicative of a systematic error, in this case maser frequency drift during the time between maser frequency measurements at each cavity frequency setting. In Chapter 6 we will discuss the need to make accurate line-Q measurements in order to investigate spin-exchange effects with the CHM.

We note that in general the line-Qs we measured with the CHM were up to a factor of 10 less than expected (expected $Q_l \approx 10^{10}$). We have evidence that this is chiefly due to the increased wall relaxation rate caused by running with unsaturated superfluid films: With an (unsaturated) superfluid film flow of 0.5 sccm, we found $Q_l \approx 5{\times}10^9$, while at 0.2 sccm, this dropped further to $Q_l \approx 1{\times}10^9$.

An additional difficulty with the maser tuning was a thermal-cycle-induced shift of the cavity tuning range. It had been observed that once the CHM was fully assembled, a thermal cycle to room temperature and then back to 0.5 K would lead to a negative shift in the mechanical tuning range relative to the atomic hyperfine frequency. We speculate that this shift can be attributed to a thermal-contraction-induced loosening of the screws which seal the copper pot that contains and compresses the maser cavity. Such a loosening would reduce the compression, physically enlarging the cavity and leading to a net downward shift of the tuning range.

Following the room temperature warm-up preceding the final few months of CHM work, the mechanical tuning range of the maser cavity was shifted below the atomic hyperfine frequency; the highest cavity frequency achievable was about 1420.38 MHz (or about 25 kHz below atomic resonance). The tuning range shift was discovered once the maser was at 0.5 K, and since a warm up, disassembly, and recool would have taken about one month, the decision was made to continue work with the maser slightly detuned from resonance. The ramifications of this limitation will be discussed more in Chapter 6.

Chapter 6

Spin-exchange in hydrogen masers

The earliest treatments of spin-exchange in hydrogen-hydrogen collisions were an effort to understand the interaction and equilibration of interstellar atomic hydrogen [71–73]. Today, spin-exchange collisions are seen to have direct consequences in conventional [19, 30,31] and cryogenic [29] hydrogen masers, and more generally, in all forms of cold atomic clocks.

An electron spin-exchange collision involves the exchange interaction between electrons in the colliding atoms, the same interaction which stabilizes the hydrogen molecule. Therefore, a spin-exchange collision between hydrogen atoms can be treated as the short term creation of a hydrogen molecule. The molecular interaction potential depends on whether the electrons' spins are aligned or anti-aligned, forming a triplet $^3\Sigma_u^+$ or singlet $^1\Sigma_g^+$ potential, respectively. The triplet and singlet potentials $E_T(R)$ and $E_S(R)$ are plotted as functions of the internuclear separation R in Figure 6.1 [93]. However, since the $m_F = 0$ hyperfine states in hydrogen can be admixtures of electron spin up and down, spin-exchange collisions can cause changes in level populations and decoherence of the hyperfine transition (characterized by a spin-exchange relaxation cross section σ) as well as shifts in the hyperfine transition frequency (characterized by a spin-exhange shift cross section λ). Therefore, a proper treatment of spin-exchange in hydrogen-hydrogen collisions is required for a complete understanding of the hydrogen maser.

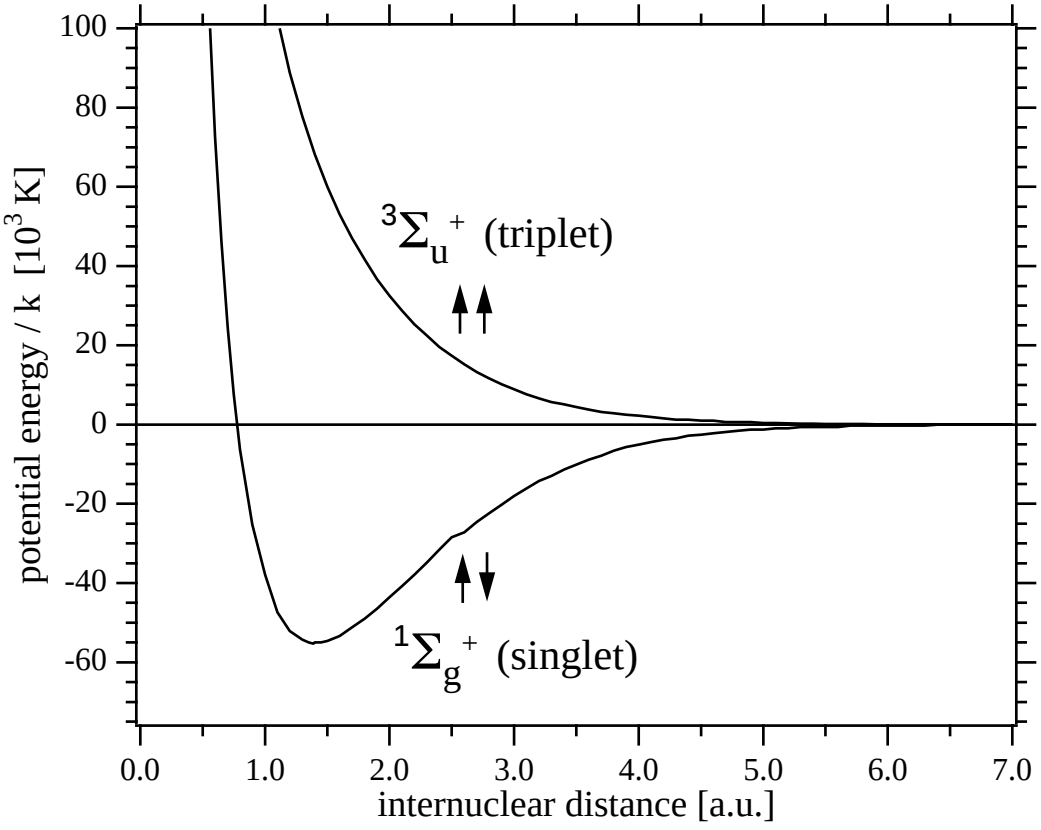

Figure 6.1: Potential energy curves for the triplet ${}^3\Sigma_u^+$ and singlet ${}^1\Sigma_g^+$ states of the hydrogen molecule, taken from reference [93].

Early investigations of spin-exchange effects in hydrogen-hydrogen collisions used the approximation that the small hyperfine energy splittings could be neglected relative to the interaction potentials and collision energies [17,68,71–75,77,94,95]. In Section 6.1, we review this approximation, known as the degenerate internal states (DIS) approximation, which accurately describes spin-exchange effects in room temperature hydrogen masers. In Section 6.2, we review the first attempt to include the hyperfine interaction which did so perturbatively using a semi-classical description [76]. This work led to the prediction of a new, hyperfine-induced maser frequency shift which was confirmed experimentally using a room temperature hydrogen maser. In Section 6.3 we consider the first fully quantum mechanical treatment of hydrogen-hydrogen spin-exchange collisions [19,29–31]. This treatment also predicts a number of small, hyperfine-induced (h-i) effects which may become important in the operation of the cryogenic hydrogen maser and other cold atomic clocks. In Section 6.4 we review previous experimental investigations of h-i effects in hydrogen masers, and note the significant discrepancies that persist between experiment and theory. In Section 6.5 we discuss the investigation of low temperature spin-exchange collisions using the SAO CHM.

6.1 Degenerate internal states approximation

All of the early work on spin-exchange in hydrogen-hydrogen collisions neglected the small hyperfine energy splitting (≈ 0.07 K) relative to the colliding atoms thermal energy and the depth of the molecular potential ($\approx 50{,}000$ K). The first results using this so-called degenerate internal states (DIS) approximation calculated spin-exchange induced variations in the population of the hyperfine states [71], the spin-exchange broadening cross sections [72, 73], the hyperfine frequency shift [72], and changes in the atomic hydrogen density matrix [74] due to spin-exchange collisions.

The first attempt to use DIS theory to calculate the effects of spin-exchange collisions in a hydrogen maser was made by Bender in 1963 [68]. His analysis proceeded similarly

to our hydrogen maser analysis of Chapter 2 in that the steady state density matrix for the hydrogen ensemble is found by solving a Bloch equation that included the effects of the microwave cavity field, atom flow into and out of the bulb, and spin-exchange (using a more sophisticated treatment than given in Chapter 2). All other forms of relaxation were neglected, as well as the interaction of the atomic ensemble with the microwave cavity.

The first step of Bender's treatment was to determine the effect of spin-exchange collisions on the hydrogen ensemble density matrix. The basic idea was to assume that as two atoms approach one another, their 4×4 single atom density matrices (in the $|F, m_F\rangle$ basis) can be written via a direct product as a single, 16×16 collision matrix. The collision matrix is then rotated from the $|F_1, m_{F_1}; F_2, m_{F_2}\rangle$ basis into the $|S, m_S; I, m_I\rangle$ basis. Those elements of the density matrix with $S = 1$ evolve under the molecular triplet potential $E_T(R)$, while those with $S = 0$ evolve under the singlet potential $E_S(R)$. The time dependence enters through the relative motion of the atoms and therefore the time-variation of the internuclear separation R. A classical collision trajectory was assumed, and as the collision proceeds the triplet and singlet parts of the combined wavefunction acquire different phases $\Delta_{T,S}$, given by

$$\Delta_{T,S} = \frac{1}{\hbar} \int E_{T,S}(R) dt. \tag{6.1}$$

The differential phase shift $(\Delta_T - \Delta_S)$ was then averaged over the impact parameter of the collision and the thermal velocity distribution. The post-collision density matrix was rotated back to the $|F_1, m_{F_1}; F_2, m_{F_2}\rangle$ basis, and by taking the trace of the final 16×16 collision density matrix over the second atom's quantum numbers, the final form of the 4×4 single atom density matrix, post-spin-exchange-collision, was found. This was then used to characterize the relaxation due to spin-exchange in the Bloch equation. Finally, by solving the Bloch equation, the effect on the hydrogen hyperfine transition was found. This treatment predicted a hyperfine frequency shift proportional to the spin-exchange collision contribution to the atomic linewidth. Since this contribution is essentially the

spin-exchange collision rate, which depends on the atomic density, Bender's calculation predicted that spin-exchange collisions could limit the frequency stability of hydrogen masers, where density fluctuations are difficult to control.

In 1967, Crampton [17] extended the work of Bender to include the effects of power broadening and cavity pulling, along with spin-exchange, in the hydrogen maser. In his analysis, Crampton discovered that the hydrogen maser frequency ω was shifted away from the density-independent hyperfine frequency ω_{24} by an amount given by

$$\omega = \omega_{24} + (\Delta + \alpha\lambda)\,\gamma_2 \tag{6.2}$$

where λ is the spin-exchange frequency shift cross section,[1] γ_2 is the total line broadening, and Δ is a measure of cavity detuning given by

$$\Delta = Q_C \left(\frac{\omega_C}{\omega_{24}} - \frac{\omega_{24}}{\omega_C}\right) \approx 2Q_C \left(\frac{\omega_C - \omega_{24}}{\omega_{24}}\right) \tag{6.3}$$

with Q_C and ω_C the cavity-Q and cavity frequency, respectively. Crampton also introduced a system constant

$$\alpha = \frac{\hbar V_C \bar{v}_r}{\mu_0 \mu_B^2 \eta Q_C V_b} \tag{6.4}$$

where V_C and V_b are the cavity and bulb volumes, $\bar{v}_r$ is the average relative atomic velocity, and η is the cavity filling factor, defined in Chapter 3. Crampton showed that the linewidth-dependent cavity pulling term could be used to compensate for the linewidth-dependent spin-exchange shift if the maser cavity was tuned such that $\Delta = -\alpha\lambda$. This is the "spin-exchange tuning" procedure that has turned out to be vital in reducing the effects of density variation on hydrogen maser stability (see Chapter 3). Crampton et al. later investigated these effects experimentally with a room temperature hydrogen maser [94] and found good agreement with the DIS theory.

Using the DIS approximation, Allison [75] calculated thermal-averaged spin-exchange

[1] We have redefined this parameter from Crampton's original notation to be $-\frac{1}{4}\lambda \rightarrow \lambda$ to agree with the notation introduced by VKSLC.

broadening and shift cross sections as a function of temperature from 1000 K to 10 K. A measurement of spin-exchange relaxation rates from 363 - 77 K was performed by Desaintfuscien and Audoin [95], and very good agreement with the DIS theory was found. The DIS approximation was then used by Berlinsky and Shizgal [77] to extend the calculations of Allison down to 0.25 K. Because of the technical complications of operating a hydrogen maser at such low temperature, no immediate experimental results were achieved to compare to DIS theory at low temperature where, as the kinetic energy of the colliding atoms is lowered, the DIS approximation becomes increasingly less reliable.

6.2 Semi-classical hyperfine interaction effects

In 1975, Crampton and Wang [76] made the first attempt to move beyond the DIS approximation and account for the hyperfine interaction during spin-exchange collisions. Their treatment used first-order perturbation theory in a semi-classical picture. They took as the unperturbed Hamiltonian the DIS Hamiltonian, given by

$$H(t) = E_T(t)\hat{P}_T + E_S(t)\hat{P}_S \tag{6.5}$$

where $\hat{P}_T$ and $\hat{P}_S$ are matrix operators that project out the triplet and singlet parts of the wavefunction, and $E_T(t)$ and $E_S(t)$ are the corresponding interaction potentials. Again, the time dependence enters through the varying internuclear separation during the collision. To the unperturbed Hamiltonian, they added a perturbation V_{hf} which included the intra-atomic hyperfine interaction to first order:

$$V_{hf} = \hbar\omega_{24}\left(\hat{\mathbf{I}}_\mathbf{1}\cdot\hat{\mathbf{S}}_\mathbf{1} + \hat{\mathbf{I}}_\mathbf{2}\cdot\hat{\mathbf{S}}_\mathbf{2}\right) \tag{6.6}$$

where $\hat{\mathbf{I}}_{\mathbf{1,2}}$ and $\hat{\mathbf{S}}_{\mathbf{1,2}}$ are the nuclear and electron spins of the colliding atoms and ω_{24} is the density-independent hyperfine frequency. In general, this frequency includes a number of small, density-independent shifts, such as the wall shift, or the second-order Zeeman or

Doppler shifts. The procedure of Bender [68] was then followed to determine the effect of spin-exchange collisions, now including the hyperfine interaction semi-clasically to first order, on the hydrogen ensemble's density matrix and on the oscillation frequency of the hydrogen maser.

The result of this calculation predicted that the hydrogen maser frequency would be given by

$$\omega = \omega_{24} + (\Delta + \alpha\lambda')\,\gamma_2 + \epsilon_H \gamma_H. \tag{6.7}$$

It can be seen that in addition to the cavity pulling and DIS spin-exchange shift (both proportional to the total broadening γ_2), there is also a semi-classical, hyperfine-induced maser frequency shift, characterized by ϵ_H and proportional to the spin-exchange collision rate $\gamma_H = n\sigma\bar{v}_r$, where σ is the spin-exchange broadening cross section. Also, the inclusion of the hyperfine interaction leads to a modification of the spin-exchange shift cross section:[2] $\lambda' = \lambda + 2\sigma\epsilon_H$. The semi-classical shift parameter is given by $\epsilon_H = -\omega_{24}T_D/4$, where T_D is the average duration a spin-exchange collision.

The interpretation provided for this new shift [76] was that during a hydrogen-hydrogen spin-exchange collision, the hyperfine interaction is "interrupted" for a time T_D, and this interruption leads to a negative shift in the hyperfine frequency by an amount proportional to T_D and to the spin-exchange collision rate γ_H. Crampton and Wang measured the semi-classical hyperfine-induced shift parameter ϵ_H in a room temperature hydrogen maser and found good agreement with the theory [76].

We note that the hyperfine-induced shift is proportional to that component of the broadening due solely to spin-exchange collisions γ_H, and not proportional to the full broadening γ_2. Therefore, if the canonical spin-exchange tuning technique is applied, where the maser cavity is tuned so that there is no variation in maser frequency ω with spin-exchange collision rate γ_H (i.e., the cavity detuning is set at $\Delta = -\alpha\lambda' + \epsilon_H$), then the maser oscillation frequency will no longer be density-dependent. Instead, there will be

[2] We have redefined this parameter from Crampton's original notation to be $-\frac{1}{4}\lambda \rightarrow \lambda$ to agree with the notation introduced by VKSLC.

a residual density-independent maser frequency shift of $-\gamma_0\epsilon_H$, where γ_0 is the density-independent portion of the total broadening. In this formalism, however, the residual frequency shift does not appreciably degrade the stability of a hydrogen maser operating at room temperature since γ_0 and ϵ_H are sufficiently stable in practice. By tuning the maser in this manner, Crampton and Wang were able to measure the semi-classical hyperfine-induced frequency shift. They found that $\epsilon_H = 4.04(0.35)\times10^{-4}$ at $T = 308$ K, in reasonable agreement with their calculation [76].

6.3 Quantum mechanical hyperfine interaction effects

A full, quantum mechanical treatment of hydrogen-hydrogen spin-exchange collisions and an analysis of their effect on the hydrogen maser was completed by Verhaar et al. (VKSLC) in 1987 [30, 31]. The starting point for their analysis was the Bloch equation describing the interaction of the atoms in the presence of the maser field:

$$\frac{d\rho_{\kappa\kappa'}}{dt} = -\frac{i}{\hbar}\left(E_\kappa - E_{\kappa'}\right)\rho_{\kappa\kappa'} - \frac{i}{\hbar}\left[H_1(t),\rho\right]_{\kappa,\kappa'} + \left(\frac{d\rho_{\kappa\kappa'}}{dt}\right)_{se} + \left(\frac{d\rho_{\kappa\kappa'}}{dt}\right)_{relax} \tag{6.8}$$

where $H_1(t)$ represents the maser cavity field. Assuming conventional hydrogen maser operation, the only coherence lies between the $|2\rangle$ and $|4\rangle$ hyperfine levels, so the spin-exchange relaxation term includes only off-diagonal matrix elements having the form

$$\left(\frac{d\rho_{24}}{dt}\right)_{se} = n\rho_{24}\sum_\nu \tilde{G}_\nu\rho_{\nu\nu} \tag{6.9}$$

where n is the hydrogen density and ν corresponds to a hyperfine state. Taking into account the rotational symmetry of a hydrogen-hydrogen collision, VKSLC showed that the coefficients of Eqn. 6.9 were given by $\tilde{G}_\nu = \langle v\Lambda_\nu\rangle = \bar{v}_r\bar{\Lambda}_\nu$ ($\bar{v}_r$ is the relative atomic velocity, and the brackets and overbars denote thermal averaging). The cross sections Λ_ν are written in terms of a sum of S-matrix elements [30] which follow from the same

potential used in previous DIS analyses

$$V = \hat{P}_T E_T(R) + \hat{P}_S E_S(R) + \hbar\omega_{24}\left(\hat{\mathbf{I}}_\mathbf{1}\cdot\hat{\mathbf{S}}_\mathbf{1} + \hat{\mathbf{I}}_\mathbf{2}\cdot\hat{\mathbf{S}}_\mathbf{2}\right) \tag{6.10}$$

in which $\hat{P}_T$ and $\hat{P}_S$ are the triplet and singlet projection operators, $E_T(R)$ and $E_S(R)$ are the triplet and singlet molecular potentials, ω_{24} is the density-independent atomic hyperfine frequency, and $\hat{\mathbf{I}}_{\mathbf{1,2}}$ and $\hat{\mathbf{S}}_{\mathbf{1,2}}$ are the nuclear and electron spins of the colliding atoms.

By substituting into Eqn. 6.9 a solution of the form

$$\rho_{42}(t) = \rho_{42}(0)\exp\left[i(\omega_{24} + \delta\omega + i\gamma_2)t\right], \tag{6.11}$$

they found that the hyperfine transition frequency would be shifted from the density-independent hyperfine frequency by

$$\delta\omega = \left[\bar{\lambda}_0(\rho_{22} - \rho_{44}) + \bar{\lambda}_1(\rho_{22} + \rho_{44}) + \bar{\lambda}_2\right]\bar{v}_r n \tag{6.12}$$

where the overbar indicates a thermal average. The spin-exchange shift cross sections are given by

$$\begin{aligned}
\lambda_0 &= Im\left[(\Lambda_2 - \Lambda_4)/2\right] \\
\lambda_1 &= Im\left[(\Lambda_2 + \Lambda_4)/2 - \Lambda_3\right] \\
\lambda_2 &= Im[\Lambda_3],
\end{aligned} \tag{6.13}$$

and we note that $\Lambda_3 = \Lambda_1$ due to symmetry considerations. The collision-induced broadening would be given by

$$\gamma_H = \left[\bar{\sigma}_0(\rho_{22} - \rho_{44}) + \bar{\sigma}_1(\rho_{22} + \rho_{44}) + \bar{\sigma}_2\right]\bar{v}_r n, \tag{6.14}$$

where the spin-exchange broadening cross sections σ_i are given analogously from Eqn. 6.13

in terms of the real parts of the Λ_νs. From equations 6.12 and 6.14 we now see the significance of a quantum mechanical treatment of h-i effects: the hyperfine transition frequency shift and broadening depend on the steady state populations of individual hyperfine states.

VKSLC [31] calculated thermally averaged spin-exchange shift and broadening cross sections over a temperature range of 10^{-3} K < T < 10^3. The cross sections are found to be complicated functions of temperature, as shown in Figure 6.2. Following Hayden et al. [29], we display in Table 6.1 the values of $\bar{\lambda}_i \bar{v}_r$ and $\bar{\sigma}_i \bar{v}_r$ at the (approximate) operating temperatures of our room temperature and cryogenic hydrogen masers.

Parameter	$T = 300$ K [cm^3/s]	$T = 0.5$ K [cm^3/s]
$\bar{\lambda}_0 \bar{v}_r$	-3.2×10^{-11}	-1.72×10^{-11}
$\bar{\lambda}_1 \bar{v}_r$	$+1.3\times10^{-13}$	-2.57×10^{-14}
$\bar{\lambda}_2 \bar{v}_r$	-2.4×10^{-13}	-1.67×10^{-14}
$\bar{\sigma}_0 \bar{v}_r$	-9.2×10^{-14}	$+5.93\times10^{-14}$
$\bar{\sigma}_1 \bar{v}_r$	-2.1×10^{-11}	$+7.59\times10^{-13}$
$\bar{\sigma}_2 \bar{v}_r$	$+4.3\times10^{-10}$	$+1.08\times10^{-15}$

Table 6.1: Calculated values [30, 31] of the spin exchange shift and broadening cross sections, near the operating temperatures of room temperature and cryogenic hydrogen masers, from [29].

Including the radiation and relaxation terms of the Bloch equation (Eqn. 6.8), the oscillation frequency of the hydrogen maser can be found. VKSLC predicted that this frequency will be shifted directly by the hyperfine transition frequency shift (Eqn. 6.12) and indirectly by the broadening (Eqn. 6.14, via the cavity pulling term). The predicted net maser shift was given by

$$\omega = \omega_{24} + \left[\Delta + \alpha \bar{\lambda}_0\right] \gamma_2 - \Omega \gamma_H \tag{6.15}$$

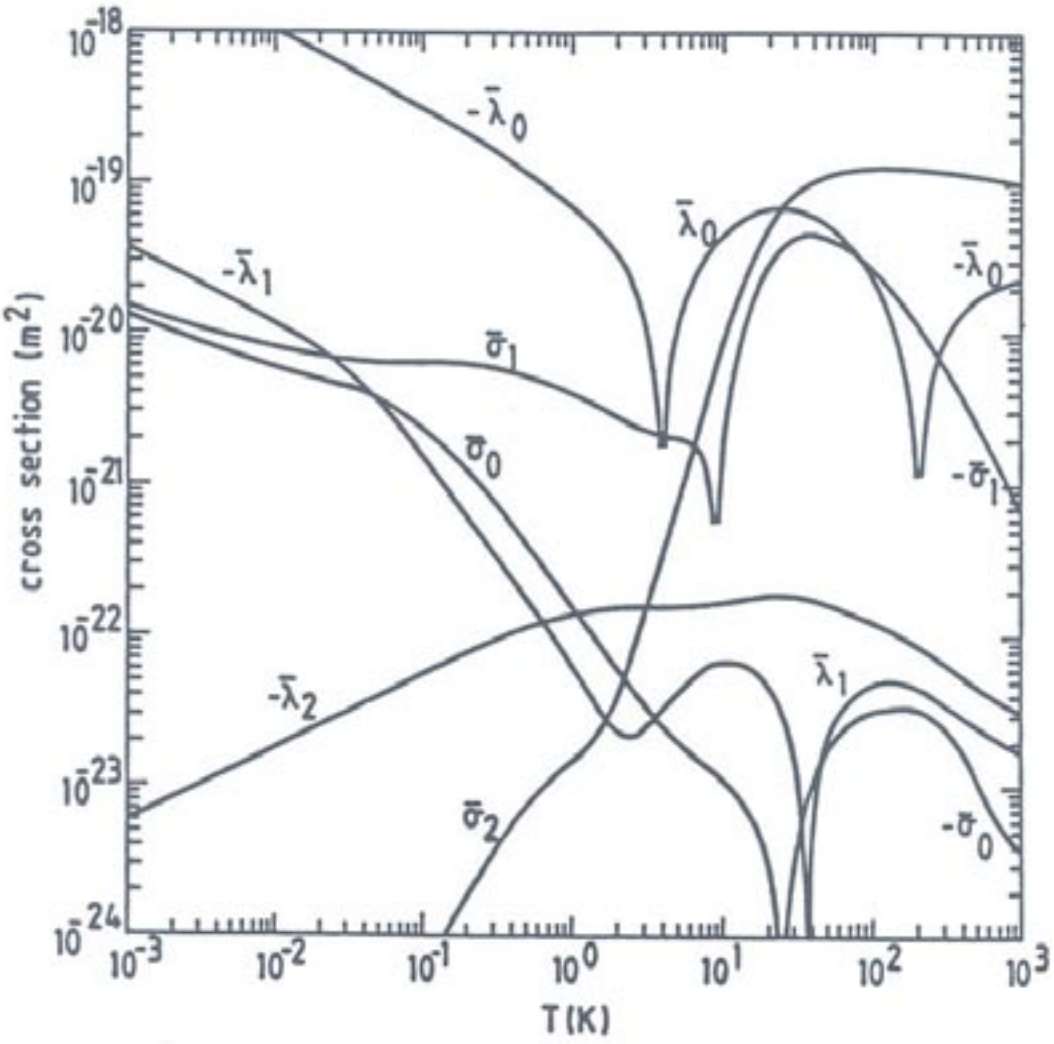

Figure 6.2: Thermally averaged spin-exchange shift and broadening cross sections [31].

with the hyperfine-induced (h-i) frequency shift parameter given by[3]

$$\Omega = -\frac{\bar{\lambda}_1(\rho_{22}+\rho_{44})+\bar{\lambda}_2}{\bar{\sigma}_0(\rho_{22}-\rho_{44})+\bar{\sigma}_1(\rho_{22}+\rho_{44})+\bar{\sigma}_2}. \tag{6.16}$$

We note that due to the thermal dependencies of the λ_i and σ_i, the frequency shift parameters $\alpha\bar{\lambda}_0$ and Ω will themselves be functions of temperature, as shown in Figure 6.3 [31]. Here we also show the shift in Ω when the hyperfine level populations change from $\rho_{22}-\rho_{44}=1.0$ to $\rho_{22}-\rho_{44}=0.5$.

Under the DIS approximation, Ω is identically zero, therefore the DIS spin-exchange tuning procedure [17] can be applied and the maser oscillation frequency will be independent of hydrogen density for $\Delta = -\alpha\bar{\lambda}_0$. In the presence of the hyperfine-induced shift, if the cavity is detuned following the procedure of Crampton and Wang [76], so that the maser oscillation frequency is independent of the spin-exchange collision rate ($\Delta = -\alpha\bar{\lambda}_0+\Omega$), the maser frequency will then be shifted by an amount $-\Omega\gamma_0$. However, since Ω depends explicitly on the populations of the $|2\rangle$ and $|4\rangle$ hyperfine states, which are generally functions of hydrogen density, the maser oscillation frequency remains dependent on hydrogen density. Thus, there is no cavity detuning where maser oscillation frequency is independent of hydrogen density.

At room temperature, the hyperfine-induced shift is small ($\Omega \approx 2\times10^{-4}$ for $\rho_{22}+\rho_{44}=0.5$) [31]. To maintain maser frequency stability at the typical room temperature limit of 1 part in 10^{15}, the linewidth not due to collisions must be kept stable at the reasonable level of $\delta\gamma_0 \approx 0.05$ rad/s. Therefore, h-i effects do not limit the performance of a room temperature maser. In a cryogenic maser, however, h-i effects can no longer be neglected since the hyperfine interaction energy is no longer small compared to the kinetic energy of the colliding atoms. It is expected that Ω will increase by more than two orders of magnitude from room temperature to 0.5 K [31]. VKSLC predict that in order to achieve

[3]Since the population difference $\rho_{22}-\rho_{44}$ is much smaller in a hydrogen maser than the population sum $\rho_{22}+\rho_{44}$, the broadening term in Eqn. 6.14 proportional to $\rho_{22}-\rho_{44}$ is often neglected relative to the other two terms [30].

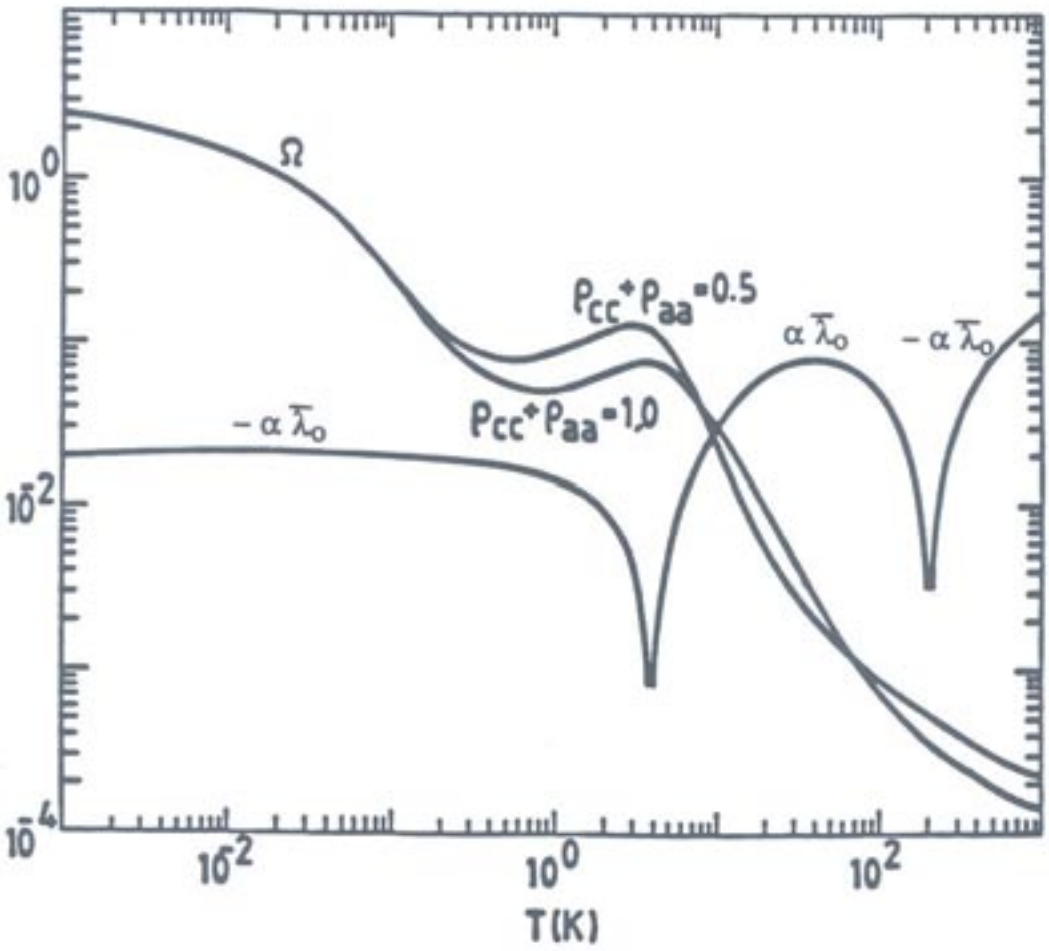

Figure 6.3: Dimensionless frequency shift parameters $\alpha\bar{\lambda}_0$ (for a typical room temperature maser system constant α) and Ω as functions of temperature. (Figure adapted from reference [31].)

the predicted CHM fractional frequency stability limit of 2×10^{-18}, the maximum allowed instability in the linewidth not due to collisions would be $\delta\gamma_0 \approx 10^{-7}$ rad/s, a stability unlikely to be achieved in practice [31]. Therefore, hyperfine-induced effects in a cryogenic hydrogen maser may significantly reduce the expected improvement in cryogenic hydrogen maser stability.

6.4 Prior measurements

The hyperfine-induced hydrogen maser frequency shift predicted by VKSLC [30, 31] has been investigated with a room temperature hydrogen maser [19] and with a cryogenic hydrogen maser [29]. In both cases, a hyperfine-induced maser shift frequency was observed, however there are disagreements both in magnitude and sign with the theoretical calculations. These disagreements induced further theoretical investigations [96, 97], but to date the discrepancies between experiment and theory have not been explained.

The room temperature experiment was carried out by our group using a room temperature SAO hydrogen maser (maser P-27). In this study, the maser frequency shift's dependence on hyperfine level population was exploited to detect hyperfine-induced effects. The hydrogen maser was equipped with an adiabatic fast passage (AFP) state selector. This device allowed for a switch in the composition of the input beam from approximately half the atoms in each of states $|1\rangle$ and $|2\rangle$ (the AFP "off" configuration), to an input beam of pure state $|2\rangle$ atoms (the AFP "on" configuration). Because of the dependence of Ω on $(\rho_{22}+\rho_{44})$, VKSLC predicted a measurable difference of the hyperfine-induced maser shift between the two configurations of $\Omega_{on}-\Omega_{off} = -0.76\times10^{-4}$ to -1.12×10^{-4} (for the range of masing state populations used in the experiment). However, the experimentally determined value was $\Omega_{on} - \Omega_{off} = +5.38(1.06)\times10^{-4}$ [19]. Equivalently, the theoretical prediction was $\bar{\lambda}_1 = 3.0\times10^{-19}$ cm^2, while the measured value was $\bar{\lambda}_1 = -1.8\times10^{-19}$. Although this result confirmed the dependence of the hyperfine-induced maser frequency shift on hyperfine level populations, it produced a glaring discrepancy between measurement

and theory in the sign of the effect. Walsworth et al. discussed in detail the possibility of experimental systematic error leading to the observed discrepancy [19]. In particular, they considered a density-dependent wall frequency shift, cavity frequency drift, second-order Zeeman shift, wall degradation, and magnetic-inhomogeneity shift. After analyzing each effect in turn, however, they eliminated them as sources of experimental error sufficient to cause the observed discrepancy.

Parameter	Temperature	Theory [30, 31]	Experiment
$\bar{\lambda}_1$	323 K	$+3.0\times10^{-19}$ cm^2	-1.8×10^{-18} cm^2 [19]
$\bar{\lambda}_0$	0.5 K	-1.19×10^{-15} cm^2	$(-2.17\pm0.28)\times10^{-11}$ cm^2 [29]
$\frac{1}{2}\bar{\lambda}_1+\bar{\lambda}_2$	0.5 K	-2.04×10^{-18} cm^2	$(+2.2^{+0.5}_{-1.0})\times10^{-18}$ cm^2 [29]
$\frac{1}{2}\bar{\sigma}_1+\bar{\sigma}_2$	0.5 K	$+26.3\times10^{-18}$ cm^2	$(+38.5\pm4)\times10^{-18}$ cm^2 [29]
Ω	0.5 K	$+0.078$	$-0.057^{+0.009}_{-0.021}$ [29]

Table 6.2: Theoretical values for the spin exchange shift and broadening cross sections compared with previous hydrogen maser experiments. The reported values for Ω assume $(\rho_{22}-\rho_{44})=1/2$.

The low temperature experiment was carried out by the group of Hardy et al. at the University of British Columbia (UBC) using their cryogenic hydrogen maser [10]. In this experiment, the maser oscillation frequency was measured as a function of maser cavity detuning and hydrogen density. From these data, a number of the hyperfine-induced spin exchange parameters could be inferred. These results are shown in Table 6.2. Here it can be seen that their experiment clearly reports a departure from the previous DIS theory in that hyperfine-induced effects were seen. However, once again there is considerable discrepancy between experiment and theory. For example, the UBC group reported a value for $\bar{\lambda}_0$ almost twice the theoretical value, while $\bar{\sigma}_1(\rho_{22}-\rho_{44})+\bar{\sigma}_2$ disagree in magnitude and $\bar{\lambda}_1(\rho_{22}-\rho_{44})+\bar{\lambda}_2$ disagree in sign (in their experiment, $(\rho_{22}-\rho_{44})=1/2$). The leading systematics reported by the UBC group include uncertainties in the determination of the absolute atomic hydrogen density, the absolute maser cavity tuning, and the relative maser cavity tuning. They conclude, however, that these systematics are not large enough to account for the discrepancies with theory.

A third experiment has been conducted which allows a test of VKSLC theory [98]. This experiment was also carried out by the UBC group, however it was not done with an oscillating hydrogen maser. Using pulsed NMR techniques in a gas of hydrogen atoms at 1.2 K, they measured the longitudinal broadening cross section for the hydrogen hyperfine transition to be $\sigma_{T_1} = +0.51(2)$ Å^2. The theoretical prediction from VKSLC was $\sigma_{T_1} = +0.37$ Å^2 [96]. This discrepancy is particularly significant because it compares parameters which are independent of the operation of a hydrogen maser.

These discrepancies between theory and experiment bring into question the accuracy of the theoretical calculations of VKSLC [96]. A possible source of error in these calculations would be the use of inaccurate interatomic potentials, however it has been reported that no reasonable variation of these potentials has been shown to be sufficient to account to the observed disagreement [29, 96]. Other possibilities are a breakdown of some of the theoretical assumptions, such as the neglect of spin-dipole interactions [96] or the way in which nonadiabatic corrections are treated. Finally, there remains the possible that there is some overlooked physics in the hydrogen maser which could mimic the hyperfine-induced frequency shift, although this would not explain the observed disagreement in the longitudinal relaxation measurement which was not carried out in a hydrogen maser. In sum, an important problem in atomic physics is reconciling experiment and theory for binary spin-exchange collisions for the simplest atom, hydrogen.

6.5 SAO CHM measurement

Because of the relative simplicity of low-energy hydrogen-hydrogen collisions, and because an understanding of spin-exchange between atomic species is critical for the understanding of all cold atomic clocks, there is a great impetus to resolve the current discrepancies between theory and experiment for hydrogen-hydrogen spin-exchange collisions. Therefore, it would be valuable to measure these spin-exchange parameters in a new cryogenic hydrogen maser system, which could have different systematic considerations than the UBC

CHM.

At the end of Chapter 5, we described a number of practical limitations to the performance of the SAO CHM, including the necessity of running with unsaturated superfluid ^{4}He films, the necessity of running at temperatures below the collisional shift minimum (and therefore in a regime dominated by H-^{4}He collisional wall shift), and the need to run with a relatively low range of maser powers. These factors combine to limit the frequency stability of the CHM, and place a limit on maser frequency stability at a level where only one of the low temperature hydrogen-hydrogen spin-exchange parameters is accessible for study, the semi-classical frequency shift cross section $\bar{\lambda}_0$. We describe here our measurement of this parameter and then compare it with its theoretical value [30,31] and previous experimental value [29].

6.5.1 Experimental procedure

Overview

We begin our discussion by considering the maser frequency shift due to the semi-classical frequency shift cross section $\bar{\lambda}_0$. Neglecting the other spin-exchange parameters in Eqn. 6.15, and including the quadratic cavity detuning term, we see that the maser frequency ω is shifted from the density-independent hyperfine frequency ω_{24} as

$$\omega = \omega_{24} + \left[\Delta + \alpha\bar{\lambda}_0(1+\Delta^2)\right]\gamma_2 \tag{6.17}$$

where Δ is the cavity detuning parameter given in Eqn. 6.3, α is the system constant given in Eqn. 6.4, and γ_2 includes all sources of maser line broadening.

The traditional spin-exchange tuning method, described in detail in Chapter 3, would conceptually be the most natural method with which to measure $\bar{\lambda}_0$. Here the maser frequency is measured as a function of cavity detuning at two different flux settings, and therefore two different γ_2 values. Interpolating for the cavity setting where the maser frequency is independent of flux, Δ_{tuned}, the spin-exchange parameter can be found using

the relation

$$\bar{\lambda}_0 = -\frac{\Delta_{tuned}}{\alpha(1+\Delta_{tuned}^2)}. \tag{6.18}$$

This method requires the ability to change the maser cavity setting without perturbing the system and relies on the ability to stably set two values of population inversion flux. As discussed at the end of Chapter 5, however, neither of these can be achieved without difficulty with the SAO CHM in its current realization.

Therefore, a second method was devised which utilizes one easily resettable CHM operating parameter. Instead of varying γ_2 by changing hydrogen density, we utilize the fact that a portion of γ_2 is set by broadening due to magnetic field inhomogeneities across the atomic storage bulb. Such magnetic field inhomogeneities could easily be established by changing the current in the trim coils of the maser's static field solenoid. A set of solenoid coil settings which produce varying magnetic field gradients but do not change the average magnetic field over the bulb will broaden the atomic line (increase γ_2) but will not shift the oscillation frequency (no second-order Zeeman shift in ω_{24}). Once the relative change in line broadening for each of the gradient settings is known, and the maser frequency shift per change in line broadening, $d\omega/d\gamma_2$, is measured, the spin-exchange parameter can be found from the relation

$$\bar{\lambda}_0 = \frac{d\omega/d\gamma_2 - \Delta}{\alpha(1+\Delta^2)}. \tag{6.19}$$

We applied this technique to measure $\bar{\lambda}_0$ at 0.5 K using the CHM. We note that this method was also employed using room temperature maser P-8, and the value of $\bar{\lambda}_0$ at 325 K was found to be in good agreement with the value determined using the spin-exchange tuning method and Eqn. 6.18.

Operating conditions

As described at the end of Chapter 5, the selection of a set of operating conditions (mainly superfluid film flow and temperature) involves a trade-off between maser frequency sta-

bility and maser power. Thinner superfluid films and lower temperatures provide more maser power, but lead to a reduction in maser frequency stability (due to the temperature dependence of the H-^{4}He collisional wall shift). For these reasons, an intermediate superfluid film flow setting near 0.5 sccm seemed a good compromise. However, since it was discovered that running at this superfluid film flow led to a significant reduction in CHM operating time (due to the finite storage capacity of the sorption pump), lower superfluid film flows were more suitable. For a majority of our investigation of spin-exchange effects, we chose to operate at a superfluid film setting of 0.2 sccm. We note that as a systematic check for sensitivity on superfluid film setting, one measurement of $\bar{\lambda}_0$ was made at an elevated superfluid film flow of 0.4 sccm. There was no apparent effect on our value of $\bar{\lambda}_0$ for varying the superfluid film flow over this range. While running with this flow, however, the single spin-exchange measurement was enough to exhaust the total running time of the CHM between 20 K warming cycles.

A plot of the CHM power and frequency dependence on temperature for a superfluid film setting of 0.2 sccm is given in Figure 6.4. These data were taken at the beginning of the run in which all the spin-exchange measurements were made. From Figure 6.4(a) it can be seen that for this superfluid film flow setting, the maser power was maximum at a temperature of about 500 mK. Therefore, all of our measurements were made within a temperature range of 495 to 505 mK. There was no apparent effect on our value of $\bar{\lambda}_0$ for varying the maser temperature over this range.

From Figure 6.4(b) it can be seen that near 500 mK, the (wall shift dominated) frequency dependence on temperature is approximately 35 mHz/mK. During this run, the maser frequency control we typically achieved was about 150 μK (rms), which would therefore lead to short-term maser frequency fluctuations of about 5 mHz. While this temperature and frequency stability were not as good as during previous runs, they were sufficient to resolve the spin-exchange effects under study. As we will describe in Section 6.5.2 the measurement error due to frequency stability was insignificant relative to the other sources of measurement error.

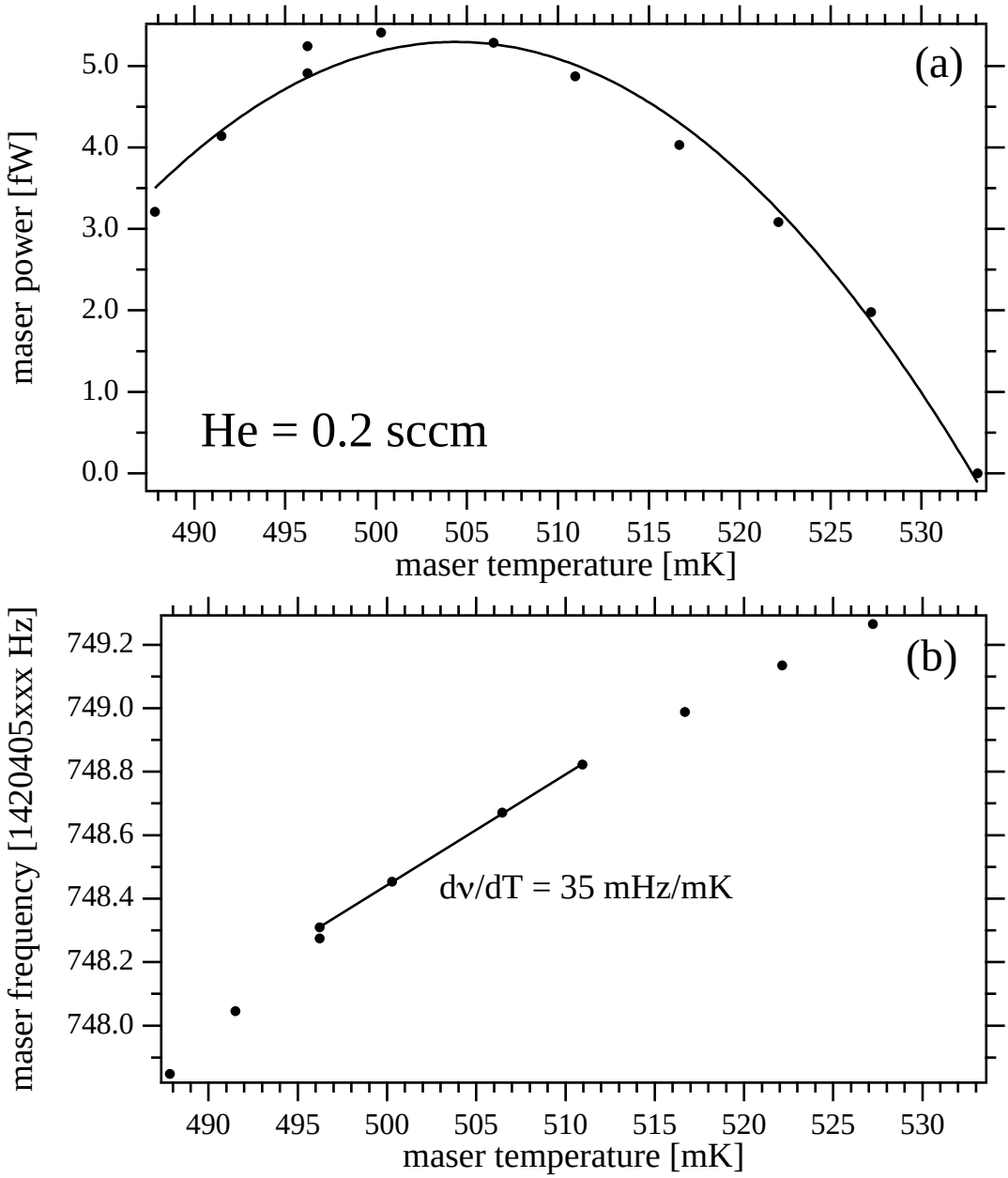

Figure 6.4: CHM power (a) and frequency (b) for a superfluid ^{4}He film setting 0.2 sccm.

Because the length of maser running time between 20 K warming cycles was also decreased as hydrogen flux was increased, the choice of hydrogen flux also involved a trade-off between running time and maser power. We have found that a molecular flux setting of 1.2 units (corresponding to an upstream pressure of 2.4 PSI) was sufficient to allow stable running of the discharge and ample maser power without significantly reducing the maser running time. We note that as a systematic check for sensitivity on molecular hydrogen flux setting, one measurement of $\bar{\lambda}_0$ was made at an elevated flux setting of 1.7 units (corresponding to an upstream pressure of 3.4 PSI). There was no apparent effect on our value of $\bar{\lambda}_0$ for varying the molecular flux over this range.

As described at the end of Chapter 5, the CHM suffered from a negative shift of the microwave cavity tuning range during thermal cycles to room temperature and back to 0.5 K. After the room temperature warm-up immediately preceding the run in which these spin-exchange measurements were made, the cavity tuning range was shifted low enough that the cavity could not be tuned to atomic resonance. The highest achievable cavity tuning was about 1420.38 MHz, about 25 kHz (one half the cavity linewidth) below atomic resonance. The cavity-Q was typically about 26,500, and all spin-exchange measurements were made with the cavity set between 1,420,381,792 and 1,420,378,996 Hz, resulting in a cavity tuning parameter Δ range of -0.891 to -0.998. There was no apparent effect on our value of $\bar{\lambda}_0$ for varying Δ over this range.

Selection of magnetic gradients

Our method of determining $\bar{\lambda}_0$ by measuring the maser frequency shift due to varying the magnetic-inhomogeneity-induced broadening required us to find a collection of solenoid field settings which vary γ_2 but do not shift the atomic hyperfine frequency ω_{24}. Equivalently, these settings would vary the magnetic field gradient across the bulb, but would not shift the ensemble-average magnetic field experienced by atoms in the bulb. To find these settings, we kept the lower trim coil setting fixed and varied the upper trim and main solenoid settings. The lower coil was left untouched since changing its current led to

large changes in overall maser power, implying that the lower coil helps to maintain the quantization axis for the atomic beam into the storage bulb.

Our gradient search was done by applying the double resonance techniques discussed in Chapter 2. By applying a oscillating transverse field with the CHM's Zeeman coils, and sweeping this field through the atoms $F = 1$, $\Delta m_F = \pm 1$ Zeeman frequency, the maser power was reduced as shown in Figure 6.5. A Lorentzian fit to these maser power data (with a linear background to account for maser power drift during the scan) was used to determine the Zeeman frequency and Zeeman linewidth.

Initially, a solenoid setting was found which produced the narrowest Zeeman linewidth. In a room temperature maser, this search is conducted by simply varying the current in the solenoid's trim coils while monitoring the Zeeman linewidth. Unfortunately, due to the presence of superconducting indium rings (used for cryogenic vacuum seals), this technique was considerably less effective because of the magnetic flux expulsion from the superconducting indium rings. Thus, shimming of the CHM solenoid involved a series of maser warmings above the 3.4 K critical temperature of indium, followed by recoolings to "freeze in" the magnetic flux for the new solenoid setting. An iterative approach was applied, where the solenoid settings were varied to find the narrowest line and then held there through a warming/cooling cycle. Once recooled, the settings were changed slightly to narrow the line, and then held through another warming/cooling cycle. Eventually a solenoid setting was found where the Zeeman linewidth was narrowest for the frozen-in setting, with no narrowing found by making small deviations from it. This setting produced a Zeeman frequency of 3360 Hz (corresponding to an average solenoid field of 2.4 mG) and a Zeeman width of approximately 30 Hz.

Once this minimum magnetic inhomogeneity setting was found, a set of four additional settings were found which increased γ_2 but did not shift ω_{24}. To find them, the current in the upper trim coil was reduced, thus increasing the gradient across the bulb, until a measurable reduction in the maser power was observed. This power reduction signified the increase in γ_2. Then, the current in the main solenoid coil was increased until the

measured $F = 1$, $\Delta m_F = \pm 1$ Zeeman frequency was restored to the original value.

The Zeeman resonances for the five solenoid settings used for the spin-exchange studies are shown in Figure 6.5(a). Here it can be seen that solenoid setting 1 produces the narrowest line and maximum maser power. The subsequent settings broaden the Zeeman line and reduce the maser power (increase γ_2), but produce only a small shift in the Zeeman frequency. A plot of maser power and fit Zeeman frequency vs gradient setting (Figure 6.5(b)) shows a uniform reduction in maser power as the magnetic gradient is increased, while the overall Zeeman frequency shift (away from the average value of 3360.5 Hz) is less than 10 Hz. For this average 2.4 mG main field, a shift of 10 Hz in the $F = 1$, $\Delta m_F = \pm 1$ Zeeman frequency would produce a second-order Zeeman shift in the hyperfine frequency $\omega_{24}/2\pi$ of less than 0.1 mHz, more than an order of magnitude below the typical spin-exchange shifts measured in this study. We note that the Zeeman frequencies for these gradients, and therefore the second-order Zeeman shift in the hyperfine frequency, were not changed significantly by a 20 K warming cycle.

Measurement of γ_2

To determine $\bar{\lambda}_0$ from the maser frequency shift caused by magnetic-inhomogeneity-induced line broadening, it is necessary to quantify the changes in γ_2 caused by the magnetic field gradients. In particular, the relative broadening, $\delta\gamma_2$ must be known as the field gradients are changed between settings.

At the highest achievable cavity frequency setting of around 1420.38 MHz, the maser power was reduced by about 10% from its maximum value for the cavity tuned to atomic resonance. Since we could then only shift the cavity frequency even further from resonance (thereby reducing further the maser power), our ability to measure γ_2 using the cavity pulling effect was severely compromised. Furthermore, mechanical cavity tuning involved the undesirable effect of warming the maser.

A considerably different method was therefore employed to determine the relative γ_2 values. Instead of making these measurements with the maser actively oscillating,

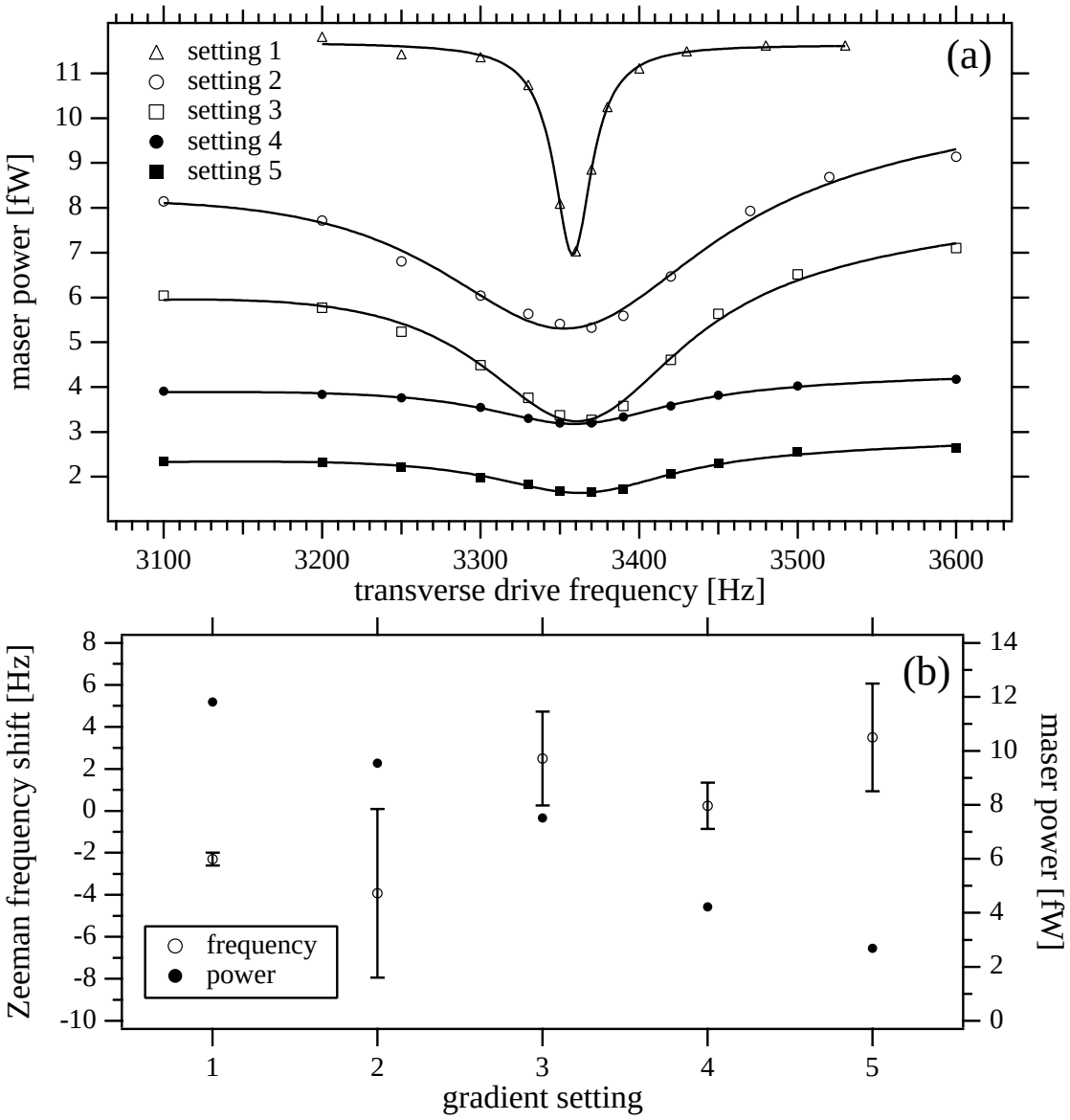

Figure 6.5: (a) Maser power reductions while sweeping a transverse oscillating field through the $F = 1$, $\Delta m_F = \pm 1$ Zeeman resonance for the five magnetic gradient settings used for our spin-exchange measurements. (b) Fit Zeeman frequency shift (open circles) away from the average value of 3360.5 Hz and unperturbed maser power (filled circles) for the five gradient settings. Among the five gradients, the Zeeman shift is maintained within a 10 Hz bound, which corresponds to a negligible 0.1 mHz second-order Zeeman shift in the the hyperfine frequency $\omega_{24}/2\pi$.

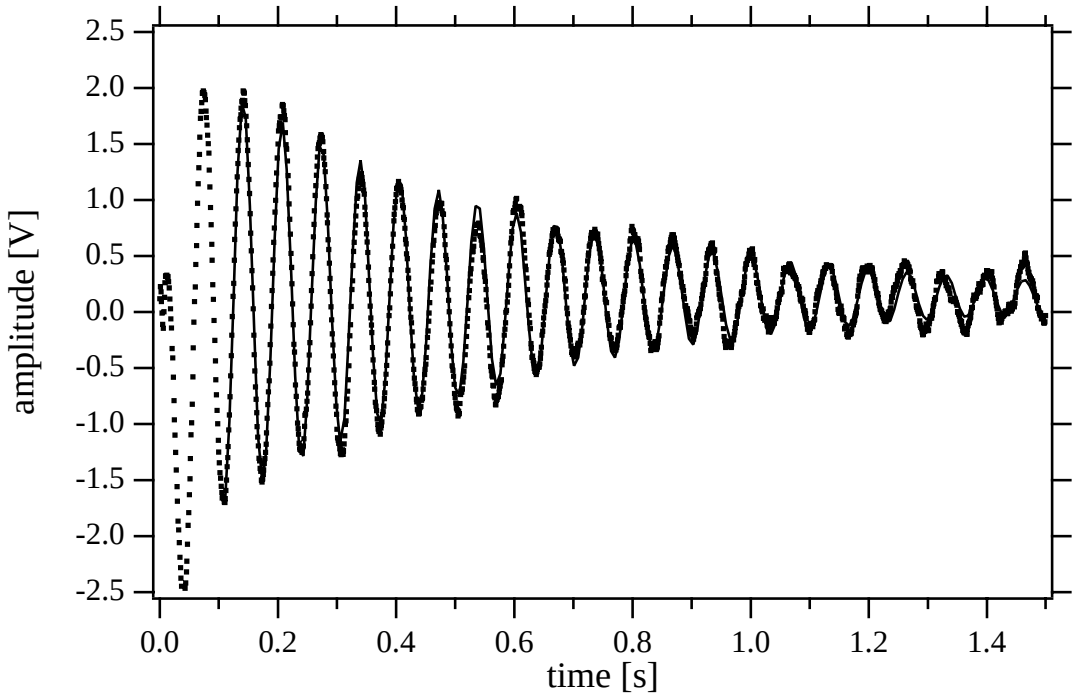

Figure 6.6: Atomic free induction decay signal (markers) and a damped sinusoidal fit (line). With the maser conditions set below oscillation threshold, a $\pi/2$ pulse of microwave radiation transfers atoms in the upper state $|2\rangle$ to the radiating superposition state $\frac{1}{\sqrt{2}}(|2\rangle + |4\rangle)$. This state rings down near the atomic hyperfine frequency with a decay time set by the decoherence rate γ_2.

oscillation was quenched and the relative γ_2 values were measured in pulsed mode. (This mode of operation is described more in Chapter 5). By injecting a pulse of radiation in through the cavity coupling loop (with amplitude and pulse width tailored to make a "$\pi/2$" pulse), the atoms in the upper hyperfine state $|2\rangle$ are transferred to the radiating superposition state $\frac{1}{\sqrt{2}}(|2\rangle + |4\rangle)$. If the conditions are such that radiation damping can be neglected, the radiating atoms then exhibit a free induction decay (FID) with a decay time set by the decoherence rate γ_2. By fitting an exponentially damped sinusoid to the FID amplitude (Figure 6.6) the broadening can be determined from the exponential decay time constant as $\gamma_2 = 1/\tau$.

There are several different methods with which maser oscillation can be quenched. The

maser could be warmed until the H-^{4}He vapor scattering reduces the population inversion flux. This method was not used, however, since we observed that the relative γ_2 values changed with maser temperature. Thus, our relative γ_2 measurements and spin-exchange measurements needed to be made at the same temperature. Maser quenching could also be achieved by reducing the population inversion flux directly by reducing hydrogen flow into the maser. This method was not employed out of concern that the change in the thermal load could lead also to local maser temperature changes. In addition, hydrogen flux was one systematic parameter under investigation, therefore the relative γ_2 measurements and spin-exchange measurements had to be made with the same hydrogen flux setting.

Instead, we chose to measure the relative γ_2 values after quenching the maser by detuning the cavity far away from resonance, such that the coupling between the cavity and the atomic ensemble is sufficiently reduced. This method ensured that the relative γ_2 values and the spin-exchange frequency shifts would be measured under the same operating conditions (temperature, hydrogen flux, and superfluid film flow). To ensure that the maser was sufficiently below oscillation that radiation damping could be neglected, the γ_2 measurements were made at a large enough detuning that their values were insensitive to further changes in cavity setting. Typically, the measurements were made with a cavity tuning parameter $\Delta < -2$, or about one full cavity width (50 kHz) below atomic resonance.

The pulser we used to generate the $\pi/2$ pulses did not allow us to phase lock the pulses to one another, so averaging in the time domain was not possible. Therefore, to improve our measurements we first applied a fast Fourier transform (FFT) to the time domain ringdowns and then averaged the FFTs from several pulses together. For the smallest magnetic gradient applied (setting 1), the decay time was approximately 0.5 s. We generated the FFTs from time domain traces 3 seconds in duration which produced frequency domain spectra with points spaced by 0.3 Hz (see Figure 6.7(a)). Typically, 10 frequency domain spectra were averaged together, and a Lorentzian fit was applied to the averaged spectra. The broadening γ_2 was then extracted as π times the full width at half maximum of the Lorentzian fit to the FFT power spectrum. The measured values of γ_2

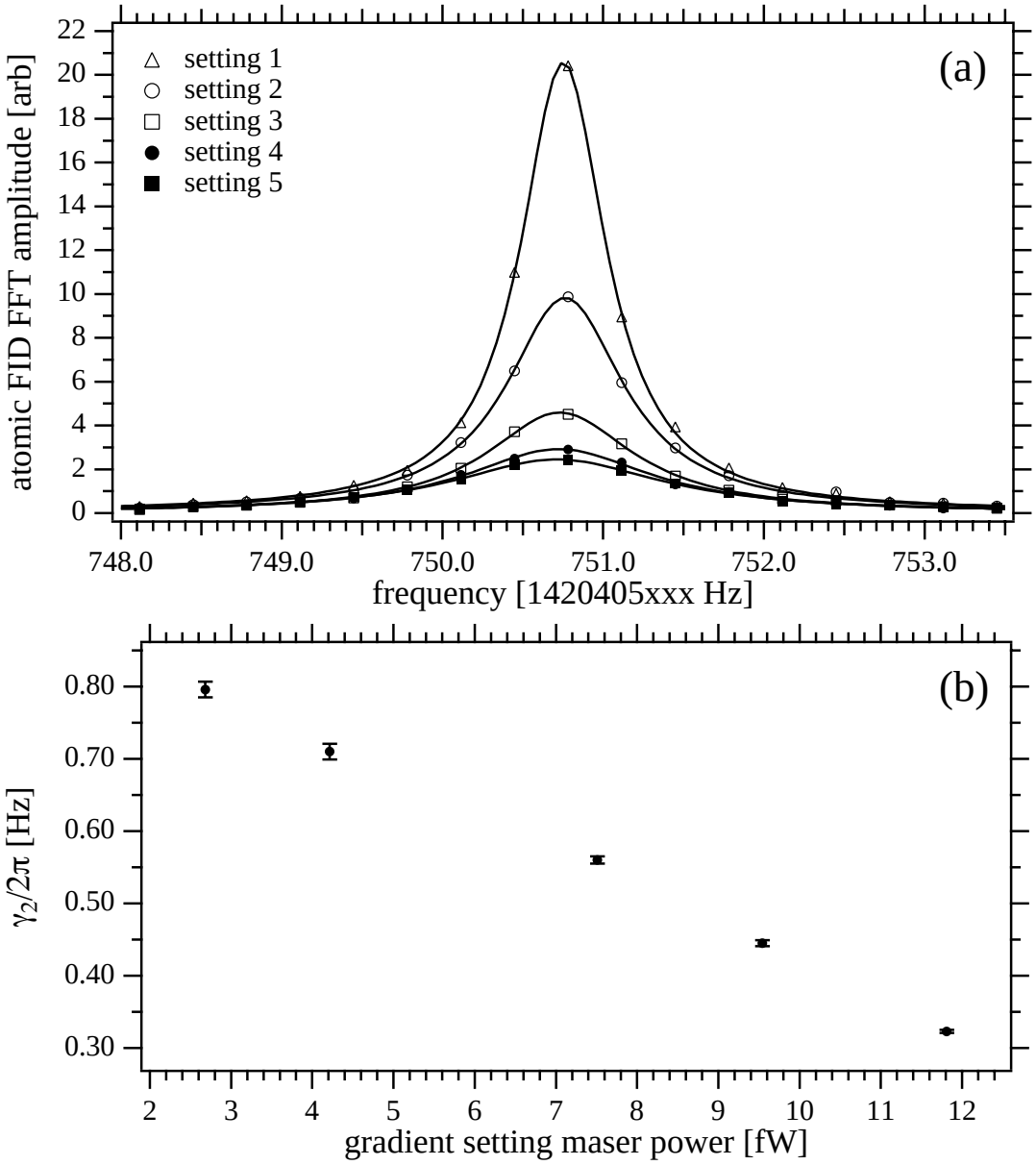

Figure 6.7: (a) Fast Fourier transforms (FFTs) of atomic free induction decays for the five magnetic gradient settings used in our spin-exchange measurements. Each FFT is an average of 10 FFTs taken from amplitude traces in the time domain 3 seconds in duration. The value of γ_2 for each setting is given by the half width at half maximum of a Lorentzian fit to the data. (b) The extracted $\gamma_2/2\pi$ values for each setting plotted against the maser power for that setting measured in Figure 6.5. The error bars here are from the statistical error in the Lorentzian fit.

for each of the gradient settings' FFTs are plotted in Figure 6.7(b) as a function of the unperturbed maser power for each setting (taken from Figure 6.5).

When determining the relative γ_2 values for a spin-exchange frequency shift measurement, multiple 10 average points were taken for each gradient setting. Since the frequency domain FID amplitude was considerably smaller for the larger magnetic field gradient settings, more averages were taken of these points. As shown in Figure 6.8 the FFT averages were taken in the gradient setting sequence 1-2-1-3-1-4-1-5-1... such that any drift in the overall γ_2 (e.g., due to slow superfluid film variation) could be monitored and corrected for. By fitting any such drift for gradient setting 1 to a slowly varying drift function (typically a one- or two-piece quadratic), and then subtracting this drift from each of the gradient settings, the average value of the residuals for each setting was a measure of the relative magnetic-inhomogeneity-induced broadening $\delta\gamma_2/2\pi$. These values are given in Figure 6.8 for a superfluid film setting of 0.2 sccm, a hydrogen flux of 1.2 units (upstream pressure 2.4 PSI), and a maser temperature of 496 mK. From the averages of these values it can be seen that our measurement technique allowed us to determine $\delta\gamma_2$ for each gradient setting with a statistical precision of a few percent.

It was observed that the overall broadening γ_2 (for a given gradient setting) would vary from day to day even with the operating conditions reproduced. We believe that this variation is due to small changes in the superfluid film thickness. The relative magnetic-inhomogeneity-induced broadening $\delta\gamma_2$, however, was found to be very stable from day to day (to within a few percent), and showed no significant variation even between 20 K warming cycles. In Figure 6.9 we plot four measurements of the relative γ_2 values at two different temperatures made on four different days and between different 20 K warming cycles. Here, it can be seen that there is a noticeable shift in relative γ_2 values between the two temperatures, however the shift for a given temperature is within the experimental uncertainty of a few percent.

Since the relative γ_2 values were stable from day to day, it was not necessary to complete both the γ_2 measurements and the spin-exchange frequency shift measurements

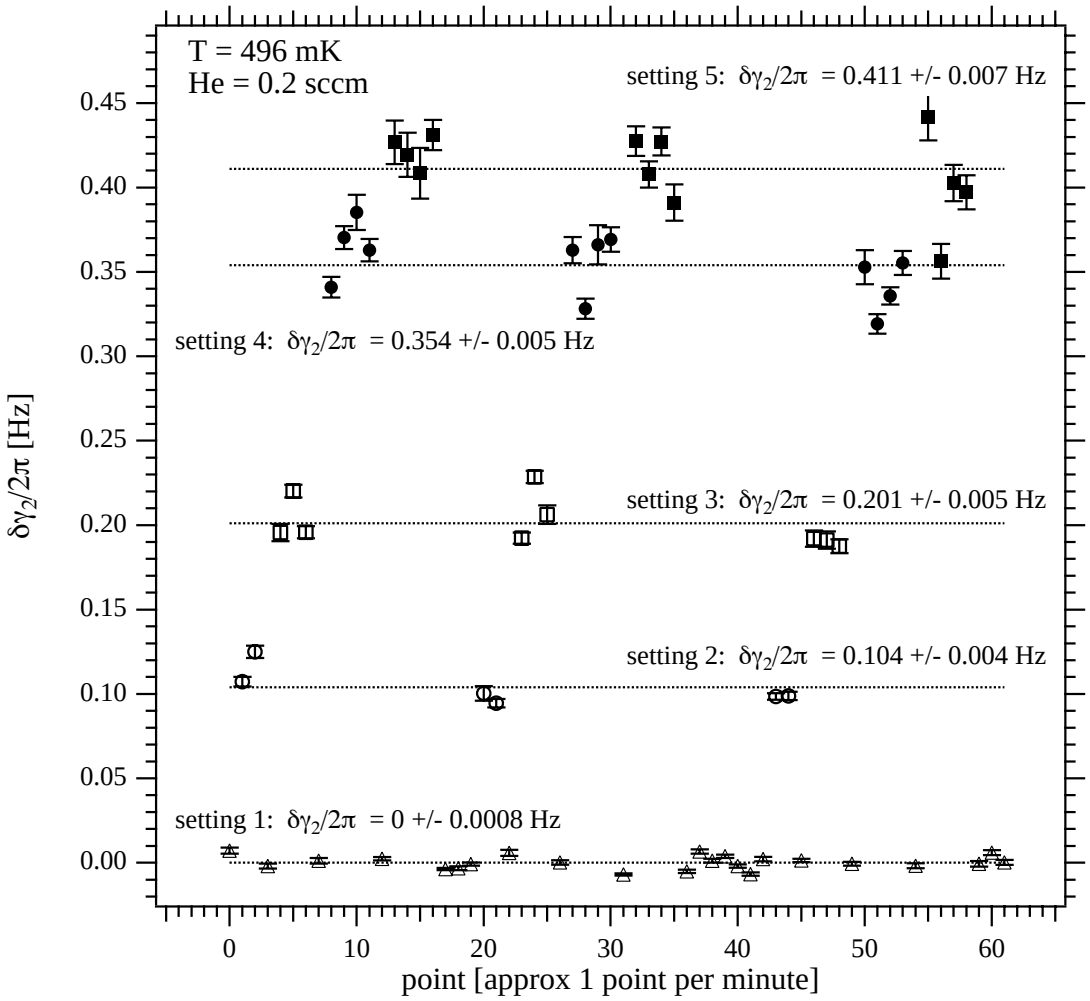

Figure 6.8: Typical measurement of the relative magnetic-inhomogeneity-induced broadening $\delta\gamma_2/(2\pi)$ between magnetic gradient settings. Each point comes from the Lorentzian fit to a 10 average FFT spectrum (as shown in Figure 6.7). The relative γ_2 values are measured while toggling between the different gradient settings. Any drift in the overall broadening γ_2 is corrected for by fitting a slowly varying drift function to the values measured for gradient setting 1. This drift is subtracted from the data at each setting, and the residual values give the relative broadening $\delta\gamma_2/(2\pi)$.

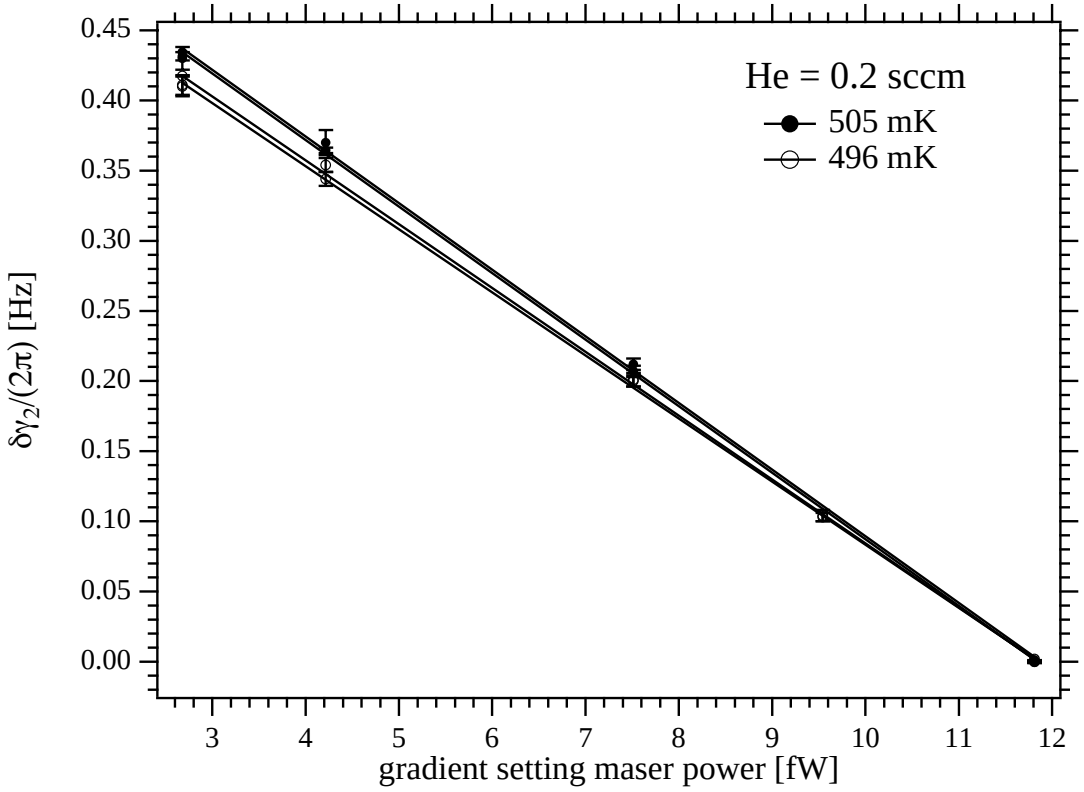

Figure 6.9: Relative magnetic-inhomogeneity-induced broadening values $\delta\gamma_2/(2\pi)$ plotted against the maser power for each magnetic gradient setting. Two measurements at 505 mK (solid markers) and two measurements at 496 mK (open markers) are shown, each taken with a superfluid film setting of 0.2 sccm. For a given temperature the two measurements were made on different days during different 20 K warming cycles; their variation is less than a few percent.

during the same day. To do so would require the maser to continue running while the cavity was tuned back to its value nearest atomic resonance. This amount of mechanical tuning would require up to one hour of thermal re-equilibration. For some of the measurements reported below, the relative γ_2 and spin-exchange frequency shift data were taken on the same day. For others, previously measured γ_2 values for the same operating conditions were used in the analysis of the spin-exchange maser frequency shift data.

Measurement of Δ

From Eqn. 6.17 it can be seen that the maser frequency shift due to cavity detuning combines additively with the maser shift due to spin-exchange collisions. For this reason, the absolute error in the cavity detuning parameter Δ must be sufficiently small to resolve the spin-exchange shift product $\alpha\bar{\lambda}_0$. A considerable effort was therefore made to refine our measurement of Δ, and two measurement techniques were developed.

The first technique used cw microwave power to interrogate the cavity through reflection. The setup for this reflection technique is given in Figure 6.10. A frequency generator,[4] locked to a room temperature hydrogen maser and initially set about one cavity linewidth below the resonant frequency, was stepped through the cavity resonance. The cw power was directed toward the cavity using a 20 dB directional coupler. The first port of a second 20 dB directional coupler directed a portion of the microwave power towards one input of a vector voltmeter.[5] The remainder of the cw power passed into the cryostat, along the transmission line to the cavity's coupling loop. Here, some of the microwave power was absorbed by the cavity (maximum absorption on resonance) and the rest of the power was reflected back. After traveling back up the transmission line, 20 dB of this reflected power was directed with the second port of the second 20 dB directional coupler into the second input of the vector voltmeter. (The remainder of the reflected power was absorbed into a 50 Ohm terminator).

A computer running a LabVIEW program controlled the frequency steps of the fre-

[4]Hewlett-Packard model 8660D.
[5]Hewlett-Packard model 8508A.

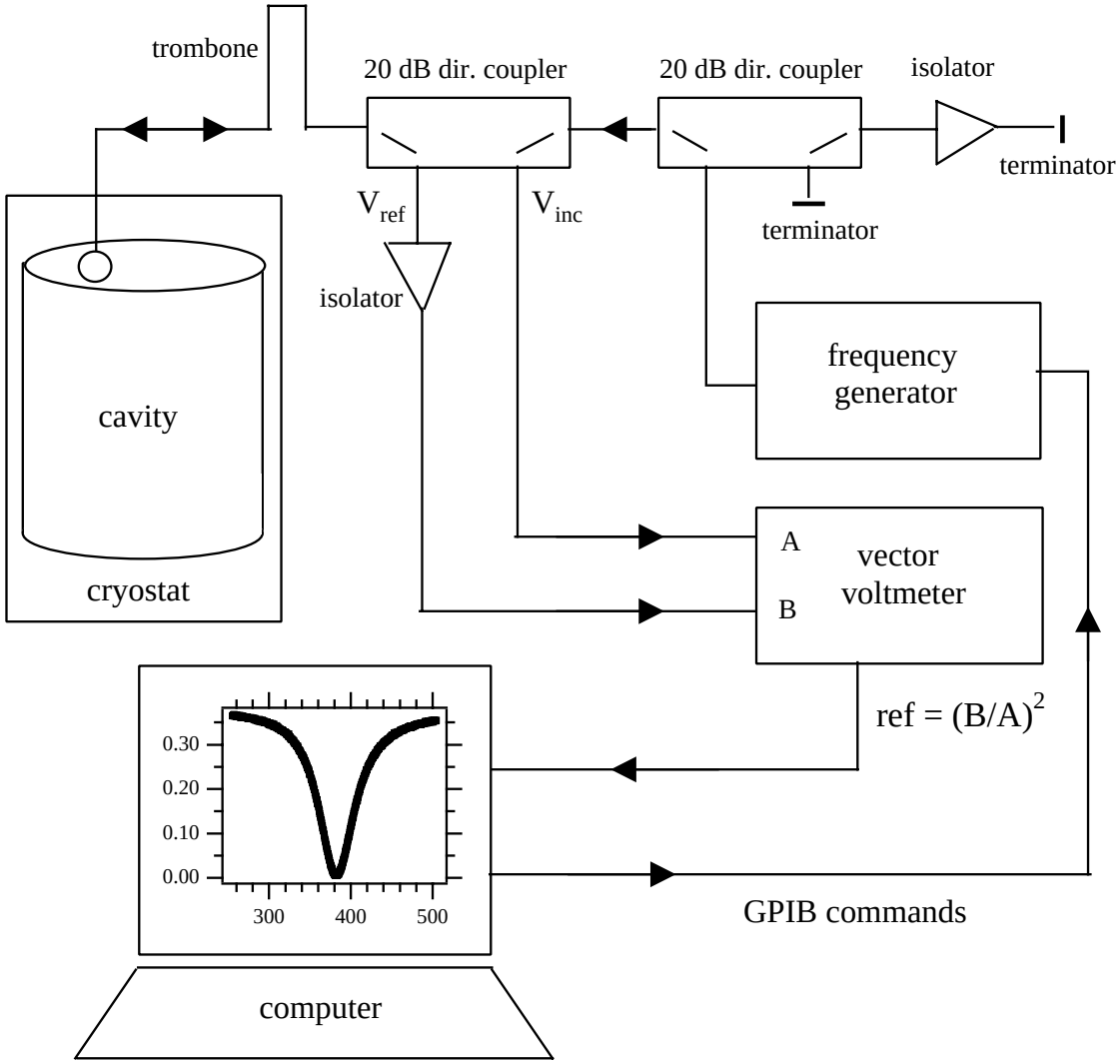

Figure 6.10: Experimental setup to measure the cavity detuning parameter Δ using the reflection technique. See text for details.

quency generator and also read the incident and reflected voltages from the vector voltmeter. At each frequency step, the reflection coefficient, defined as the square of the reflected to the incident voltage, was recorded. A plot of reflection coefficient vs microwave drive frequency showed a Lorentzian lineshape from which the cavity tuning parameter could be determined. A typical cavity resonance is given in Figure 6.11(a). For this spectrum, -10 dBm of power was output from the frequency generator so that -30 dBm of power was incident on the cavity and -50 dBm of incident power directed into the vector voltmeter. The cw power was stepped through a 250 kHz span in 500 steps and an entire spectrum took about 90 seconds to acquire.

In addition to power absorbed by the high-Q microwave cavity, there will also be absorption by low-Q components in the transmission line, such as imperfect microwave connections. As a result, the cavity resonance will not be a simple Lorentzian, but will also contain a slowly varying background. We tested several different fitting functions to account for this background, and chose the optimal fitting function based on an analysis of the fit residuals. For all the reflection technique measurements of Δ, the cavity resonances were fit to a function of the form

$$fit = (K_0 + K_5 x) + \frac{(K_1 + K_4 x)}{((x - K_2)^2 + K_3)}. \tag{6.20}$$

From the fit parameters, the cavity frequency is given by $\nu_C = K_2$ and the cavity width is given by $\Delta\nu_C = 2\sqrt{K_3}$. The cavity-Q is then $Q_C = \nu_C/\Delta\nu_C$ and Δ is found using Eqn. 6.3. From Figure 6.11(a) it can be seen that the cavity frequency was typically determined to a precision within about 30 Hz and the cavity-Q to about 0.1%, giving us about 0.1% statistical precision in measuring Δ. From Figure 6.11(b) it can be seen that the fit residuals from our fitting function were normally distributed about zero, indicating that our fit properly accounted for the slowly varying background.

While our statistical precision with this technique was sufficient for our measurement of the spin-exchange parameter $\bar{\lambda}_0$, we note that this microwave reflection technique is

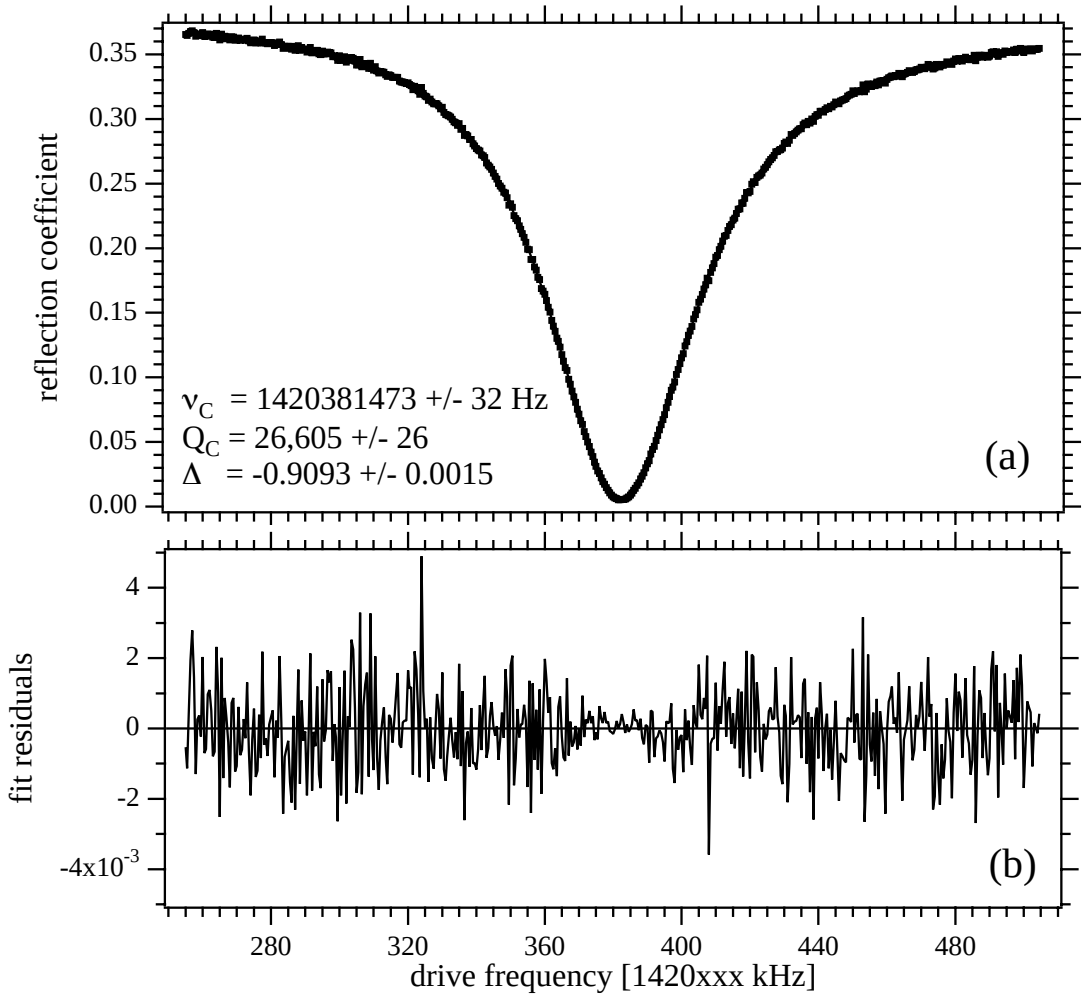

Figure 6.11: (a) Typical cavity resonance for the reflection technique of measuring Δ. From a fit to these data using Eqn. 6.20 the cavity's resonant frequency ν_C and resonant linewidth $\Delta\nu_C$ can be found, from which the cavity-Q Q_C and detuning parameter Δ can be determined. From this technique, we achieve 0.1% statistical precision in Δ. (b) Fit residuals for the fit to Eqn. 6.20.

particularly susceptible to systematic errors due to spurious microwave reflections in the transmission line. In the CHM this error could be especially prevalent because of the large temperature gradient along the transmission line and the presence of numerous low temperature microwave connections and heatsinks.

Concern over this possible source of systematic error led us to devise a second method with which to measure Δ. Instead of measuring incident and reflected power of a cw microwave drive, this second technique looked at the decay of a microwave pulse injected into and reflected off of the microwave cavity.

The setup for this ringdown technique is given in Figure 6.12. An amplitude modulated microwave frequency generator,[6] locked to a room temperature hydrogen maser, was tuned near the cavity resonance. The amplitude modulation, controlled by a pulse shaping synthesizer,[7] created -12 dBm pulses at a rate of 1 kHz with an on/off duty cycle of 25%. To reduce the amount of bleedthrough and improve the switching-off time of the pulse, these 1 kHz pulses were then fed into a second microwave switch controlled by a second pulse shaping synthesizer[8] triggered by the first. Using both the amplitude modulation and the microwave switch, the switching-off time of the pulse was approximately 6 μs, and less than 0.04% of the microwave power was transmitted after this switching-off time.

The microwave pulse was directed toward the cavity via a 20 dB directional coupler and it traveled into the cryostat, down the transmission line, and into the cavity through the coupling loop. The pulse then excited the cavity, and a reflected decay pulse was transmitted back up the transmission line. A fraction of this "ringdown" was directed via a 20 dB directional coupler through an isolator, a preamplifier (gain $\approx$ 40 dB), and into one arm of a double balanced mixer. The ($\approx$ 1420.38 MHz) ringdown was mixed with a 1419.000000 MHz local oscillator,[9] also locked to a room temperature hydrogen maser, and the mixed ringdown near 1.38 MHz was input into a digital oscilloscope.[10] From the

[6] Hewlett-Packard model 8660D.
[7] Wavetek model 29.
[8] Stanford Research Systems model DS345.
[9] Agilent model 8648B.
[10] Tektronix model TDS 224.

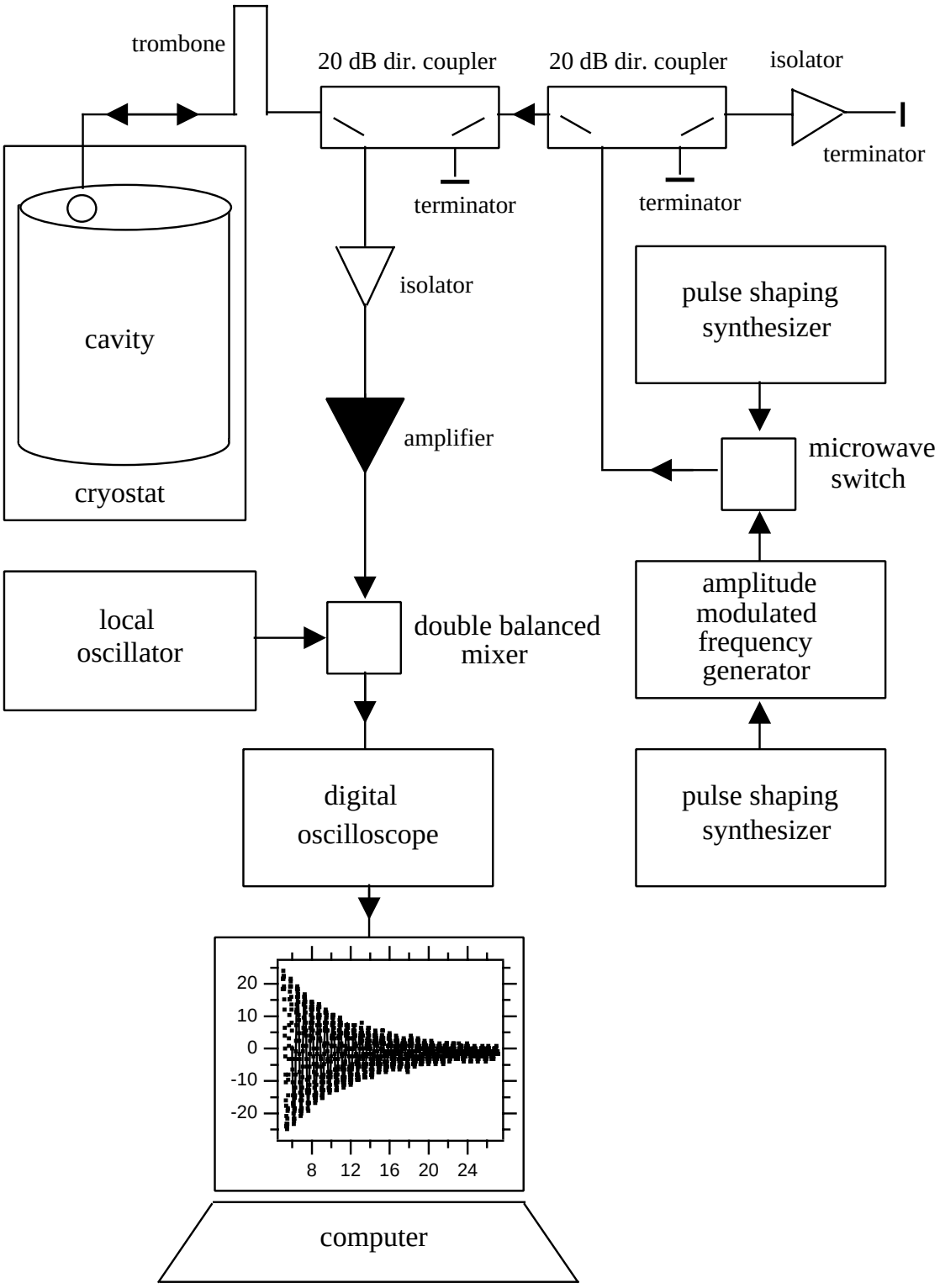

Figure 6.12: Experimental setup to measure the cavity detuning parameter Δ using the ringdown technique. See text for details.

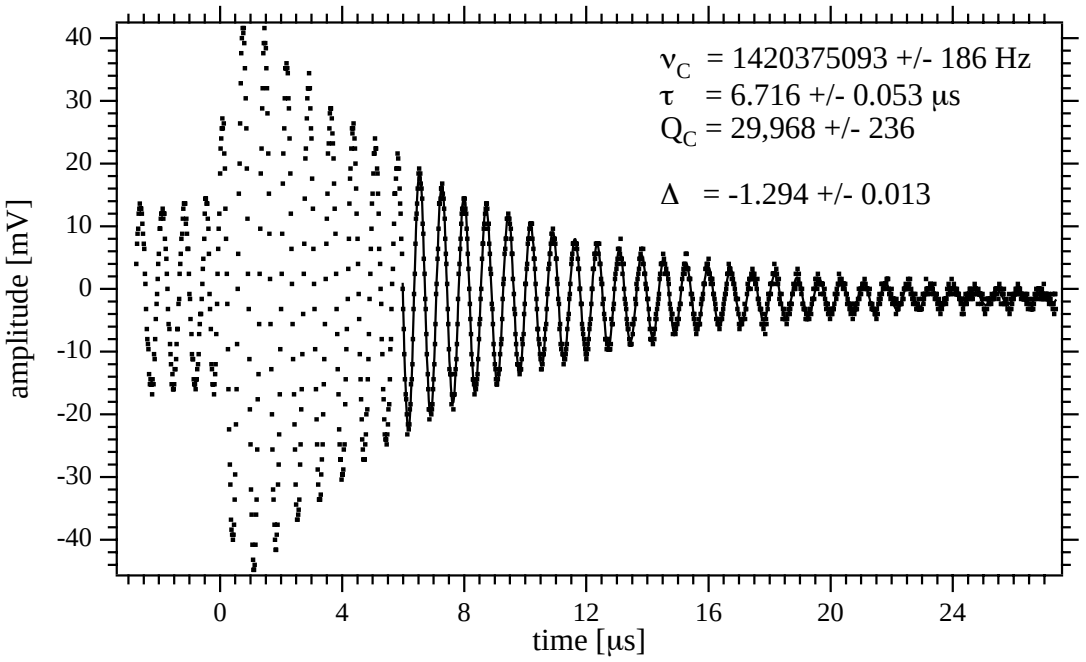

Figure 6.13: Typical cavity ringdown used for measuring Δ (points) and a fit to Eqn. 6.21 (line). The fit begins after a 6 μs delay so as not to include artifacts due to the finite switching-off time of the pulse. From the fit the cavity's resonant frequency ν_C and cavity-Q Q_C can be found from which the detuning parameter Δ can be determined. Using this technique, we achieve 0.4% statistical precision in Δ after ten ringdown averages.

scope, a LabVIEW program read off the ringdown trace (see Figure 6.13).

To determine the cavity's resonant frequency and linewidth,the cavity ringdown amplitude was fit to the following exponentially decaying sinusoid:

$$fit = K_0 \exp(-x/K_1) \sin(K_2 x + K_3) + K_4. \tag{6.21}$$

The fits were begun after a 6 μs delay so as not to include any effect of the pulse. From the fit parameters, the cavity frequency was given by $\nu_C = K_2/2\pi + 1419.000000$ MHz, the cavity-Q was given by $Q_C = \pi \nu_C K_1$ and the cavity detuning parameter was given by Eqn. 6.3. From Figure 6.13 it can be seen that a single ringdown allowed the cavity frequency to be measured with a precision of about 200 Hz, the cavity-Q to about 1%, and Δ to about 1.5%. To improve this precision, typically 10 ringdowns were separately

fit and the fit parameters were averaged together which improved the statistical precision in Δ to about 0.4%, comparable to that from the reflection method measurements.

Unfortunately we observed that the microwave cavity parameters measured using the reflection technique disagreed with those measured using the ringdown technique (ν_C by parts in 10^6, Q_C and Δ by a few percent). We believe the source of the disagreement to be microwave reflections in the transmission line. In order to investigate these effects, a microwave trombone was installed between the cryostat and the first 20 dB directional coupler (see Figures 6.10 and 6.12). Changing the length of the trombone varied the line length between the cavity and the detection devices and allowed us to make our measurements at different places on the transmission line. This potentially allowed us to find the proper place on the line where spurious microwave reflections would be eliminated.

A comparison of the cavity frequency, cavity-Q, and detuning parameter measured by the two techniques is shown in Figure 6.14 for a small variation in the trombone setting and therefore the measurement position along the transmission line. From these plots, it can be seen that the individual cavity parameters (ν_C, Q_C, and Δ) agree between the two measurement techniques at different locations on the transmission line. Because the cavity pulling maser shift depends on the complete detuning parameter Δ, most of our spin-exchange measurements were made with the trombone set such that there was agreement in Δ between the two techniques. Good agreement in $\bar{\lambda}_0$ was found between all measurements made at this trombone setting. An additional measurement was made with the trombone set such that the cavity frequencies (ν_C) were in agreement, and it was unfortunately found that both values of $\bar{\lambda}_0$ (extracted using the reflection method Δ and the ringdown method Δ) were in statistical disagreement with the data from the trombone setting for agreement in Δ. As will be discussed in Section 6.5.2, uncertainty in Δ turned out to be the dominate source of systematic error for our measurement of the spin-exchange parameter $\bar{\lambda}_0$.

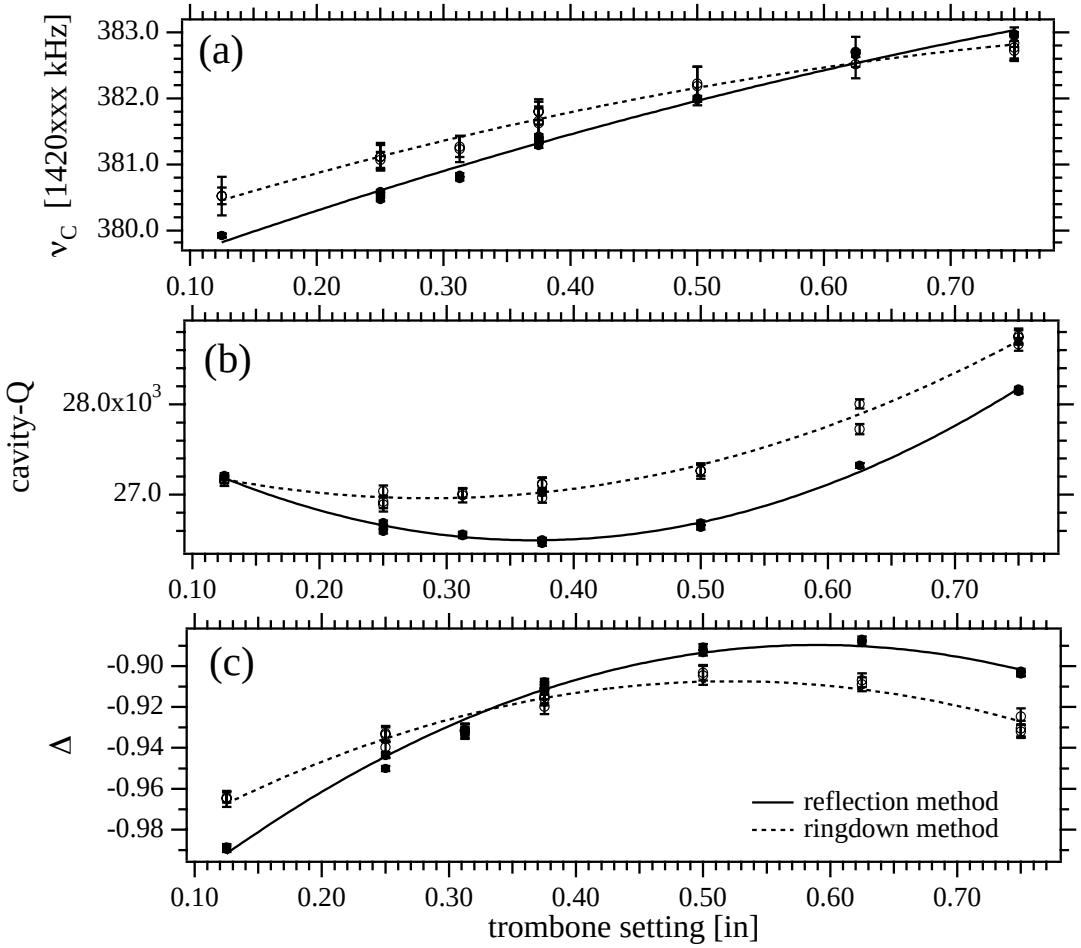

Figure 6.14: Measured cavity parameters (a) ν_C, (b) Q_C and (c) Δ as a function of the measurement position on the transmission line (determined by the length of the microwave trombone). The full markers and solid lines are data from the reflection method, while the open markers and dashed lines are from the ringdown method. Most of our measurements of $\bar{\lambda}_0$ were made with the trombone setting such that there was agreement in Δ between the two methods. Measurements of $\bar{\lambda}_0$ made at different trombone settings were in statistical disagreement with each other, and hence error in determining Δ was the largest source of systematic error in this study, as described in Section 6.5.2.

Measurement of $\bar{\lambda}_0$

Once the cavity detuning parameter Δ and the relative magnetic-inhomogeneity-induced broadening $\delta\gamma_2/2\pi$ for each gradient setting were determined, a simple measurement of the maser frequency shift between the gradient settings was sufficient to determine the spin-exchange parameter using Eqn. 6.19.

With our level of maser temperature control, the short term (10 s) stability of the maser was on the order of 5 mHz. By taking multiple points at each setting the maser frequency shift resolution was improved to about 0.3 mHz. As we toggled between magnetic gradient settings, the CHM frequency was compared to an unperturbed room temperature maser (maser P-13). (For a detailed description of the maser receivers, see Chapters 3 and 5). The output frequencies of the two voltage controlled crystal oscillators in the maser receivers were set such that there was about a 1.2 Hz offset between the oscillators. The two output signals were combined in a double-balanced mixer and the resulting beat note (period $\approx$ 0.8 s) was averaged for 10 s (about 12 periods) with a counter[11] and logged with a LabVIEW routine. From this measured beat period we determined the frequency of the CHM relative to that of maser P-13. The frequency stability of maser P-13 (parts in 10^{14}) was more than two orders of magnitude smaller than the induced spin-exchange effects (parts in 10^{12}), therefore we neglected any variation in our reference frequency.

Over longer intervals (tens of minutes), the CHM frequency exhibited slow drifts on the order of tens of mHz presumably due to slow variation of superfluid film thickness. Therefore a correction was made for this slow drift. To monitor the maser drift, the data were taken in 120 s "bunches" in the gradient setting sequence 1-2-1-3-1-4-1-5-1... (see Figure 6.15(a)) so that a bunch of data from gradient setting 1 was taken between each bunch at the other gradient settings. Then, the setting 1 data were fit to a piecewise continuous quadratic function where a new quadratic was allowed for every six bunches

[11]Hewlett-Packard model HP 53131A.

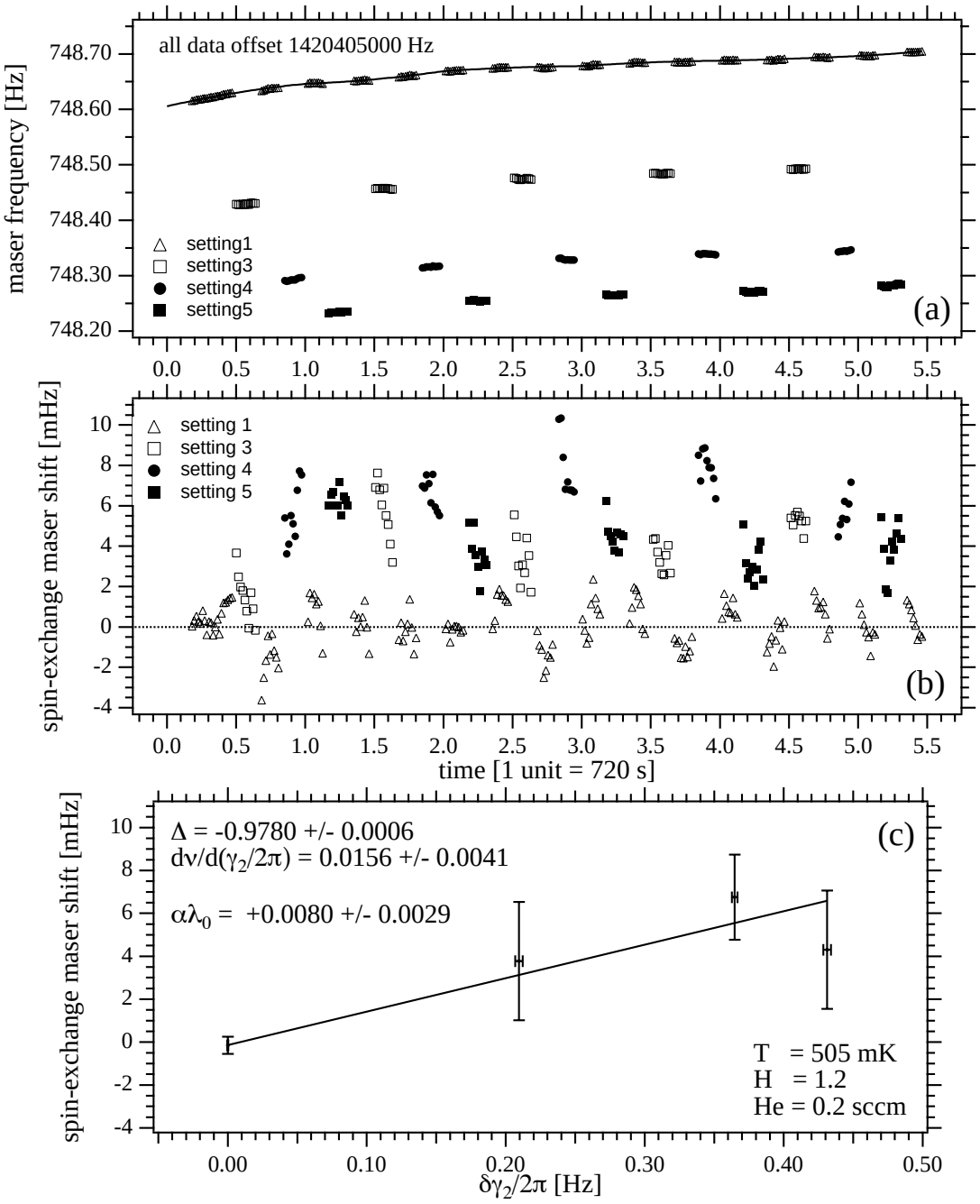

Figure 6.15: Typical data from a spin-exchange frequency shift measurement. For this particular measurement, only data at gradient settings 1, 3, 4, and 5 were collected. (a) Raw maser frequency data for each of four gradient settings. Each point is a 10 s average. A slow drift function was fit to the data from setting 1. (b) Spin-exchange shift data found after subtracting the slow drift and the cavity pulling shift from each point. (c) Spin-exchange shift vs relative magnetic-inhomogeneity-induced broadening $\delta\gamma_2/2\pi$. The slope from this plot, combined with the cavity detuning Δ, determined $\alpha\bar{\lambda}_0$ using Eqn. 6.19.

(720 s) of data. For data in the nth 720 s window, this function is given by

$$f_n(t) = \sum_{i=0}^{2n} A_i + A_{2n+1}(t-n) + A_{2n+2}(t-n)^2. \tag{6.22}$$

This drift function, plotted along with the setting 1 frequency data in Figure 6.15(a), was then subtracted from the data at each of the gradient settings.

After correcting for the slow drift, the cavity pulling maser shift was subtracted from the data at each gradient setting. This shift is formed by the product of the cavity detuning parameter Δ and the relative magnetic-inhomogeneity-induced broadening $\delta\gamma_2/2\pi$ for each gradient setting.

After these two corrections, the residual shift is therefore the spin-exchange maser frequency shift, given for each gradient setting as $\delta\nu = \alpha\bar{\lambda}_0\delta\gamma_2/2\pi$ and plotted in Figure 6.15(b). At each gradient setting, the maser frequency shift was averaged and these values are plotted as a function of relative magnetic-inhomogeneity-induced broadening in Figure 6.15(c). The error bar for each gradient setting was found by adding in quadrature the fractional statistical error in maser frequency (error in the mean), the error due to imprecision in determining the cavity detuning Δ (given that the microwave trombone was set for agreement between the reflection and ringdown methods to measure Δ), and the error due to uncertainty in the relative magnetic-inhomogeneity-induced broadening $\delta\gamma_2/2\pi$. After fitting these data to a line, the spin-exchange shift parameter (multiplied by the system constant α) is found from the slope $d\nu/d(\gamma_2/2\pi)$ and the detuning Δ using Eqn. 6.19.

In order to extract the spin-exchange parameter $\bar{\lambda}_0$, the system constant α must be determined. This parameter is given by

$$\alpha = \frac{\hbar V_C \bar{v}_r}{\mu_0 \mu_B^2 \eta Q_C V_b} \tag{6.23}$$

where V_C and V_b are the cavity and bulb volumes, $\bar{v}_r$ is the average relative atomic velocity, and η is the cavity filling factor, defined in Chapter 3. Calculation of η for the CHM is

complicated by the presence of the dielectric doping sapphire cylinder, however this was accounted for using a graphical technique following an analysis by Folen et al. [99]. As a function of the cavity length $L = 17$ cm, cavity radius $b = 5$ cm, bulb radius $a = 2.2$ cm, and distance into the cavity of the bottom $l_1 \approx 0.8$ cm and top $l_2 \approx 16.2$ cm of the atomic storage region, the CHM filling factor is given by

$$\eta \frac{V_b}{V_C} = 0.0395 \frac{4Lb^2}{\pi^2 a^2 (l_2 - l_1)} \left(\cos \frac{\pi l_1}{L} - \cos \frac{\pi l_2}{L} \right)^2 = 0.357. \tag{6.24}$$

(The numerical forefactor accounts for the dielectric doping.) For atoms at 0.5 K ($\bar{v}_r = 145$ m/s) and for the CHM cavity-Q ($Q_C \approx 26{,}500$), the CHM system constant is therefore $\alpha \approx 1.49 \times 10^{-4}$ Å^{-2}.

6.5.2 Data reduction and error analysis

Overall, six measurements of $\bar{\lambda}_0$ were made over a variety of settings of maser temperature, superfluid film flow, and hydrogen flux. The results of these measurements, all made with the microwave trombone set for agreement in Δ between the two cavity measurement techniques, are given in Table 6.3 and Figure 6.15. These six values are in good statistical agreement and the weighted mean and error in the mean are found to be $\bar{\lambda}_0 = 56.70 \pm 15.51$ Å^2.

No.	T [mK]	He [sccm]	H_2 flux	Δ	α [Å^{-2}]	$\bar{\lambda}_0$ [Å^2]
1	502	0.2	1.7	-0.9079	1.483×10^{-4}	62.71 ± 42.48
2	496	0.2	1.2	-0.9459	1.486×10^{-4}	-2.69 ± 110.36
3	505	0.2	1.2	-0.9780	1.486×10^{-4}	53.84 ± 19.52
4	505	0.2	1.2	-0.9982	1.488×10^{-4}	63.71 ± 49.73
5	505	0.2	1.2	-0.8912	1.492×10^{-4}	71.91 ± 52.28
6	505	0.4	1.2	-0.9766	1.493×10^{-4}	63.63 ± 89.08

Table 6.3: Results of $\bar{\lambda}_0$ measurements made with the microwave trombone set for agreement between the two cavity measurement techniques for Δ.

In addition to these measurements, an additional measurement was made with the

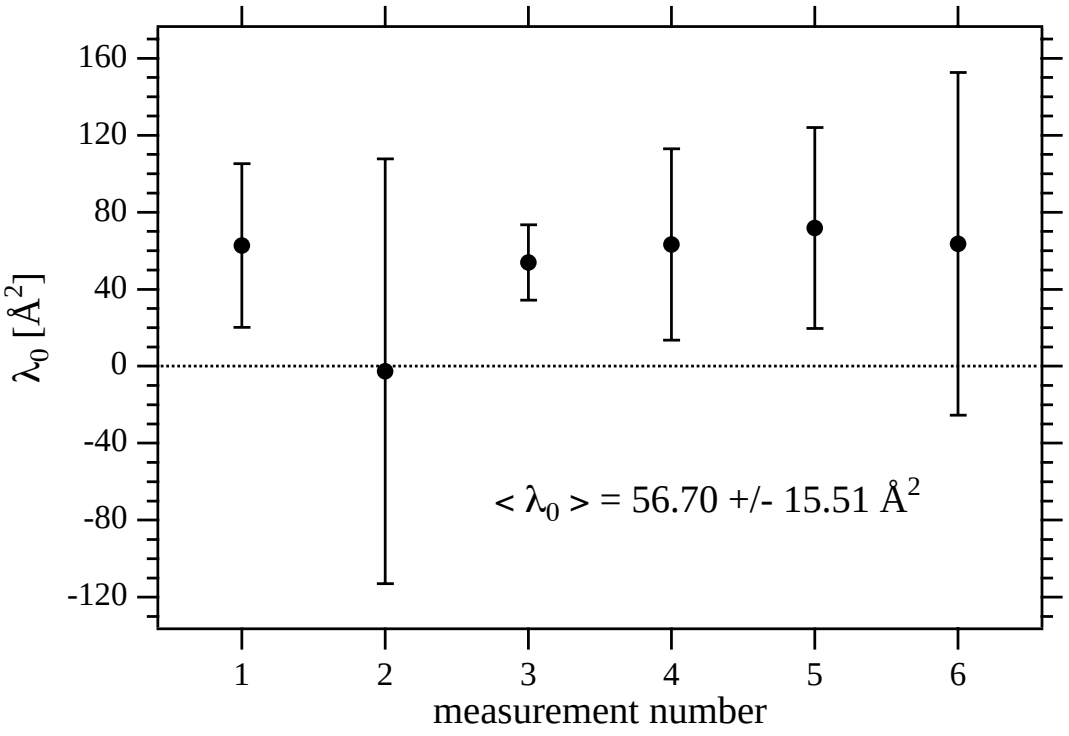

Figure 6.16: Results of $\bar{\lambda}_0$ measurements made with the microwave trombone set for agreement between the two cavity measurement techniques for Δ.

microwave trombone set for agreement in the cavity frequency. This measurement was made with a maser temperature of 496 mK, a superfluid film flow of 0.2 sccm, and a hydrogen flux of 1.2 units (upstream pressure of 2.4 PSI). Using the reflection method value of Δ at this point, the result of this measurement was $\bar{\lambda}_0 = -70.89 \pm 24.09$ [Å^2]. Using the ringdown method value, the result was $\bar{\lambda}_0 = -31.66 \pm 32.35$ [Å^2]. Both of these values are in statistical disagreement with the results from the original setting of the microwave trombone. This therefore reveals the dominant source of systematic error in our measurement, inaccuracy in our measurement of the cavity detuning parameter Δ, presumably due to an uncontrolled offset in the cavity detuning parameter Δ due to reflections in the transmission line.

To try and characterize the uncertainty in Δ, we have made an estimation using two different methods. The first of these utilizes the fact that the maser power should be

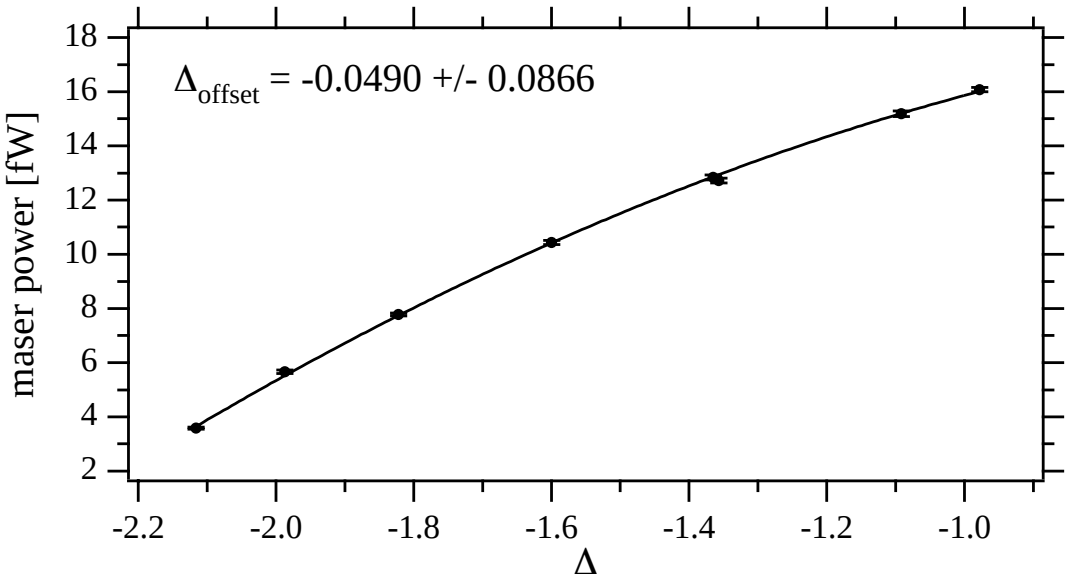

Figure 6.17: Maser power vs cavity detuning as an estimate of the systematic uncertainty in Δ. The maser power should be maximum for $\Delta = 0$. A quadratic fit to these data implies there is an offset of -0.0490 ± 0.0866 in our measurement of Δ. From this we estimate a systematic error in detuning of $\sigma_\Delta = 0.087$.

maximum at a detuning of $\Delta = 0$. We therefore measured the maser power as a function of Δ and fit the results to a parabola (see Figure 6.17). There was a sizable uncertainty in this measurement due to the fact that we could not tune Δ through the atomic resonance because of the shift in the cavity tuning range. An additional complication arose from the thermal equilibration time needed after moving the mechanical plunger, during which time the maser power drifted. The raw data was corrected for this drift prior to the quadratic fit. From the quadratic fit parameters, we find that the data had a peak for $\Delta_{offset} = -0.0490 \pm 0.0866$. We therefore take as a coarse estimate of the systematic error in the cavity detuning parameter $\sigma_\Delta = 0.087$. When this error is propagated back to the spin-exchange parameter, we find a systematic uncertainty of $\sigma_{\bar{\lambda}_0} = 319$ Å^2.

A second estimate in the systematic uncertainty in Δ was made by comparing the Δ measured with the reflection and ringdown methods over a linelength variation of one microwave wavelength. As the trombone is moved by one microwave wavelength, the

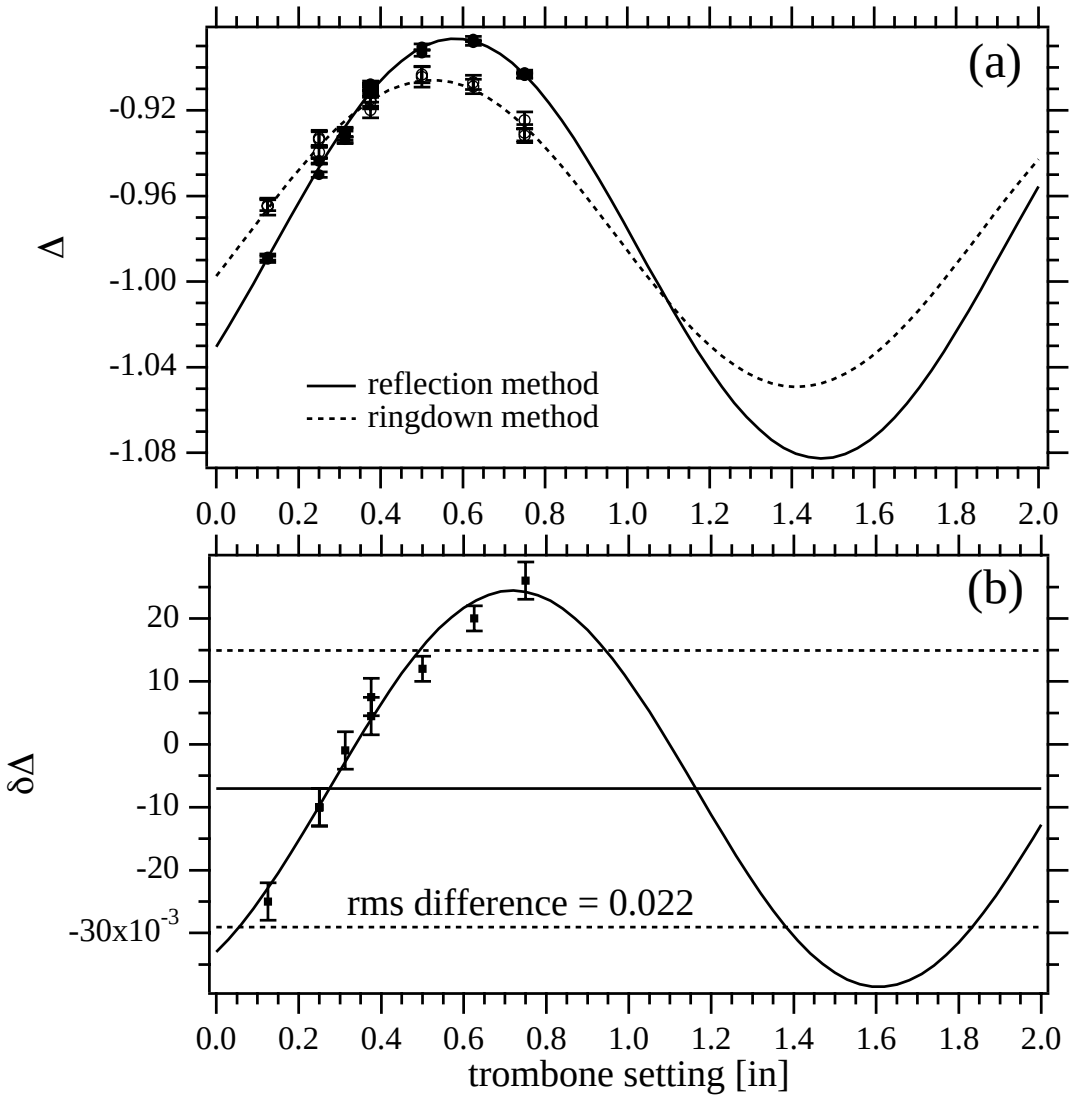

Figure 6.18: Comparison of Δ measured using the reflection and ringdown method as an estimate of the systematic uncertainty in Δ. (a) Measured values of Δ from the two techniques and sinusoidal fits of the same period to the data. (b) The differences in values for Δ from the two methods (points) and the difference sinusoid from the two fits in (a) (line). From the rms value of the difference sinusoid we estimate a systematic error in detuning of $\sigma_\Delta = 0.022$.

measured values of Δ shift through one sinusoidal period. To make this estimate, we took the reflection and ringdown method data from Figure 6.14(c) and fit each to a sinusoid of the same wavelength but differing amplitude and phase. These two fits are displayed in Figure 6.18(a). The difference between these two fits is the sinusoid displayed in Figure 6.18(b). We take as a more refined estimate of the systematic error in Δ the rms value of this difference sinusoid, and find $\sigma_\Delta = 0.022$. When this error is propagated back to the spin-exchange parameter, we find a systematic uncertainty of $\sigma_{\bar{\lambda}_0} = 81$ Å^2.

6.5.3 Conclusions

We now make a comparison between our result ($\bar{\lambda}_0 = +56.7 \pm 15.5 \pm 319/81$ Å^2) and previous results for the semi-classical spin-exchange shift parameter. At 0.5 K, this parameter was found by the group at UBC to be $\bar{\lambda}_0 = -21.7 \pm 2.8$ Å^2 [29]. We point out that their maser had a significantly lower cavity-Q than ours and because of this, their system constant α was approximately 50 times larger than ours. Therefore, although the statistical error in our experiment for the measurable $\alpha\bar{\lambda}_0$ was comparable to theirs, our statistical error in $\bar{\lambda}_0$ is considerably larger.

Nevertheless, our measurement suffered from a significant systematic uncertainty in determining Δ. Because of this uncertainty, our measurement unfortunately cannot address the discrepancy between the original theoretical value (-11.86 Å^2) [30, 31] and the measurement made by the UBC group (-21.7 ± 2.8 Å^2) [29]. Within our systematic error, however, our measurement is in agreement with both of these previous works.

The obvious place for improvement of this measurement is the elimination of the systematic uncertainty in the cavity detuning Δ. An independent determination of the proper setting of the microwave trombone, such that the effects of reflections in the transmission line are eliminated, would be the cleanest way of doing so; however at the moment there is no candidate practical approach for such a determination.

If the effects of reflections in the line could not be removed, a precise and accurate measure of the offset in cavity detuning Δ would be sufficient to reduce the systematic

uncertainty of our measurement. This offset in Δ could then be applied as a correction to the data. We note that this is precisely the method used by the UBC group in their $\bar{\lambda}_0$ measurement [29]. Specifically, they used the same method as in our coarse estimate of the uncertainty in Δ (see Figure 6.17): a measurement of maser power vs detuning followed by a quadratic fit to determine the detuning for which power is maximized. (Their estimate had the advantage of tuning Δ through zero and therefore tuning through the maser power peak, so their systematic uncertainty from this technique was about 4 times smaller than ours.) However, the heightened cavity sensitivity of our experiment (due to our significantly higher cavity-Q) inflates our systematic error extracted using this technique.[12]

Therefore, it would be desirable to devise a new technique in which $\bar{\lambda}_0$ could be measured with the CHM in a way that is insensitive to Δ. One possibility would be to run the device instead below oscillation threshold in pulsed mode with the cavity detuned sufficiently that radiation damping effects (i.e., sensitivity to Δ), could be eliminated.

In its present form, the CHM can only be used for a new measurement of the semi-classical spin-exchange shift parameter $\bar{\lambda}_0$. Equally important, however, would be a new measurement of the h-i parameter Ω. A significant rebuild of the CHM would be required in order to make this parameter accessible for study. At the very least, steps must be made to increase the population inversion flux and to reduce the ^{4}He vapor pressure in the beam tube and collimator so that the maser could be run with saturated superfluid films at a temperature high enough to reach the H-^{4}He collision amplitude minimum. In addition, the development of a cavity tuning mechanism that was resettable and that did not thermally perturb the maser would be highly desirable. Finally, an improved means of controlling and resettably changing the population inversion flux would greatly facilitate a probe of the h-i parameter Ω, and therefore take a new step toward resolving current theoretical and experimental discrepancies in our understanding of low temperature hydrogen-hydrogen spin-exchange collisions.

[12]Note that the SAO CHM cannot be operated as an active maser with a low cavity-Q, as in the UBC CHM, because of the modest input hydrogen flux.

Appendix A

Dressed atom double resonance Bloch equations

Here, we present some of the details of the dressed atom treatment of the double resonance hydrogen maser frequency shift. We refer the reader to notation introduced in Chapter 2.

We begin with several definitions. First, the interaction Hamiltonian matrix elements coupling each of the dressed states $|a\rangle$, $|b\rangle$, and $|c\rangle$ to bare state $|4\rangle$ will be given by

$$\begin{aligned} H_{a4} &= -\langle a|\hat{\mu}\cdot\mathbf{H_C}|4\rangle = \frac{X_{12}}{2\Omega}H_{24} \\ H_{b4} &= -\langle b|\hat{\mu}\cdot\mathbf{H_C}|4\rangle = \frac{\delta}{\Omega}H_{24} \\ H_{c4} &= -\langle c|\hat{\mu}\cdot\mathbf{H_C}|4\rangle = -\frac{X_{12}}{2\Omega}H_{24} \end{aligned} \tag{A.1}$$

where we recall that $H_{24} = -\langle 2|\hat{\mu}\cdot\mathbf{H_C}|4\rangle$ is the bare atom interaction Hamiltonian matrix element, $\delta = \omega_T - \omega_Z$ is the detuning of the transverse field from the mean atomic Zeeman frequency $\omega_Z = \frac{1}{2}(\omega_{12}+\omega_{23})$, $\Omega = \sqrt{\delta^2 + \frac{1}{2}X_{12}^2}$ represents the generalized Rabi frequency of the driven Zeeman transition, and $X_{12} = \mu_{12}H_T/\hbar$ is the transverse field Rabi frequency. We also define a modified maser Rabi frequency

$$Z_{24} = \frac{X_{24}}{2i\Omega} = \frac{\mu_{24}H_C}{2i\hbar\Omega} \tag{A.2}$$

and we recall the maser frequency shift is given by

$$\Delta = \omega - \omega_{24}. \tag{A.3}$$

Then, after transforming to the interaction picture and making the rotating wave approximation, the sixteen independent dressed state Bloch equations are given by:

$$\begin{aligned}
\dot{\tilde{\rho}}_{aa} &= \tilde{\rho}_{a4}\frac{X_{12}Z_{42}}{2}e^{-i(\Omega-\Delta)t} - \tilde{\rho}_{4a}\frac{X_{12}Z_{24}}{2}e^{i(\Omega-\Delta)t} \\
&\quad -(\gamma+r)\tilde{\rho}_{aa} + \frac{\gamma}{4} + \frac{r}{2}\left[\left(\frac{X_{12}}{2\Omega}\right)^2 + \frac{1}{4}\left(1-\frac{\delta}{\Omega}\right)^2\right] \\
\dot{\tilde{\rho}}_{ab} &= \tilde{\rho}_{a4}\delta Z_{42}e^{i\Delta t} - \tilde{\rho}_{4b}\frac{X_{12}Z_{24}}{2}e^{i(\Omega-\Delta)t} - (\gamma+r)\tilde{\rho}_{ab} + \frac{r}{2}\left[\frac{X_{12}}{4\Omega}\left(1+\frac{\delta}{\Omega}\right)\right]e^{i\Omega t} \\
\dot{\tilde{\rho}}_{ac} &= -\tilde{\rho}_{a4}\frac{X_{12}Z_{42}}{2}e^{i(\Omega+\Delta)t} - \tilde{\rho}_{4c}\frac{X_{12}Z_{24}}{2}e^{i(\Omega-\Delta)t} \\
&\quad -(\gamma+r)\tilde{\rho}_{ac} + \frac{r}{2}\left[-\left(\frac{X_{12}}{2\Omega}\right)^2 + \frac{1}{4}\left(1-\frac{\delta^2}{\Omega^2}\right)\right]e^{2i\Omega t} \\
\dot{\tilde{\rho}}_{a4} &= \tilde{\rho}_{aa}\frac{X_{12}Z_{24}}{2}e^{i(\Omega-\Delta)t} + \tilde{\rho}_{ab}\delta Z_{24}e^{-i\Delta t} - \tilde{\rho}_{ac}\frac{X_{12}Z_{24}}{2}e^{-i(\Omega+\Delta)t} \\
&\quad -(\gamma+r)\tilde{\rho}_{a4} - \tilde{\rho}_{44}\frac{X_{12}Z_{24}}{2}e^{i(\Omega-\Delta)t} \\
\dot{\tilde{\rho}}_{ba} &= \dot{\tilde{\rho}}^{\dagger}_{ab} \\
\dot{\tilde{\rho}}_{bb} &= \tilde{\rho}_{b4}\delta Z_{42}e^{i\Delta t} - \tilde{\rho}_{4b}\delta Z_{24}e^{-i\Delta t} - (\gamma+r)\tilde{\rho}_{bb} + \frac{\gamma}{4} + \frac{r}{2}\left[\frac{\delta^2+(X_{12}/2)^2}{\Omega^2}\right] \\
\dot{\tilde{\rho}}_{bc} &= -\tilde{\rho}_{b4}\frac{X_{12}Z_{42}}{2}e^{i(\Omega+\Delta)t} - \tilde{\rho}_{4c}\delta Z_{24}e^{-i\Delta t} \\
&\quad -(\gamma+r)\tilde{\rho}_{bc} + \frac{r}{2}\left[\frac{X_{12}}{4\Omega}\left(1-\frac{\delta}{\Omega}\right)\right]e^{i\Omega t} \\
\dot{\tilde{\rho}}_{b4} &= \tilde{\rho}_{ba}\frac{X_{12}Z_{24}}{2}e^{i(\Omega-\Delta)t} - \tilde{\rho}_{bc}\frac{X_{12}Z_{24}}{2}e^{-i(\Omega+\Delta)t} - (\gamma+r)\tilde{\rho}_{b4} + (\tilde{\rho}_{bb}-\tilde{\rho}_{44})\delta Z_{24}e^{-i\Delta t} \\
\dot{\tilde{\rho}}_{ca} &= \dot{\tilde{\rho}}^{\dagger}_{ac} \\
\dot{\tilde{\rho}}_{cb} &= \dot{\tilde{\rho}}^{\dagger}_{bc} \\
\dot{\tilde{\rho}}_{cc} &= -\tilde{\rho}_{c4}\frac{X_{12}Z_{42}}{2}e^{i(\Omega+\Delta)t} + \tilde{\rho}_{4c}\frac{X_{12}Z_{24}}{2}e^{-i(\Omega+\Delta)t} \\
&\quad -(\gamma+r)\tilde{\rho}_{cc} + \frac{\gamma}{4} + \frac{r}{2}\left[\left(\frac{X_{12}}{2\Omega}\right)^2 + \frac{1}{4}\left(1+\frac{\delta}{\Omega}\right)^2\right] \\
\dot{\tilde{\rho}}_{c4} &= \tilde{\rho}_{ca}\frac{X_{12}Z_{24}}{2}e^{i(\Omega-\Delta)t} + \tilde{\rho}_{cb}\delta Z_{24}e^{-i\Delta t} - \tilde{\rho}_{cc}\frac{X_{12}Z_{42}}{2}e^{-i(\Omega+\Delta)t}
\end{aligned} \tag{A.4}$$

$$
\begin{aligned}
& -(\gamma+r)\tilde{\rho}_{c4} + \tilde{\rho}_{44}\frac{X_{12}Z_{24}}{2}e^{-i(\Omega+\Delta)t} \\
\dot{\tilde{\rho}}_{4a} &= \dot{\tilde{\rho}}^{\dagger}_{a4} \\
\dot{\tilde{\rho}}_{4b} &= \dot{\tilde{\rho}}^{\dagger}_{b4} \\
\dot{\tilde{\rho}}_{4c} &= \dot{\tilde{\rho}}^{\dagger}_{c4} \\
\dot{\tilde{\rho}}_{44} &= \tilde{\rho}_{4a}\frac{X_{12}Z_{24}}{2}e^{i(\Omega-\Delta)t} - \tilde{\rho}_{a4}\frac{X_{12}Z_{42}}{2}e^{-i(\Omega-\Delta)t} + \tilde{\rho}_{4b}\delta Z_{24}e^{-i\Delta t} - \tilde{\rho}_{b4}\delta Z_{42}e^{i\Delta t} \\
& \quad -\tilde{\rho}_{4c}\frac{X_{12}Z_{24}}{2}e^{-i(\Omega+\Delta)t} + \tilde{\rho}_{c4}\frac{X_{12}Z_{42}}{2}e^{i(\Omega+\Delta)t} - (\gamma+r)\tilde{\rho}_{44} + \frac{\gamma}{4}.
\end{aligned}
$$

We solve these equations in the steady state, where the populations in the interaction picture are static, $\dot{\tilde{\rho}}_{\nu\nu} = 0$, and the coherences exhibit sinusoidal precession. In particular, $\tilde{\rho}_{4a} = R_{4a}e^{-i(\Omega-\Delta)t}$, $\tilde{\rho}_{4b} = R_{4b}e^{i\Delta t}$, and $\tilde{\rho}_{4c} = R_{4c}e^{i(\Omega+\Delta)t}$, where the $R_{\mu\nu}$ are time independent, and $\Delta = \omega - \omega_{24}$. The other coherences precess at frequencies $\omega_{\mu\nu} = (E_\mu - E_\nu)/\hbar$. Making these steady state substitutions, the sixteen Bloch differential equations transform into

$$
\begin{aligned}
(\gamma+r)R_{aa} &= R_{a4}\frac{X_{12}Z_{42}}{2} - R_{4a}\frac{X_{12}Z_{42}}{2} + \frac{\gamma}{4} + \frac{r}{2}\left[\left(\frac{X_{12}}{2\Omega}\right)^2 + \frac{1}{4}\left(1-\frac{\delta}{\Omega}\right)^2\right] \\
(\gamma+r+i\Omega)R_{ab} &= R_{a4}\delta Z_{42} - R_{4b}\frac{X_{12}Z_{24}}{2} + \frac{r}{2}\left[\frac{X_{12}}{4\Omega}\left(1+\frac{\delta}{\Omega}\right)\right] \\
(\gamma+r+2i\Omega)R_{ac} &= -R_{a4}\frac{X_{12}Z_{42}}{2} - R_{4c}\frac{X_{12}Z_{24}}{2} + \frac{r}{2}\left[-\left(\frac{X_{12}}{2\Omega}\right)^2 + \frac{1}{4}\left(1-\frac{\delta^2}{\Omega^2}\right)\right] \\
(\gamma+r+i(\Omega-\Delta))R_{a4} &= (R_{aa}-R_{44})\frac{X_{12}Z_{24}}{2} + R_{ab}\delta Z_{24} - R_{ac}\frac{X_{12}Z_{24}}{2} \\
R_{ba} &= R^{\dagger}_{ab} \\
(\gamma+r)R_{bb} &= R_{b4}\delta Z_{42} - R_{4b}\delta Z_{24} + \frac{\gamma}{4} + \frac{r}{2}\left[\frac{\delta^2 + (X_{12}/2)^2}{\Omega^2}\right] \\
(\gamma+r+i\Omega)R_{bc} &= -R_{b4}\frac{X_{12}Z_{42}}{2} - R_{4c}\delta Z_{24} + \frac{r}{2}\left[\frac{X_{12}}{4\Omega}\left(1-\frac{\delta}{\Omega}\right)\right] \\
(\gamma+r-i\Delta)R_{b4} &= R_{ba}\frac{X_{12}Z_{24}}{2} - R_{bc}\frac{X_{12}Z_{24}}{2} + (R_{bb}-R_{44})\delta Z_{24} \\
R_{ca} &= R^{\dagger}_{ac} \\
R_{cb} &= R^{\dagger}_{bc}
\end{aligned}
\tag{A.5}
$$

$$
\begin{aligned}
(\gamma + r)R_{cc} &= -R_{c4}\frac{X_{12}Z_{42}}{2} + R_{4c}\frac{X_{12}Z_{24}}{2} + \frac{\gamma}{4} + \frac{r}{2}\left[\left(\frac{X_{12}}{2\Omega}\right)^2 + \frac{1}{4}\left(1 + \frac{\delta}{\Omega}\right)^2\right] \\
(\gamma + r - i(\Omega + \Delta))R_{c4} &= R_{ca}\frac{X_{12}Z_{24}}{2} + R_{cb}\delta Z_{24} - R_{cc}\frac{X_{12}Z_{42}}{2} + R_{44}\frac{X_{12}Z_{24}}{2} \\
R_{4a} &= R_{a4}^{\dagger} \\
R_{4b} &= R_{b4}^{\dagger} \\
R_{4c} &= R_{c4}^{\dagger} \\
(\gamma + r)R_{44} &= R_{4a}\frac{X_{12}Z_{24}}{2} - R_{a4}\frac{X_{12}Z_{42}}{2} + R_{4b}\delta Z_{24} - R_{b4}\delta Z_{42} \\
&\quad -R_{4c}\frac{X_{12}Z_{24}}{2} + R_{c4}\frac{X_{12}Z_{42}}{2} + \frac{\gamma}{4}.
\end{aligned}
$$

The results of a numerical solution to these equations is provided in Chapter 2.

Bibliography

[1] H. Goldenberg, D. Kleppner, and N. Ramsey, Phys. Rev. Lett. **5**, 361 (1960).

[2] D. Kleppner, H. Goldenberg, and N. Ramsey, Phys. Rev. **126**, 603 (1962).

[3] D. Kleppner *et al.*, Phys. Rev. **138**, A 972 (1965).

[4] J. Vanier and C. Audoin, *The Quantum Physics of Atomic Frequency Standards* (Adam Hilger, Bristol, 1989), Chap. 6.

[5] N. Ramsey, Phys. Rev. **78**, 695 (1950).

[6] S. Crampton, W. Phillips, and D. Kleppner, Bull. Am. Phys. Soc. **23**, 86 (1978).

[7] R. Vessot, M. Levine, and E. Mattison, in *Proceedings of the 9th Annual Precise Time and Time Interval Conference* (NASA, Greenbelt, MD, 1978), p. 549, conference publication 2129.

[8] W. Hardy and M. Morrow, Journal de Physique **42**, C8 (1981).

[9] H. Hess *et al.*, Phys. Rev. A **34**, 1602 (1986).

[10] M. Hurlimann, W. Hardy, A. Berlinsky, and R. Cline, Phys. Rev. A **34**, 1605 (1986).

[11] R. Walsworth *et al.*, Phys. Rev. A **34**, 2550 (1986).

[12] J. Gordon, H. Zeiger, and C. Townes, Phys. Rev. **95**, 282 (1954).

[13] K. Shimoda, T. Wang, and C. Townes, Phys. Rev. **102**, 1308 (1956).

[14] A. Rogers and J. Moran, IEEE Trans. Instrum. Meas. **IM-30**, 283 (1981).

[15] P. Kuhnle and R. Sydnor, J. Physique **Suppl. C8**, 373 (1981).

[16] E. Fortson, D. Kleppner, and N. Ramsey, Phys. Rev. Lett. **13**, 22 (1964).

[17] S. Crampton, Phys. Rev. **158**, 158 (1967).

[18] P. Winkler, D. Kleppner, T. Myint, and F. Walther, Phys. Rev. A **5**, 83 (1972).

[19] R. Walsworth, I. Silvera, E. Mattison, and R. Vessot, Phys. Rev. A **46**, 2495 (1992).

[20] R. Vessot *et al.*, Phys. Rev. Lett. **45**, 2081 (1980).

[21] J. Turneaure *et al.*, Phys. Rev. D **27**, 1705 (1983).

[22] R. Walsworth, I. Silvera, E. Mattison, and R. Vessot, Phys. Rev. Lett. **64**, 2599 (1990).

[23] R. Walsworth and I. Silvera, Phys. Rev. A **42**, 63 (1990).

[24] H. Andresen, Z. Phys. **210**, 113 (1968).

[25] M. Humphrey, D. Phillips, and R. Walsworth, Phys. Rev. A **62**, 063405 (2000).

[26] D. Phillips *et al.*, Phys. Rev. D **63**, 111101 (2001).

[27] V. Kostelecký and C. Lane, Phys. Rev. D **60**, 116010 (1999).

[28] V. Kostelecký and C. Lane, J. Math. Phys. **40**, 6245 (1999).

[29] M. Hayden, M. Hurlimann, and W. Hardy, Phys. Rev. A **53**, 1589 (1996).

[30] B. Verhaar *et al.*, Phys. Rev. A **35**, 3825 (1987).

[31] J. Koelman *et al.*, Phys. Rev. A **38**, 3535 (1988).

[32] J. Vanier and C. Audoin, *The Quantum Physics of Atomic Frequency Standards* (Adam Hilger, Bristol, 1989), p. 118.

[33] J. Vanier and C. Audoin, *The Quantum Physics of Atomic Frequency Standards* (Adam Hilger, Bristol, 1989), p. 119.

[34] J. Vanier and C. Audoin, *The Quantum Physics of Atomic Frequency Standards* (Adam Hilger, Bristol, 1989), p. 983.

[35] J. Vanier and C. Audoin, *The Quantum Physics of Atomic Frequency Standards* (Adam Hilger, Bristol, 1989), p. 121.

[36] N. Ramsey, Phys. Rev. **100**, 1191 (1955).

[37] H. Andresen, Technical report, United States Army Electronics Command (unpublished).

[38] J.-Y. Savard *et al.*, Can. J. Phys. **57**, 904 (1979).

[39] P. Bender, Phys. Rev. **132**, 7154 (1963).

[40] C. Cohen-Tannoudji, J. Dupont-Roc, and G. Grynberg, *Atom-Photon Interactions* (J. Wiley and Sons, New York, 1992), Chap. VI.

[41] R. Bluhm, V. Kostelecký, and N. Russell, Phys. Rev. Lett. **82**, 2254 (1999).

[42] E. Mattison and R. Vessot, Technical report, Jet Propulsion Laboratory (unpublished).

[43] N. Ramsey, *Molecular Beams* (Clarendon Press, Oxford, 1956), Chap. 2.

[44] M. Sucher and J. Fox, *Handbook of Microwave Measurements* (Polytechnic Press, New York, 1963), Vol. 2, Chap. VIII.

[45] E. Mattison, W. Shen, and R. Vessot, in *Proceedings of the 39th Annual Frequency Contol Symposium* (IEEE, New York, 1985), p. 72.

[46] R. Vessot and E. Mattison, Technical report, Jet Propulsion Laboratory (unpublished).

[47] D. Allan, Proc. IEEE **54**, 221 (1966).

[48] J. Barnes *et al.*, Trans. on Instr. and Meas. **20**, 105 (1971).

[49] R. Vessot, L. Mueller, and J. Vanier, Proc. IEEE **54**, 199 (1966).

[50] V. Kostelecký and S. Samuel, Phys. Rev. Lett. **63**, 224 (1989).

[51] V. Kostelecký and S. Samuel, Phys. Rev. D **40**, 1886 (1989).

[52] V. Kostelecký and S. Samuel, Phys. Rev. Lett. **66**, 1811 (1991).

[53] V. Kostelecký and S. Samuel, Phys. Rev. D **39**, 683 (1989).

[54] V. Kostelecký and R. Potting, Nucl. Phys. B **359**, 545 (1991).

[55] V. Kostelecký and R. Potting, Phys. Lett. B **381**, 89 (1996).

[56] V. Kostelecký, M. Perry, and R. Potting, Phys. Rev. Lett. **84**, 4541 (2000).

[57] V. Kostelecký and R. Potting, in *Gamma Ray-Neutrino Cosmology and Planck Scale Physics*, edited by D. Cline (World Scientific, Singapore, 1993), see also (hepth/9211116).

[58] V. Kostelecký and R. Potting, Phys. Rev. D **51**, 3923 (1995).

[59] D. Colladay and V. Kostelecký, Phys. Rev. D **55**, 6760 (1997).

[60] D. Colladay and V. Kostelecký, Phys. Rev. D **58**, 116002 (1998).

[61] R. Mittleman, I. Ioannou, H. Dehmelt, and N. Russell, Phys. Rev. Lett. **83**, 2116 (1999).

[62] C. Berglund *et al.*, Phys. Rev. Lett. **75**, 1879 (1995).

[63] B. Heckel, presented at the International Conference on Orbis Scientiae 1999, Fort Lauderdale, Florida, Dec., 1999.

[64] D. Bear *et al.*, Phys. Rev. Lett. **85**, 5038 (2000).

[65] H. Dehmelt, R. Mittleman, R. V. Dyck, and P. Schwinberg, Phys. Rev. Lett. **83**, 4694 (1999).

[66] E. Adelberger *et al.*, in *Physics Beyond the Standard Model*, edited by P. Herczeg, C. Hoffman, and H. Klapdor-Kleingrothaus (World Scientific, Singapore, 1999), p. 717.

[67] M. Harris, Ph.D. thesis, Univ. of Washington, 1998.

[68] P. Bender, Phys. Rev. **132**, 2154 (1963).

[69] W. Press, S. Teukolsky, W. Vetterling, and B. Flannery, *Numerical Recipes in C*, 2nd ed. (Cambridge University Press, Cambridge, 1988), p. 689.

[70] P. R. Bevington and D. K. Robinson, *Data Reduction and Error Analysis for the Physical Sciences* (McGraw Hill, New York, 1992), p. 64.

[71] E. Purcell and G. Field, Astrophys. J. **124**, 542 (1956).

[72] J. Wittke and R. Dicke, Phys. Rev. **103**, 620 (1956).

[73] A. Dalgarno, Proc. R. Soc. London, Ser. A **262**, 132 (1961).

[74] L. Balling, R. Hanson, and F. Pipkin, Phys. Rev. **133**, A607 (1964).

[75] A. Allison, Phys. Rev. A **5**, 2695 (1972).

[76] S. Crampton and H. Wang, Phys. Rev. A **12**, 1305 (1975).

[77] A. Berlinsky and B. Shizgal, Can. J. Phys. **58**, 881 (1980).

[78] M. Desaintfuscien, Ph.D. thesis, University of Paris, 1975.

[79] R. Vessot, E. Mattison, and E. Imbier, in *Proceedings of the 37th Annual Frequency Control Symposium* (IEEE, New York, 1983), p. 49.

[80] J. Krupczak *et al.*, in *Proceedings International Cryogenic Materials Conference/Cryogenic Engineering Conference* (Plenum Press, New York, 1996), p. 1769.

[81] S. Crampton *et al.*, Phys. Rev. Lett. **42**, 1039 (1979).

[82] I. Silvera and J. Walraven, Phys. Rev. Lett. **44**, 164 (1980).

[83] R. Jochemsen, M. Morrow, A. Berlinsky, and W. Hardy, Phys. Rev. Lett. **47**, 852 (1981).

[84] M. Morrow, R. Jochemsen, A. Berlinksky, and W. Hardy, Phys. Rev. Lett. **46**, 195 (1981).

[85] M. Morrow, R. Jochemsen, A. Berlinksky, and W. Hardy, Phys. Rev. Lett. **47**, 455 (1981).

[86] R. Walsworth, Ph.D. thesis, Harvard University, 1991.

[87] J. Walraven and I. Silvera, Rev. Sci. Instrum. **53**, 1167 (1982).

[88] G. White, *Experimental Techniques in Low-Temperature Physics* (English Universities Press LTD, London, 1964).

[89] J. Groslambert, D. Fest, M. Oliver, and J. Gagnepain, in *Proceedings of the 35th Annual Frequency Control Symposium* (Electronics Industries Association, Washington, D.C., 1981), p. 458.

[90] G. Nunes, in *Experimental Techniques in Condensed Matter Physics at Low Temperatures*, edited by R. Richardson and E. Smith (Addison-Wesley, Reading, MA, 1988), Chap. 2.

[91] F. Pobell, *Matter and Methods at Low Temperatures*, 2nd ed. (Springer, Berlin, 1996).

[92] A. Rose-Innes, *Low-Temperature Techniques* (Oxford University Press, Oxford, 1979), p. 6.

[93] W. Kolos and L. Wolniewicz, J. Chem. Phys. **43**, 2429 (1965).

[94] S. Crampton, J. Duvivier, G. Read, and E. Williams, Phys. Rev. A **5**, 1752 (1972).

[95] M. Desaintfuscien and C. Audoin, Phys. Rev. A **13**, 2070 (1976).

[96] S. Kokkelmans and B. Verhaar, Phys. Rev. A **56**, 4038 (1997).

[97] B. Zygelman, A. Dalgarno, M. Jamieson, and P. Stancil, Phys. Rev. A (in press).

[98] M. Hayden and W. Hardy, Phys. Rev. Lett. **76**, 2041 (1996).

[99] V. Folen *et al.*, Technical report, Naval Research Laboratory (unpublished).